Extending the Senses of Ubiquitous Devices

Anandghan Waghmare

A dissertation
submitted in partial fulfillment of the
requirements for the degree of

Doctor of Philosophy

University of Washington

2025

Reading Committee:
Shwetak Patel, Chair
Vikram Iyer
Joshua Smith

Program Authorized to Offer Degree:
Computer Science and Engineering

University of Washington

Abstract

Extending the Senses of Ubiquitous Devices

Anandghan Waghmare

Chair of the Supervisory Committee:
Shwetak Patel
Computer Science and Engineering

Modern smart devices come equipped with a wide array of sensors, many of which can be repurposed for functionalities beyond their original intent through side-channel sensing. While this technique offers innovative uses without altering hardware, the enhancements it provides are often modest. In contrast, incorporating new hardware can dramatically expand a device's capabilities but entails significant costs and lengthy redesign cycles. This thesis investigates two strategies to bridge this trade-off, aiming to unlock the full potential of side-channel sensing on existing platforms. The first strategy involves user-friendly, low-cost, low-power sensor add-ons that enhance device functionality without requiring internal hardware changes. The second strategy targets manufacturers, proposing selective hardware upgrades to improve performance with minimal cost and development overhead.

To demonstrate the efficacy of these approaches, the thesis presents several real-world applications: a smartphone-based glucose testing add-on for accessible at-home pre-diabetes screening; a toolkit to streamline the development of rapid diagnostic test attachments; a versatile, energy-efficient sensor platform for smartwatches that supports integration of external sensors; and targeted hardware enhancements—such as increased bio-impedance sensing bandwidth in rings and wristbands—that enable richer contextual interactions and novel input methods.

These research projects demonstrate the practical viability and versatility of augmenting side-channel sensing through both user-centric and manufacturer-driven enhancements. The thesis concludes by outlining how strategic improvements to existing devices can democratize access to advanced sensing technologies and inform future research and design in ubiquitous computing.

Extending the Senses of Ubiquitous Devices

Anandghan Waghmare

TABLE OF CONTENTS

LIST OF FIGURES

Figure Number Page

ACKNOWLEDGMENTS

Completing this doctoral journey would not have been possible without the unwavering support, guidance, and encouragement of numerous individuals. I am deeply grateful to each of them.

First and foremost, I extend my profound gratitude to my advisor, Dr. Shwetak Patel, for his constant support, trust, and mentorship throughout my PhD. His vision and belief in my abilities were instrumental in shaping this research.

I am immensely thankful to my committee members, Dr. Joshua Smith and Dr. Vikram Iyer, for their invaluable guidance, insightful feedback, and the intellectual rigor they brought to this work. Their expertise significantly enriched the scope and depth of my research. I sincerely appreciate Dr. Beth Kolko for her dedicated service as my Graduate Student Representative (GSR). Her support and advocacy were invaluable.

I would also like to thank all my industry collaborators for their partnership and for providing the crucial real-world context and invaluable resources..

To the exceptionally talented Master's and Bachelor's students with whom I had the privilege to work. Your dedication, enthusiasm, and contributions were truly inspiring.

My heartfelt thanks to my labmates, past and present, for making the PhD journey a delightful and memorable experience. Your company, lively discussions, and countless shared moments made every challenge more manageable and every success so much more meaningful.

And to my friends, thank you for your constant support, understanding, and for being there through every up and down. Your friendship was a vital source of strength.

I am sincerely grateful to the Paul G. Allen School of Computer Science & Engineering

(UW CSE) department and its dedicated staff for providing an exceptional environment, resources, and support throughout my doctoral studies.

Finally, and most importantly, I want to express my deepest gratitude to my family. To my parents, thank you for allowing me the freedom to pursue my aspirations and for your unwavering and constant support. Your belief in me has been my greatest gift. To my sister and brother-in-law, thank you for your steadfast support and encouragement. And to my tiny niece and nephew, thank you for being the pure joy and light in my life; your presence always reminded me of what truly matters.

DEDICATION

Dedicated to my आई (mom) and पप्पा (dad).

Chapter 1

SIDE-CHANNEL SENSING

As consumer electronics advanced, manufacturers harnessed the potential of sensors to transform device capabilities. These sensors didn't just enhance functionality; they also provided insights into user context and intentions. For instance, an Inertial Measurement Unit (IMU) is used to detect phone orientation for automatic screen rotation. What began as straightforward applications soon inspired technologists to think creatively. They found that these sensors could be used for purposes beyond their intended design. For example, earlier research showed how a phone's microphone and speaker could enable gestural interactions with the phone, while its camera and flash could measure heart rate. Even ambient light sensors, typically used to adjust screen brightness, can detect subtle physiological shifts like altered breathing patterns, as these can cause minor, detectable light fluctuations.

Today, we are surrounded by ubiquitous devices such as smartphones and smartwatches, each equipped with advanced sensors designed for specific functions. The widespread presence of these sensors offers a compelling opportunity: repurposing them for applications beyond their original intent to enhance device functionality and enable entirely new use cases. This thesis designates this paradigm as "side-channel sensing". This approach involves creatively leveraging sensors in unconventional ways to detect subtle signals and infer information beyond their primary purpose. By tapping into underutilized sensor data, we can unlock innovative applications and enrich user experiences. Side-channel sensing not only maximizes the utility of existing hardware but also pushes the boundaries of what our devices can achieve—supporting new capabilities even if they weren't initially designed for them. This thesis explores novel techniques in

side-channel sensing to drive advancements in healthcare and spatial computing.

1.1 Defining Side-Channel Sensing

The term “side-channel” originated in cybersecurity, where it referred to exploiting unintended information leaks from a system. These leaks could be electrical signals, electromagnetic waves, or even timing variations. By analyzing these leaks, attackers could gain unauthorized access or extract sensitive data. Classic examples include power analysis attacks, where monitoring a device’s power consumption reveals information about the data being processed, and cache timing attacks, where analyzing how long it takes a processor to access data from its cache can reveal details about the data itself.

I adapt this concept to the field of ubiquitous computing, utilizing data streams with user consent from existing or augmented sensors in common consumer electronic devices to unlock new functionalities. Unlike traditional side-channel attacks that exploit unintended leaks, this approach leverages sensor data streams with direct and authorized access. The goal is to utilize these data streams for new, beneficial functionalities for the user without requiring significant modifications to the device itself. These data streams can originate from various sources, like ambient sensors that capture information about the user’s environment or data generated during user interactions with the device, either explicitly (e.g., holding the phone in a certain way) or implicitly (e.g., typing patterns on a phone).

By employing signal processing and machine learning techniques on these combined data streams, side-channel sensing can provide functionalities across various domains, such as health sensing and human-computer interaction.

1.2 Primary Dimensions of Side-Channel Sensing

Side-channel sensing aims to extend the functionality of users’ existing devices by leveraging the capabilities of built-in or augmented sensors. The range of functionalities that

can be offered varies significantly based on the device's inherent capabilities and the extent to which it is modified. For example, using a smartphone's camera (possibly with the flash) to detect heart rate through publicly available software APIs is a straightforward application that utilizes the device's existing hardware without any modifications. On the other end of the spectrum, more complex functionalities, such as thermal imaging with a phone, might require substantial enhancements to the device's hardware and software.

The augmentation of a device can significantly boost its functionality, but this also introduces practicality trade-offs. For instance, if a side-channel application only necessitates the installation of a smartphone app, it is highly practical and easily adoptable by a broad audience of users with compatible phones. On the contrary, applications that require new hardware updates entail a more complicated setup. The feasibility of such applications and their broad adoption hinge on manufacturers' willingness to make these changes, which may not always align with market readiness or consumer demand.

Therefore, the two pivotal aspects of side-channel sensing involve the sources of data acquisition, which provide different levels of "functionality" and the "practicality" of each approach, which dictates the ease of adoption and overall user experience. This balance between enhancing device functionality and maintaining user convenience is crucial in determining the success and impact of side-channel sensing technologies.

1.3 Relationship between the Primary Dimensions

The success of side-channel sensing hinges on a critical balance between functionality and practicality. Generally, applications offering more advanced features require greater modifications to the device, which can hinder user adoption.

Functionality is directly tied to the richness of software and hardware available. On the software side, access to relevant data streams plays a crucial role. Manufacturers often provide public APIs for accessing data from common sensors like accelerometers and gyroscopes (IMU data). However, some data streams, like raw data from the capacitive

touch screen, remain hidden from developers for various reasons. For these hidden data streams, developers might resort to custom OS patches that expose the data. Alternatively, manufacturers may choose to open up access to these streams through over-the-air software updates. This approach allows for broader adoption of side-channel sensing applications, even if initial software limitations exist.

Hardware presents a steeper challenge. If an application requires new hardware updates, it faces a significant hurdle in transitioning from research to widespread use. Applications that leverage existing hardware are more practical, even if they offer limited functionality, than those requiring new hardware with greater capabilities.

However, the ideal scenario for users would be to achieve both high functionality and high practicality. In this thesis, I will outline my efforts to develop hardware augmentations that push the boundaries of functionality without sacrificing practicality. By exploring hardware augmentations, my research aims to unlock the full potential of side-channel sensing while ensuring widespread adoption and user satisfaction.

1.4 Achieving Practical Side-Channel Sensing

This thesis explores two key approaches to achieve the ideal balance of higher functionality and high practicality in side-channel sensing. The first approach focuses on developing cost-effective and power-efficient hardware add-ons for existing devices and the second looks into hardware modifications for enhanced capabilities. Figure 1.1 shows the design space between functionality and practicality [21] and comparison between the different approaches and the tradeoffs as explored in this thesis.

1.4.1 Low-Cost and Low-Power hardware add-ons

This approach revolves around designing and testing hardware add-ons that prioritize three key aspects: cross-device compatibility, affordability, and low power consumption. Firstly, these add-ons should be versatile, working seamlessly with various commercially

available devices. This ensures broader user adoption and avoids limitations specific to certain device models. Secondly, cost is a crucial factor. Users should be able to readily afford these add-ons, making the technology accessible to a larger audience. Finally, minimizing power consumption is essential. The add-ons should have minimal impact on battery life, avoiding the need for frequent charging and ensuring a smooth user experience. By focusing on these priorities, we can create side-channel sensing add-ons that are practical, user-friendly, and widely adoptable.

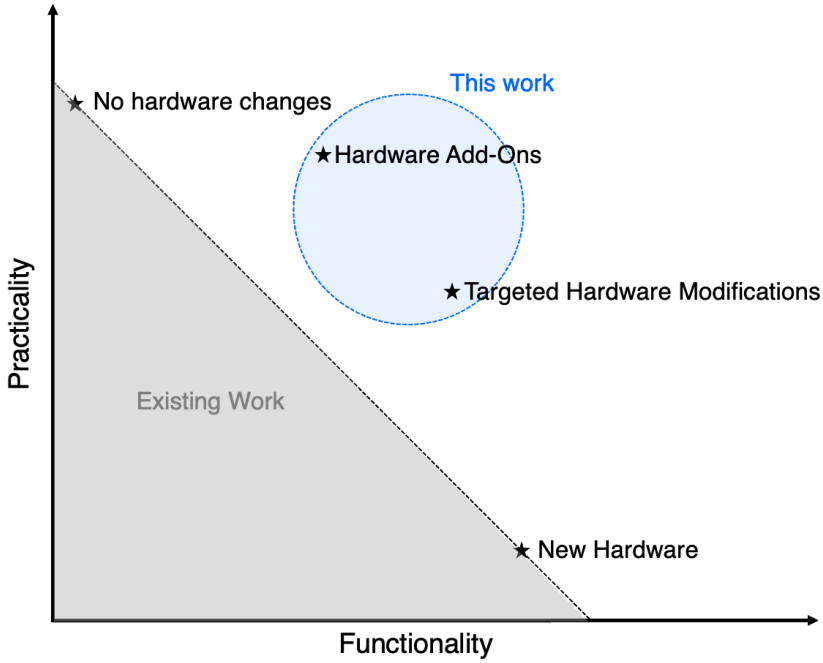

Figure 1.1: This figure illustrates the trade-off between functionality and practicality in side-channel sensing. Applications requiring minimal hardware changes offer the most practicality, while those requiring new hardware may offer greater functionality but at the cost of reduced practicality. The ideal scenario lies in the middle ground, where functionality is enhanced without sacrificing ease of use. Hardware add-ons and modifications can offer a practical way to achieve this balance.

Hardware add-ons offer a compelling solution with several key benefits. Firstly, by offloading complex data processing to the smart device itself, the add-on can remain simple in design and cost-effective to produce. This division of labor ensures efficient utilization of resources – the add-on collects the raw data, while the smart device handles the heavy lifting of analysis. Secondly, these add-ons can act as bridges, making data from external sources accessible to the smart device. This opens doors to a wider range of functionalities and unlocks the potential for side-channel sensing to interact with a much richer ecosystem of data streams, going beyond the limitations of the built-in sensors.

1.4.2 Hardware Modifications for Enhanced Capabilities

Hardware add-ons offer a compelling solution for expanding functionalities, but some applications might demand a deeper dive – modifications to the existing hardware on the smart devices themselves. While this approach may seem less practical compared to simple add-ons, it holds significant advantages over a complete redesign or developing entirely new components from scratch.

The key lies in reducing costs and development time. Modifying existing hardware is generally less expensive and time-consuming than a complete overhaul. This translates to lower Bill of Materials (BOM) costs for manufacturers, making the technology more commercially viable. Since existing components form the base, development cycles are shorter compared to designing entirely new hardware from scratch.

Furthermore, this approach helps preserve user familiarity. Extensive hardware modifications can drastically alter the form and function of a device, potentially alienating users. By modifying existing hardware, we can introduce new functionalities without significantly changing the user experience. This ensures a smoother transition for existing users who are already familiar with the device's form and operation. In essence, we can enhance functionalities without sacrificing user comfort and ease of use.

1.5 Document Organization

This dissertation is structured to systematically present the exploration of novel techniques for enhancing side-channel sensing capabilities on ubiquitous devices. The document is organized into three main parts, followed by a concluding summary.

Part I: Introduction lays the foundational groundwork for the thesis. Chapter 1 introduces the concept of side-channel sensing, defining its scope and discussing the trade-offs between functionality and practicality in extending device capabilities through this paradigm. Chapter 2 provides an overview of existing background work in side-channel sensing, setting the stage for the novel contributions presented in subsequent chapters.

Part II: Enhancing Side-Channel Sensing with Sensor Add-ons delves into the first key approach: developing low-cost, low-power sensor add-ons that enhance functionality without requiring internal modifications to the host device. Chapter 3 details GlucoScreen, a cost-effective, smartphone-based glucose testing add-on designed for at-home pre-diabetes screenings, aiming to make healthcare more accessible. Building on this, Chapter 4 introduces PhoneScreen, a hardware development toolkit for rapid test strip integration, which streamlines the development process for diverse diagnostic add-ons. Chapter 5 then broadens the scope to wearables, presenting WatchLink, a modular add-on platform that extends smartwatch sensing by allowing the integration of external sensors with minimal additional hardware, utilizing the smartwatch's ECG interface for low-cost, low-power communication.

Part III: Enhancing Side-Channel Sensing with Targeted Hardware Modifications explores the second key technique, focusing on making targeted upgrades to existing hardware to improve functionalities at reduced time and cost. This approach aims to introduce new functionalities without significantly changing the user experience, preserving user familiarity. This part specifically focuses on enhancing bio-impedance sensing hardware commonly available on smartwatches and smart rings by upgrading its tradi-

tional tens-of-kHz operational range to the MHz range with a wider bandwidth, thereby unlocking a new spectrum of applications. Chapter 6 presents Z-Ring, a ring-based system that leverages wideband bio-impedance sensing for gesture, object, touch, and user recognition, demonstrating how subtle modifications to a ring form factor can unlock rich interaction. Chapter 7 then showcases Z-Band, a wristband-based wideband bio-impedance sensing system for touch interaction on everyday uninstrumented surfaces, illustrating how a similar principle can transform a common wearable into a versatile interface for the physical world.

Finally, Chapter 8 provides a summary of the thesis, distilling key insights gained throughout the research and outlining promising avenues for future research.

Chapter 2

BACKGROUND

Side-channel sensing has emerged as a promising technique to unlock hidden capabilities within existing devices, leveraging unintended emissions or signals from devices to gather information about their operation or environment. Unlike traditional sensing methods that rely on dedicated sensors, side-channel sensing repurposes existing hardware components or exploits subtle side effects of their operation.

Research in this field has revealed a wealth of information hidden within these seemingly innocuous signals. For example, typing patterns (keystroke dynamics) are shown to be used for user authentication, acting as a continuous biometric [186, 39]. Additionally, phone usage patterns have been shown to correlate with mental health and can even predict depression [233, 102, 222]. The applications of side-channel sensing are far-reaching and diverse. In healthcare, it has enabled non-invasive health monitoring by extracting physiological signals, such as heart and respiratory rates, from subtle body movements captured by smartphone accelerometers. In the realm of security, side-channel attacks have exposed vulnerabilities in cryptographic systems through information leakage via variations in execution time or power consumption [184, 154]. Additionally, side-channel sensing finds applications in smart homes, monitoring occupancy and energy usage, and in environmental monitoring, detecting changes in temperature, humidity, and other factors [51, 89].

Prior research has explored the concept of side-channel sensing, utilizing various diverse sensing approaches. For example, ElectriSense utilizes the powerline infrastructure in a home to detect EMI events for home energy monitoring [89], while SNUPI employs a home's power lines as the antenna for low-power wireless communication

throughout the premises [51]. Similarly, uTouch detects touch on unmodified LCD screens by observing noise on the power line [47], and Ambient Backscatter advances this by modulating the reflection of existing ambient radio power from TV broadcasts for wireless communication [151]. PaperID modulates the response from a printed RFID tag with human touch, enabling a battery-free method to alter the RFID tag response [140].

These techniques have also been adapted to smart devices to specifically facilitate ultra-low-power systems that interact with unmodified commodity devices. A wide array of modalities has been explored: audio, RF, optical light, LiDAR, capacitive, vibration motor, IMU, and more. UbiquiTouch is a 31 microWatt wireless touch interface that co-opts the radio receiver on an FM-radio-enabled smartphone to relay its touch points [228], entirely powered by solar energy, thus eliminating the need for batteries. SideSwipe leverages the GSM cellular radio on phones to detect non-contact swipe gestures over the phone [274]. LightAnchors [22] and InfoLED [247] enable visible light communication to a smartphone via its 240 Hz high-speed camera by modulating single LEDs found in various electronics. SoundWave [88] facilitates non-contact, real-time, in-air gestures on commodity devices by examining Doppler shifts in reflected audio. Additionally, Wang et al. use audio phase shifts to detect hand movement on a commodity phone [235]. For testing water contamination, alcohol concentration, and proteinuria diagnosis, Yue and Katabi [251] employ the phone's vibration motor, flashlight, and camera to capture the surface tension of liquids. Likewise, Chan et al. [42] have successfully observed the reflected laser speckle pattern from smartphone LiDAR to distinguish between ten liquids and monitor the coagulation of a single drop of blood.

Existing side-channel sensing techniques, while promising, offer only limited capabilities, providing a slight enhancement to current functionalities. Achieving more significant advancements typically necessitates adding complex new hardware, a solution that boosts functionality but compromises practicality and increases adoption barriers.

This thesis addresses these limitations by introducing novel side-channel sensing techniques. My approach significantly improves functionality while maintaining a crucial

balance with practicality. I aim to unlock the hidden potential within existing devices, transforming them into powerful sensing platforms, and I demonstrate these advancements through real-world applications.

INTRODUCTION TO PART II: ENHANCING SIDE-CHANNEL SENSING WITH SENSOR ADD-ONS

Part II of this work introduces side-channel sensing through the development of simple, low-cost, low-power hardware add-ons. This approach centers on designing and testing these add-ons with a strong emphasis on cross-device compatibility, affordability, and low power consumption. The goal is to create versatile solutions that integrate seamlessly with a wide range of commercially available devices, making the technology accessible to a broader audience without incurring high costs or draining device batteries. This strategic focus ensures the add-ons are not only practical and user-friendly but also widely adoptable for various sensing applications.

This part of the thesis delves into several innovative applications of this philosophy. Chapter 3 explores adding diagnostic capabilities to smartphones, specifically detailing a glucose test strip add-on for prediabetes screening. Building on this, Chapter 4 focuses on accelerating the add-on development itself, presenting a toolkit for rapid test strip integration to streamline future diagnostic add-on creation. Finally, I broaden the scope to wearables in Chapter 5, which demonstrates how smartwatches can be transformed into more powerful and versatile sensing hubs.

Chapter 3

ADDING DIAGNOSTIC CAPABILITIES TO SMARTPHONES: A GLUCOSE TEST STRIP ADD-ON FOR PREDIABETES SCREENING

In this section, I present GlucoScreen which is a smartphone-based low-cost readerless glucose test strip for prediabetes screening. GlucoScreen attaches to the phone as an add-on and enables the phone to perform blood glucose testing, eliminating the need for a separate glucose testing strip reader. This approach significantly reduces screening costs while leveraging the widespread availability of smartphones.

3.1 Introduction

Diabetes mellitus (DM), a chronic medical condition, is known for causing severe health complications such as kidney failure, heart disease, and stroke, with an increasing number of cases globally. By 2021, the number of adults diagnosed with diabetes reached 537 million [8]. Over the past two years, this number has increased by 16% and is projected to surge by 46% to 783 million by 2045, surpassing the rate of population growth and resulting in one in every eight adults requiring medical attention. In the United States, it is estimated that 38% of adults have prediabetes [10], a state where blood sugar levels are elevated but not high enough to qualify as type 2 diabetes, yet it signals a high risk of developing the condition in the future. Alarmingly, only 19% of these individuals with prediabetes have been informed of their status by a healthcare professional [10], highlighting a significant disconnect between the recognition of risk and actual awareness.

Accessible preventive screening for diabetes and prediabetes can facilitate early detection and, potentially, reversal through lifestyle changes. Current screening methods encompass blood sugar assessments conducted through laboratory tests or point-of-care

devices, known as portable glucose monitors (PGMs) or glucometers [167]. Although these techniques are effective, they are also expensive [33] and often necessitate the use of additional devices or access to specialized testing facilities [166]. Consequently, many cases remain undiagnosed and untreated, underscoring the need for a more accessible and affordable method to screen individuals likely to develop prediabetes.

The most commonly utilized blood glucose testing device is the portable glucometer, a standalone device that interfaces with an electrochemically activated test strip to deliver quick blood glucose readings. Glucometers operate by analyzing a small blood sample, typically obtained from the fingertip, which is applied to a test strip. Although the cost of individual test strips is less than a dollar, they are sold in batches, and the glucometer itself generally costs between $20-80$ [13].

The initial expense of acquiring a glucometer setup gradually becomes more economical for regular users, such as individuals diagnosed with diabetes who need to check their blood sugar levels daily. However, this amortization does not necessarily benefit those using the device for screening purposes, as screening for at-risk individuals is advised only every three years [4].

Hence, reducing the financial and accessibility barriers to preventive screening for prediabetes is not only medically advisable but also economically sensible in the long run, particularly in low- and middle-income countries [110].

To respond to the need for a cost-efficient, effective, and in-home prediabetes testing approach, I developed GlucoScreen, a low-cost, battery-free, standalone glucose testing strip readable by any smartphone that measures blood glucose without the need for an external reader. A smartphone app guides GlucoScreen users through steps needed to perform a fasting blood sugar or glucose tolerance self-test, both of which can indicate whether they have diabetes or prediabetes[212]. Such screening can help users make informed decisions about whether to follow up and seek in-person medical care from a clinician. At-home screening also lowers the barrier to action for getting screened, thereby increasing the likelihood of more people getting screened.

GlucoScreen uses a novel means of communication from the test strip to the phone: it electronically generates touch events from the test strip through the phone's capacitive touchscreen. This technique uses conventional glucose test strips enhanced with low-cost components. Once the smartphone processes the touchscreen events, they become available for immediate readout and storage locally or in an internet-connected health record.

This communication method between test strip and phone consumes only 10 μW of power, orders of magnitude less than conventional low-power communication approaches, which can be easily harvested from the phones' flash. This technique eliminates the need for batteries – which are common in other wireless communication methods, such as BLE (Bluetooth Low Energy), ZigBee, or ANT [57] – lowering costs and extending shelf life.

This research demonstrates and evaluates the touchscreen-based communication technique for blood sugar testing. This new technique holds additional promise for building readerless assays for other electrochemical reaction-based tests, such as detecting heavy metals in water, detecting sodium in urine, and detecting malaria [169].

This work presents the following key contributions:

1. I introduce the design of an economical, low-power blood glucose test strip that facilitates diabetes prescreening through smartphones.

2. I develop a hardware solution for amperometric detection in glucose testing, which encodes and transmits results directly to a smartphone via its capacitive touchscreen.

3. I provide findings from both benchtop and clinical evaluations of this system. In the benchtop analysis, I utilized various artificial glucose solutions, multiple smartphone models, and different brands of test strips to confirm that the test strip operates effectively across different devices and glucose levels. In the clinical trial involving 75 participants, I validate the accuracy of this method with real blood samples and benchmark the results against those obtained from conventional glucometers.

3.2 Related Work

I explore three critical areas essential for developing a low-cost, readerless glucose monitoring system: glucose sensing technologies, smartphone-based biosensing interfaces, and capacitive touchscreen-based sensing on smartphones. I assess the latest technological advancements in these fields and identify the technological gaps in creating an affordable, readerless glucose monitoring system.

3.2.1 Glucose Sensing

Common glucose biosensors typically involve blood interactions with external enzymes to determine glucose levels. Widely used enzymes include hexokinase, glucose oxidase (GOx), and glucose-1-dehydrogenase (GDH) [250, 179]. In many clinical settings, the hexokinase method, which utilizes spectrophotometry, is the standard [202]. Point-of-care glucose monitoring devices generally rely on the enzymatic activities of GOx and GDH. GOx is favored for its affordability, ease of access, and straightforward storage requirements, making it suitable for non-laboratory environments [97, 32]; thus, it is regarded as the gold standard for glucose testing [72] and is commonly used in self-monitoring blood glucose devices.

Commercially, GOx-based sensors are marketed as glucose test strips that work with a dedicated reader. These enzyme-based biosensors require a small blood sample, usually obtained through a finger prick or venous draw, and come in two forms: standalone test strip readers [16] and models that connect to smartphones via Bluetooth or USB [17, 18]. Standalone devices display and sometimes store results, while smartphone-connected variants utilize an app for display and storage.

Non-invasive glucose measurement methods include optical, microwave, and electrochemical techniques. Optical techniques, such as near-infrared (NIR) and mid-infrared (MIR) spectroscopy, optical polarimetry (OP), Raman spectroscopy, fluorescence methods, and optical coherence tomography (OCT), measure glucose by analyzing light

interactions with body tissues [128, 30, 178, 180, 160, 90, 197, 127, 74]. Microwave techniques analyze the dielectric changes in blood and tissues caused by glucose fluctuations, providing another non-invasive, continuous monitoring method. However, these methods generally show low correlation with actual glucose levels and are influenced by factors like skin tone and age [214].

Electrochemical techniques correlate biofluids like saliva, tears, sweat, and interstitial fluid with glucose levels, offering indirect glucose measurements. These methods face challenges such as low sensitivity, delayed results, and the need for calibration [214].

Colorimetric methods offer a visual indication of glucose levels by changing color in response to glucose in bodily fluids like saliva, sweat, and blood [163, 78, 198, 96, 258, 65, 68, 230]. However, they can be prone to interference from other substances in clinical samples, affecting their reliability and causing challenges in visual interpretation [62].

3.2.2 Phone-Based Biosensing

The widespread availability and connectivity of smartphones are transforming mobile health, making them viable platforms for biosensing. I review recent developments in smartphone-based biosensing systems.

Research has employed smartphone cameras alongside attachments to analyze standard cholesterol test strips for cholesterol testing [175], detect influenza viruses using fluorogenic assays [165], measure vitamin D levels [139], detect allergens in food [54], and identify biomarkers in milk extracts [155]. Systems that use camera sensors can be sensitive to ambient lighting conditions, often requiring additional components like specific housing units and external lighting to mitigate these issues [181].

Other methods include detecting fluid viscosity and surface tension using smartphone sensors like LiDAR, cameras, and accelerometers, which can indicate the composition of liquids [26, 101, 43, 252]. However, such techniques have proven unreliable for predicting blood glucose [27].

Some devices display test results and communicate them to smartphones wirelessly via

Bluetooth [125, 108, 256, 77] or NFC/RFID [246, 111, 31], or physically connect through USB dongles [148, 219, 132, 61, 29]. While wireless devices are portable, they require complex, battery-dependent components. In contrast, USB and NFC devices utilize sophisticated microcontrollers, which add to the cost.

Methods that connect via the phone's analog audio jack allow for simpler, battery-free operations [236, 207, 206, 170], but as phone manufacturers phase out analog audio ports, there remains a need for a cost-effective, low-power interface for connecting biosensors to smartphones.

3.2.3 Capacitive Sensing on Smartphones

Modern capacitive touchscreens enable versatile multitouch interactions. Recent studies have expanded the use of capacitive sensing to novel applications [45, 129, 194, 223, 193, 107]. For instance, they have been used to predict finger touch angles [185], identify users via body imaging [87, 98], and recognize body postures and facilitate human-object interactions through extended capacitive sensing [239]. These advancements illustrate the vast potential of capacitive touch sensing; this work details how it can be leveraged for low-power data communication with smartphones.

3.3 Theory of Operation

Addressing the critical need for scalable, cost-effective prediabetes screening to enhance public health, and the absence of affordable, efficient glucose testing options, I introduce GlucoScreen.

3.3.1 Concept

GlucoScreen is a standalone, disposable glucose testing strip engineered for economical, single-use blood glucose measurement. It transmits glucose data directly to a smartphone without requiring any additional devices like a dedicated reader. To conduct a test, users

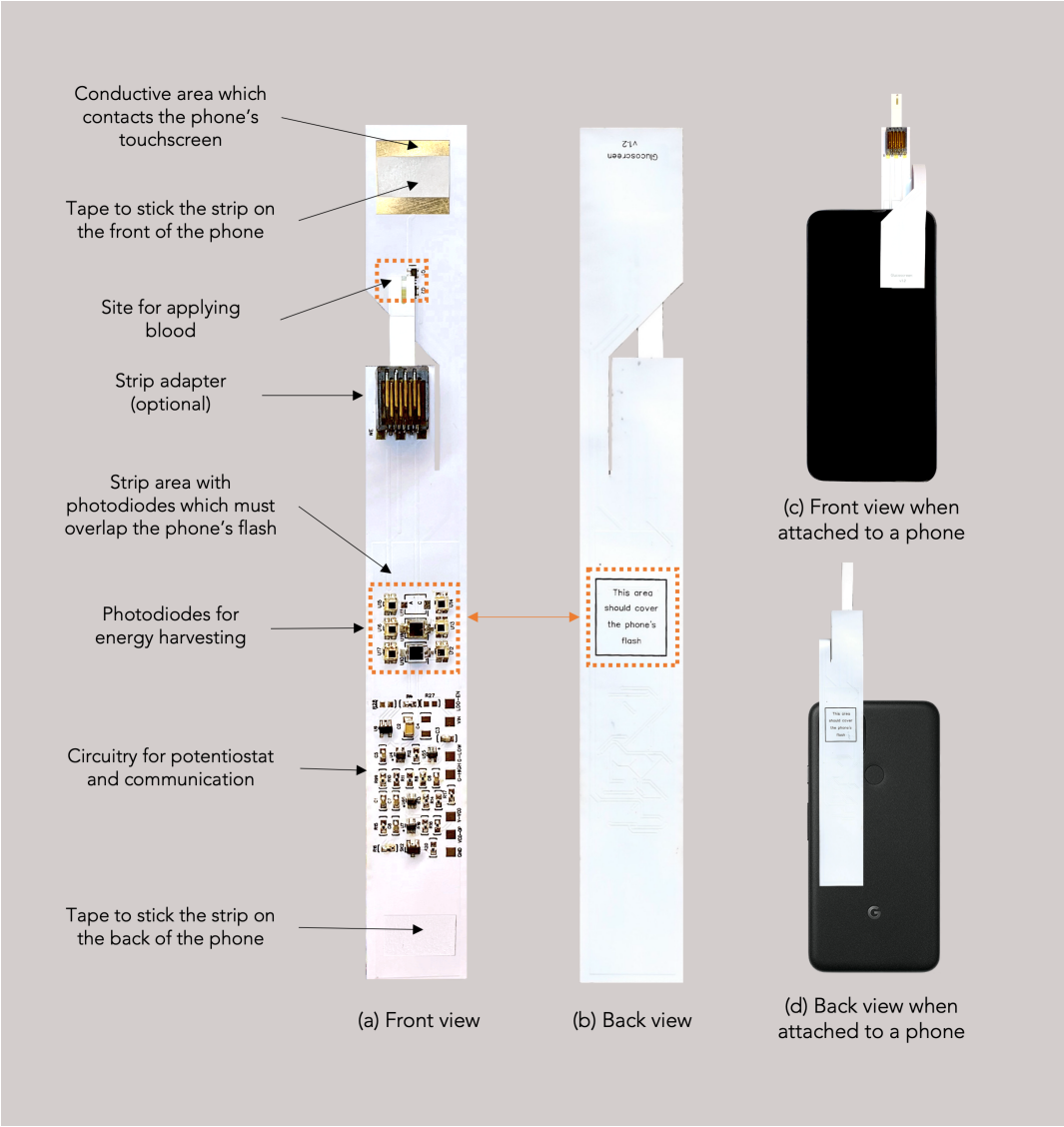

Figure 3.1: GlucoScreen prototype. The GlucoScreen prototype contains circuitry that lets it conduct the response signal from commercially available electrochemical blood-glucose test strips directly to the capacitive touch sensor of any smartphone via pulse-width-modulated "touch events" interpretable by any phone with a capacitive touch screen. This is done via ultra-low power energy harvesting from the phone's flash module, resulting in a novel, low-cost, self-contained blood-glucose test that obviates the need for an external reader.

attach the GlucoScreen strip to their smartphone, then apply a small blood sample obtained via a finger prick with a disposable lancet to the strip's designated area. The strip, coupled with a specialized mobile application, processes and displays the glucose levels on the smartphone. Figure 3.1 illustrates the GlucoScreen prototype.

The device quantifies glucose concentrations through a well-documented process where glucose oxidase catalyzes the oxidation of glucose to gluconic acid, a reaction that is measurable electrochemically [2]. This current shift is detected via amperometry—specifically, it measures ions in a solution based on changes in electric current. Currently, the prototype utilizes commercially available glucose test strips, such as Accu-Chek [7] and True Metrix [12], to facilitate the enzyme-catalyzed reaction. All essential components for conducting an amperometric glucose assay and relaying the data to a smartphone are integrated within the strip.

3.3.2 Low-Cost and Battery-Free Operation

To achieve affordability, GlucoScreen is designed to solely execute the glucose detection reaction, utilizing the smartphone's capabilities for all other functions. The strip captures the amperometric reaction results and communicates them to the smartphone in real-time, displaying the outcomes via the mobile app. The amperometric measurement is conducted using a bespoke low-power, three-electrode potentiostat embedded in the strip. Communication with the smartphone occurs through simulated touch events on the touchscreen, encoded with pulse width modulation (PWM) to reflect the amperometric data.

The communication starts from the potentiostat output, which is linked to a voltage-controlled oscillator (VCO). The VCO governs a cascode field effect transistor (FET) output stage that simulates touch interactions on the smartphone's touchscreen (detailed in Section 4). This innovative method drastically reduces the need for power—using four orders of magnitude less energy than traditional communication methods like BLE, NFC,

or ANT [57]—and minimizes component costs. The GlucoScreen prototype operates on merely 20 μW, powered by the phone's flash via photodiodes, thus eliminating the dependency on batteries or USB components, reducing costs, and prolonging shelf life.

3.3.3 Prototype and Usage

The GlucoScreen prototype incorporates a custom-designed flexible printed circuit board connected to a standard microfluidic reaction chamber. Its functional design wraps over the smartphone's top edge, enabling it to harness energy from the phone's flash and communicate results through direct contact with the touchscreen. Figure 3.2 displays the installation process of the GlucoScreen.

To ensure compatibility across different smartphones, the physical design of the GlucoScreen strip is adaptable to various screen sizes and flash positions. It attaches securely to the phone using double-sided tape, which provides strong adhesion yet removes cleanly without leaving residues.

A user-centric mobile application complements the hardware, guiding users through the setup, blood application, and reading interpretation processes. This app enhances user interaction with on-screen videos and step-by-step graphical instructions, ensuring the system's ease of use and accuracy.

3.4 Implementation

3.4.1 Prototype Construction

The GlucoScreen strip prototype is crafted from a 0.23 mm thick polyimide base, forming a flexible printed circuit of 19 cm x 2.7 cm. It features copper circuit traces of 55 µm thickness. To protect the base and traces, a polymer-based solder mask is applied, followed by gold plating of the exposed copper using the electroless nickel immersion gold (ENIG) process. Components are affixed to the circuit board via reflow soldering. For ease of replacing glucose strips, a strip adapter removed from standard devices is

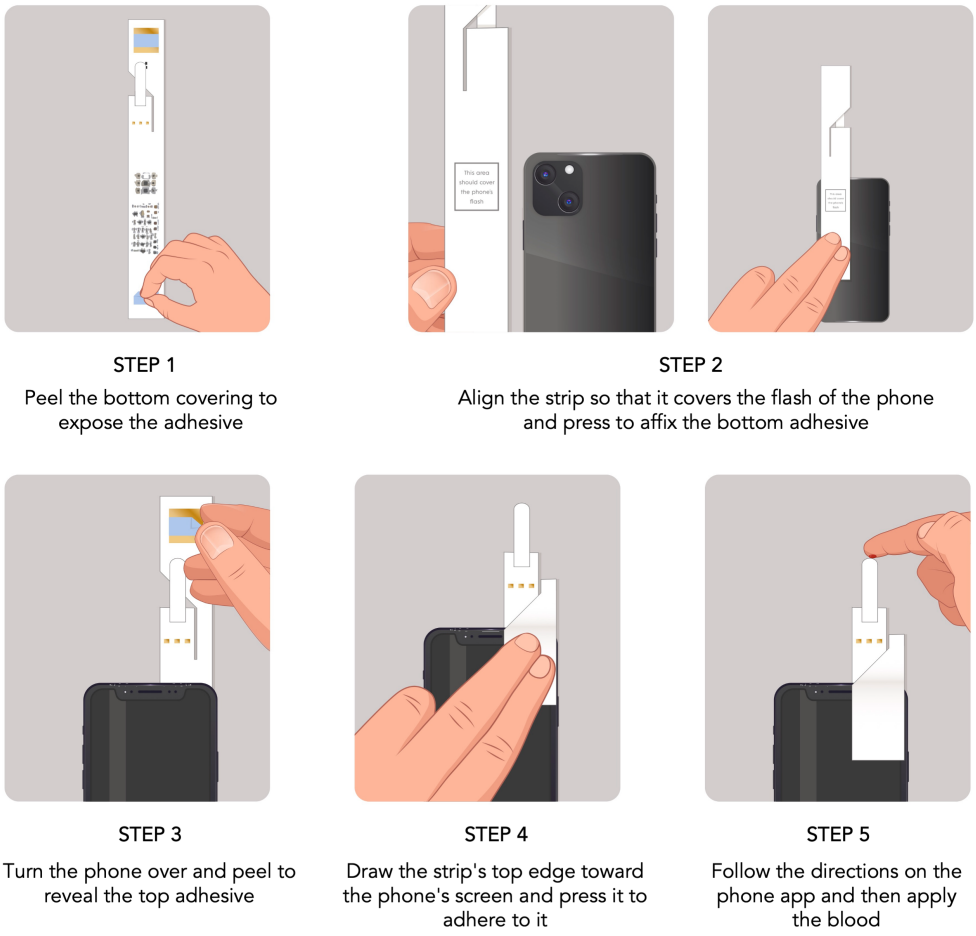

Figure 3.2: Step-by-step instructions for attaching the GlucoScreen prototype to a smartphone. The GlucoScreen prototype strip temporarily attaches to the phone via two adhesive contacts on the front side of the strip. Users first align the designated spot on the prototype strip (as shown in Figure 3.1) with the phone's flash. Then, they attach the strip to the back and front of the phone using the adhesive contacts. The strip features a long neck, which enables it to wrap around the phone and make adequate contact with the touchscreen.

integrated into the prototype. Separate adapters accommodate Accu-Chek and True Metrix glucose strips, resulting in two prototype versions tailored to these brands.

3.4.2 Circuit Design

The prototype includes a three-electrode potentiostat, constructed with dual operational amplifiers, to measure amperometric glucose concentration. It maintains a constant potential difference of 400mV across the glucose biosensor strips from Accu-Chek and True Metrix. The current resulting from glucose reactions is monitored as a voltage output, with different output gain settings for Accu-Chek and TrueMetrix to optimize glucose detection sensitivity.

The output from the potentiostat is channeled into a voltage-controlled oscillator (VCO), which integrates the voltage and then triggers a Schmitt trigger to generate voltage pulses. The width of these pulses corresponds to the potentiostat's output voltage. These pulses drive a MOSFET setup, creating simulated touch interactions on the smartphone's touchscreen that vary in duration according to the input pulse widths.

This MOSFET arrangement, in a cascode configuration, effectively mimics touch by altering the impedance at the point of contact, allowing the touchscreen to register it as human touch. This configuration enhances electrical isolation between the touchscreen and the strip circuitry, improving the fidelity of touch simulation.

3.4.3 Power Management

Three parallel photodiodes, along with an additional six photodiodes arranged in series, harness energy from the phone's flash to power the circuit, generating around 2.5V. This setup avoids the costlier alternative of a voltage booster IC. A capacitor bank smooths this output, catering to power fluctuations, while a low-dropout regulator (LDO) stabilizes it at 1.8V. The schematic of this arrangement is detailed in Figure 3.3.

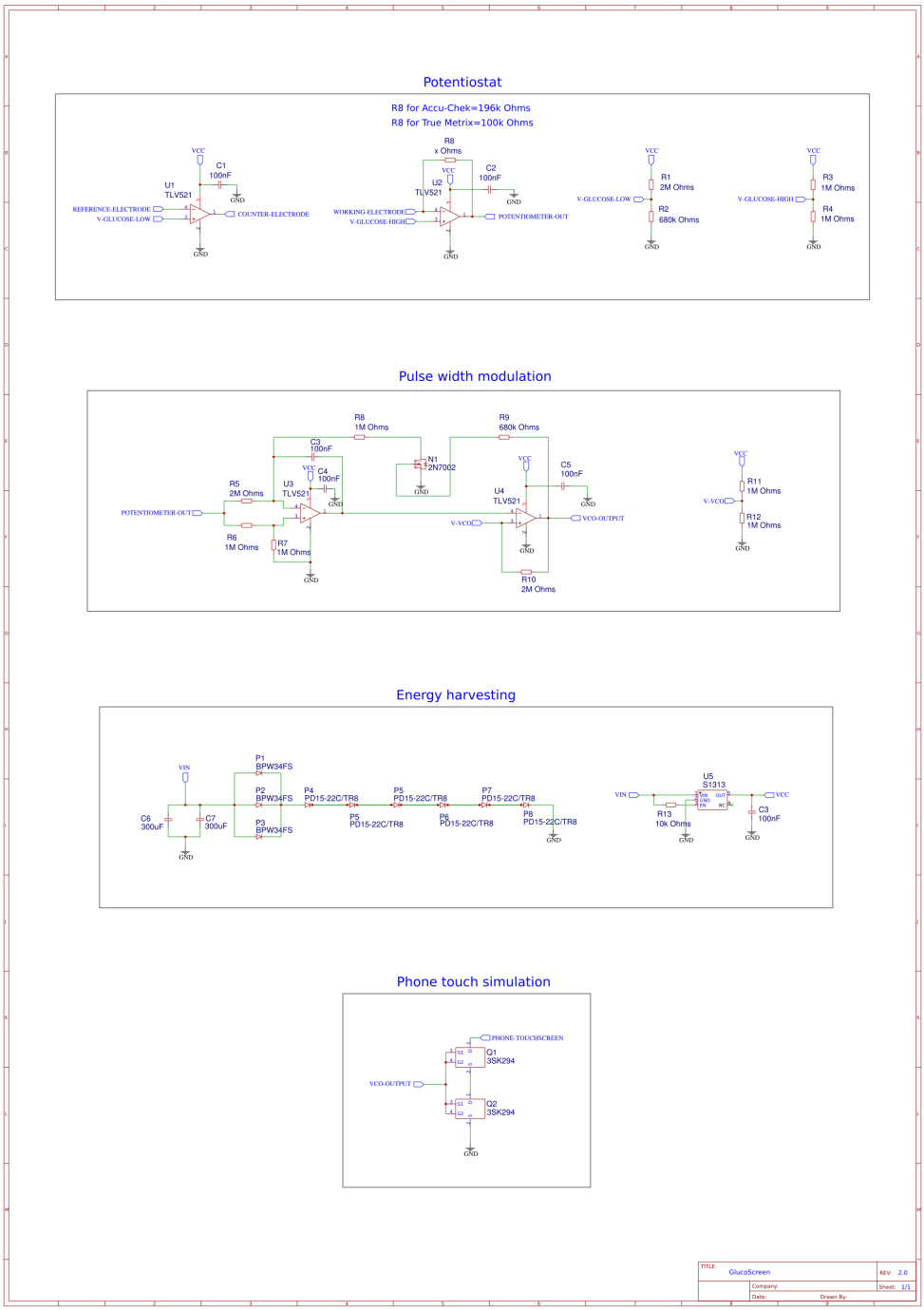

Figure 3.3: Schematic for GlucoScreen prototype circuitry.

3.4.4 Smartphone Applications

I developed three smartphone applications: a primary app for end users and two for data collection during the study. The user app includes a comprehensive tutorial and guides users through the glucose testing process. The data collection apps, designed for both Android and iOS, streamline rapid data recording with minimal user interaction by capturing the timing of touch events, which can be exported for analysis.

The user application is built for Android, compatible with API level 29, while the data collection apps support Android and iOS, the latter written in Objective-C for iOS version 14.

3.4.5 Data Processing

During a glucose test, the user's phone app records touchscreen data, signaling the user to apply the glucose solution or blood to the strip with a beep. It then continues to collect data for an additional 60 seconds.

Data from the glucose test is decoded from the touchscreen's pulse width modulated signals, with each pulse's width representing a data point directly proportional to glucose concentration. These data points are processed using a Butterworth low-pass filter with a 3Hz cutoff to eliminate high-frequency noise. The resultant waveform, indicative of the glucose concentration, shows a characteristic sharp drop and subsequent peak at the point of glucose application, which is used to delineate the effective data range for analysis. This refined signal is then analyzed to determine the glucose concentration, as illustrated in Figure 3.5.

3.5 Evaluation and results

3.5.1 In Vitro Testing

To assess its precision, I performed an in vitro study, testing GlucoScreen across nine concentrations of artificial glucose solution ranging from 45 to 210 mg/dl, which is significant for diagnosing diabetes and prediabetes conditions [212]. I utilized five different smartphones (four unique models): Samsung A21, Google Pixel 5, iPhone 11, and two Motorola Moto G7 phones, including two identical Moto G7 models, to evaluate consistency across similar devices. These specific models were chosen due to their widespread use internationally and representation of both major operating systems, Android and iOS.

For a comparative analysis, the GlucoScreen prototype was tested using two commercially available glucose strips, Accu-Chek and True Metrix. These brands are FDA-approved, broadly accessible, and have verified accuracy[6, 103]. Figure 3.4 illustrates the setup for the in vitro testing plan.

For calibration and validation, I used control solutions provided by AccuChek and True Metrix to prepare the artificial glucose solutions for in vitro testing. True Metrix provides three levels of control solution, whereas AccuChek offers two. I created nine distinct glucose concentrations for each brand by blending their respective control solutions in varying proportions.

To estimate glucose concentrations from the processed study data, as depicted in Figure 3.5, I trained a linear regression model. Although I explored other predictive models like random forest and support vector regressor, linear regression was selected due to its simplicity and resistance to overfitting, enabling accurate predictions for glucose concentrations not included in the training set. I analyzed 30 seconds of the decoded signal starting from when the glucose was applied to the test strip, segmenting it into ten equal parts and summing these segments to form a ten-dimensional feature vector.

My initial analysis focused on assessing GlucoScreen's accuracy in determining unknown glucose concentrations. I employed a leave-one-out cross-validation approach,

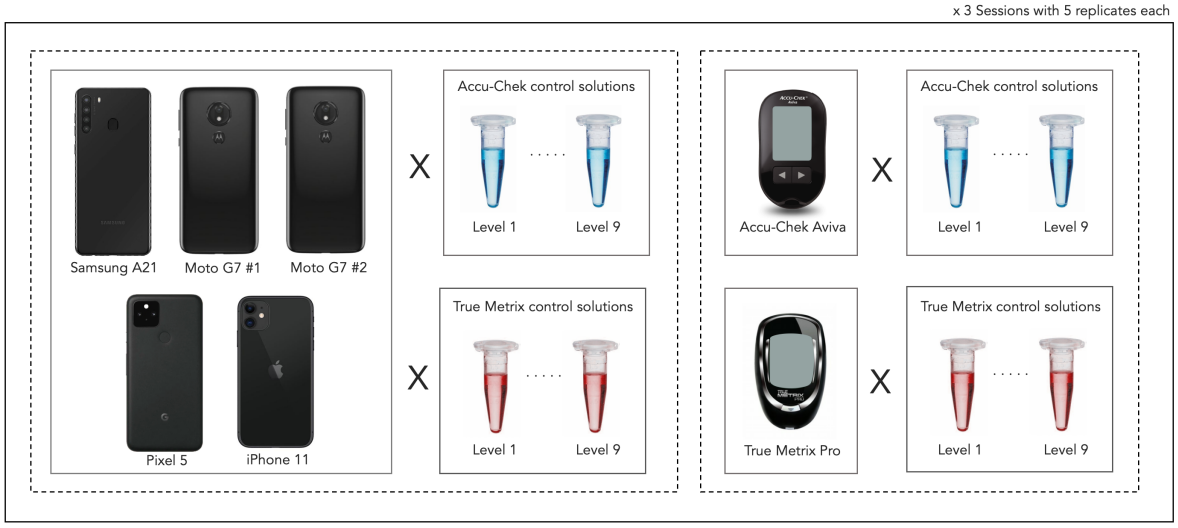

Figure 3.4: In vitro test plan. I conducted three in vitro testing sessions for each of the five phone models. Every session included a total of five repetitions of each of nine distinct glucose solution levels: 45, 70, 90, 110, 130, 150, 170, 190, and 210 mg/dl. These sessions were performed using both commercially available (Accu-Chek and True Metrix) glucose test strips. Each test strip was tested with its own control solutions. In total, 1350 tests were conducted across all phones (5 phones * 3 sessions * 9 levels * 5 replicates * 2 test strip brands). Similar testing was conducted with commercial Accu-Chek and True Metrix glucometers and their respective strips and control solutions over three sessions, totaling 270 tests (2 test strip brands * 3 sessions * 9 levels * 5 replicates).

training the model on all concentrations except one and then testing it on the omitted concentration. The mean absolute error (MAE) for GlucoScreen with Accu-Chek strips averaged 4.52 mg/dl, compared to 4.98 mg/dl for the Accu-Chek glucometer. For True Metrix strips, GlucoScreen achieved an MAE of 3.7 mg/dl, better than the 5.44 mg/dl MAE for the True Metrix glucometer. Thus, GlucoScreen consistently outperformed the True Metrix glucometers, while the results with Accu-Chek strips varied, with the glucometer sometimes performing better. Figure 3.6 displays these results.

In a subsequent analysis, I applied cross-validation by excluding data from one phone at a time, training the regression model on data from the remaining phones, and then testing it on the excluded phone's data. This cycle was repeated for each phone. Across all glucose concentrations, the MAE for each phone using GlucoScreen was lower than that for its corresponding glucometers. Notably, the iPhone 11 showed the lowest MAE at 3.27 mg/dl with Accu-Chek strips, whereas Moto G7 #1 had the highest MAE at 4.41 mg/dl with True Metrix strips. The differences between the two Motorola phones were minimal, demonstrating GlucoScreen's consistent accuracy across different devices. Figure 3.7 illustrates the findings from this cross-phone evaluation.

For my final evaluation, I employed a cross-validation method, excluding data from one session and building a linear regression model based on the data from the remaining two sessions. In this assessment, the mean absolute error (MAE) values were consistently below 0.5 mg/dl for all glucose concentrations, using both Accu-Chek and True Metrix strips. Since these sessions were conducted on different days and utilized test strips from various batches, these findings confirm that GlucoScreen delivers reliable performance regardless of the day of testing or the batch of test strips used.

3.5.2 Clinical Study

To assess performance in a setting that closely mimics actual clinical conditions, I conducted a clinical study at a pathology department's blood collection center in India,

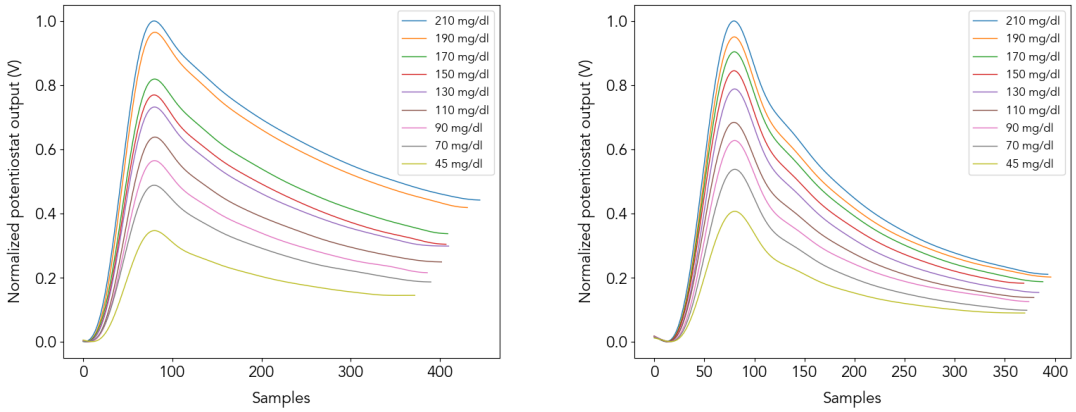

(a) Accu-Chek

(b) True Metrix

Figure 3.5: One repetition of data collected from a Google Pixel 5 phone during a single session for all glucose solution concentrations utilized in the in vitro testing. Figures (a) and (b) exhibit results from the GlucoScreen prototype with Accu-Chek and True Metrix test strips, respectively. The Y-axis represents amplitude on both graphs; the X-axis represents data samples. The plotted data is shown after pre-processing. Each curve depicts the response of the GlucoScreen prototype to a single solution; the lowest curve depicts the lowest concentration, while successively higher curves represent higher concentrations.

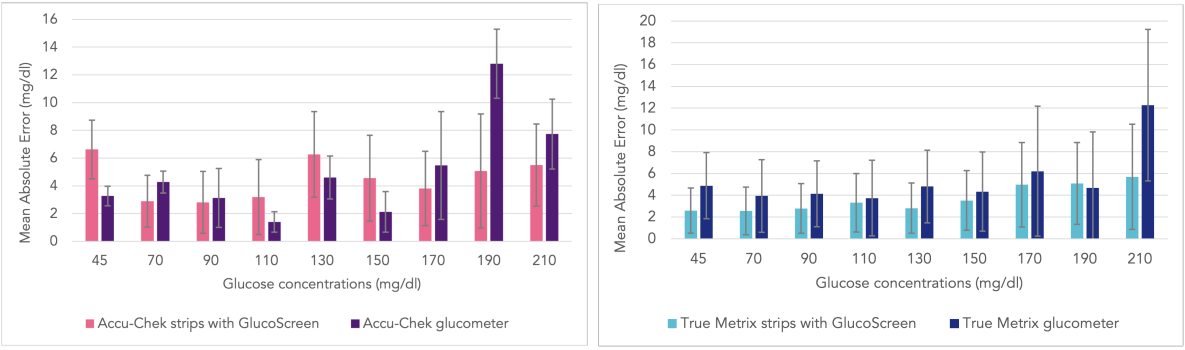

(a) Accu-Chek (b) True Metrix

Figure 3.6: Outcomes of cross-validation when one glucose concentration is excluded from the training set of a regression model. The figure depicts the result at each concentration. For comparison, I present the MAE result from the corresponding glucometers (Accu-Chek and True Metrix) along with GlucoScreen's.

supervised by a trained phlebotomist. I invited patients coming in for blood glucose tests to participate in the study. Of those, 75 patients consented, and for some (N=7), multiple samples were taken at different times during the day.

Blood was drawn from a vein in the antecubital fossa using venipuncture. Each sample (totaling N=85) was tested using the GlucoScreen prototype, which employed Accu-Chek glucose test strips and was connected to an iPhone 11. For each sample, glucose levels were also measured with a standard Accu-Chek glucometer and a laboratory auto analyzer for comparison.

The collected clinical data were not uniformly distributed across the observed glucose concentration range of 71 mg/dl to 370 mg/dl. Figure 3.8 illustrates the distribution of glucose concentrations. To ensure balanced cross-validation, I categorized the glucose samples into 28 bins and performed stratified splits into three groups. I confirmed the uniformity of these splits by conducting the Kolmogorov-Smirnov test on the subsets, selecting splits with a p-value above 0.98 and a KS-value below 0.1. A random forest

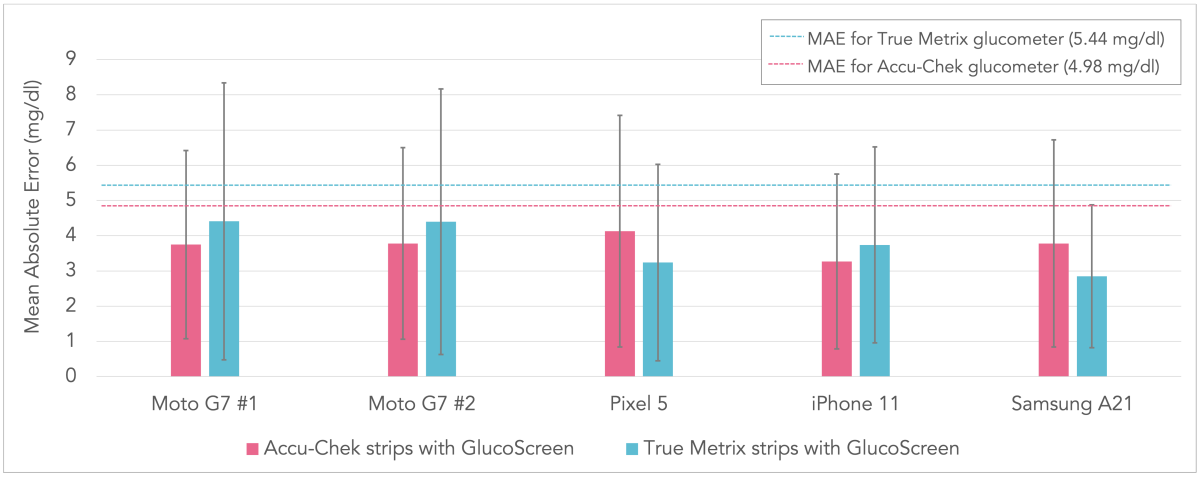

Figure 3.7: Cross-validation study results when I excluded data from one phone and trained the model using data from the remaining phones. I show the GlucoScreen results side by side with Accu-Chek strips and True Metrix strips. The two dotted lines on the graph indicate the MAE for the Accu-Chek and True Metrix glucometers (across all glucose concentrations).

regressor, chosen over linear regression due to its superior performance, was used to conduct the cross-validation on the three subsets.

For the clinical analysis, I segmented the decoded signal from the moment of glucose application into ten equal parts. I then calculated the mean, standard deviation, sum, and median for each segment, creating a 40-point feature vector (10x4) used as the input for the random forest regressor (with 50 estimators). The reference glucose level was determined by the laboratory auto analyzer results. GlucoScreen's MAE using Accu-Chek strips was 10.47 mg/dl, slightly higher than the Accu-Chek glucometer's 9.82 mg/dl. The standard deviations were 9.71 mg/dl for GlucoScreen and 9.88 mg/dl for the glucometer, as depicted in Figure 3.9. The Leave-One-Out Cross Validation MAE for GlucoScreen was 10.91 mg/dl.

Despite the slight variability, GlucoScreen's performance is comparable to conventional

glucometers. When considering the necessary thresholds for diabetes screening — where fasting blood sugar under 99 mg/dL is normal, 100 to 125 mg/dL indicates prediabetes, and 126 mg/dL or higher suggests diabetes [9] — my results affirm that GlucoScreen effectively identifies diabetes and prediabetes conditions.

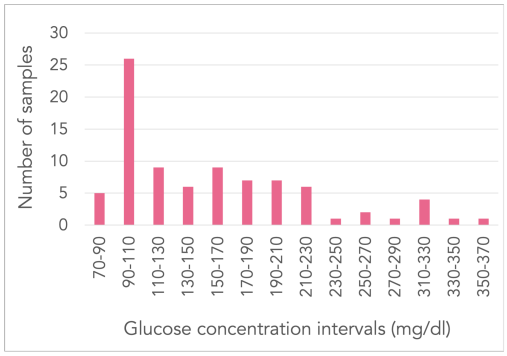

Figure 3.8: The distribution of glucose sample concentrations in clinical trial data. I determined the glucose concentrations used to prepare this figure through laboratory examination of blood samples.

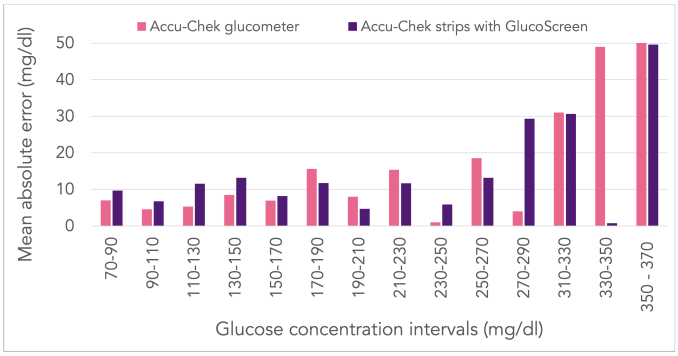

Figure 3.9: Results derived from the cross-validation analysis of clinical study data. The results were binned into intervals of glucose concentration. The MAE values of GlucoScreen with AccuChek strips and the Accu-Chek glucometer are compared side by side.

3.6 Discussion

Undetected and untreated prediabetes and diabetes pose serious health risks, potentially leading to life-threatening complications. Early detection combined with lifestyle changes can significantly enhance health outcomes. However, the logistical and cost barriers associated with visiting healthcare facilities or acquiring blood testing equipment for infrequent use often deter prescreening efforts, thereby limiting opportunities for preemptive treatment. These factors contribute to increased healthcare costs over time, which has motivated the development of the GlucoScreen prototype.

GlucoScreen is designed to be an affordable, user-friendly, and reliable in-home testing solution that capitalizes on widespread technologies—smartphones and cost-effectively modified test strips. A key innovation is the use of the phone's capacitive touchscreen for data transmission between the test strip and the phone, which eliminates the need for an external reader. This method is more cost-effective than alternatives like USB, BLE, WiFi, or NFC, which involve expensive and power-intensive integrated circuits. With most phones featuring capacitive touchscreens, this solution holds promise for the vast and growing number of smartphone users.

The device requires only a minimal 20 μW of power, sourced from the phone's flash, thus avoiding the need for batteries or a USB connection. While audio-port-based communication could also utilize low-cost circuitry, the phasing out of audio ports in newer phone models makes this less viable. I also considered using the phone's USB port for power, but this would necessitate multiple test strip versions to accommodate various USB types. However, using photodiodes allows for a single, universally compatible test strip version at a comparable cost to the USB connector.

The clinical evaluation showed a higher mean absolute error (MAE) compared to the benchtop study, likely due to the differences between testing with artificial solutions and actual blood samples. Unlike artificial solutions, blood includes cells and biochemical interference and has higher viscosity, leading to noisier test strip responses. Moreover, the clinical study had less training data available for building the regression model than the benchtop study. I anticipate that increasing the volume of clinical data could reduce the MAE.

Future efforts might include usability studies to evaluate whether general smartphone users would embrace this testing option and to confirm the prototype's accuracy under real-world conditions faced by non-expert users, such as understanding software instructions and applying blood samples correctly.

I estimate that large-scale production (10,000 units) could bring the cost of a GlucoScreen strip down to approximately $2.8 each. With potential for each strip to accommo-

date multiple glucose biosensors, the cost per test could effectively be halved to about $1.4, making the cost of prescreening comparable to current market prices but without the need for an external glucometer, potentially reducing initial screening costs by over 90

Currently, GlucoScreen utilizes a polymer substrate, but my goal is to transition to more sustainable materials. Modern test strips using paper substrates suggest that electronic components could be directly affixed and later recycled, enhancing environmental sustainability. Future developments might also include integrating printable organic photodiodes, which are eco-friendly and could further reduce the costs of test strips.

Table 3.1: GlucoScreen prototype component cost for large quantities (N=10,000 units). Electrical component pricing was obtained from Octopart.com [15] for 10,000 units each. Glucose strip manufacturing cost estimates were obtained from [1].

Part number	Price per unit ($)	Quantity	Total Price
BPW34FS	0.308	3	0.924
PD15-22C/TR8	0.091	6	0.546
3SK294	0.115	2	0.23
2N7002	0.012	1	0.012
TLV521	0.134	4	0.536
S1313	0.097	1	0.097
Passive components	-	-	<0.01
Glucose Test Strip	0.15	1	0.15
			Total price = $2.813

Chapter 4

ACCELERATING ADD-ON DEVELOPMENT FOR DIAGNOSTICS: A TOOLKIT FOR RAPID TEST STRIP INTEGRATION

4.1 Motivation and Design Goals

In the previous chapter, I successfully developed a low-cost glucose test strip add-on for prediabetes screening, demonstrating strong, robust sensing and accurate results. This achievement highlights the immense potential for such diagnostic approaches to significantly impact public health, particularly in regions where traditional lab facilities are less accessible. It is important to note that this technology is not limited to glucose measurement; its core principles can be applied to many other electrochemical assays. To help researchers quickly explore and implement these diverse assays for various diagnostic uses, I developed PhoneScreen (shown in Figure 4.1). PhoneScreen is a hardware development toolkit designed to accelerate the creation of low-cost, rapid electrochemical diagnostic assays for smart devices. By providing an accessible platform for testing new electrochemical assays and developing affordable test strip add-ons, PhoneScreen aims to democratize access to this crucial technology, significantly lowering the barrier for innovators in global health and personalized medicine.

The design goals for PhoneScreen are centered around three key pillars: cross-device compatibility, affordability, and low power consumption. Firstly, the toolkit must be versatile, seamlessly integrating with various commercially available devices, primarily smartphones, to ensure broad user adoption and avoid limitations tied to specific hardware models. Secondly, cost-effectiveness is paramount. The components and overall system should be readily affordable, making this advanced diagnostic development capability accessible to a larger community of researchers and developers. Finally, minimizing

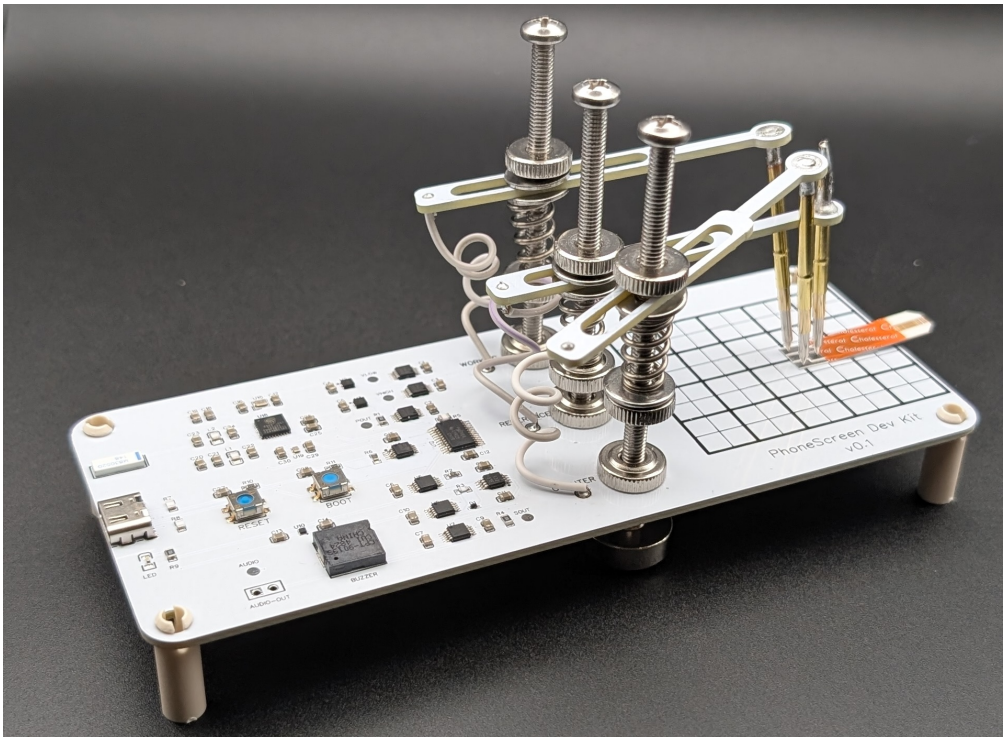

Figure 4.1: The PhoneScreen hardware development kit featuring the main PCB with integrated potentiostat circuitry and adjustable probes for test strip connection.

power consumption is critical. The toolkit should have a negligible impact on the host device's battery life, eliminating the need for frequent charging and ensuring a smooth, practical user experience for both development and eventual deployment. By adhering to these principles, PhoneScreen facilitates the creation of practical, user-friendly, and widely adoptable side-channel sensing add-ons for diagnostics.

4.2 System Overview

PhoneScreen is a comprehensive hardware development kit designed to enable researchers to quickly develop and test low-cost, rapid electrochemical diagnostic assays. The system comprises a specialized printed circuit board (PCB) with adjustable probes

and a companion software application. The core concept involves seamlessly integrating a standard electrochemical test strip with the PhoneScreen hardware for rapid prototyping and validation. The system is designed to provide precise control over electrochemical parameters and enable real-time data acquisition, simplifying the experimental setup often associated with diagnostic development. Its modular nature allows for easy adaptation to various test strip designs and assay types, thereby accelerating the iterative design and testing process for new diagnostic solutions.

4.3 Hardware Design

The PhoneScreen hardware is meticulously engineered to provide a flexible and precise interface for electrochemical test strips. The central component is a compact PCB, equipped with a potentiostat circuit, signal conditioning elements, and a microcontroller for data acquisition and communication. A key feature is the Strip Adapter mechanism 4.2. This adapter features adjustable, spring-loaded gold-plated probes that provide reliable electrical contact with the test strip's electrodes. The adjustable nature of these probes allows for compatibility with a wide range of test strip designs, accommodating varying electrode layouts and sizes without requiring custom fabrication for each new assay. The underlying PCB also incorporates a grid pattern, assisting in the precise placement and alignment of different test strips. The hardware is designed for low power consumption, making it suitable for integration with mobile devices, and its modular design ensures durability and ease of use in a research and development environment.

4.4 Companion Software

To complement the versatile hardware, PhoneScreen features a comprehensive Companion Software interface 4.3. This intuitive application provides researchers with real-time control over electrochemical parameters and immediate visualization of experimental data. Users can fine-tune critical settings such as voltage low, voltage high, potentiostat gain,

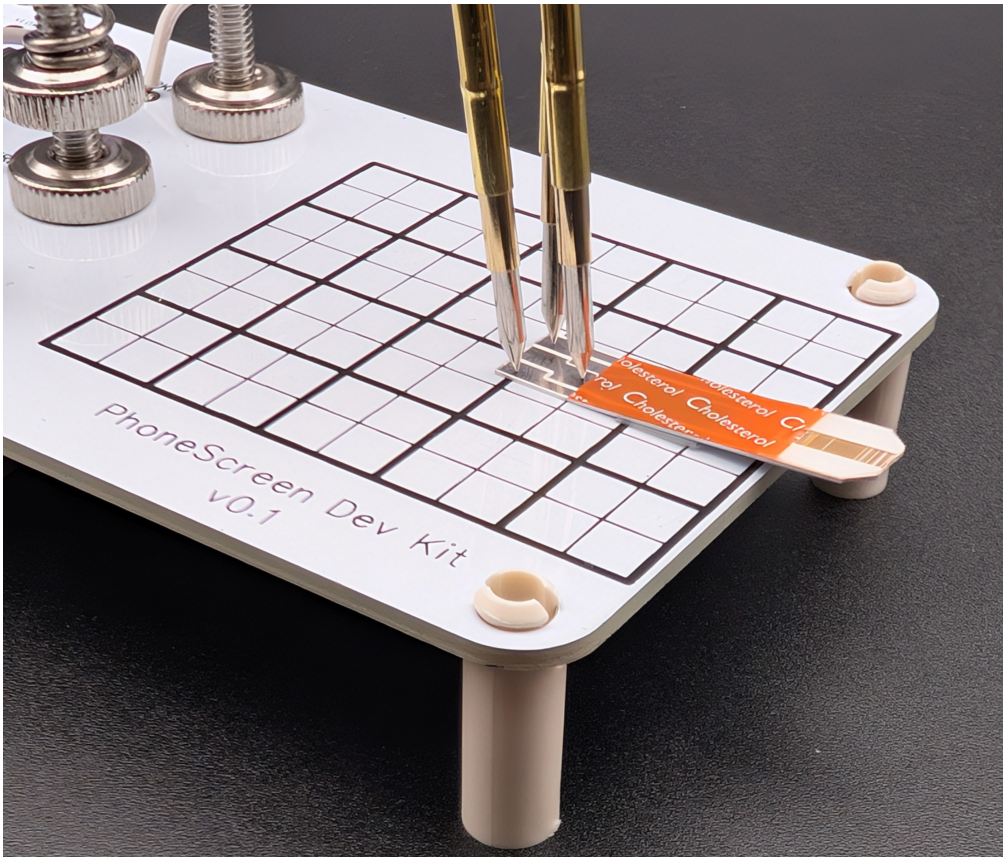

Figure 4.2: Close-up view of the PhoneScreen Strip Adapter, showing the adjustable, spring-loaded gold-plated probes making contact with an electrochemical test strip. The grid pattern on the PCB assists in precise placement.

and audio communication parameters, all accessible via sliders and input fields. The software also offers real-time audio capture, displaying audio waveforms and spectrograms, which are essential for analyzing the modulated signals from the electrochemical reaction. A demodulation module processes the raw audio data, extracting the relevant signal for concentration calculation. The user interface prominently displays the “Calculated Concentration,” providing instant feedback on assay performance. The software streamlines the entire process: users attach a new test strip, adjust settings for accurate readings, run tests to validate the assay, and then, crucially, can generate a new hardware list/design

for a more integrated solution. This integrated software-hardware ecosystem significantly accelerates the development cycle for new diagnostic add-ons.

Figure 4.3: The PhoneScreen Companion Software interface, displaying real-time potentiostat settings, audio input visualization (waveform and spectrogram), and signal demodulation results, including calculated concentration.

4.5 Usability and Workflow Evaluation

For a development kit intended to accelerate research, usability is paramount. A complex or frustrating workflow would undermine its core purpose. To gather initial feedback on PhoneScreen's usability and workflow, I conducted an early-stage evaluation with three prospective users.

4.5.1 Objective

The primary objective of this preliminary evaluation was to assess the clarity of the PhoneScreen setup process, the intuitiveness of the companion software, and the efficiency of the overall assay development workflow. I aimed to identify initial pain points, validate key design decisions, and gather qualitative insights to guide further refinement.

4.5.2 Participants

I recruited three participants (P1, P2, P3), each with varying levels of experience in electrochemistry and hardware prototyping. P1 had extensive experience with lab-grade potentiostats but a limited software development background. P2 had moderate experience with electrochemical assays and good software proficiency. P3 was new to electrochemistry but keen on exploring rapid prototyping tools.

4.5.3 Methodology

Each participant was provided with a PhoneScreen development kit, a set of electrochemical test strips, and a brief introductory tutorial. They were then asked to complete a series of tasks:

- Connect the PhoneScreen hardware to a laptop and launch the companion software.
- Properly insert and secure a test strip using the adjustable probes.
- Navigate the companion software to adjust potentiostat settings (e.g., set “Voltage Low” and “Voltage High”).
- Initiate a simple electrochemical measurement.
- Observe and interpret the real-time audio spectrogram and demodulated signal.

- Save a custom configuration for the potentiostat settings.
- Load a previously saved configuration.
- Throughout the tasks, participants were encouraged to think aloud. Their interactions were observed, and an informal interview was conducted post-task to gather subjective feedback on ease of use, perceived efficiency, and suggestions for improvement.

4.5.4 Key Findings

The early evaluation provided valuable insights:

- Positive Aspects: All participants found the hardware setup, particularly the adjustable probes, to be straightforward and intuitive, requiring minimal instruction. The real-time audio spectrogram was highly praised for providing immediate visual feedback on the signal quality. The ability to digitally change parameters and save/load configurations was highlighted as a significant advantage over traditional benchtop potentiostats.
- Identified Challenges: Participants with less electrochemistry experience (P3) initially found the specific terminology of potentiostat settings (e.g., “Wiper Setting” values) less intuitive, suggesting a need for more contextual help or user-friendly labels. P1, accustomed to more complex lab software, desired more advanced data analysis features directly within the application. Some minor confusion arose regarding the precise mapping between slider values (0-128) and physical units (Volts, kHz).
- Workflow Efficiency: The overall workflow for rapid test strip integration was perceived as significantly faster than setting up conventional lab equipment. The quick feedback loop between adjusting settings and observing results was particularly beneficial for iterative development.

- Limitations: This early evaluation, with its small sample size, served as a qualitative assessment to identify initial usability heuristics rather than a quantitative measure of performance. The findings will inform subsequent design iterations, which will then undergo more rigorous and extensive user studies with a larger, more diverse group of researchers to validate the toolkit's impact on accelerating diagnostic development.

4.6 Discussion

PhoneScreen represents a significant step towards democratizing diagnostic add-on development. By providing a flexible, affordable, and user-friendly toolkit, I enable researchers to rapidly prototype and test electrochemical assays. The emphasis on cross-device compatibility and low power consumption ensures that the solutions developed with PhoneScreen can be easily integrated into existing mobile ecosystems, broadening their potential impact on public health, especially in underserved regions. The system's ability to facilitate quick iteration and validation of test strips significantly reduces the time and cost associated with bringing new diagnostic tools to fruition. The ultimate vision is to foster a community of innovators who can leverage PhoneScreen to create a new generation of accessible, personalized diagnostic solutions.

Chapter 5

EXTENDING SMARTWATCH SENSING: A MODULAR ADD-ON PLATFORM FOR EXTERNAL SENSOR INTEGRATION

In this chapter, I design and develop an add-on sensor platform for smartwatches named WatchLink, shown in Figure 5.1. This platform enables users to connect external sensors to smartwatches in a low-cost and low-power manner by transmitting sensor data through the smartwatch's ECG hardware. I will demonstrate various applications and the design space of this technology throughout this chapter.

5.1 Introduction

As smartwatches become integral to modern health assessments and lifestyle, their embedded sensors play a pivotal role by capturing diverse environmental and physiological data. These devices track everything from heart rate and sleep patterns to physical activity and environmental exposure, providing valuable insights into individual well-being.

However, wearable manufacturers often prioritize broad market appeal over the niche demands of specific user groups. For example, field researchers or construction workers who are frequently exposed to sunlight could benefit from a wearable with a UV light sensor to monitor their UV exposure and prevent skin-related health issues. Similarly, those in polluted environments might find air quality monitoring wearables useful for avoiding hazardous conditions. Moreover, certain features like a breathalyzer may only be necessary after specific activities, such as drinking. Additionally, users with particular motor abilities might prefer physical buttons over touchscreens for ease of use.

Creating single-function devices with specialized sensors entails high costs due to the need for dedicated processors, communication systems, and unique hardware. Mass-

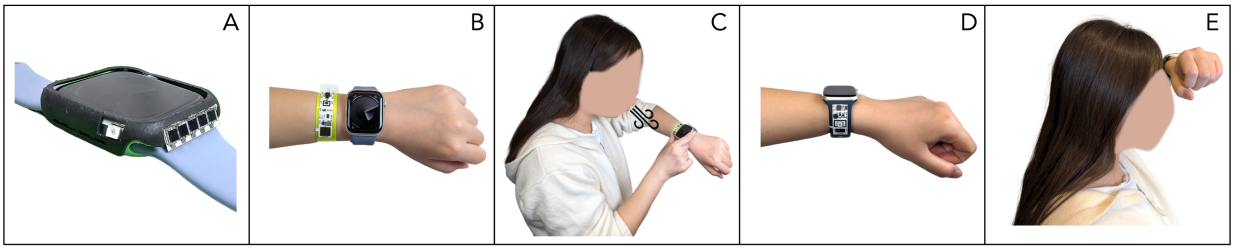

Figure 5.1: WatchLink allows sensors to be added to commodity smartwatches via the ECG interface. Sensors can be (A) integrated into a watch case or (B) worn as a companion accessory, like this alcohol sensor. (C) A user is blowing on the worn breath alcohol sensor, and ECG communication is coupled through the user's fingers. (D) Sensors can also be added to watch straps, like this body temperature sensor, which (E) can be touched to the forehead for measurement.

producing smartwatches with these specialized sensors is often not feasible due to the high costs, complex integration, and limited market demand for such specific features. This challenge presents an opportunity for developing niche add-on sensors that can significantly extend the utility of smartwatches for particular needs by utilizing the existing capabilities of these devices for display, data logging, and processing. Designing these sensors to be low-power further enhances usability by minimizing the need for frequent recharging. Nevertheless, the primary challenge lies in developing an economical and low-power method to integrate these sensors with the watch.

I propose a novel solution utilizing the widely available electrocardiogram (ECG) hardware on smartwatches to receive data from external sensors, enabling low-power and cost-effective communication. This method employs frequency modulation to encode sensor data into voltage variations, which the ECG hardware, designed to detect small voltage potentials generated by the heart, can then capture.

This approach is superior to traditional methods like Bluetooth Low Energy (BLE) and WiFi in terms of energy efficiency and cost. It uses significantly less power and requires

fewer expensive components[1].

To demonstrate the feasibility and versatility of this method, I designed and implemented four different sensor modules: a UV light sensor, a body temperature sensor, external buttons for smartwatch control, and a breath alcohol sensor. These modules communicate with mainstream smartwatches—Apple Watch Series 9 and Google Pixel Watch 2—via the ECG interface, illustrating the practicality of my proposed communication technique. I also explored the ECG interfaces of these devices to assess their suitability for data transmission and examined various form factors and power sources for the sensors.

This work contributes in the following ways:

- Introduces a novel technique for data transmission using smartwatch ECG hardware, alongside an evaluation of these interfaces for communication purposes.

- Explores the design space for integrating add-on sensors, proposing various methods for seamless connection to smartwatches.

- Develops and tests four unique add-on sensor devices, demonstrating diverse interfacing and powering methods.

5.2 Related Work

WatchLink aims to enhance the sensing capabilities of smartwatches affordably, with low power consumption, and without compromising the watch's inherent functionalities. This project focuses on extending the utility of widely available smartwatches through add-on sensors, a concept driven by both past and present market needs.

---

[1]WatchLink communication utilizes a low-dropout voltage regulator (LDO) (TPS7A0318PDBVR, $0.118/unit) and a 555 timer (ICM7555IBAZ-T, $0.010/unit) for a total cost under $0.13. This combination consumes less than 100μW during active transmission. In comparison, Bluetooth Low Energy (BLE) communication with the NRF52805 chip (from $1.214/unit) consumes about 5.7 mW during active transmission (datasheet from Nordicsemi.com). All component costs in this paper are sourced from Octopart.com (on a 10,000-unit basis).

Detachable Watch [114] investigated the potential of modifying existing smartwatches to detach the watch body from the wristband to increase functionality, revealing significant user interest in modular sensor capabilities for watches. Additionally, early smartwatch manufacturers, including the now-defunct Pebble, explored this area with "smartstraps" that connect to the watch via a pogo pin interface for power and data transfer [3]. Another initiative, ReserveStrap, attempted to augment early Apple Watches with additional batteries through a hidden debugging port, although this was later disabled by software updates from Apple [5].

With limited physical access to ports on modern smartwatches, newer designs have turned to wireless connections. Traditional connections like Wi-Fi and BLE consume significant power—over 100 mW and 5 mW, respectively—for active transmissions [218, 183, 172, 69]. NFC offers a battery-free option but is restricted in current smartwatches to only tag functionality, not supporting reading capabilities [245, 79]. Ultrasound communication [76, 100] presents an affordable audio-based alternative; however, its higher power requirements necessitate frequent battery replacements.

Alternative technologies have been explored to develop energy-efficient, cost-effective communication methods compatible with common devices like smartphones. For instance, WiFi [56, 112, 113, 261, 263, 262] and BLE backscatter [67, 259, 260] leverage ambient signals to create interactive tags. Despite their innovations, these approaches typically rely on a continuous power supply and complex hardware, escalating costs and complexity. Ultra-Wideband (UWB) communication stands out for its low power requirements and compatibility with new smart devices but suffers from high costs due to specialized hardware requirements [182].

My approach, leveraging the ECG hardware already present in smartwatches, avoids the complexity and cost associated with additional microcontrollers, radios, and power management systems required by other wireless protocols. This enables us to develop inexpensive, power-efficient sensor add-ons using simple components, which altogether cost significantly less than a single BLE microcontroller IC [57, 195]. For example, the

commercial AURA Strap—a BLE-enabled body composition and hydration monitor—retails for $159 USD [19].

Furthermore, research has extensively explored utilizing existing infrastructures for low-cost, low-power communication and sensing [89, 51, 47, 151, 140]. Various sensing modalities have been examined, including audio [88], RF [228], optical light [22, 247], LiDAR [42], and capacitive [227] methods.

Among these, GlucoScreen is notably similar to this project. It is a blood glucose monitor powered by a phone's flash and communicates through the phone's touchscreen, using basic components like an oscillator and transistor, thus avoiding more costly and power-intensive alternatives [227]. However, touch panel communication is not ideal for smartwatches due to limited screen space and the need for continuous functionality without interference. WatchLink explores a novel approach by employing the ECG sensor in smartwatches for low-cost, low-power communication, a method not yet fully explored in existing literature.

5.3 ECG Sensing For Communication

Electrocardiography (ECG or EKG) is a vital medical technique that records the heart's electrical activity over time, playing a crucial role in diagnosing and monitoring heart conditions. This method captures the electrical patterns of heart muscle contractions, which pump blood throughout the body. Typically, an ECG involves placing electrodes on specific skin areas—around the chest, arms, and legs—to detect the small electrical changes caused by heart muscle contractions during each heartbeat. In standard practice, ten electrodes are used to provide 12 different cardiac views (leads), each offering unique insights into the heart's health and functioning.

The essential components of an ECG setup include electrodes, amplifiers, and filters. Amplifiers are critical for enhancing the faint electrical signals of the heart to a level suitable for processing and analysis, given that heart signals can range from 1μV to 100mV, typically

around 1mV [64]. Filters play a vital role in removing noise and interference, ensuring the signals accurately reflect the heart's activity. These signals are then digitally processed to improve the signal-to-noise ratio (SNR), providing clearer and more accurate readings.

The integration of ECG technology into smartwatches has marked a significant advancement in personal health monitoring. Most smartwatches with ECG capabilities offer a single-lead ECG, which, while less comprehensive than the 12-lead ECG used in clinical environments, still provides valuable information on heart rhythm and rate.

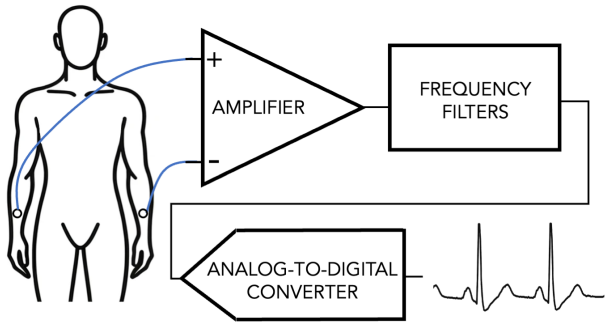

Figure 5.2: Simplified view of an ECG sensing system in a smartwatch.

Smartwatches simplify ECG recording, as depicted in Figure 5.2. Typically, one electrode is incorporated into the watch's back plate, making contact with the wrist, while another is placed on the side or a button. Initiating an ECG recording and touching the second electrode with the opposite hand completes an electrical loop across the heart, enabling the measurement of cardiac electrical signals. This configuration effectively creates a single-lead ECG, measuring the electrical potential difference between the wrist and finger during a heartbeat to record the heart's electrical activity.

At a more technical level, the ECG system is designed to measure low-amplitude heart signals with high gain. This sensitivity to voltage fluctuations allows us to repurpose the ECG interface for data transmission by encoding data as voltage variations that the watch can interpret. Additionally, the system's high gain enables the detection of even weak

signals, enhancing the communication's robustness and reliability. These features make the ECG system ideal not only for monitoring heart rate but also for new communication applications.

5.4 Characterizing the ECG Channel

To determine the feasibility and limitations of utilizing ECG interfaces for communication with smartwatches, I conducted a series of tests using commercially available smartwatches. These tests examined the following channel characteristics:

- Signal Type: Evaluating the ECG interface's capability to detect both DC (Direct Current) and AC (Alternating Current) signals.
- Signal Amplitude: Identifying the minimum and maximum signal amplitudes that the ECG interface can accurately read.
- Signal Frequency: Determining the range of frequencies, from lowest to highest, that the ECG interface can effectively detect for AC signals.

5.4.1 Test Setup

I utilized two widely used smartwatches in the market for the experiments—the Apple Watch Series 9 and the Google Pixel Watch 2—without any modifications to their hardware or software.

For my tests, I established two connection points on each watch: one on the back plate and another on the crown, using thin copper sheets affixed with scotch tape as shown in Figure 5.3. These were connected to a function generator, with the back contact serving as the ground and the crown contact as the signal point.

I utilized the native ECG apps on both watches to record the ECG data, which can capture for up to 30 seconds and export the data as a PDF file. Advanced image

Figure 5.3: ECG contact points (highlighted in yellow) on the Apple Watch Series 9 and Google Pixel Watch 2.

processing techniques[2] were applied to convert the waveform data from the PDFs into a CSV format for detailed analysis.

5.4.2 Signal Type

DC

I started by injecting a DC signal starting at 1 microvolt (μV) and gradually increasing to 1 volt (V). The increments were in stages: 100 microvolts (μV) from 1 μV to 1000 μV, then in 100 millivolts (mV) up to 1V. Observations from both watches indicated a rapid recentering of the signal to remove any DC offset, suggesting the presence of a built-in filter designed to negate DC signals.

AC

For AC testing, I introduced a 1 Hz sine wave with a peak-to-peak amplitude typical of ECG signals (1 mV). Both watches successfully captured the signal, though a Fast Fourier Transform (FFT) indicated minor distortions (Figure 5.4). These results demonstrate the

[2]For processing, the ECG PDFs were cropped to isolate the ECG signal, followed by contour-based sub-cropping, color-based signal extraction, and concatenation of signal parts.

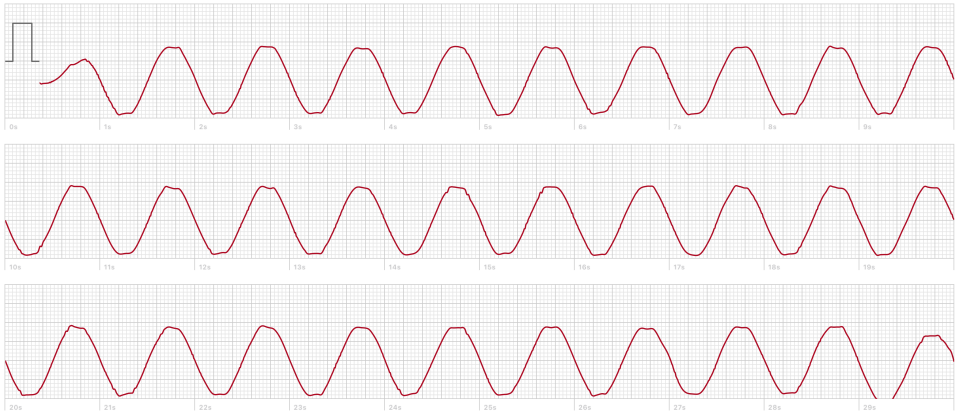

25 mm/s, 10 mm/mV, Lead I, 512Hz, iOS 17.1.1, watchOS 10.1.1, Watch7,2, Algorithm Version 2 — The waveform is similar to a Lead I ECG. For more information, see Instructions for Use.

(a) Apple Watch

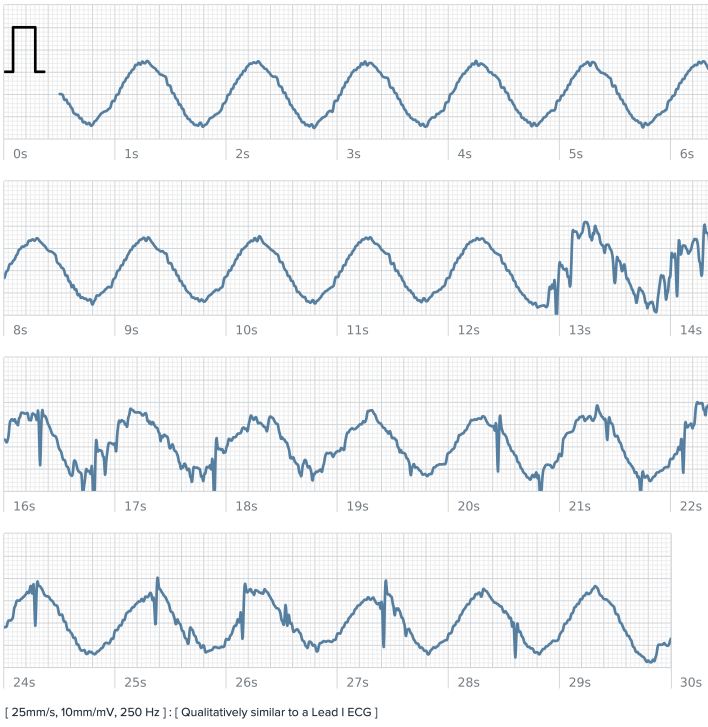

(b) Google Pixel Watch

Figure 5.4: Sample of a 1 Hz sine wave signal captured by the ECG apps on the Apple and Google Pixel Watches.

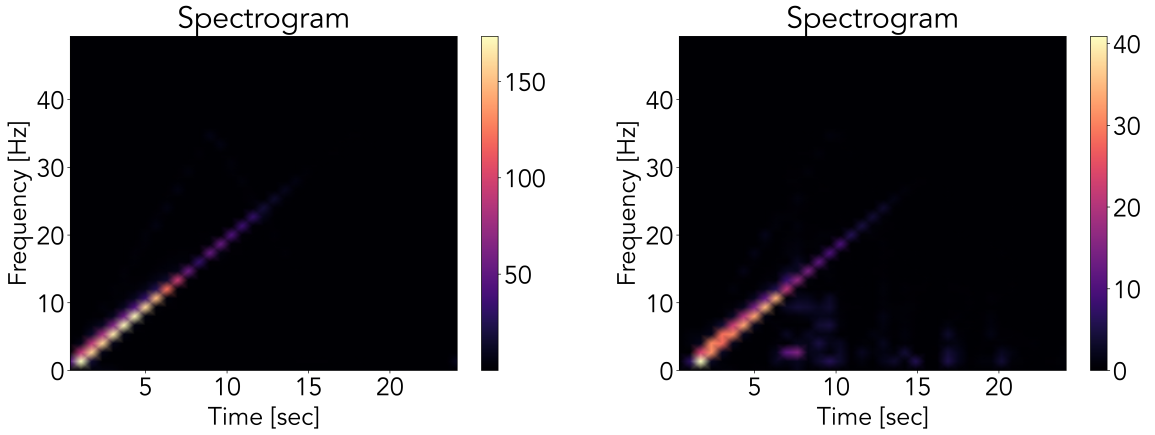

(a) Apple Watch

(b) Pixel Watch

Figure 5.5: Spectrogram showing the frequency response from 0.1 Hz to 50 Hz in the Apple and Google Pixel Watches.

interface's capacity to handle AC signals but not DC.

5.4.3 Signal Frequency

In this phase, I injected a linear chirp signal sweeping from 0.1 Hz to 50 Hz over 25 seconds, set at an amplitude of 10 mV. Both watches tracked the frequency sweep up to around 20Hz, as shown in the spectrogram (Figure 5.5), with decreasing amplitude at higher frequencies.

5.4.4 Signal Amplitude

For amplitude testing, I tested various frequencies (0.1 Hz to 20 Hz) at amplitudes from 100μV to 5mV. The data indicated that a minimum amplitude of 100μV was necessary for effective detection, with signal quality decreasing significantly below this threshold.

These tests underscore that while smartwatches with ECG capabilities can effectively

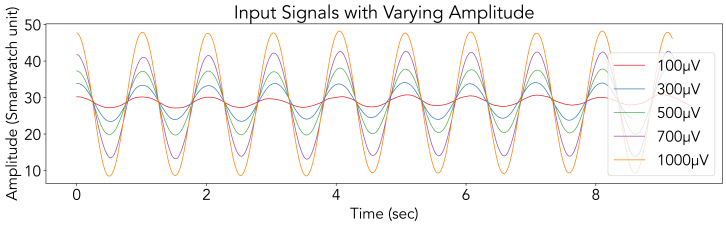

(a) Apple Watch

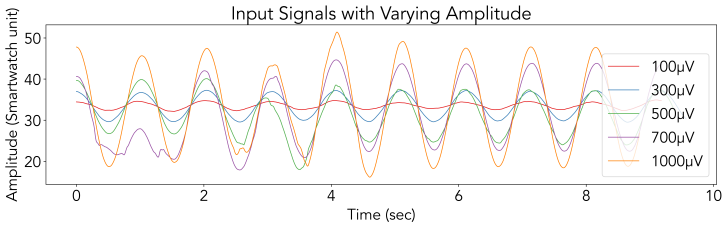

(b) Pixel Watch

Figure 5.6: Amplitude response at 1Hz in both watches, showing effective signal capture above 100μV.

process AC signals within certain frequency and amplitude ranges, their ability to handle direct DC signals is limited by design. This highlights the potential for specialized applications that fit within these parameters, expanding the utility of ECG technology in wearable devices.

5.5 A Sensor Platform for Smartwatches

The ECG interface on smartwatches, which includes accessible electrodes and the capability to access raw data via native ECG apps, offers a distinctive platform for low-level communication. This method circumvents the complexities and energy demands associated with standard protocols like BLE, NFC, or WiFi, providing a more energy-efficient means of data transmission. Utilizing the ECG interface as a communication channel involves considering two main aspects:

1. Communication Protocol for Devices. The goal is to create sensor devices that are both cost-effective and power-efficient. Given these constraints, adopting a complex communication protocol may not be feasible. Instead, the protocol should be simple and efficient, designed to facilitate effective data transmission without the need for the elaborate hardware that more advanced protocols require.

2. Establishing a Physical Connection to the Watch. A significant challenge is developing a stable physical connection to the watch's ECG electrodes, which are typically located on the back of the watch and on its crown. This requires crafting a reliable method for attaching sensors to these points to ensure consistent and clear data transmission.

These considerations are crucial for integrating additional functionalities into smartwatches without compromising their existing capabilities, thereby enhancing their utility through novel yet straightforward technological solutions.

5.5.1 Communication via ECG Sensing

This work capitalizes on the ECG interface's capability to receive data, facilitating one-way communication from external sensors to the smartwatch. Based on the ECG channel characteristics described in Section 5.4, I know the ECG interface can effectively process AC signals and sometimes encounters noise. While the time-domain signal may exhibit distortions, the primary components within the frequency domain remain largely intact. Consequently, I chose Frequency Modulation (FM) as the encoding method, which is well-suited for operation in the frequency domain and is less affected by amplitude variations. Additionally, FM modulation can be achieved with basic circuit components, making it an economical choice.

For FM modulation, both square waves and sine waves (used during the initial tests) are viable, but square waves are preferred for their ease of generation using simple circuits such as timers, which simplifies the design and reduces component count. However, square waves generate harmonic frequencies that might cause interference, necessitating a balance between simplicity and spectral efficiency. To understand this balance better, I performed experiments (Section 5.5.3) to test the ECG interface's response to FM using square waves, evaluating the effectiveness of this approach in practical applications.

5.5.2 WatchLink Sensor Design

I envision WatchLink as a versatile platform that integrates various sensors into a smartwatch, tailored to diverse use cases and operational frequencies. For example, sensors like those monitoring ambient UV radiation may need to run continuously in the background, while others, such as forehead temperature sensors, are activated manually when needed. Additionally, some sensors, such as breath alcohol level detectors, are useful only under specific circumstances, such as at certain events or locations.

To accommodate these different applications and usage scenarios, I propose three distinct methods for attaching WatchLink sensors to smartwatches. The first method

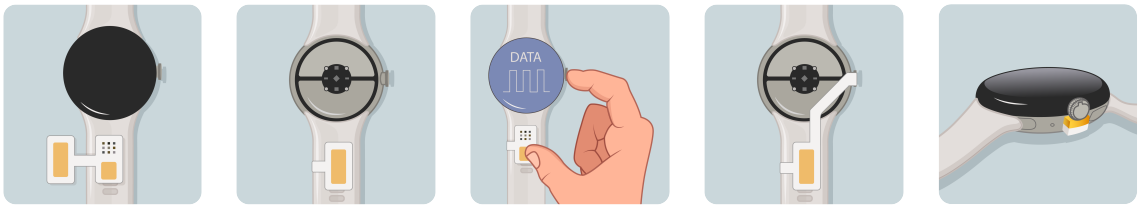

(a) (b) (c) (d) (e)

Figure 5.7: The configuration of a strap sensor. Sub-figures (a) and (b) illustrate the initial two steps in affixing a strap sensor to a watch's strap. The sensor is affixed to the strap using double-sided adhesive tape. Subsequently, (c) demonstrates the process of establishing a connection between the watch and the sensor through manual activation, utilizing fingers. In contrast, (d) illustrates how persistent contact can be maintained for continuous sensing. Additionally, (e) provides a side view of continuous contact, highlighting an electrode making a sliding contact with the watch's crown.

involves integrating the sensors into the watch strap, and the second method utilizes a sensor-embedded case that allows for interchangeable straps. Both methods support continuous sensing and manual activation. The third option is a separate accessory worn alongside the smartwatch, primarily for manually activated sensors. I detail each method below.

Watch Strap Sensors

These sensors are integrated directly into the watch strap, allowing users to switch between straps equipped with different sensors as needed. Figure 5.7 showcases a design for such a sensor. These sensors make contact with the body via an exposed electrode 5.7(b) positioned under the strap to ensure direct skin contact.

For sensors that require continuous sensing, this design includes an extension that

maintains contact with the watch's crown for data transfer. This extension features a fixture that slides under the watch to contact the crown directly, as illustrated in Figure 5.7(e). This fixture, typically made from a 3D-printed part, is designed to interact with the crown without obstructing the watch's other sensors, such as those for PPG, SpO2, and EDA. The conductive surface of the fixture is supported by soft foam to establish reliable ohmic contact with the crown while allowing unimpeded functionality for the user.

For sensors that require manual activation, the design includes another exposed electrode 5.7(c) on the side facing the user. To activate the sensor, the user touches this electrode and the watch crown simultaneously. This completes a circuit through the user's body, allowing the sensor signals to be transmitted to the watch.

Watch Case Sensors

These sensors incorporate sensor components and electrical circuits within a custom watch case, as depicted in Figure 5.8(a). This design allows users to attach or detach sensors easily by changing the case, providing flexibility to switch watch bands without needing to replace the sensors. The case snaps onto the watch, connecting the ground contact to the watch's back, suitable for both continuous and manual activation sensing.

For continuous sensing, the case is designed to maintain consistent contact with the watch's crown. As shown in Figure 5.8(c), a 3D-printed case for the Apple Watch includes a gold finger on the side that makes sliding contact with the crown's center. This ensures a reliable ohmic connection while allowing normal crown functionality. For manual activation, users can initiate sensing by touching an exposed electrode on the case, positioned similarly to the strap sensors, and simultaneously touching the crown with their fingers, as illustrated in Figure 5.8(b).

Companion Sensors

This approach allows for the use of add-on sensors as separate accessories, not necessarily attached directly to the watch. These sensors can be integrated into a separate band or accessory, which can be placed anywhere on the body, not just the wrist. Figure 5.8(d) shows an example of this configuration. To transfer data, the user touches an exposed electrode on the sensor with one finger and the watch's crown with another, effectively completing the circuit for data transfer, as seen in Figure 5.8(e).

This manual connection method is particularly suitable for sensors that require activation only at specific times, such as a breath alcohol sensor before attending a social event, or a smart bandage equipped with sensors to monitor wound healing. This setup is optimal for sensors that are used sporadically or need activation based on specific conditions, providing a flexible and user-friendly solution for diverse sensing applications.

(a) (b) (c) (d) (e)

Figure 5.8: The design and usage of case and companion sensors. (a) The case sensor with electrical circuitry embedded inside the case. (b) The procedure for establishing electrode contact between the sensor and the watch for manual activation. (c) The mechanism of achieving continuous sensing through sliding contact with a crown. (d) A companion sensor worn as a wristband accessory in conjunction with a smartwatch. (e) The process of establishing a connection between a sensor and a watch for a companion sensor.

5.5.3 Background Experiments

Frequency Resolution

A critical aspect of frequency modulation (FM) is the frequency resolution, defined as the smallest detectable change in frequency. Theoretically, frequency resolution is calculated by dividing the sampling rate by the number of samples used in the Fast Fourier Transform (FFT) analysis. However, due to the significant processing and filtering applied to signals captured from smartwatches, I opted to determine the frequency resolution empirically.

I performed an experiment where I injected a square wave into the watch and gradually reduced the frequency difference between it and another square wave until the system could no longer distinguish between the two. This test was conducted across various frequencies to see how frequency resolution changes across the bandwidth. Both the Apple Watch and the Pixel Watch were tested using the setup described in section 5.4.

Initially, I attempted a frequency sweep, but found that both watches stopped recording midway through the test, likely due to harmonics exceeding the designed frequency handling capabilities of the ECG systems. Therefore, I adjusted my approach to focus on discrete frequencies instead.

Using square waves between 1 Hz and 20 Hz, I observed significant harmonic content, though the primary frequency remained dominant (Figure 5.9). The Apple Watch displayed signals on its screen at higher frequencies but applied an additional filter before storage, resulting in a loss of data above 10 Hz. Conversely, the Pixel Watch did not apply such filtering, but signals captured above 10 Hz showed frequency domain shifts, not present at lower frequencies. I found that both watches could differentiate frequencies separated by at least 0.05 Hz, leading us to limit the sensor's operation to 10 Hz and below, ensuring a minimum frequency gap of 0.05 Hz for reliable operation.

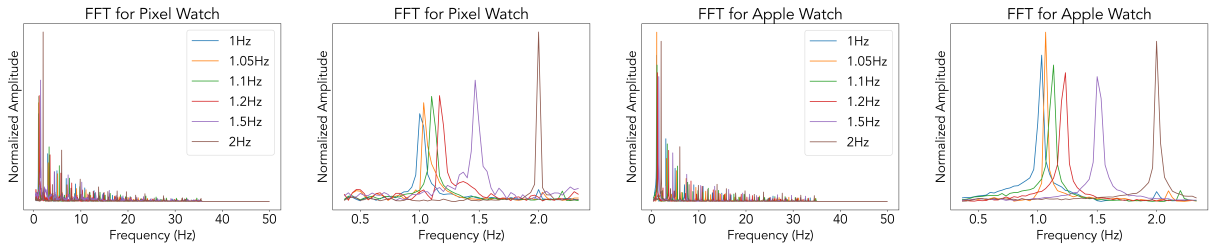

(a) Pixel Watch (original)

(b) Pixel Watch (zoomed)

(c) Apple Watch (original)

(d) Apple Watch (zoomed)

Figure 5.9: Spectrograms from the frequency resolution study for Apple and Pixel Watches (with the right-side images being zoomed-in versions of the left ones), illustrating six frequency responses triggered by a single frequency application on the watch. The plots on the right show that both watches can distinguish frequencies as close as 0.05 Hz.

Through-Body Signal Propagation

In exploring signal transmission through the body, particularly for 'companion sensors' where the sensor is connected to the watch via the user's fingers, transmission could suffer losses, potentially requiring an increase in signal strength. To determine the necessary signal strength for consistent performance, I conducted a user study where participants formed a circuit by connecting their thumb to an electrode linked to a function generator and their index finger to the watch's crown.

Participants tested various frequencies (1Hz, 5Hz, 10Hz) and amplitudes (50mV, 100mV, 300mV, 500mV, 700mV, 1000mV) on both Google and Apple smartwatches with five individuals. Signals below 300mV were inconsistently detected, while amplitudes of 300mV and above showed consistent detection across all participants. Higher amplitudes (500mV, 700mV) were only detected in two participants, and a 1000mV signal was not detected by either watch for any participant. As a result, 300mV was identified as the optimal signal strength for reliable detection in companion sensor applications.

5.6 Example Applications

WatchLink Designs

Sensing	Connection Type
Continuous	Watch Case Sensor
	Watch Strap Sensor with crown contact electrode
On-Demand	Watch Strap Sensor with finger contact electrode
	Companion Sensor

WatchLink Example Applications

Application	Energy Source	Domain
UV Light	Ambient Light	Environmental
Watch Buttons	Ambient Light	Input
Body Temperature	Battery	Health
Breath Alcohol	Battery	Health

Figure 5.10: A display of WatchLink designs and their respective applications.

I have developed four distinct sensor applications to extend the capabilities of smartwatches, all leveraging WatchLink's ECG-based communication for connectivity. These applications demonstrate different ways WatchLink can be integrated with smartwatches, as illustrated in Figure 5.10. The applications include sensors for ambient UV light detection, body temperature measurement, breath alcohol levels, and additional input buttons for enhanced user interaction.

In designing each of these sensor add-ons, I prioritize cost-effectiveness and energy efficiency. This focus aims to improve both the affordability and the operational longevity of the sensors, making them viable for everyday use while minimizing their environmental impact.

5.6.1 UV Light Sensor

Exposure to UV light can lead to severe skin damage, including sunburn, premature aging, and heightened skin cancer risks. Furthermore, UV rays can damage the eyes, increasing the risk of conditions like cataracts, and suppress the immune system, which decreases

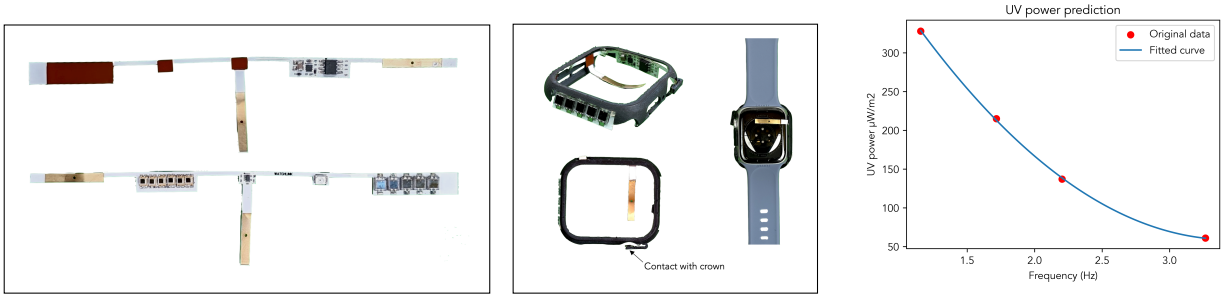

(a) (b) (c)

Figure 5.11: (a) The UV light sensor from both front and back is built on a flexible PCB with a design that allows it to be integrated into a 3D printed case designed for the Apple Watch. (b) The case is equipped with the PCB, demonstrating how the case engages in sliding contact with the watch's crown and how the PCB establishes a connection with the watch's ground. (c) A graph depicting the correlation between the sensor's prediction of UV light intensity and the actual measured values.

the body's ability to combat certain infections [243]. It is crucial to monitor UV exposure, particularly during outdoor activities, to reduce these health risks.

The UV Index measures UV radiation, quantifying the risk of sunburn based on the UV rays at a specific location and time. This index aids in understanding the potential damage to skin and eyes from UV rays and highlights the necessary protective measures. Higher UV Index values indicate increased risk and the need for enhanced sun protection. To facilitate monitoring, I developed a sensor add-on using WatchLink that provides real-time UV Index readings.

The sensor add-on is designed as an Apple Watch case that continuously measures UV Index values. It incorporates a flexible printed circuit board (PCB) that fits inside a 3D-printed case as depicted in Figure 5.14. The case interacts with the watch's crown through a gold finger and connects with the watch's ground through a flexible electrode. I utilize the GUVA-S12SD UV light sensor with its nano-level output amplified by a TLV521DCKR op-

amp, frequency modulated by a CSS555 555 timer as described in [147], and transmitted to the watch. The prototype harnesses ambient light for power through 11 photodiodes, with 5 (VBPW34S) optimized as a current source and 6 (PD15-22C/TR8) as a voltage source. This arrangement ensures low-cost and adequate power for the circuit, which includes voltage regulation to 1.8V via a TPS7A0318PDBVR LDO. The material cost totals $6.077, with a power consumption of 90μW, allowing operation in light conditions exceeding 8000 Lux, typical of outdoor daylight.

I tested this sensor add-on with an Apple Watch under various UV light conditions and compared the results to readings from a commercial UV light meter [24]. The data, shown in figure 5.14, indicates that the UV index readings from the prototype correlate well with the commercial meter's readings.

5.6.2 Body Temperature Sensor

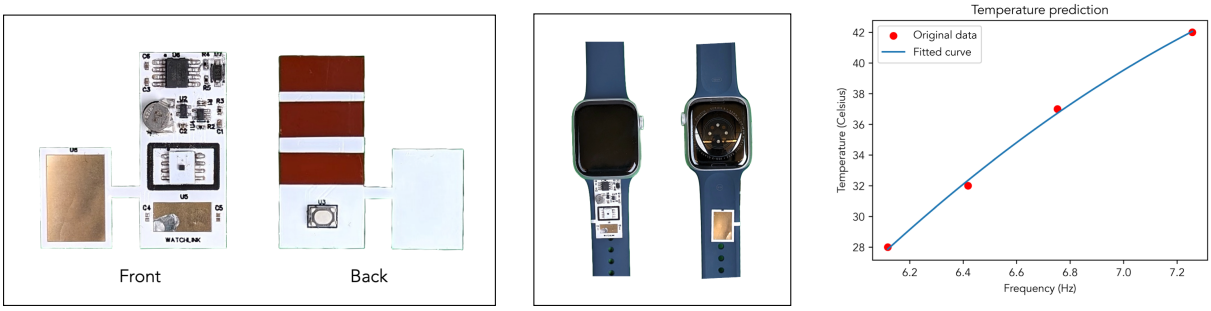

(a) (b) (c)

Figure 5.12: (a) The body temperature sensor from both front and back views. (b) The method of attaching the sensor to the watch strap, where the sensor, constructed on a flexible PCB, wraps around to adhere to the inner side of the strap, establishing a ground connection with the user's body. (c) The relationship between the sensor's temperature predictions and recorded temperatures.

Modern smartwatches like the Apple Watch Series 8 and various Garmin models now feature skin temperature sensors as part of their health monitoring capabilities. While these sensors offer valuable health insights, they fall short in accurately measuring core body temperature compared to traditional methods such as forehead or ear thermometers. This is due to the influence of external factors on readings taken at the wrist, which is significant when precise temperature readings are essential for detecting fevers or other medical conditions.

To address this, companies like Google, with its Pixel 8 Pro smartphone, are incorporating dedicated temperature sensors capable of measuring forehead temperature directly. This reflects a growing trend towards more accurate and practical body temperature monitoring solutions. Nonetheless, most devices currently lack such integrated sensors, creating an opportunity for additional sensor attachments that provide more accurate measurements. These add-ons could enhance smartwatches, making them more dependable for health-related temperature monitoring.

My design for a body temperature sensor add-on is a strap sensor that attaches to a watch strap, wrapping around to maintain skin contact for grounding. The prototype, shown in Figure 5.12, is designed for on-demand temperature measurements and includes an accessible electrode that initiates communication with the watch when touched by the user. To use, individuals can press the sensor against their forehead, as demonstrated in Figure 5.1E, and establish a connection through touch, as outlined in Figure 5.7.

The prototype employs an LMT70YFQR temperature sensor with a ±0.13°C accuracy. The sensor's analog voltage output is amplified by a TLV521DCKR op-amp, frequency modulated by an ICM7555IBAZ-T 555 timer as per the circuit described in [147], and transmitted to the watch when the user makes a connection. The circuit is powered by a small 3mAh coin cell battery (MS421R IV03E), with voltage regulated at 2.7V by an NCP663SQ27T1G LDO. Battery conservation is achieved via a switch (CKN12215-1-ND) under the contact electrode, which users can activate by pressing until a click is felt, as shown in Figure 5.12.

Notably, activating the circuit via the button is unnecessary for measurement since the temperature IC needs to reach thermal equilibrium with the body. The power is only needed for data transmission to the watch. With a minimal power consumption of 243μW, the circuit is highly efficient, allowing for years of operation on a single battery and facilitating multiple daily measurements. The total cost for the materials in this sensor is $1.983.

I validated the prototype's performance by raising the sensor's temperature using a commercial hot plate and recording its readings. The data, presented in Figure 5.12, confirm that the device provides accurate temperature measurements.

5.6.3 Breath Alcohol Sensor

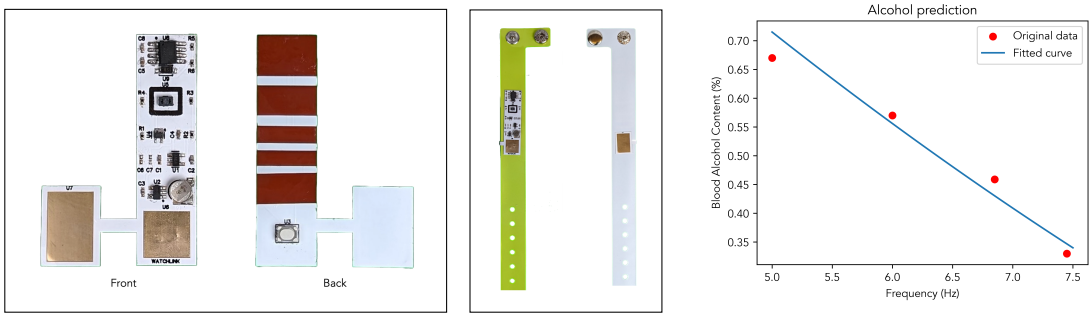

(a) (b) (c)

Figure 5.13: (a) The breath alcohol sensor, from both front and back views. (b) The sensor is attached to a wristband, with the sensor built on a flexible PCB, wrapping around to stick to the inner side of the strap, thus making a ground connection with the user's body. (c) The correlation between the sensor's predicted alcohol levels and the readings obtained from a commercial breath alcohol meter.

An alcohol breath sensor, also known as a breathalyzer, measures Blood Alcohol Content (BAC) from a person's breath. BAC represents the percentage of alcohol in the

bloodstream. Breathalyzers operate by detecting a chemical reaction with alcohol that causes either a color change or an alteration in electrical signals. The primary technologies utilized in these sensors are semiconductor oxide and fuel cell technology [220]. To obtain a BAC reading, a person blows into the device, which analyzes the alcohol level in the exhaled breath.

I developed an alcohol breath sensor as an independent wristband accessory that interfaces with a watch. Figure 5.13 illustrates the sensor prototype. This design allows users the flexibility to wear or remove the sensor as needed without modifying the watch. The wristband features an electrode on one side to connect with the watch's crown and another on the opposite side to maintain a ground connection with the skin.

The prototype utilizes a commercial Metal Oxide (MOX) gas sensor (CCS803), which senses alcohol levels and outputs an analog voltage. This voltage is amplified by a TLV521DCKR op-amp and frequency modulated by a CM7555IBAZ-T 555 timer as described in [147]. The circuit is powered by a compact 3mAh battery (MS421R IV03E), measuring 4.8mm x 2.1mm, and includes a switch (CKN12215-1-ND) under the finger contact electrode. This switch is easily activated simultaneously as the user establishes contact with the watch's crown. The gas sensor consumes 20 mW, enabling the battery to support approximately 27 breath tests, each lasting 20 seconds. The total cost of components for this sensor is $6.595.

To verify the prototype, connected to a Google Pixel Watch, I performed tests using various ethanol concentrations alongside a commercial breath analyzer [23]. The results, shown in Figure 5.13, demonstrate a strong correlation between the prototype and the commercial device's readings.

5.6.4 Touch Buttons for Interaction

Smartwatches often struggle with user input due to their small screens, which complicate precise touch interactions and limit the addition of extra controls such as buttons. While

voice control is an alternative, it may not be suitable in public due to privacy concerns and convenience issues.

To enhance user interaction without increasing the watch size, I suggest integrating additional buttons into the watch strap, specifically forming a directional pad (D-pad). This D-pad allows users to navigate more easily and assigns each button as a shortcut for quick access to various functions. These buttons can also work in tandem with other watch features, such as the crown, to adjust scrolling speeds or access different menus, thereby enhancing the user experience.

In my design, I power the strap's additional buttons using ambient light captured by photodiodes (3 x VBPW34S + 6 x PD15-22C/TR8), with a storage capacitor (2mF) to maintain charge even without light. The power from the photodiode array is regulated to 1.8V by an LDO (TPS7A0318PDBVR).

I replaced the previously used 555 timer with an op-amp-based (TLV521DCKR) relaxation oscillator for frequency control [217], adjusting feedback paths and resistance to change the output frequency with each button press. This system consumes less power but offers lower frequency resolution; however, it is sufficient to distinguish four unique button inputs.

The entire circuit consumes just 10μW, allowing continuous operation on the energy from the photodiodes without needing sleep cycles. It requires a minimum of 400 lux to function effectively—this is achievable in most indoor settings, such as well-lit offices (500 lux) and homes (300 lux), as noted by Wen-Shing[208]. The total cost for these components is $0.402.

I tested this system by pressing each button individually and recording the frequencies of the resulting signals. The results show that the D-pad's four distinct frequencies can be successfully identified, confirming the efficacy of my design in improving smartwatch usability.

(a) (b) (c)

Figure 5.14: (a) The external button attachment from both front and back sides. (b) The buttons attached to the watch strap. (c) The sensor establishing a sliding contact with the watch's crown affixed to a 3D-printed component.

5.7 Limitations and Future Work

My prototypes are currently designed to integrate single sensors; however, they can inherently support multiple sensors operating simultaneously due to distinct carrier frequencies for each sensor's data stream, similar to channel separation in FM radio. The frequency resolution achieved is 0.05 Hz across a bandwidth ranging from 0.5 to over 10 Hz, allowing for multiple concurrent sensor channels.

There is potential for interference between sensors like UV light detectors or buttons on a smartwatch with ECG readings, as they may transmit data within the same frequency band as ECG signals. To address this, one approach is to temporarily disable other sensors during ECG measurements using a hardware switch to isolate ECG data, although this could impair the user experience by deactivating sensor functionality. A preferable alternative might be to adjust the data transmission frequencies of these sensors to fall outside the ECG frequency range (0.5 Hz to 150 Hz [216]), ensuring minimal interference while maintaining continuous sensor operation. The capability of the Watchlink setup to operate below 0.5 Hz can be utilized here.

Currently, the batteryless prototypes harvest energy from ambient light. Future designs could explore alternative energy-harvesting techniques such as harnessing power from watch vibrations, capturing sound energy from speaker output, or utilizing the energy from the watch's charging process to charge a supercapacitor or battery. These methods would allow the sensors to function independently of ambient light conditions, ensuring their consistent availability.

As of now, the prototypes consist of bare flex printed circuits. For optimal integration with wearable environments, these circuits require more robust mechanical protection. To achieve this affordably, the circuits could be encapsulated within injection-molded parts to enhance water and dust resistance. Given the simplicity of these devices and their firmware-free design, they do not necessitate their own firmware updates beyond what may be required for the associated watch.

INTRODUCTION TO PART III: ENHANCING SIDE-CHANNEL SENSING WITH TARGETED HARDWARE MODIFICATIONS

Part III explores an alternative, yet powerful, strategy for enhancing side-channel sensing: targeted modifications to existing smart device hardware. The previous sensor add-on approach was developed for end-users of the device; this approach is targeted towards the manufacturers of the device. While perhaps appearing less immediately practical than simple add-ons, this approach offers significant advantages over a complete redesign of existing devices or the development of entirely new components from scratch. The core benefits lie in substantial reductions in both cost and development time for manufacturers, leading to a lower Bill of Materials (BOM) and accelerated development cycles. This strategic decision enables the introduction of novel sensing capabilities more efficiently, making advanced technologies commercially viable and faster to bring to market.

Crucially, this method also prioritizes the preservation of user familiarity. Drastic hardware overhauls can disrupt user experience by altering a device's form and function, potentially alienating its existing user base. By focusing on targeted modifications, we can seamlessly integrate new functionalities without fundamentally changing how users interact with their familiar devices. This is a broad idea applicable to modifying any hardware; however, in this part, I specifically focus on enhancing bio-impedance sensing hardware, commonly available on smartwatches and smart rings. Traditionally, bio-impedance sensors operate in the tens of kHz range. My work upgrades this capability to the MHz range with a wider bandwidth, which unlocks a wide range of new applications not previously possible.

This section will delve into two key examples of this philosophy: Chapter 6 introduces

Ring–Based Wideband Bio-Impedance Sensing for Gesture, Object, Touch, and User Recognition, demonstrating how subtle modifications to a ring form factor can unlock rich interaction. Following this, Chapter presents Wristband–Based Wideband Bio-Impedance Sensing for Touch Interaction on Everyday Uninstrumented Surfaces, showcasing how a similar principle can transform a common wearable into a versatile interface for the physical world.

Chapter 6

RING–BASED WIDEBAND BIO-IMPEDANCE SENSING FOR GESTURE, OBJECT, TOUCH, AND USER RECOGNITION

In this chapter, I explore how a hardware modification can enhance the functionality of a smart ring. Typically, smart health devices utilize bio-impedance sensing to measure skin conductance, which correlates with stress levels. This sensing usually occurs within a bandwidth of several hundred kilohertz. However, by expanding this bandwidth into the megahertz range, we can significantly enrich the device's sensing capabilities.

The smart ring developed in this work, called Z-Ring, shown in Figure 6.1, can support a wider array of functions using a single sensing modality. This expansion allows the ring to perform gesture recognition, external surface touch detection, object identification, and user recognition. This chapter details how extending the operational bandwidth facilitates these advanced features.

6.1 Introduction

Our hands provide insight into our intentions, context, and activities. As the body's primary means of interaction, hands engage in various tasks such as grasping objects, gesturing to convey intentions, and manipulating interactive controls. Wearable sensing technologies can capture these dynamics, offering valuable input to enhance computational experiences across gaming, augmented and virtual reality (AR/VR), and ubiquitous computing.

In this research, I introduce a novel sensing system utilizing electric field sensing within a unique antenna topology. This system can detect four distinct hand-related activities: held-object recognition, gesture sensing, tangible UI interaction, and biometric

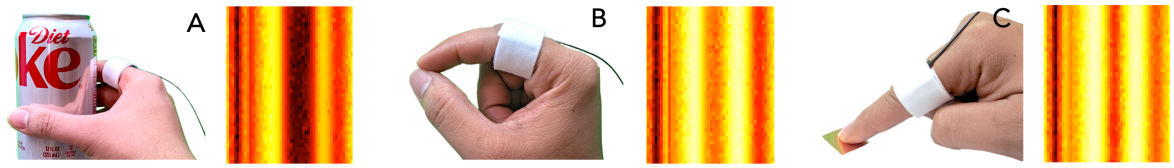

Figure 6.1: Z-Ring senses bio-impedance changes caused by various interactions, e.g., with objects, finger motions, and metallic surface elements like copper tape. By analyzing impedance over time and frequency, shown via spectrograms (A, B, C right), these impedance changes can drive (A) object identification, (B) gestural interactions, and (C) interaction with tangible user interface elements.

identification, all from a single instrumentation point on the base of the user's finger. To my knowledge, this is the first system to capture such a broad range of hand-related activities with a single hardware component.

This method exploits the electrical conductivity of the human body by using the hand as an antenna. As the hand adopts various poses, handles objects, or interacts with conductive surfaces, the electromagnetic properties of this antenna change. These alterations are quantified by measuring the hand's bio-impedance, typically represented by Z, which forms the core of this sensing approach.

The Z-Ring, my custom-designed ring prototype, detects subtle touches and finger movements, enabling micro-gesture interactions. Electrical signals from the ring can propagate through the hand to external objects or surfaces, allowing the Z-Ring to identify variations in the hand's impedance profile caused by these interactions. This capability enables the recognition of objects held by the hand without needing to modify those objects.

Additionally, I have developed a suite of interfaces, including buttons, a 1D slider, and a 2D trackpad, that integrate seamlessly with the Z-Ring. These interfaces are designed

with specific geometries that yield different impedance profiles upon interaction, which the Z-Ring detects to pinpoint the contact location without the need for extra interface electronics or batteries. Furthermore, the Z-Ring can identify its wearer through unique anatomical variations that produce distinctive frequency response signatures.

Contrary to prior approaches that required instrumenting an object (e.g., a doorknob) to serve as an antenna [176] or embedding an antenna in a device that the hand must grasp [122], the Z-Ring uses the hand itself as a duplex antenna. This wearable format significantly broadens the interactive possibilities across various application areas. Previous body-as-antenna work [49] depended on ambient RF signals, restricting its functionality to specific locations, or required RF emissions from active devices [136]. However, the Z-Ring's active impedance sensing approach allows for operation anywhere and with any passive external objects. Moreover, it utilizes a wide range of frequencies, offering more extensive sensing capabilities than systems limited to discrete frequency impedance sensing [117, 268].

This work contributes the following:

1. A novel duplex topology employing multi-frequency impedance sensing, enabling a single-point-of-instrumentation, wearable format for human-computer interaction.

2. The demonstration of the Z-Ring's versatility across multiple applications: (a) single and dual-hand gesture recognition, (b) recognition of held objects, (c) both discrete and continuous touch input on passive user interfaces, and (d) user identification and authentication.

3. Evaluation of the Z-Ring's effectiveness through user studies, showing consistent and robust performance across different users, applications, and over time.

6.2 Related Work

The Z-Ring project intersects with five key research domains, enhancing and broadening the scope of existing technologies in radio-frequency and electric field sensing via a novel antenna design. This distinctive setup increases the Z-Ring's applicability in interactive scenarios. In terms of applications, the Z-Ring facilitates advancements in four crucial areas: hand gesture recognition, object recognition, surface UI interaction, and user identification. Initially, I analyze the contributions of Z-Ring to existing work in RF and electric field sensing, focusing on various sensing topologies. Later, I examine related non-electric sensing technologies and their interplay with Z-Ring across different application contexts.

6.2.1 Electric Field and RF Sensing of the Hand and Body

The human body acts as a lossy conductor for high-frequency electric fields [75], enabling its use as a medium for transmitting AC signals or serving as a ground shunt. This property has been extensively utilized in human-computer interaction for a variety of applications, including proximity detection, touch interactions, communication, identification, medical imaging, and motion sensing. I explore these applications through the lens of their electrode (i.e., antenna) topology, building on the classifications provided by Zimmerman et al. [280] and Grosse-Puppendahl et al. [82], as shown in Fig. 6.2.

Mutual Capacitance

In the mutual capacitance or shunt mode configuration, the proximity of a hand or body to a pair of transmitting and receiving electrodes alters the mutual capacitance between them. This principle is commonly applied in touchscreens and trackpads. AuraSense [276] implements various configurations with a single transmitting and four receiving electrodes around a watch body to facilitate radial input in the air and on-skin buttons

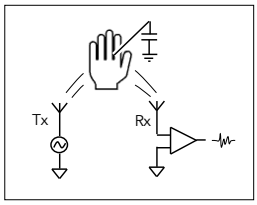

Mutual Capacitance

Ex.: AuraSense [276]

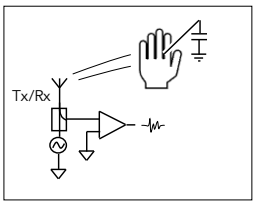

Self Capacitance

Ex.: eRing [242], PeriSense [241], Touché [176], Capacitive Fingerprinting [93], AtaTouch [122], EtherPose [120]

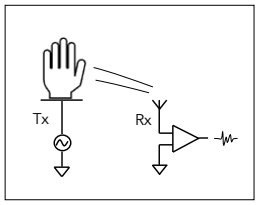

Hand-as-a-Transmitter

Ex.: Hantenna [188], Vu et al. [224], Biometric Touch Sensing [99]

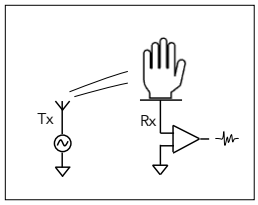

Hand-as-a-Receiver

Ex.: DiamondTouch [59], Carpacio [231], EM-Sense [137], Maekawa et al. [156]

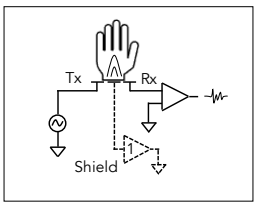

Hand-as-a-Waveguide

Ex.: Personal Area Network [279], Tomo [266], Zensei [191], Cornelius et al. [53], SkinTrack [272], BodyRC [238], ActiTouch [268], ElectroRing (w/ active shield) [117]

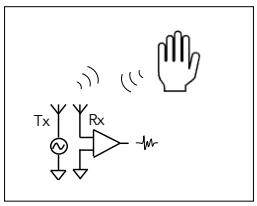

Hand-as-a-Reflector

Ex.: Soli [146], ThuMouse [143]

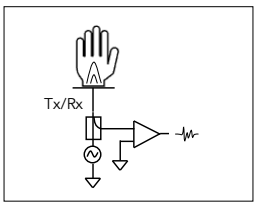

Hand-as-a-Transceiver

Ex.: Z-Ring (this work)

Figure 6.2: Various electric field sensing topologies categorized by transmit and receive antenna coupling configuration (see [280, 82]). Z-Ring's unique topology combines and extends elements of existing topologies. Note: Body capacitance to ground is present in all systems but is omitted here, where it is parasitic rather than utilized for sensing.

and sliders. However, a noted limitation of mutual capacitance in such applications is that as the transmitting and receiving electrodes are positioned closer, the electric field (E-field) tends to cling closely to the electrodes, requiring close interactions. While this characteristic benefits touchscreen applications by reducing power consumption and noise, it presents challenges for far-field sensing in compact wearable devices. In contrast to mutual capacitance setups, the Z-Ring employs a smaller electrode configuration that injects signals into the body, utilizing the body itself as a transmission medium.

Self Capacitance

Self-capacitance or loading mode sensing involves using a single electrode for both transmission and reception. When a ground-coupled body approaches the electrode, part of the electric field is redirected through the body, altering the electrode's capacitance. eRing [242] and PeriSense [241] both introduce a ring-based accessory with external electrodes that detect adjacent finger positions to identify distinct hand gestures. Similarly, Touché [176] utilizes a swept frequency capacitive sensing technique to make conductive objects (like door knobs or water tanks) touch-sensitive.

Like Touché, I adopt a swept frequency method that allows us to detect changes in object interaction and user identity (refer to Capacitive Fingerprinting [93]); however, my approach covers a wider frequency spectrum. In contrast to Touché, I employ galvanic coupling to inject an AC signal into the body via a wearable device, enabling hand gesture recognition without the need for touching an instrumented object.

AtaTouch [122] presents a VR controller that effectively detects pinching movements. As the user's fingers close around a central 6 cm linear antenna embedded in the handle, there is a measurable change in the antenna's far-field coupled return loss value. Building on this, EtherPose [120] designs two wrist-mounted cloverleaf antennas to capture continuous hand poses and microgestures. To ensure robust signal detection, the antennas are tuned to resonate at 1.4 GHz with a diameter of 2 cm and an extensive tuning ground plane.

Similar to AtaTouch and EtherPose, Z-Ring also utilizes impedance sensing with a vector network analyzer (VNA) using the same electrode for both transmitting and receiving. Yet, unlike these systems, Z-Ring employs a swept frequency approach with the hand acting as an antenna, allowing for a more compact electrode configuration. This setup enables Z-Ring to sweep a broader frequency range (1 MHz to 1 GHz), facilitating richer interaction modalities.

Body-as-Transmitter

As a lossy conductor, the human body can effectively serve as a transmitting antenna, such as when one holds a car key fob to their head to increase its range in a busy parking lot. Hantenna [188] investigates the human body's capability as a transmitting (or receiving) dipole antenna, where users make direct contact with electrodes connected to a Vector Network Analyzer (VNA). Their findings show that the body can enhance link levels by a significant 15 to 20 dB. Similarly, Vu et al. [224] and Biometric Touch Sensing [99] employ a signal injected into the body through a ring and wristband, respectively, to authenticate users on a sensing tablet. Z-Ring also utilizes body-injected signaling but differs in that it detects the reflected signal using the same electrode, eliminating the need for external devices for sensing.

Body-as-Receiver

The body can also function as a receiver. Similar to Biometric Touch Sensing, DiamondTouch [59] facilitates user identification through touch interactions; in this setup, the interactive table serves as the transmitter, while the body and chair act as receivers. Carpacio [231] employs a similar principle to detect touches on a car touchscreen.

For interactions with touched objects, Cohn et al. [49] place an electrode on the back of the neck to detect changes in ambient RF signals from sources like power lines and appliances as users touch various objects, such as appliances, light switches, and walls.

Humantenna [50] expands this technique to sense whole body poses.

In the realm of detecting held objects, EM-Sense [137] and Maekawa et al. [156] utilize a radio and a wire coil, respectively, to capture broadband electromagnetic noise emitted by electrically active household objects. Unlike these methods, Z-Ring employs an active sensing approach that stimulates the hand and held objects, enabling it to recognize objects that are electrically passive.

Body-as-Waveguide

The body-as-waveguide or intrabody coupling setup utilizes both transmit and receive modalities with the body making direct galvanic contact with the electrodes. This configuration has been explored for intrabody and interbody communication networks [279] and medically to non-invasively probe internal body composition and tissue characteristics [34]. For instance, Usman et al. introduced a ring-based bioelectrical impedance analyzer to estimate body fat [221].

Zensei employs wide-spectrum bio-impedance sensing to identify users through six electrodes on instrumented objects [191]. Similarly, Cornelius et al. [53] developed an eight-electrode bio-impedance sensing wristband, achieving a 98% identification accuracy among eight individuals and an authentication accuracy of 86.9%. Z-Ring also utilizes body composition variations for biometric user identification and authentication, but it uses just one pair of electrodes on the index finger.

Intrabody coupling has also been applied in gesture recognition applications. Tomo [266] uses a band of eight electrodes around the forearm to perform Electrical Impedance Tomography (EIT), allowing the system to identify 11 distinct hand gestures. Technologies such as BodyRC [238], ActiTouch [268], SkinTrack [272], and ElectroRing [117] all inject high-frequency AC into the body and monitor impedance variations due to skin contact. BodyRC employs electrodes on each arm to distinguish touches, while ActiTouch pairs an electrode on a VR headset with a wristband. SkinTrack transmits an 80 MHz frequency

through a ring and measures impedance at four locations on a watch, enabling 2D interaction on the skin nearby. ElectroRing uses a ring with transmit and receive pairs separated by an active shield to accurately detect pinches, touchdowns, and releases. In contrast, Z-Ring's impedance sensing method uses a single active electrode for both transmission and reception, eliminating the need for an active shield. Moreover, Z-Ring employs a wideband frequency sweep instead of single-frequency measurements, broadening the range of detectable gestures and expanding interactive possibilities beyond simple touch recognition.

Body-as-Reflector

Radio-frequency electromagnetic (EM) waves reflect off interfaces where there is a sharp impedance change, such as the transition from air to body. Doppler radar capitalizes on this effect to detect spatial changes, even subtle movements like thumb-to-finger microgestures. Various studies have explored radar techniques using external benchtop antennas to detect these microgesture interactions [84, 95]. Google's Soli project successfully miniaturized a 60 GHz radar system onto a single integrated circuit (IC), enabling it to track dynamic gestures [146, 234]. ThuMouse expanded on this by facilitating continuous motion detection [143]. In contrast to these methods that employ external antennas to emit RF signals into the air, Z-Ring utilizes lower frequencies that are injected into the body through a wearable device, enabling it to detect signal variations caused by actions like pinches, touchdowns, or touch releases.

Body-as-Transceiver

Z-Ring utilizes a distinctive topology known as body-as-transceiver, which amalgamates and expands upon elements from previous configurations. Similar to the *body-as-waveguide* approach, this topology injects and receives current through the body as a transmission medium but can operate with a single active electrode (akin to self-

capacitance) for both transmission and reception, facilitating a single-point-of-instrumentation setup. As an active transmit sensing method, my system exhibits less sensitivity to EM noise compared to passive techniques, though it is still susceptible to potential voltage fluctuations between the system's ground and the earth ground (such as when a user removes their shoes). To mitigate these fluctuations, I implement a bias resistor between an electrode and the local body ground connected to Z-Ring's sensor ground (refer to Sec. 6.3.1). Moreover, the signal processing techniques incorporate or adaptively learn normalization over time.

Z-Ring's system sweeps a broad frequency range from the low MHz to low GHz, capturing a comprehensive impedance profile—an advantage not shared by previous works like EtherPose and ElectroRing. This capability enables four distinct interactive applications using the same hardware: gesture sensing, held object detection, passive UI interaction, and user identification. To my knowledge, no other work, whether involving E-field sensing or not, covers such a wide array of tasks.

6.2.2 Non-Electric Field Sensing Approaches

I now explore non-electric field (EF) sensing methods across the four application domains of Z-Ring.

Hand Gesture Detection via Non-EF Wearables

Commercial hand gesture detection systems [164, 14, 11] often use optical methods, employing cameras mounted on devices such as AR/VR headsets or necklaces. These systems need a clear line of sight to the hands, which limits their ability to detect gestures made outside the camera's field of view. To address this, various systems incorporate sensors on the wrist, hand, or fingers, utilizing diverse modalities such as optical ([46], [124], [159], [44], [153]), thermal ([81], [264]), bio-acoustic ([25], [168], [255]), ultrasonic ([104], [254]), mechanical ([213], [149], [130]), and inertial ([85], [162], [73], [144]). These

devices can detect anything from simple pinches to discrete gesture sets and can drive full kinematic models.

Despite their capabilities, these methods have notable drawbacks: (1) Passive IMUs and bio-acoustic sensors can detect finger contacts but struggle with release detection, crucial for actions like dragging and dropping; (2) Gesture sensing with IMUs often requires multiple instrumentation points, complicating the setup; (3) Optical and ultrasonic systems need an unobstructed view of the gesturing limbs, restricting sensor placement and complicating pinch detection; (4) Mechanical and magnetic approaches necessitate full hand, back of the hand, or fingertip instrumentation, which can be cumbersome.

In contrast, Z-Ring requires instrumentation only at the base of the index finger—an ergonomic and socially acceptable location. By utilizing the body as a transmission medium, Z-Ring avoids the need for a line of sight, allowing it to reliably sense microgestures. Additionally, it can robustly detect both touchdown and touch-up events for single and dual-handed gestures, even with low touch velocity.

Held Object Detection via Non-EF Wearables

Recognizing the object a user is holding can provide valuable insights into their activities or intentions. InDexMo [145] utilizes a finger-worn RFID transceiver to identify tagged objects, but this method requires each object to be tagged or modified, which is impractical. Other techniques assess the object by analyzing the user's grasp, such as using EMG [71], wrist topography [187], and inertial sensors [38]; however, these approaches can be overly sensitive to variations in how the user holds the object.

Viband [135] and VibEye [174] both employ vibrations to identify objects. Viband detects the characteristic vibrations of active objects, like drills or blenders, using an oversampled IMU. VibEye, on the other hand, identifies passive objects by mechanically inducing vibrations in them and measuring the resulting vibrations, achieving an accuracy of 92.5% across 16 different objects. Similarly, Z-Ring also employs active excitation, but

it does so in the electrical domain, allowing it to identify electrically passive objects, a capability not shared by EM-Sense [137] and Maekawa et al. [156] (refer to Sec. 6.2.1).

Passive User Interfaces

Passive user interfaces offer an input medium that operates without the need for an external power source or batteries. Various sensing modalities have been explored to enable this functionality. Audio-based input methods like Scratchinput [91] facilitate passive interaction on textured surfaces by analyzing the sounds produced when dragging a fingernail across them. Acoustruments [133] also uses sound to enable passive input by integrating low-cost, powerless mechanisms with portable devices. OptoSense [257] employs an array of photodiodes to detect motions above the sensor, powered by ambient light from the environment. Other optical techniques, such as Magic Finger [248] and LightRing [115], use miniature cameras and sensors mounted on the fingertip to transform any surface into an input medium. UbiquiTouch [229] utilizes a low-power touch sensor energized by ambient light.

RFID-based approaches like IDsense [142], PaperID [141], RIO [177], and RapID [203] provide passive input through RFID tags, with nearby RFID readers detecting and interpreting backscatter signals from these tags. MARS [28] offers passive touch surfaces via an ultra-low power sensing and back-scatter communication system.

Although these research initiatives enable passive input, they are often constrained in terms of interactivity, can be costly to deploy, or require specialized infrastructure like RFID readers in the environment. In contrast, Z-Ring overcomes these challenges by offering robust input capabilities through low-cost interfaces that function without electronic components or batteries.

User Identification via Non-EF Wearables

Biometric recognition systems are crucial for regulating access to resources or enhancing personalization in interactive applications. Wearable technologies employ a variety of sensing methods to capture distinctive biometric data, including impedance (Sec. 6.2.1), photoplethysmography (PPG), electrocardiography (ECG), iris recognition, gait analysis via accelerometers, heartbeat acoustics, and skin conductance [35]. Since wearables typically incorporate multiple sensors for fitness and activity tracking, these modalities can be combined with each other or with traditional security measures like passwords to enhance accuracy or enable continuous authentication [209]. For instance, Nymi [173] integrates an onboard fingerprint reader for initial user authentication, utilizes ECG for continuous “liveness” verification, and includes an NFC transmitter for communication with host systems. Similarly, Z-Ring provides methods for continuous user recognition, offering more secure, context-aware, and personalized experiences. Beyond just non-electric field (EF) methods, Z-Ring also supports extensible authentication capabilities, allowing for verification when the user is physically in contact with a resource by leveraging its features for held object recognition, user identification, and signal transmission through the body.

6.3 A Ring Wearable for Multi-Modal Hand Interaction

The Z-Ring prototype features a ring equipped with an electrical system that monitors the impedance of a user’s hand. Changes in impedance may arise from finger movements, holding an object, or touching an external surface. By tracking these impedance variations over time, Z-Ring can discern user gestures, identify interactions with specially designed passive user interfaces, recognize objects held in the user’s hand, and authenticate the user’s identity. In the studies presented in this paper, the Z-Ring prototype is worn on the index finger.

6.3.1 Sensing Technique

When an electromagnetic wave encounters a boundary between two transmission mediums, it partially transmits into the new medium and partially reflects back due to the impedance mismatch between the mediums. By measuring the magnitude and phase of the reflected wave at the boundary, one can determine the impedance characteristics of the new medium. This method is commonly used in electrical engineering for assessing antenna impedance: a vector network analyzer (VNA) sends a frequency-varying continuous wave signal to the antenna under test and evaluates the reflected signals to ascertain the antenna's impedance across frequencies. I utilize this technique to analyze the hand as if it were an antenna, measuring its impedance over a range of frequencies.

The human body, capable of absorbing RF waves and allowing transmission at specific frequencies [75], enables the hand to function as an RF antenna. The Z-Ring capitalizes on this by introducing a small RF signal into the body through contact with the finger, then capturing the reflected signal to assess hand impedance. As the hand's posture changes, so does the antenna geometry, altering the associated impedance.

Impedance may also vary if the hand contacts external surfaces, like other objects or parts of the user's body. The signal from the ring flows through the hand to these surfaces, causing reflections at the new boundaries formed between the hand and the surface, leading to further impedance changes. These variations are informative for identifying how the hand interacts with external surfaces.

6.3.2 Electrical Setup

Z-Ring assesses impedance by measuring the reflection coefficient, or S11, which quantifies the amount of a wave that is reflected due to an impedance discontinuity in the transmission medium. This coefficient's magnitude is expressed as the ratio of the reflected wave's amplitude to that of the incident wave. To perform this measurement, Z-Ring uses the S11 port of a vector network analyzer (VNA). The Z-Ring prototype includes

two electrodes for impedance measurement: the signal electrode, which both sends the signal into the hand and captures the reflected signal, and the bias electrode, which connects the hand to a local ground through a 2 M biasing resistor. Figure 6.3a illustrates this setup.

Figure 6.3b depicts Z-Ring's electrical model as a simplified circuit. Here, the hand is modeled as a combined variable resistor R_b, capacitor C_b, and inductor L_b, with values that vary depending on hand posture and external contacts. An AC signal is fed into the hand through a 50 transmission line. Due to impedance mismatch at the ring-skin interface, part of this signal is reflected back, while the rest travels into the hand. R_e and C_e represent the components of this impedance mismatch, influenced by factors such as skin moisture and the tightness of electrode contact with the skin, respectively.

Additionally, the hand is connected to the sensor's local ground via a 2 M resistor. C_p represents the parasitic capacitance resulting from the body's weak coupling to the earth ground, influenced by variables such as the material and thickness of the user's shoe soles and whether the feet are in contact with the floor. Given the minimal coupling to earth, C_p is relatively small, and the impedance characteristics of the hand predominantly define the circuit's overall impedance.

6.4 Background Experiments

My sensing approach treats the human hand as a broadband, full-duplex antenna. Given its complex structure of skin, muscle, fat, and bone, each layer influences its function as an antenna. To better understand these properties, I conducted simulations to analyze the frequency response of the hand and how it varies across different postures, when holding objects, or when touching external surfaces.

I utilized CST Microwave Studio [211], a commercial electromagnetic analysis tool, for the simulations. This software applies numerical methods like the finite element method and finite integration technique to study electromagnetic fields within complex structures.

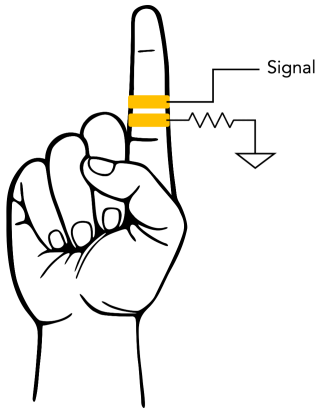

(a) Electrodes (shown in yellow) on the finger. The signal electrode is towards the finger's tip, and the ground electrode is below it.

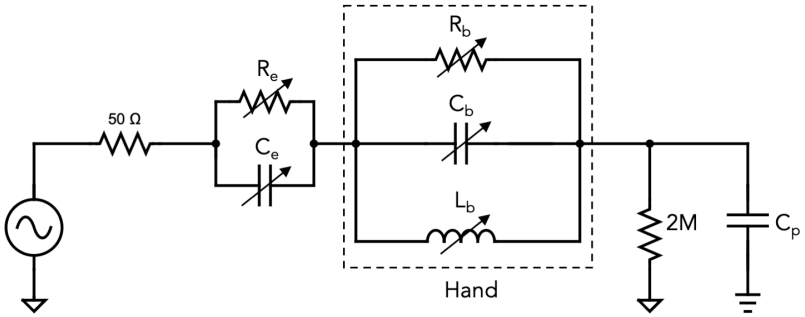

(b) Simplified equivalent circuit of Z-Ring's electrical model.

Figure 6.3: Z-Ring's electrical setup.

I used Hugo [200], an electromagnetically precise 3D human body model from the US National Library of Medicine, as the simulation base. In CST Studio's PoserGUI, I modeled the hand in various postures and their corresponding electrodes using copper material. Figure 6.4 displays an example of a hand model equipped with ring electrodes.

The results indicate that the frequency range from 1MHz to 1000MHz is optimally absorbed by the human body, making it suitable for gesture recognition; this range also proved ideal in simulations for passive interfaces. For object detection, I observed that frequencies above 500MHz, up to 1000MHz, begin to couple with objects through the air as the signal wavelength aligns with object dimensions. Therefore, I utilize the 1MHz to 500 MHz range for object recognition experiments. For user identification and authentication, the 1MHz-400MHz range yielded the most distinct responses, which guided the choice of frequencies for these applications.

6.4.1 RF Energy Absorption

In the quest to determine the most efficient excitation frequency for the prototype, I conducted modeling of the specific absorption rate (SAR) of the hand across a spectrum of frequencies. SAR quantifies the rate at which RF (radio frequency) energy is absorbed per unit mass by the human body. The testing spanned frequencies from 1 MHz to 2000 MHz, known for their high absorption rates by the body [188]. The results, depicted in Figure 6.4, revealed a continuous decrease in the body's absorption rate from 1 MHz (maximum normalized SAR = 1) to 2000 MHz (maximum normalized SAR = 0.2). Notably, the absorption rate experiences a significant reduction after 1000 MHz (maximum normalized SAR = 0.47). Based on these findings, I opted for the frequency range of 1 MHz to 1000 MHz for the prototype's excitation frequencies.

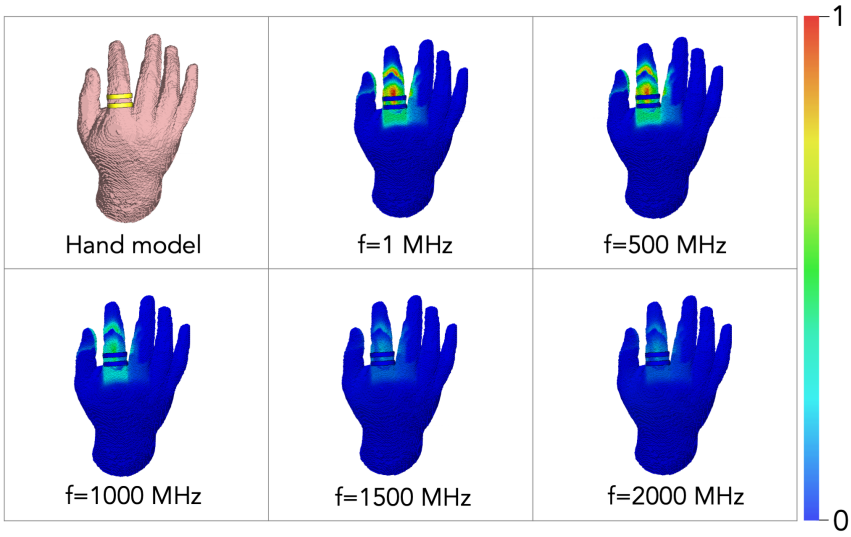

Figure 6.4: Illustration of the biomedical hand model employed in the analysis of Specific Absorption Rate (SAR) of the human hand, along with simulation results at various frequencies (f). The figure showcases the ring electrodes on the hand model highlighted in yellow, with the color bar indicating normalized SAR values.

6.4.2 S11 Variations Based on Hand Pose

The investigation now delves into the variations of S11 during one-handed gestures, with a particular focus on interactions between the thumb and index finger. Specifically, I aim to elucidate how the contact between the thumb and index finger influences S11 and how the location of this contact (e.g., at the tip or middle of the index finger) impacts S11. I examine three scenarios:

1. When the index finger and thumb are not in contact.

2. When the thumb touches the tip of the index finger.

3. When the thumb touches the middle of the index finger.

Hand pose models were constructed for each scenario and simulated across a frequency sweep from 1 MHz to 1000 MHz. The resulting S11 plots are depicted in Figure 6.5. The simulation outcomes reveal a significant decrease in S11 when the thumb and index finger make contact. This reduction occurs because the thumb, upon touching the index finger, loads the index finger antenna, diverting the signal away from the ring. Consequently, less power is reflected through the signal electrode, leading to a drop in S11. This discernible change in S11 enables robust differentiation between a pinch and no pinch. Moreover, when the thumb makes contact with the index finger and swipes closer to the ring, the S11 value also diminishes. As the physical distance between the thumb and the contact point on the ring decreases, additional signal shunting occurs, resulting in reduced reflected power and a lower S11 value.

6.4.3 S11 Variations When Holding Objects

This investigation delves into how S11 measurements fluctuate when a user holds various objects. For this exploration, I selected four objects: a sphere, a disk, a cube, and a cylinder. These objects encompass a range of shapes and sizes, contributing to diversity

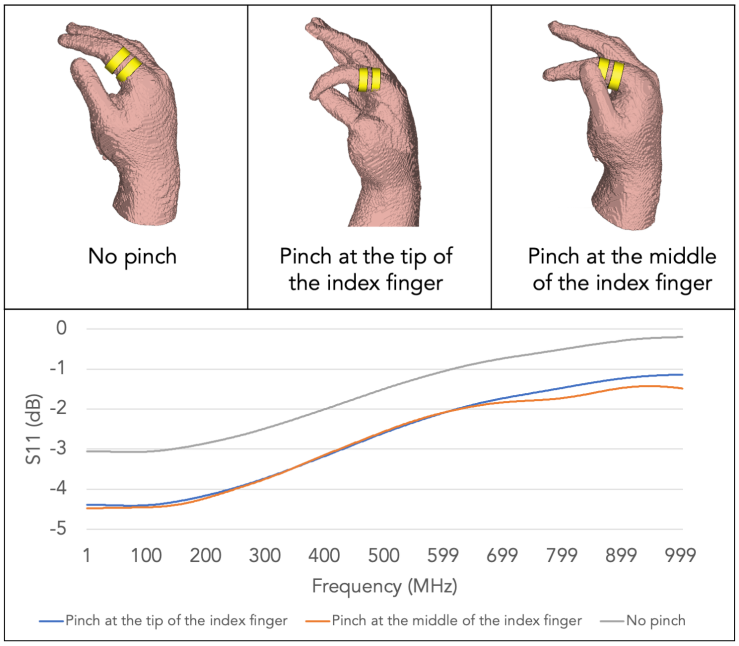

Figure 6.5: Various hand poses and their corresponding S11 measurements.

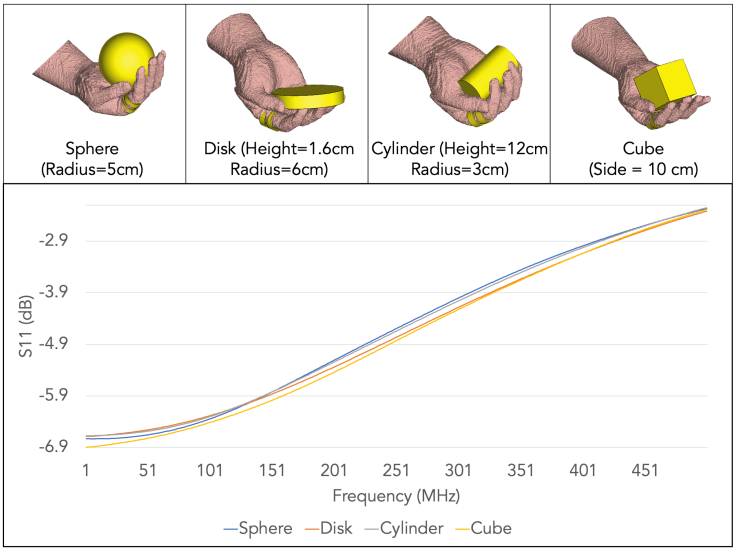

Figure 6.6: The figure shows four simulation models of hand holding different objects and the corresponding S11 curves for those scenarios

in the analysis. Additionally, each object necessitates a distinct holding grip, further enhancing variation. While many materials can impact impedance, metal elicits the most pronounced impedance changes. Therefore, I modeled these objects as solid aluminum shapes. Four hand models were crafted to simulate the act of holding each object, as depicted in Figure 6.6.

During the experiments, I observed that at higher frequencies, the dimensions of the objects approached the quarter wavelength of the excitation signal (for instance, at 500 MHz, the quarter wavelength is approximately 15 cm, and at 1000 MHz, it is approximately 7.5 cm). This similarity, coupled with the close proximity of the objects to the ring, led to direct coupling between the objects and the ring over the air, thereby influencing the impedance measurements [278]. To mitigate this issue, I confined the sweep frequency from 1 MHz to 500 MHz. The S11 results obtained from the simulation, as depicted in Figure 6.6, reveal subtle yet discernible differences in the S11 curves corresponding to different objects.

6.4.4 S11 Variations When Touching External Surfaces

The investigation comprised two distinct sets of experiments aimed at elucidating the impact of touching passive surfaces on impedance. In the initial set, I manipulated the shape and size of copper sheets, while in the subsequent set, I delved into the effect of touching the same surface at different locations. These experiments were conducted using a thin sheet of copper measuring 0.03 mm in thickness.

In the first set of experiments, I examined three different shapes: square (with sides measuring 3 cm), triangle (with sides measuring 3 cm), and circle (with a diameter of 3 cm). The outcomes of this experiment are showcased in Figure 6.7a. The observations revealed that the S11 measurements for the copper-based shapes exhibited greater diversity at lower frequencies, gradually diminishing towards the higher end of the frequency spectrum. Additionally, experiments involving the same shape (a square) but with different sizes

(sides measuring 1 cm, 3 cm, 5 cm, and 7 cm) unveiled that S11 measurements were more sensitive to shape rather than size. For instance, when comparing the square with 3 cm sides to the triangle with 3 cm sides, the maximum difference in S11 values was 0.124 dB at 10 MHz. Conversely, when comparing the square with 1 cm sides to the square with 7 cm sides, the maximum difference in S11 values was 0.07 dB at 10 MHz. This underscores the notion that the shape of the surface exerts a more pronounced influence on S11 measurements than its size, at least within the range of sizes examined.

In the subsequent experiment, I positioned a finger on three distinct locations (labeled A, B, and C) of a 10-centimeter square piece of copper. The simulation outcomes for this scenario are depicted in Figure 6.7b. These results unequivocally validate that S11 measurements exhibit variations contingent upon the touch point.

6.4.5 S11 Variations for Different Users

Given that the sensing methodology relies on utilizing the hand as an antenna, the distinct anatomical features of each individual exert an influence on impedance measurements. To explore how S11 measurements may differ among various individuals, I constructed hand models exhibiting identical postures but divergent anatomical characteristics. These differences were introduced by adjusting the values of biological components such as bone, blood, fat, muscle, and skin. Table 6.1 provides an overview of these characteristic values. Figure 6.8 illustrates the simulation outcomes. Notably, the results demonstrate that disparities in S11 readings between individuals are most pronounced within the frequency range spanning from 1 MHz to approximately 400 MHz.

6.5 Implementation

The Z-Ring prototype is equipped with two electrodes: the signal electrode, which both transmits the signal into the hand and captures the reflected signal, and the bias electrode, which grounds the hand to a local ground through a 2 M resistor. Each electrode is crafted

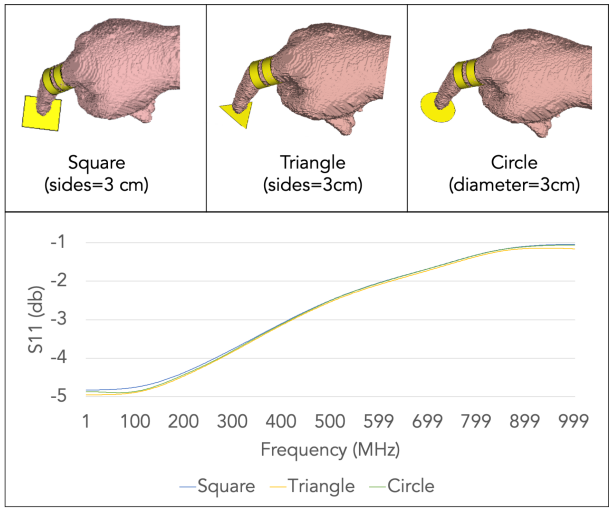

(a) The figure shows a hand model interacting with three different copper shapes and the corresponding S11 curves from the interaction.

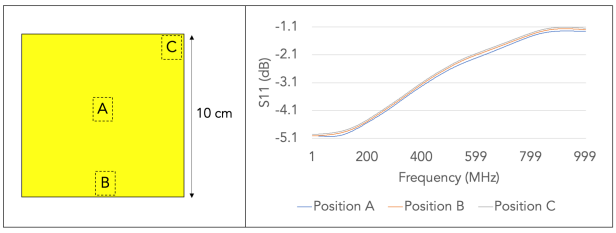

(b) The figure shows three positions (A, B, and C) on a copper square where the hand made contact and the corresponding S11 curves from the interaction.

Figure 6.7: Simulation results for hands interacting with a variety of passive copper shapes.

	Hand Model #1		Hand Model #2		Hand Model #3	
	ϵ	σ	ϵ	σ	ϵ	σ
Blood	76.82	1.233	80.66	1.294	72.97	1.17
Bone	15.28	0.064	16.04	0.067	14.51	0.061
Fat	6.07	0.036	6.37	0.038	5.76	0.034
Muscle	65.97	0.708	69.26	0.743	62.67	0.673
Skin	69.45	0.507	72.92	0.532	65.97	0.481

ϵ = Dielectric constant | σ = Electrical conductivity (S/m)

Table 6.1: The table lists the different dielectric constants and electrical conductivity values for modeling the three different hand types in user identification simulation experiments [200, 211]

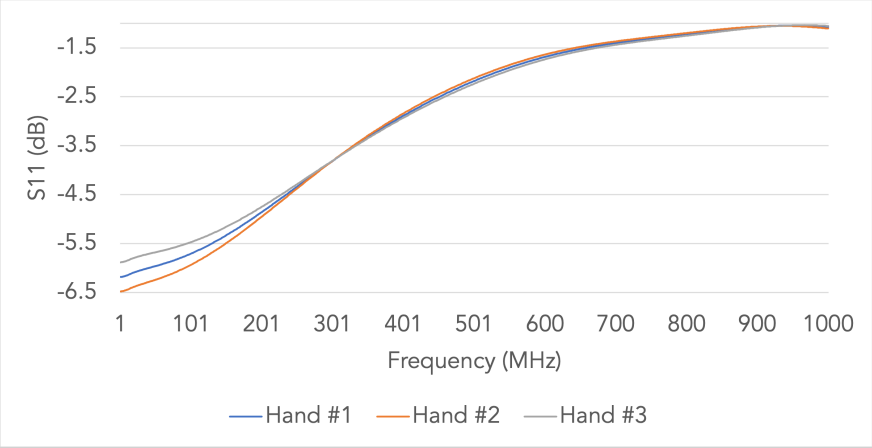

Figure 6.8: The figure shows the S11 simulation results for three hand models representing three different people and carrying the same posture

from a 65 mm by 8 mm strip of exposed copper on a flexible printed circuit board (PCB) made from polyimide. This configuration is displayed in Figure 6.9a. The flexibility of the PCB allows the electrodes to conform snugly around the user's finger, encased within the ring. The electrodes are positioned adjacent to each other along their entire length with a 4 mm gap between them. To prevent oxidation from skin and environmental moisture, the electrodes are coated with gold using the electroless nickel immersion gold (ENIG) process.

On the opposite side of these electrodes, the flexible PCB includes a U.FL connector to attach a shielded coaxial cable that links the electrodes to the vector network analyzer (VNA). This side also houses the bias resistor associated with the ground electrode. The PCB is attached to a velcro strip using double-sided tape, facilitating adjustable fitting around fingers of various sizes. This setup, including the PCB mounted on velcro, constitutes the ring configuration as shown in Figure 6.9b.

The S11 measurements are taken using a portable VNA, LiteVNA [253], which operates between 51 kHz and 6 GHz and is powered by a rechargeable battery. The device consumes 2.4 W, split between its measurement circuitry and display driver (1.16 W) and the LCD backlight (1.22 W). The VNA is conveniently strapped to the user's wrist with velcro, keeping the connection to the ring's S11 port short; its compact size of 91 mm by 58 mm suits this wearable application.

S11 measurements involve transmitting a frequency sweep and recording the reflected signals. The VNA captures this data as a 51-point array, conducting 30 sweeps per second, establishing a sampling rate of 30 Hz. The frequency range for these sweeps, adjustable between 1 MHz and 1 GHz, is set according to the user application. Data from these sweeps is transmitted via a wired USB connection to a MacBook Pro laptop, where they are logged and analyzed by a custom Python application. Notably, the prototype maintains consistent S11 amplitude changes during interactions, whether or not it is connected to the laptop and operating on battery power. The VNA's output power is capped at 5 dBm to ensure safety [20]. Section 6.6 details the software processing

pipeline for each type of interaction.

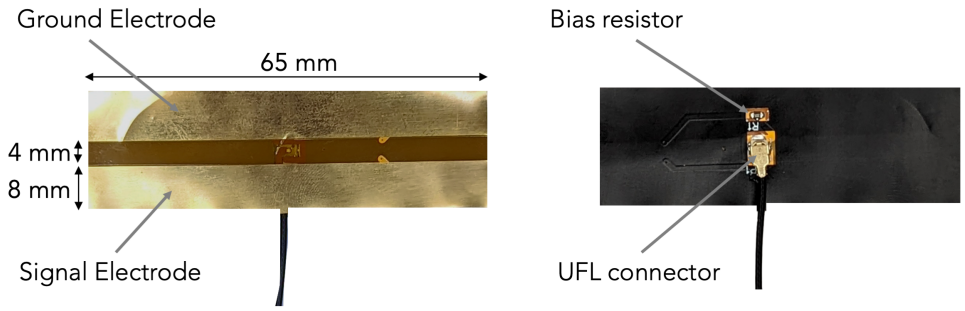

(a) Both sides of the electrode setup utilized in the Z-Ring prototype on a flexible printed circuit board.

(b) A user wearing the Z-Ring prototype with a portable VNA strapped to their wrist.

Figure 6.9: Electrodes for the Z-Ring prototype.

6.6 Application Domains

I now outline the data processing pipeline, evaluation, and results from the user studies across four application domains: gesture recognition, object recognition, tangible user

interfaces, and user identification. The study involved 21 participants (4 female; average age 27.7, ranging from 18 to 33 years). Not all participants took part in each application sub-study due to logistical constraints. Each sub-study lasted between one to three hours, and participants completed them in a single session. No data was excluded based on performance. The user research was conducted over a period of three months.

6.6.1 Gesture Input

Z-Ring enables input through hand gestures, facilitating always-available control for wearable or environmental computing. It supports two interaction types: one-handed and two-handed. The one-handed interactions involve subtle gestures between the thumb and index finger, while two-handed interactions involve one hand interacting with the back of the other hand. I have designed five specific gestures for both interaction scenarios: tap, double tap, long tap, and swipes to the left and right. Figure 6.10 illustrates how these gestures are performed. For instance, the various taps allow for different selection actions in user applications, and the swipes facilitate navigation.

Recognition

Gesture recognition in the system is predicated on the frequency domain changes and temporal patterns captured in the S11 measurements during gesture execution. Changes in the frequency domain arise from alterations in the signal propagation paths while performing gestures. Figure 6.11 illustrates these new signal paths for one- and two-handed gestures. Temporal patterns emerge from the finger movements involved in each gesture. For instance, the motion pattern of a double tap is distinct from that of a single tap. In the analysis, I primarily use S11 magnitude as the key feature, although phase shifts were also considered. However, phase shifts proved unstable due to the lossy nature of the hand as a transmission medium, which leads to unpredictable phase changes.

For gesture recognition, S11 measurements are conducted using a frequency sweep

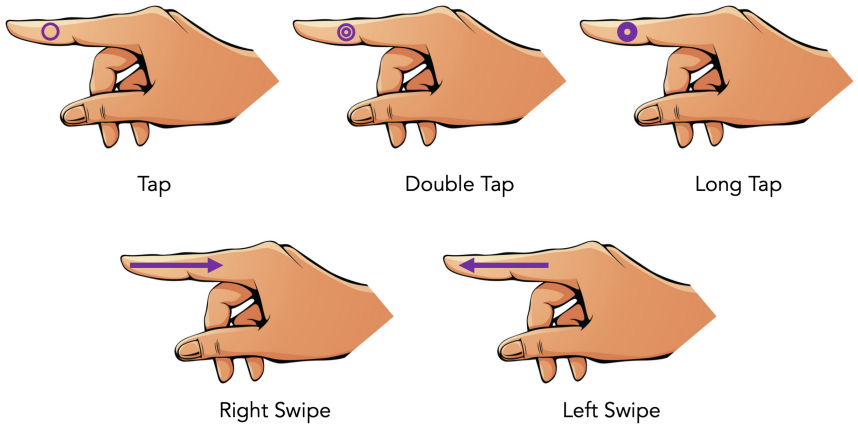

(a) One-handed Z-Ring gestures. The gestures are performed with the thumb on the side of the index finger. Different taps occur near the tip of the index finger, while swipes are made from the tip to past the middle of the finger.

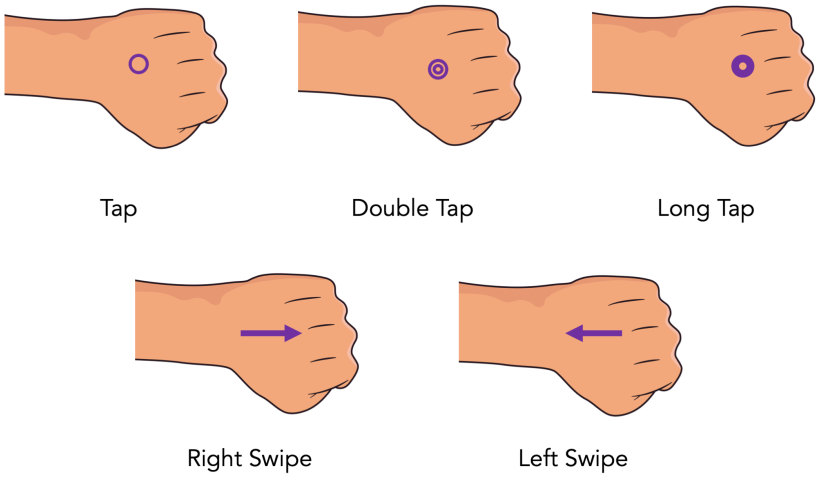

(b) Two-handed Z-ring gestures. The gestures are made with the index finger of the hand wearing the ring on the back of the other hand's palm. Taps are made near the center of the back of the hand, and swipes span most of the hand's back length.

Figure 6.10: The Z-Ring gesture set for one- and two-handed input and the optimal locations to perform these gestures.

from 1 MHz to 1 GHz. The recognition process begins with applying a moving median filter to the real-time S11 data with a 200-millisecond sliding window, which highlights impedance changes and reduces noise from motion artifacts. Subsequently, 1.5-second windows of S11 data (about 45 S11 samples at 30Hz) are individually analyzed to detect gestures. All S11 samples within each window are compiled into a spectrogram; Figure 6.12 displays spectrograms for the five gestures and a null state where no gesture is performed.

Each spectrogram is resized to a 25x25 matrix and input into a convolutional neural network (CNN) for gesture classification. Figure 6.13 depicts the architecture of the CNN. To accommodate the possibility of gestures occurring at any point within the 1.5-second window, I generate synthetic data by shifting this window between -600 and +600 milliseconds in 30-millisecond increments. This time shifting involves rolling the spectrogram along the time axis and wrapping the data around the edges.

For evaluation, I developed both user-independent and user-dependent models. For the user-independent model, I augmented the training set by rolling the spectrograms along the frequency axis. This adjustment accounts for individual variations in hand anatomy, which affect impedance responses across different frequency bands. Specifically, I shift the spectrogram by 500 MHz in the increasing frequency direction in 20 MHz steps and wrap it around the edges. This dual augmentation in both time and frequency domains enhances the model's ability to generalize across different users.

Evaluation

I conducted user studies to evaluate both one-handed and two-handed gestures, involving 14 and 15 participants, respectively. Each participant was seated in front of a computer screen which displayed visual cues prompting them to perform specific gestures. The protocol for both one- and two-handed gestures was identical, requiring participants to execute each of the five designated gestures as well as a null gesture. The null gesture

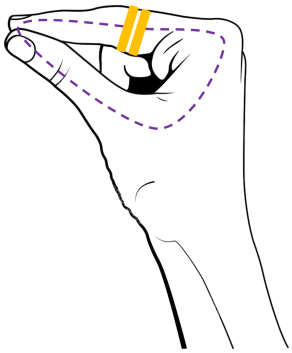

(a) For one-handed gestures, the path is a loop completed between the index finger and thumb.

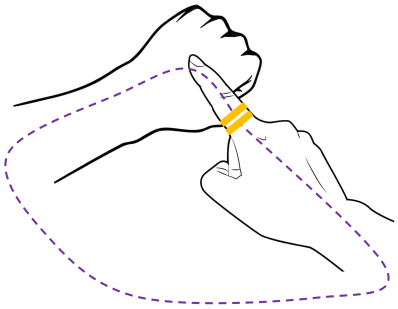

(b) For two-handed gestures, the path is a loop via both hands through the torso.

Figure 6.11: The new electrical paths created (purple) between the two ring electrodes (yellow) when performing a one- or two-handed gesture.

involved participants engaging in typical desk interactions such as touching their phones, wallets, keys, and other personal belongings with both hands, serving as a control to assess how the recognition system handled non-gestural activities.

In total, each participant performed 180 gestures, broken down into 6 sessions with each session including 6 gestures (the five designated gestures and one null gesture)

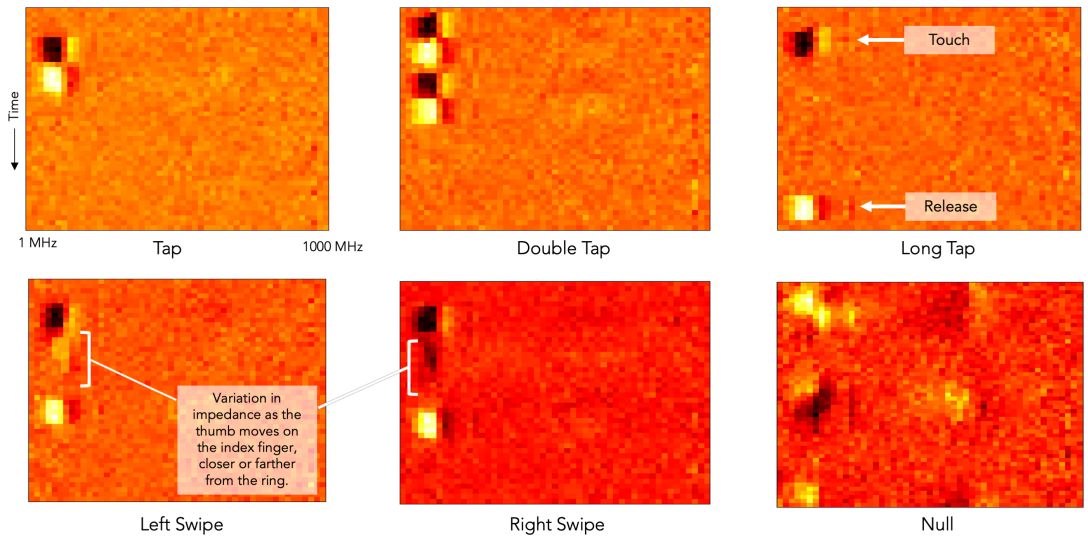

Figure 6.12: Spectrogram images illustrate various one-handed gestures and a data window where no gesture occurred (Null). These spectrograms are created using S11 data that has been processed with a median filter. In each spectrogram, the y-axis represents time, and the x-axis represents frequency, ranging from 1 MHz to 1000 MHz. As demonstrated in the Long Tap gesture spectrogram, a darker blob indicates the touch-down event, and a lighter blob marks the touch-up event between the thumb and index finger. It's important to note that these spectrogram images are based on data from a single user; thus, spectrograms from different users might display variations in highlighted frequency bands.

repeated 5 times. This structure allowed us to thoroughly evaluate the interaction set for either one-handed or two-handed gestures. To ensure accurate assessment of cross-session performance, participants were instructed to remove and then re-wear the ring after each session.

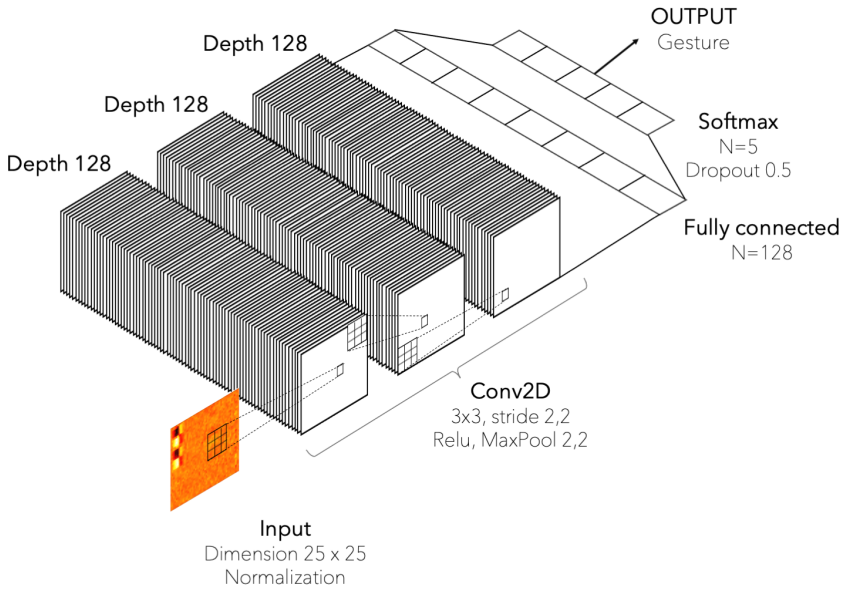

Figure 6.13: The CNN architecture for gesture recognition. Input is initially normalized, and multiple convolution layers are then applied, each followed by a MaxPool layer; finally, dropout and softmax are used.

Results

I selected accuracy as the primary metric to evaluate the performance of the recognition system. I examine both user-dependent and user-independent models. For the user-dependent models, I trained the CNN with the first four of the six collected data sessions and tested it on the remaining two sessions.

For the user-dependent model for one-handed gestures, Figure 6.14 illustrates the recognition accuracy per participant. The average recognition accuracy stands at 93.14%, with the highest being 100% for participant P4 and the lowest at 89% for participant P2. The confusion matrix depicted in Figure 6.15a highlights that the left swipe is the most difficult gesture to distinguish, often confused with the right swipe and tap gestures. We could enhance these results by substituting the tap gesture with a double tap or long tap

in the user application. The null gesture achieves a high recognition accuracy of 96.1%, indicating that the system effectively minimizes false positives while accurately identifying gestures.

The average recognition accuracy for the user-dependent model for two-handed gestures is 92.67%, with the highest at 98% for participant P21 and the lowest at 86% for participants P1 and P10. Figure 6.14 presents the accuracy per participant. The confusion matrix in Figure 6.15c shows that the left swipe, often confused with the long tap, presents the most significant challenge; long tap is similarly mistaken for left swipe. Removing the long tap from this set could potentially improve accuracy.

For the user-independent models, I trained the CNN on data from all sessions for all but one user, then tested on the left-out user's data, repeating this for each user.

The average recognition accuracy for the user-independent model for one-handed gestures is 88%, with the highest accuracy at 99% for participant P4 and the lowest at 77% for participant P1, as illustrated in Figure 6.14. The confusion matrix in Figure 6.15b identifies the double tap as the most challenging gesture to recognize.

For the user-independent model for two-handed gestures, the average recognition accuracy stands at 83.67%, with the highest at 92% for participant P4, as shown in Figure 6.15d. This demonstrates the potential for a generalizable set of gestures.

Overall, Z-Ring offers high-accuracy gesture input across a diverse user base, though further fine-tuning through user-specific models could enhance its robustness. The data collected over three months confirms that Z-Ring's performance remains stable over time.

6.6.2 Tangible User Interfaces

Z-Ring introduces a new method for measuring surface impedance through touch, which is utilized to create distinct physical user interfaces. Each interface is designed with a unique characteristic impedance, allowing Z-Ring to differentiate interactions based on their impedance signatures. This capability facilitates the development of passive and

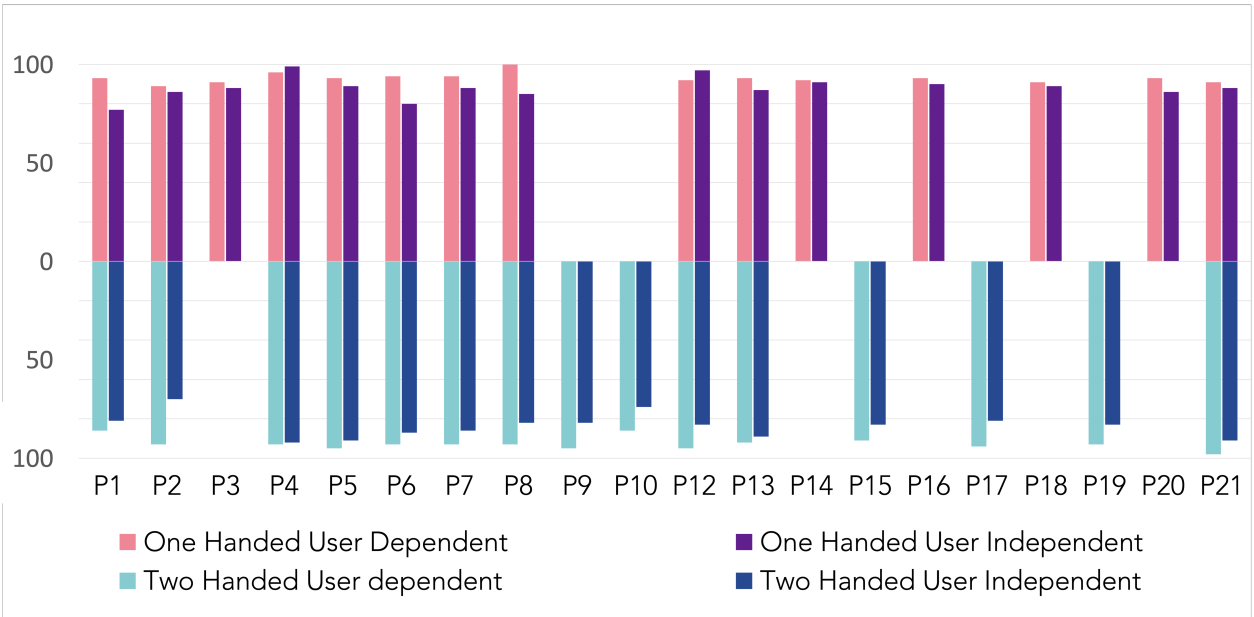

Figure 6.14: Gesture recognition accuracy per participant for one- and two-handed gestures, comparing both user-dependent and user-independent recognition models. The gesture set for the user-dependent model includes left and right swipes, unlike the user-independent model. Due to logistical constraints, some participants did not partake in both gesture tests, resulting in some blank areas in the figure.

battery-free interactive user interfaces. I have designed three types of user interfaces: buttons, a continuous 1D slider, and a continuous 2D trackpad. Figure 6.16 displays these interfaces, each engineered to provide a distinct touch experience.

Design

I fabricate these interfaces from thin copper sheets, chosen for their excellent electrical conductivity, which induces a significant impedance change when interfaced with the Z-Ring. As impedance varies with the shape and size of the conductor [192], I manipulate these parameters to craft unique impedance signatures across the frequency spectrum

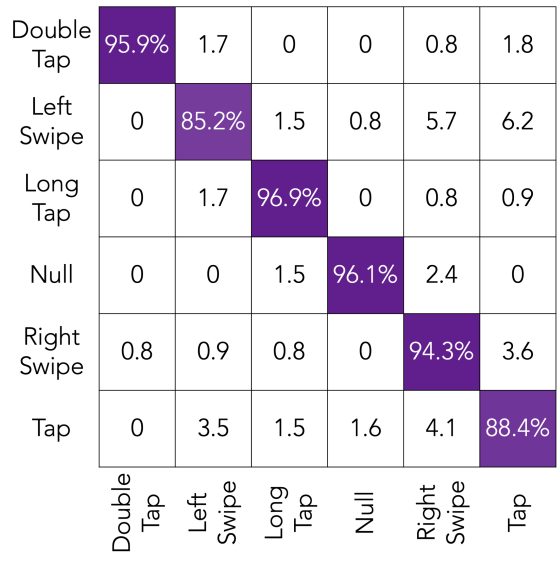

(a) Confusion matrix for one-handed gestures using the user-dependent model.

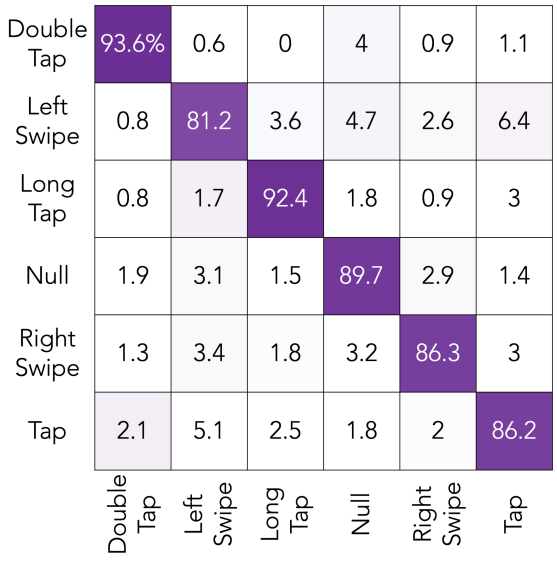

(b) Confusion matrix for one-handed gestures using the user-independent model.

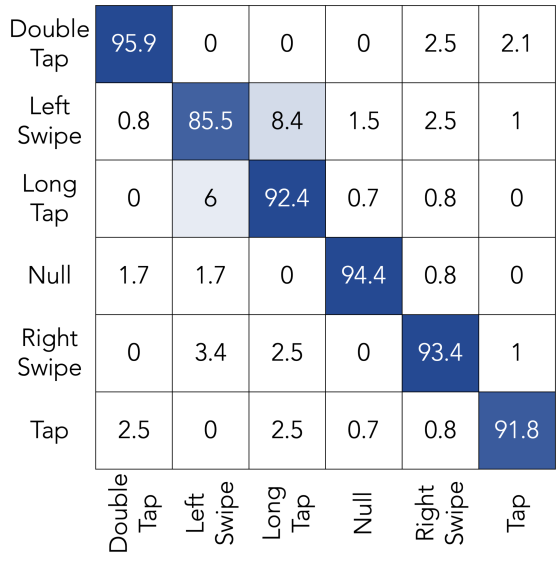

(c) Confusion matrix for two-handed gestures using the user-dependent model.

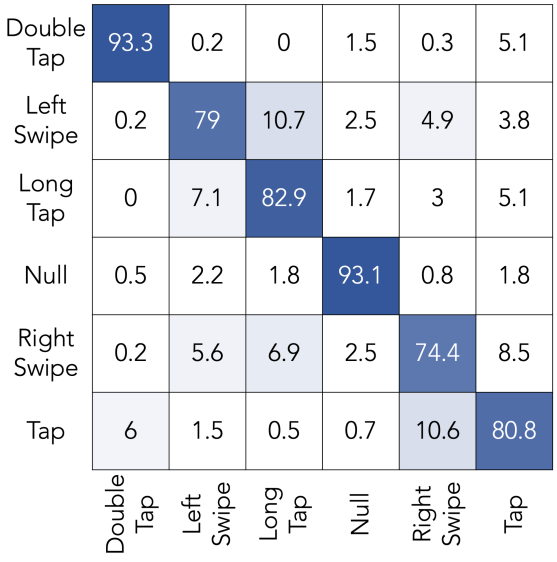

(d) Confusion matrix for two-handed gestures using the user-independent model.

Figure 6.15: Confusion matrices (displaying percentages) for one- and two-handed gestures, detailing performance for both user-dependent and user-independent recognition models.

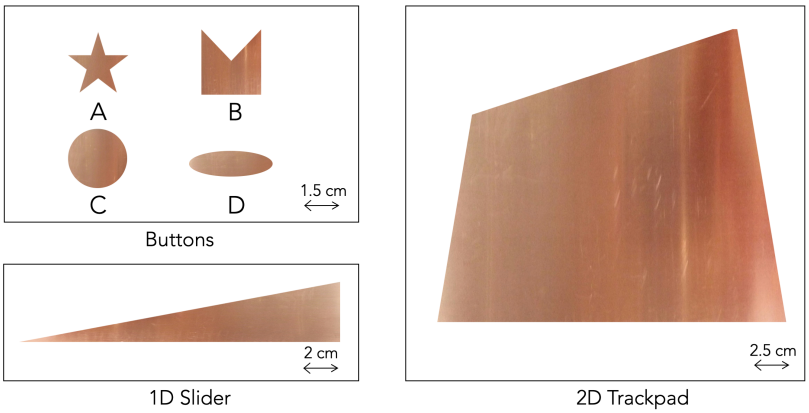

Figure 6.16: Illustration of passive tangible user interfaces developed for Z-Ring, showcasing varied impedance characteristics.

for each interface.

Each button is designed with a distinctive shape to ensure it possesses a unique impedance profile. The 1D slider is constructed with an asymmetrical shape along its length, allowing for a continuously varying impedance as the finger moves along it. This variation aids in precisely locating the finger's position on the slider. Similarly, the 2D trackpad is designed with asymmetrical geometry in two dimensions, ensuring that each point on the trackpad has a distinct impedance characteristic.

Recognition

Recognition

To recognize interactions with buttons via the Z-Ring, I utilize a support vector machine classifier (SVM) with an RBF kernel. The classifier processes the 51-point S11 measurement as a feature vector, determining if a button is touched and identifying which one. The SVM is trained on datasets where each button is touched, as well as on a null dataset where no button is touched.

For pinpointing the finger's position on the 1D slider and the 2D trackpad, I implement

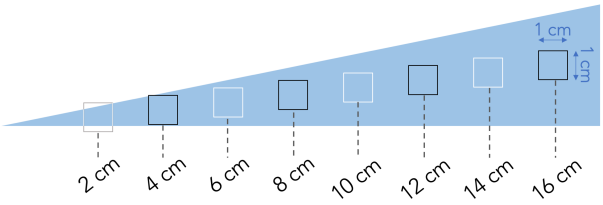

(a) Data collection setup for the 1D slider.

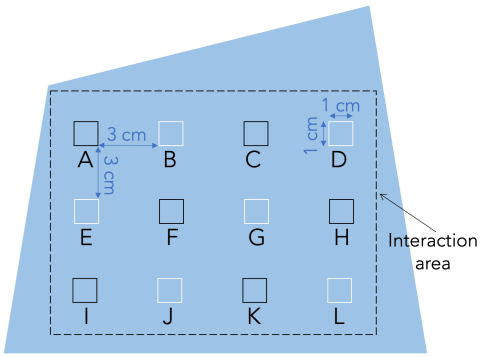

(b) Data collection setup for the 2D trackpad.

Figure 6.17: Designated touch locations on the 1D and 2D interfaces (marked as squares) utilized during data collection. Training data is gathered from the black squares, while the white squares serve to validate the model.

a random forest regressor, configured with 300 trees and a maximum depth of 30, for each interface independently. This regressor takes the S11 measurements from discrete locations across the interface as input data and outputs continuous position coordinates (x for the 1D slider and both x and y for the 2D trackpad). Figure 6.17 displays these discrete positions on both the 1D and 2D interfaces. On the actual prototypes, each discrete position was marked as a 1x1cm square with a Sharpie; users placed their fingers within these squares to ensure consistent data collection. Specifically, the 1D slider featured eight marked locations spaced 2 cm apart, while the 2D trackpad had 12 marked positions (3 rows by 4 columns) spaced 3 cm apart.

The S11 measurement sweep for all three interfaces operates between the frequencies of 1MHz and 1GHz.

Study	Number of Participants	Number of samples per participant	Duration of each sample
Button classification	14	4 buttons × 6 sessions × 5 repeats per button = 120 samples pp.	1 sec
1D slider tracking	17	8 locations × 6 sessions × 5 repeats per location = 240 samples pp.	1 sec
2D trackpad tracking	17	12 locations × 6 sessions × 5 repeats per location = 360 samples pp.	1 sec

Table 6.2: Passive user interfaces evaluation study details.

Evaluation

I conducted a user study to evaluate the effectiveness of Z-Ring in recognizing button presses. Four distinct buttons were created (as shown in Figure 6.16), and the study focused on how accurately Z-Ring could distinguish between pressing each button and not touching any button. Additionally, I assessed the accuracy of continuous position tracking on both the 1D and 2D interfaces. Details of the study are presented in Table 6.2.

Results for Buttons. I initially assessed the reliability of identifying touch to any button. I constructed a binary classifier (SVM, kernel=rbf), with one class utilizing data from button touches and the other consisting of null gesture data from the gesture testing user study; the null class encompassed users engaging with their phones, desks, and actions not involving button touches. Two models were developed: user-dependent and user-independent. The former was trained on the first four buttons and gesture study sessions and evaluated on the last two. The latter utilized all six sessions from one user for testing and all six sessions from the remaining users for training, with this process repeated for all users. This binary classifier yielded 100% accuracy for both user-dependent and independent models.

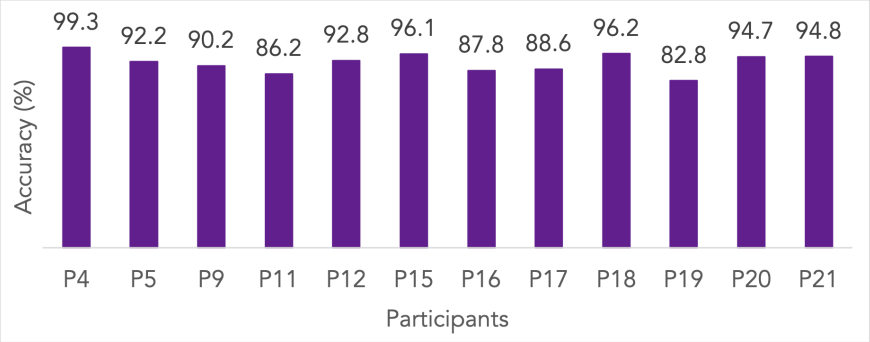

Figure 6.18: Classification accuracy per participant for differentiation among four buttons developed for Z-Ring.

Subsequently, I examined the system's capability to distinguish between buttons. An SVM classifier (kernel=rbf) was trained on the first four sessions and tested on the last two. Each user had an individual model. The average button identification accuracy across all participants was 91.8%, with the highest accuracy at 99.3% (P4) and the lowest at 82.79% (P19). Figure 6.18 illustrates these results. Moreover, I observed that user-independent models for buttons cannot be readily generalized: as the signal traverses through the user's hand, each user's unique anatomy influences the frequency profile differently, leading to distinct spectral signatures for the same button.

Results for 1D Slider I examined the accuracy of Z-Ring in predicting finger location on the 1D slider. A regression model was constructed, trained on data from slider positions '4', '8', '12', and '16' (see Figure 6.17a), and then tested on the remaining positions. For the user-dependent model, training utilized the first four sessions and testing the last two. The user-independent model incorporated data from all six sessions for both training and testing, excluding the participant being tested.

The mean absolute errors for the user-dependent and user-independent models were 3 cm and 4.4 cm, respectively. In the user-dependent model, the maximum and minimum

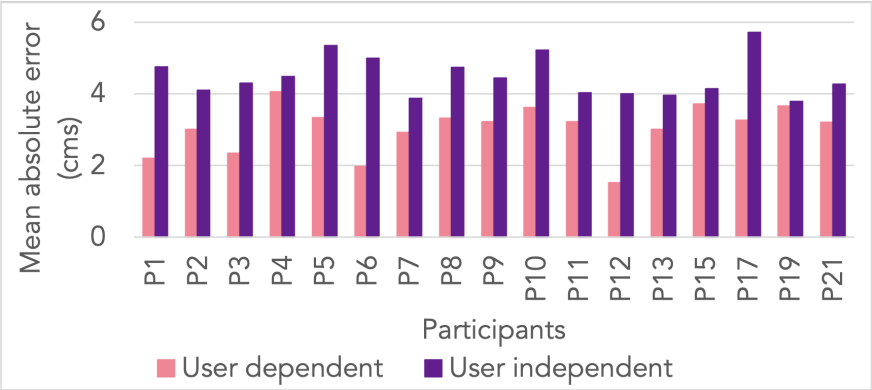

(a) Mean error per participant.

Test points	2	6	10	14
User dependent	5.2	2.3	2.1	2.7
User independent	8	3.9	2.1	4

(b) Mean error (cms) per test point.

Figure 6.19: The tracking error for the 1D slider for both user-dependent and independent regression models.

errors were 4 cm and 1.52 cm, respectively. Conversely, the user-independent model exhibited a maximum and minimum error of 5.71 cm and 3.78 cm, respectively. Notably, both models displayed the highest error at position '2', likely due to its location at the slider's thinner end, where only a portion of the user's finger could establish solid contact with the copper surface. This issue could potentially be mitigated by constructing a taller slider. Refer to Figure 6.19 for a visual representation of these findings.

Results for 2D Trackpad The investigation focused on the accuracy of Z-Ring in predicting finger location on the 2D trackpad. A regression model was constructed using data from positions A, C, F, H, I, and K (refer to Figure 6.17), with testing conducted on

the remaining positions. Both user-dependent and independent models were developed, following the same methodology employed for the 1D slider.

Error was quantified as the mean absolute Euclidean error for each position. The mean absolute error for the user-dependent model was 3.2 cm, while for the user-independent model, it was 4.14 cm. In terms of maximum and minimum errors, the user-dependent model recorded 4.39 cm and 2.67 cm, respectively, while the user-independent model exhibited 4.62 cm and 3.85 cm, respectively. Notably, positions D and L along the trackpad's right edge displayed higher errors in both models, likely due to the protrusion of the edge, which offers a broader range of impedance variations than other locations. This issue could potentially be addressed by bringing the corners closer together or by gathering more data for spots in that vicinity. Refer to Figure 6.20 for a visual representation of these findings.

In comparison to buttons, the user-independent models for 1D sliders and 2D trackpads exhibited superior performance. Despite all being copper-based topologies, the models for 1D and 2D interfaces primarily identify changes in relative impedance between different locations, whereas the button model must discern absolute impedance changes, presenting a more challenging task.

The study findings indicate that while the accuracy of sliders and trackpads may lag behind that of conventional electronic devices, they present promising avenues for inexpensive, battery-free, and low-resolution input devices. Within the constraints of their resolution, these interfaces can facilitate gestural input. For instance, sliders can accommodate 1D gestures like left and right swipes, while trackpads can support 2D gestures such as cardinal-directional swipes or unistroke character inputs. This low-cost gestural input capability renders these interfaces valuable for ubiquitous, situated user interfaces.

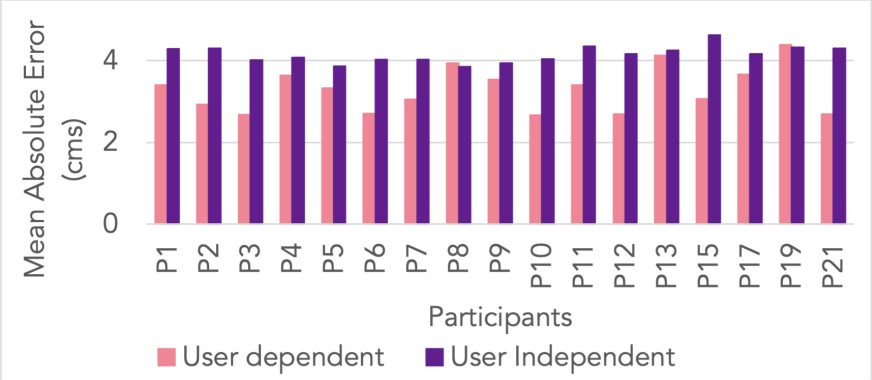

(a) Mean error per participant.

Test points	B	D	E	G	J	L
User dependent	2.5	4.8	2.7	2.8	3	4.3
User independent	3	6.2	3.7	2.7	3.4	6

(b) Mean error (cms) per test point.

Figure 6.20: The tracking error for the 2D continuous trackpad for both user-dependent and independent regression models. The error represented is the combined Euclidean distance error for both X and Y directions.

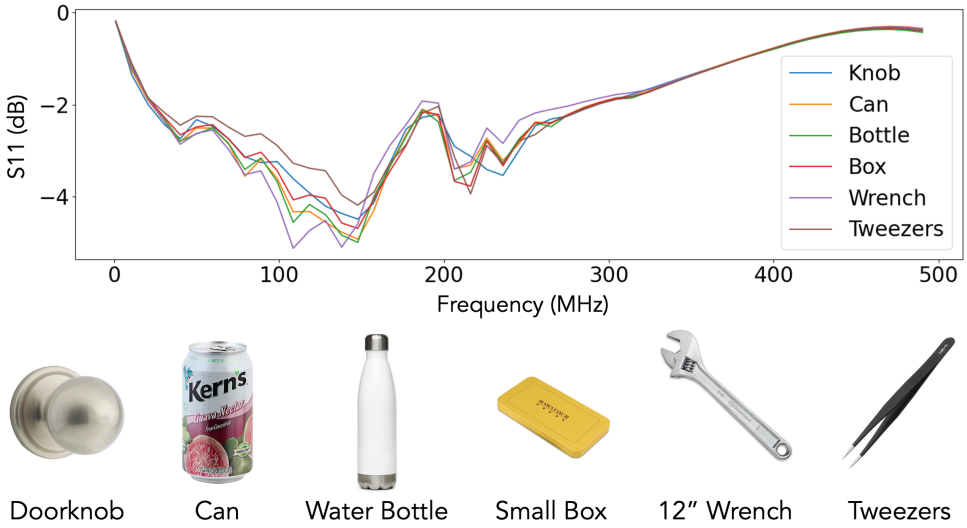

Figure 6.21: Objects utilized in the object detection study, along with their corresponding S11 curves. These curves were generated by averaging multiple measurements of data collected from a single user.

6.6.3 Object Detection

In this section, I explore the capability of Z-Ring to detect hand-held objects by leveraging its ability to measure the impedance of external surfaces the user's hand touches. Objects exhibit distinct impedance signatures due to variations in their shapes, sizes, volumes, and materials. To investigate this, I analyzed six commonly encountered objects: a doorknob, a juice can, a water bottle, a small storage box, a wrench, and tweezers. These objects span diverse categories such as size (from small tweezers to large wrenches) and composition (from hollow bottles to solid doorknobs), requiring different hand grips for manipulation. While the focus primarily lies on metallic objects due to their substantial impedance shifts, non-metallic items may also exhibit impedance changes. Figure 6.21 illustrates the unique impedance signatures of these objects. By detecting objects held in the hand, Z-Ring demonstrates potential as a contextually aware input modality.

Recognition

Object classification is performed using an SVM classifier with a polynomial kernel, utilizing a 51-length S11 measurement as the feature vector. The start and end frequencies are set to 1 MHz and 500 MHz, respectively, as most dynamic changes occur within this band.

Evaluation

In a study involving 14 participants, I evaluated the object recognition accuracy of Z-Ring. Participants were instructed to hold objects in the air using the hand wearing the ring, grasping them in a typical manner as they would during normal interaction. Each participant completed a total of 240 grabs, equivalent to 10 sessions $\times$ 6 objects $\times$ 4 repetitions per object. Each grab lasted 2 seconds, yielding approximately 60 S11 measurements. I increased the number of sessions compared to previous studies due to the diverse ways participants held the objects.

Results

The first eight user study sessions were utilized to train the classifier model, while the final two sessions were allocated for testing. A unique model was constructed for each participant. In addition to data collected during object holding, null gesture data from the gesture recognition user study was included. Null gestures encompassed participants interacting with their phones or desks or performing any action not in the gesture set. This inclusion helped assess the classifier's ability to differentiate between holding and not holding objects, as well as between holding objects from/not from the test set.

The average object recognition accuracy across all participants was 94.5%, with individual maximum and minimum accuracies of 99% (P2, P16) and 87% (P20), respectively. Tweezers and the metal box were the most frequently confused objects, followed by the bottle and can. The Null class achieved 100% accuracy for all participants. Figure 6.22 illustrates these findings.

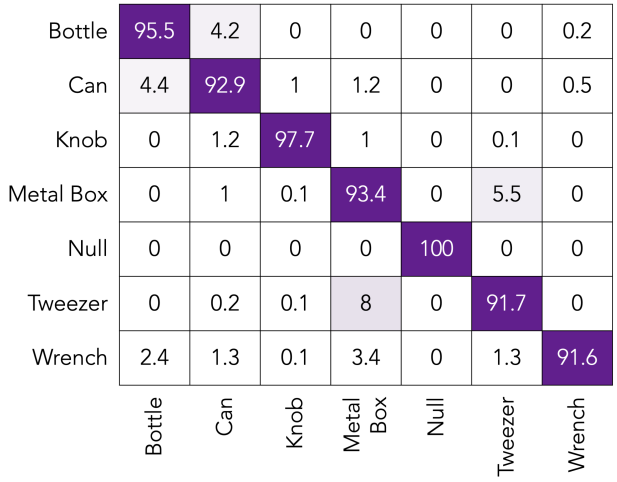

Figure 6.22: Confusion matrix illustrating object recognition performance (as percentages) across all objects and participants.

Generalizing the user-independent model across users for objects proved challenging. Similar to buttons, the impedance profile of the user's hand influences the signals transmitted to/from the object, thereby impacting its impedance response.

6.6.4 User Identification

Z-Ring offers a distinctive capability to identify and authenticate the wearer based on their unique hand impedance signatures, which are influenced by individual anatomical structures. As a wearable device, Z-Ring continuously recognizes and authenticates users, thus providing a secure input modality.

For this analysis, I repurposed data from the object detection study, as it reflects a more realistic scenario where users interact with various objects and surfaces. Given that touching external surfaces introduces additional impedance changes, I aimed to assess whether Z-Ring could still accurately identify and authenticate users amidst this added noise.

Recognition

User identification and authentication are performed using a random forest classifier (with 50 trees and a maximum depth of 30), with S11 measurements serving as input to the model. Based on simulation outcomes, I selected a frequency range of 1MHz to 400MHz. To align with this frequency range, I trimmed the data from the object detection study (originally spanning 1 MHz to 500 MHz) and repurposed it for this investigation.

Evaluation

In the evaluation, I treat all classes derived from the source data as representing the user as a single class. I conducted two analyses:

For user identification, models were trained on each user's first eight sessions and tested on the remaining two sessions.

For user authentication, a binary classifier was trained, with all test users' data comprising one class and all other users' data forming the other class. Since the data amounts were uneven between the two classes (one participant vs. the remaining participants), I uniformly resampled data from the remaining individuals to ensure comparable data volumes.

Results

In the closed-set user identification scenario, the average accuracy attained was 99%, with 12 out of 14 participants achieving perfect accuracy of 100%. The remaining two participants achieved accuracies of 89% and 97.4%, respectively.

Regarding user authentication, the average classification accuracy across participants was 98.3%, with 8 out of 14 participants achieving perfect accuracy of 100%. The remaining 5 out of 6 participants achieved accuracies exceeding 90%, while the accuracy for the last participant was 89%. I also repeated this evaluation using data from the one-handed gesture study, yielding similar results.

6.7 Prototype Refinement through Miniaturization

The VNA-based Z-Ring prototype successfully validated the concept of wide-band bio-impedance sensing. However, this implementation relied on a bulky setup, which presented inherent limitations for continuous, unconstrained data acquisition in dynamic environments. To address these constraints and enhance the practical applicability of this sensing approach, the Z-Ring++ prototype was developed. This effort represents a comprehensive refinement through miniaturization, aiming to transition the technology from a laboratory-bound proof-of-concept to a more versatile research instrument.

Z-Ring++ 6.23 constitutes a significant evolution, re-engineering the existing system into a self-contained, wearable form factor. This miniaturization involved optimizing power efficiency, signal integrity, and ergonomic design while maintaining the required fidelity for bio-impedance measurements.

(a) Z-Ring++ Ring

(b) Z-Ring++ worn on hand

Figure 6.23: Views of the Z-Ring++ prototype

6.7.1 Design Philosophy and Objectives

The primary objective of Z-Ring++ development was to realize a compact, low-power, and robust bio-impedance measurement system capable of autonomous operation. Key design objectives included:

- Miniaturization: Reduction of the physical footprint to enable integration into a finger-worn device.
- Self-Containation: Integration of all requisite components, including power management, sensing circuitry, data processing, and communication modules, within a singular device.
- Practical Applicability: Improvement of ease of use, comfort for prolonged wear, and resilience to motion artifacts in non-laboratory settings.
- Measurement Fidelity: Preservation of the accuracy and resolution of bio-impedance measurements despite physical scaling.
- Wireless Connectivity: Implementation of low-power wireless communication for data egress.

6.7.2 System Architecture and Component Integration

The Z-Ring++ system is engineered to integrate all system components within the constrained volume of a finger-worn device. As depicted in Figure 6.24, the core components are strategically arranged on a flexible printed circuit board (FPCB) to conform to the circular geometry of the ring.

The principal components include:

- Impedance Analyzer (AD5933): The Analog Devices AD5933, a high-precision impedance converter network analyzer, forms the central sensing element. While

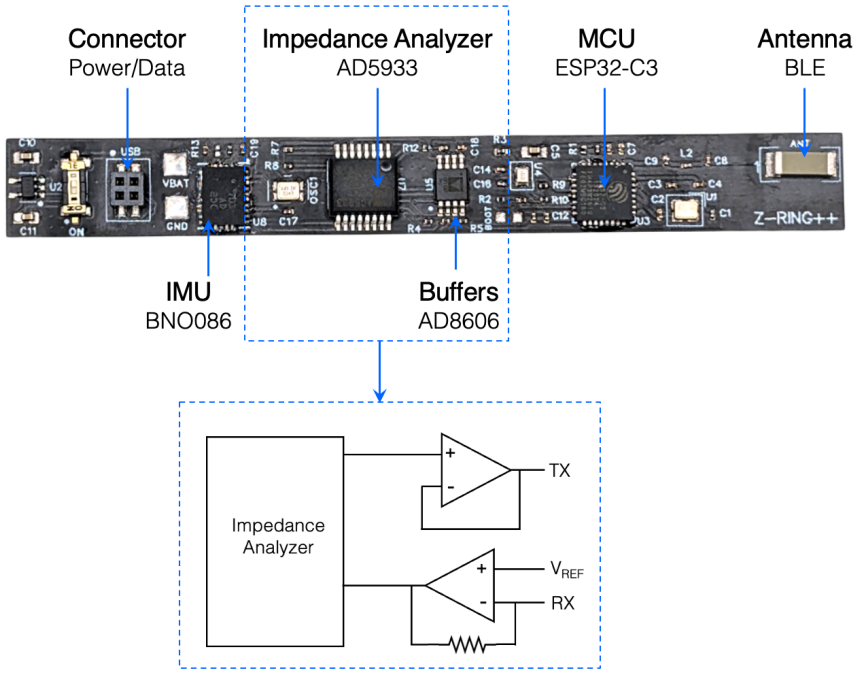

Figure 6.24: System-level overview of the Z-Ring++ showing key components including the impedance analyzer (AD5933), IMU (BNO086), buffers (AD8606), MCU (ESP32-C3), BLE antenna, and power/data connector.

its operational frequency range (1-100 kHz) differs from the MHz range of previous prototype, its integration represents a pragmatic advancement towards compact, self-contained bio-impedance sensing systems. The integrated Direct Digital Synthesizer (DDS) facilitates precise excitation frequency generation, and its 12-bit, 1 MSPS analog-to-digital converter (ADC) ensures accurate measurement of complex impedance. Buffers (AD8606) condition the excitation and receive signals, optimizing performance and protecting the analyzer.

- Microcontroller Unit (MCU - ESP32-C3): The Espressif ESP32-C3 was selected for its compact dimensions, low power consumption, and integrated Wi-Fi and Bluetooth

Low Energy (BLE) capabilities. This MCU orchestrates the AD5933, processes raw impedance data, and manages wireless communication to a host system. Its features enable on-device computation and flexible data handling.

- Inertial Measurement Unit (IMU - BNO086): A Bosch Sensortec BNO086 IMU provides tri-axial acceleration, angular velocity, and magnetic field data. This information is critical for mitigating motion artifacts inherent in wearable bio-impedance measurements, particularly during user activity, and provides complementary contextual information to the impedance data.

- Antenna (BLE): An integrated antenna facilitates robust and efficient Bluetooth low-energy communication, essential for reliable data transfer from the miniaturized form factor.

- Battery: A 20 mAh thin, curved battery providing the necessary power for autonomous operation. The device runs for about an hour with continuous usage and can run longer with duty cycling.

- Power and Data Connector: A custom-designed dongle that connects to the ring via a micro header. The dongle has a USB-C connector that enables both power delivery for battery charging and data transfer for programming and higher-bandwidth data logging, as illustrated in Figure ??.

6.7.3 Ergonomics and Electrode Design

A significant challenge in wearable device miniaturization is ensuring user comfort while maintaining reliable signal acquisition. The Z-Ring++ integrates a pair of metallic electrodes into its inner circumference (Figure 6.25c), designed to ensure consistent skin contact. The ring housing is 3D printed, allowing it to be produced in different sizes to

accommodate user finger dimensions. The flexible PCB further facilitates this adaptability to different ring sizes. The total weight of the prototype was approximately 4 grams.

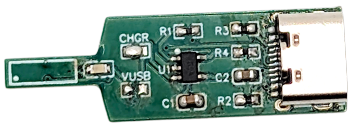

(a) Charging dongle for the Z-Ring++

(b) Charging dongle connected to the prototype

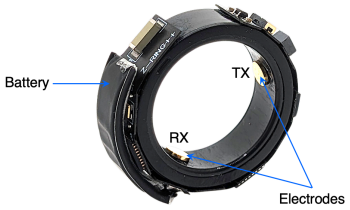

(c) Battery and electrodes in the prototype

Figure 6.25: Components of the Z-Ring++ system

6.7.4 Preliminary User Evaluation

Initial testing was conducted with three volunteer users to assess the fundamental signal response characteristics and practical usability of the Z-Ring++ prototype in a quasi-real-world context. The protocol involved users wearing the Z-Ring++ during regular daily activities, such as walking, typing, writing, and interacting with everyday objects, to simulate typical use scenarios. Additionally, specific instructed actions were performed to isolate and quantify impedance changes in response to particular stimuli.

To measure signal characteristics and quantify impedance changes, the user performed two predefined actions: making contact with a metallic surface (a doorknob) and performing a pinch gesture. Bio-impedance data were continuously recorded throughout these actions.

For this evaluation, the average signal change observed when the user made contact with a metallic surface was approximately 2 dB, indicating sensitivity to external conductive interactions. Furthermore, an averaged reproducible signal change of approximately 0.3

dB was recorded during a pinch gesture, demonstrating the prototype's capability to detect subtle physiological changes associated with finger manipulation.

To understand the users' comfort while wearing the ring, the users were asked to wear the ring for 1 hour while performing everyday activities, including walking, typing, writing, and interacting with everyday objects.

I collected qualitative feedback from the users about the comfort of wearing the device, any interference with their daily tasks, and overall user experience.

Qualitative feedback from the participants consistently indicated that wearing the prototype was comfortable and did not significantly impede their daily activities. Representative comments included:

- "I barely noticed it was there after a few minutes."
- "It felt natural, like wearing any other ring."
- "I could type and write just fine without it getting in the way."
- "It did not feel bulky or heavy at all, even when moving around."

This observation supports the design's success in achieving a practical and unobtrusive form factor for continuous physiological monitoring. These preliminary results suggest the potential of Z-Ring++ as an effective instrument for future bio-impedance research in unconstrained environments.

6.8 Discussion and Limitations

Z-Ring offers a range of functions, including gesture input, object detection, and interaction with passive user interfaces.

While the user studies focused on each application domain separately, real-world scenarios often require the simultaneous operation of multiple applications. For instance,

a user might utilize a passive button to activate a device and then employ one-handed gestures to control it. In such cases, the system must seamlessly switch between functions.

To assess the feasibility of this scenario, I trained a classifier (Random Forest, with 50 trees and a maximum depth of 30) to differentiate between various applications by amalgamating the data collected from the user studies. The confusion matrix depicted in Figure 6.26 illustrates the outcomes of this analysis, indicating the potential for high accuracy in distinguishing between different applications. In this architectural setup, a gating classifier could determine the application, while a second classifier could identify the specific interaction. Alternatively, future work could explore training a single classifier to operate across all application domains.

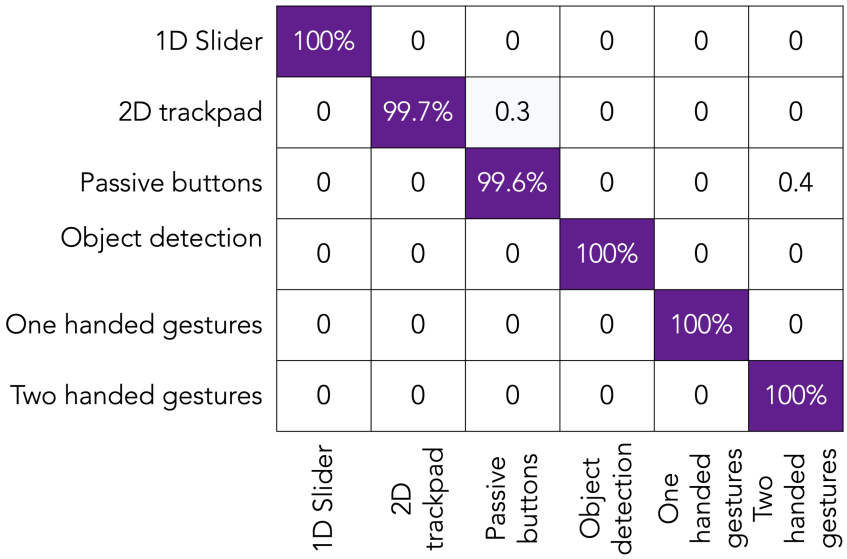

Figure 6.26: Confusion matrix illustrating the differentiation among different Z-Ring application domains.

In the exploration of tangible buttons, I concentrated on modifying the button's geometry to achieve a distinct impedance signature. Beyond altering shapes and sizes, various methods can manipulate or control impedances, some of which are commonly employed

in RF circuit design. For instance, cross-hatching, a technique frequently used, carves out large sections of copper on a PCB in a lattice pattern to regulate trace impedance. Additionally, attaching passive devices such as capacitors and inductors to button surfaces can also modify impedances. In certain chipless RFID designs, resonant structures are constructed around the main feed line to introduce peaks at specific frequencies, contributing to the generation of a unique spectral signature. This approach could potentially enhance the frequency signature of buttons. Some chipless RFID systems utilize structural features along the signal line at varying distances, generating a temporal signature as the signal bounces back; such an approach, combining temporal and impedance patterns, could be beneficial when developing user-independent models for button recognition.

I primarily investigated copper surfaces and metallic objects for passive user interfaces and object detection due to their significant impedance changes resulting from their electrical conductivity. However, non-metallic materials or dielectrically distinct objects, such as paper, cardboard, and glass, can also induce impedance changes, albeit to a lesser extent. Items with high water content, like fruits and vegetables, can produce strong impedance changes as well. Certainly, the system could detect electrically active objects similar to those explored in EM-Sense.

The current Z-Ring prototype employs a commercially available VNA device that is too large for wearable use and requires tethering to a laptop for data transmission, limiting its utility in real-world scenarios or for extended periods. Nevertheless, advancements in chip manufacturing, materials, and circuit design offer avenues toward single-chip VNAs that could substantially reduce the prototype's size. Moreover, since the processing pipeline does not necessitate the VNA's more sophisticated measurements, simpler scalar network analyzer circuit designs could be explored, or focus could be directed towards impedance measurements at only a set of discrete frequencies demonstrating the greatest discrimination in the models. I also demonstrated Z-Ring++, a miniaturized version that achieves its small size by using a different impedance AFE (Analog Front-End) instead of a VNA, showcasing another potential path to miniaturization.

Currently, most wearable devices, such as those used for fitness tracking, feature a pair of electrodes that make contact with the skin to measure stress levels through skin conductance measurements. In the future, Z-Ring can repurpose these electrode pairs to enable new interactive functionality.

Chapter 7

WRISTBAND–BASED WIDEBAND BIO-IMPEDANCE SENSING FOR TOUCH INTERACTION ON EVERYDAY UNINSTRUMENTED SURFACES

In the previous chapter, I demonstrated how increasing the frequency and bandwidth of bio-impedance sensing on a ring enables novel interaction applications. This chapter extends that concept by exploring how such a frequency and bandwidth change can be implemented within a wristband form factor, addressing the unique challenges associated with a wristband that were not present with the ring. Subsequently, I present various applications enabled by this enhanced technology.

7.1 Introduction

Modern human-computer interaction (HCI) heavily relies on touch interactions, largely thanks to contemporary touchscreens and trackpads. These interfaces offer valuable haptic feedback and closed-loop control, making surface interactions like taps and swipes quick and ergonomic [150]. However, reliably sensing these interactions often requires instrumenting the surface itself, which limits interaction to the designated touch-sensitive area [94, 58, 269].

To enable “touch anywhere” functionality for applications such as mobile or extended reality (XR) device control, researchers have explored wearable touch technologies. While promising, these solutions come with their own set of challenges. Vision-based methods, often used in augmented reality (AR) and virtual reality (VR) for hand tracking, need a direct line of sight, are prone to occlusion, and struggle with the “last centimeter problem,” making precise touch timing difficult [244, 138, 267]. Other systems require cameras to be mounted very close to the interaction point, like the fingertip, which can negatively impact

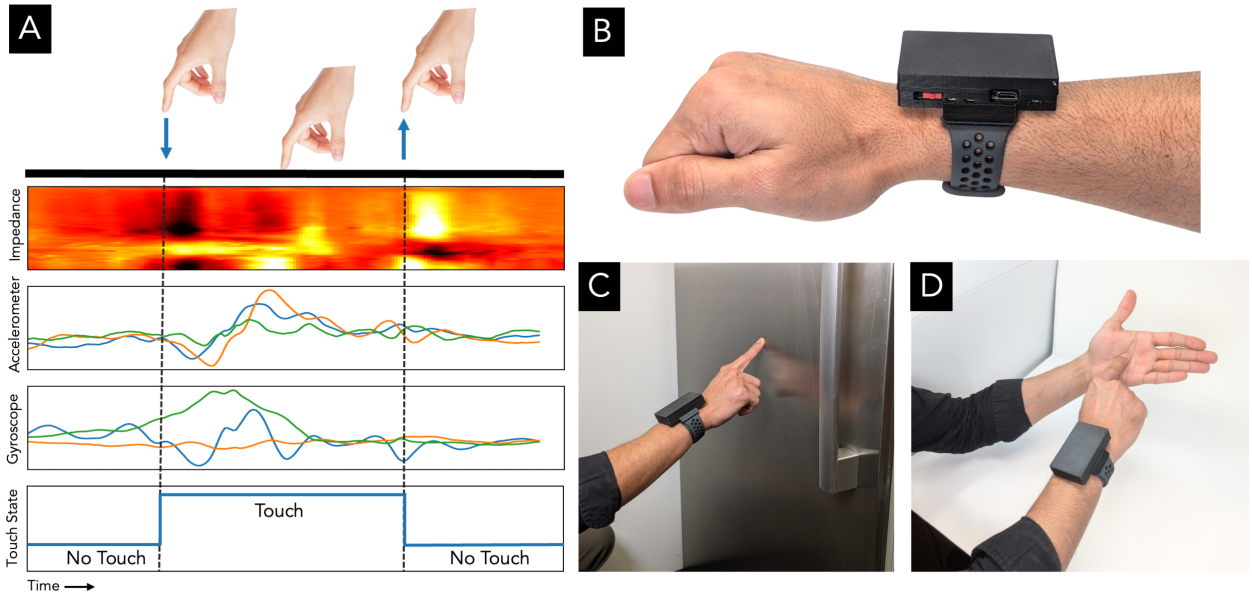

Figure 7.1: (A) Raw signal data from the Z-Band prototype, which includes both RF and IMU data, and a graph indicating the exact times when a touch started and stopped, demonstrating the Z-Band's stateful touch detection capability. (B) The Z-Band-Lite prototype device is worn by a user. Examples of surfaces on which Z-Band can be used, such as a refrigerator door (C) or the palm of the other hand (D).

ergonomics [249, 199]. Non-line-of-sight methods are typically limited to non-stateful interactions, such as quick taps [80, 161].

Accurately detecting the exact start and end of touch events is crucial for unlocking a range of stateful interactions, including dragging, dropping, and continuous input, all of which significantly enhance the user experience [86, 40]. Furthermore, while existing wearable systems have demonstrated surface interaction in stationary environments [80, 161, 123], enabling seamless interaction in mobile settings remains a significant hurdle. In mobile scenarios, sensor data from sources like inertial measurement units (IMUs) and bio-acoustic methods can become noisy due to motion artifacts, leading to reduced accuracy [109].

To address these limitations, I propose Z-Band, shown in Figure 7.1, a wrist-worn wearable device that can detect stateful touch interactions on external, un-instrumented surfaces without requiring a line of sight. Z-Band achieves this by combining electrical impedance sensing with IMU signals. This hybrid system allows for surface interaction across a broader range of materials, including soft materials like cloth or skin, where IMU-only systems struggle due to the minimal signal variations they produce [201]. The RF+IMU hybrid system enhances sensitivity, enabling accurate surface interaction detection even on soft materials. Additionally, Z-Band performs consistently in dynamic scenarios like walking and uniquely provides the ability to detect touch pressure, further expanding its capabilities.

Z-Band uses high-frequency radio signals, ranging from 1 MHz to 1000 MHz, injected at the wrist to sense touch interactions. These signals efficiently propagate along the skin's surface, reaching the fingers, and are modulated by interactions with external surfaces, allowing for the recognition of external touch events. The choice of high-frequency signals is critical because it ensures better propagation along the hand. Lower-frequency signals (kHz to low MHz) penetrate deeper into biological tissues due to their longer wavelengths [196], making them suitable for applications like electrical impedance tomography (EIT) and muscle activity monitoring, which probe internal body structures [157]. However, they also experience higher resistive losses, which can limit their propagation distance along the body's surface and restrict their suitability for sensing at the fingers [275]. In contrast, higher-frequency signals primarily interact with the skin's outer layers, minimizing deep penetration while efficiently traveling along the body's surface [63]. This effect allows the signals to travel from the wrist to the fingers, where finger interactions cause measurable variations, enabling touch detection from the wrist.

For electrical impedance sensing, Z-Band incorporates a low-cost, portable vector network analyzer [118, 225, 226] to inject radio frequency (RF) waves at the wrist. Importantly, the RF system can detect subtle touches even on challenging dielectric materials, such as plastic or wood, which typically exhibit lower signal variation compared to conductive

materials due to their limited influence on RF propagation and weaker capacitive coupling. I achieve this enhanced touch sensitivity through two key mechanisms. First, I employ a wide-band frequency sweep of high frequencies (1-1000 MHz), which are particularly responsive to hand interactions given their short wavelength [158]. Second, I designed custom front-end architectures for the VNA to boost the signal-to-noise ratio for sensing at the wrist, even when the interaction site—the fingertips—is further away. This highly sensitive signal also allows Z-Band to detect touch pressure, adding an extra layer of richness to the interactions. By combining electrical impedance sensing with inertial sensing, Z-Band further enhances the robustness of touch segmentation and captures hand motion, which facilitates interactions like swipes and taps.

In this chapter, I first delve into the theory behind impedance sensing and its functionality. Next, I present multiple simulations across various scenarios to demonstrate the feasibility of this sensing approach and to computationally optimize the sensing parameters. Following that, I introduce three front-end architecture design prototypes, discussing their results, trade-offs, and the design choices for the Z-Band. Finally, I conduct a user study to evaluate the system, demonstrating its robustness in touch detection and showcasing its effectiveness in gesture recognition.

This work makes the following contributions:

- Z-Band: A wristband system that enables stateful touch segmentation across diverse materials and in mobile scenarios, while also detecting touch pressure—all without requiring line-of-sight sensors or surface instrumentation.

- Comprehensive Examination of Wrist-Based High-Frequency Impedance Sensing: This includes electromagnetic (EM) propagation simulations, three distinct RF architecture designs, and a comparative analysis to guide optimal design choices.

- A Robust Hardware and Software Pipeline: Rigorously evaluated through user studies, this pipeline demonstrates the effectiveness of this technique for touch

segmentation across diverse scenarios and its efficacy in facilitating on-world interactions.

7.2 Related Work

This section reviews existing approaches for touch segmentation and surface interactions, followed by a focused discussion on electrical sensing mechanisms.

7.2.1 Sensing Techniques for Surface Interactions

Conventional methods for sensing surface interactions typically rely on instrumented surfaces embedded with various sensors. Researchers have deployed a broad spectrum of on-surface sensing modalities to enable interactions across different scales, from device-specific applications to expansive, room-sized installations. For instance, acoustic [92, 105], capacitive [190], and vibration [60] sensing are employed for smaller interaction areas, such as furniture or device surfaces, by utilizing mounted contact microphones, capacitive arrays, or piezo vibration sensors. Vision-based systems, incorporating overhead depth [244] or thermal cameras [138], have also been explored for surface interaction detection. Projects like Wall++ [271] and GravitySpace [36] extend the sensing area to large-scale surfaces, including walls and floors, for whole-room input detection using capacitive and optical sensors, respectively. However, these systems remain confined to predetermined, instrumented zones, which restricts their ability to switch seamlessly between different surfaces.

Wearable sensing techniques have emerged to overcome the limitations of static, instrumented surfaces. Acoustic methods, including Skinput [94], ViBand [134], Acustico [80], and SoundScroll [123], utilize body-mounted sensors to detect touch events through vibrations and sound waves. Nevertheless, these systems often face challenges in precisely segmenting touch states (e.g., touch down and touch up), particularly in scenarios where interaction lacks dynamic motion, as their detection mechanism is primarily

motion-dependent.

Inertial-based systems, such as TapID [161], employ wrist-mounted IMUs to detect taps on uninstrumented surfaces but are unable to determine distinct touch states, thereby limiting complex interactions like drag-and-drop. The performance of such systems in dynamic scenarios involving body motion (where motion introduces noise into IMU data) [109] or on diverse surfaces remains largely uninvestigated, as existing evaluations have been confined to seated contexts and single, hard surfaces. Shi et al. [199] propose using nail-mounted IMUs for touch gesture detection, offering stateful interaction capabilities but requiring direct attachment to the user's fingers.

Optical systems, as demonstrated by Niikura et al. [171], enable interaction on arbitrary surfaces but are highly susceptible to environmental conditions and require a clear line-of-sight, which diminishes their reliability in practical, everyday situations.

Acknowledging the shortcomings of these approaches, this work investigates electrical methods that facilitate accurate touch segmentation without line-of-sight constraints and effectively handle static tap interactions.

7.2.2 Electrical Sensing for HCI

Touchscreens have long served as the benchmark for precise touch segmentation, employing mutual or self-capacitance techniques to accurately detect touch gestures. By distributing multiple electrodes across the surface, continuous tracking of finger movements is achieved [58]. Electrick [269] and Touché [190] measure contact and grasp styles on conductive objects, but these systems are inherently restricted to predefined surfaces.

Recent advancements in wearable electrical sensing have expanded the possibilities for surface interactions beyond fixed locations. Electromyography (EMG) systems, exemplified by Saponas et al. [189], Meta CTRL-labs [55], and others [152, 232], utilize arrays of electrodes (ranging from eight to 64) placed around the forearm or wrist to

measure muscle activity and infer hand gestures. However, while EMG excels at gesture recognition, it is less suitable for detecting direct touch contact with surfaces, making impedance sensing a more appropriate alternative for this application.

Electrical impedance tomography (EIT) provides a method for sensing across the body using multiple electrodes (≥ 8) to map conductivity changes within the hand and forearm. Systems like Tomo [265, 270] and the EIT-Kit series [277, 131] demonstrate EIT's utility for pose recognition; however, these setups often entail complex instrumentation that may not be practical for ubiquitous use. Over-air impedance systems, such as Etherpose [118] and Pantoenna [119], explore non-contact impedance characteristic sensing methods for pose estimation. Although these systems avoid the physical constraints of EIT, they necessitate large antennae to operate effectively at the frequencies required for over-air impedance sensing.

More directly related to this work are systems that leverage the human body as a waveguide for electrical signals, enabling robust touch segmentation as contact modulates the transmission properties. Studies such as BodyRC [237] and ActiTouch [267] utilize electrodes at various body points to detect touch events, exploiting the body's intrinsic electrical characteristics. ElectroRing [116] further refines this concept by employing a single point of instrumentation on the finger for pinch segmentation. However, these systems are frequently limited to specific surfaces or gestures, underscoring the need for broader material compatibility.

The Z-Ring [225, 273] is most similar to the proposed sensing method, employing wide-band RF sensing to detect hand interactions, including touch on external surfaces; however, its demonstration has been restricted to conductive surfaces. Adapting this ring-based sensing approach to a wrist-based form factor presents two primary challenges. First, the signal-to-noise ratio (SNR) significantly diminishes as the sensing site (wrist) moves further from the interaction site (fingers). For instance, measurements using a commercial VNA show that a signal electrode at the base of the index finger yields a 0.23 dB signal change when touching a grounded metallic surface, while touching the same

surface with the same electrode at the wrist results in a signal change of only 0.04 dB. For surfaces like wood, this signal change is 0.06 dB for an electrode at the finger base and 0.02 dB for the wrist.

This reduction in signal change occurs because, when sensing from the wrist, the signal experiences greater attenuation due to the longer transmission path through the body between the wrist and fingers. This disparity highlights a key challenge for Z-Band: achieving effective operation from the wrist across diverse surfaces requires novel methods for boosting SNR. To address this, I developed a custom RF front-end capable of higher transmission power, thereby maintaining sensing performance despite the increased distance. Furthermore, I integrate additional information from an inertial measurement unit (IMU) to further compensate for the reduced SNR.

Z-Band distinguishes itself from previous RF systems in two ways. First, it incorporates a custom analog front-end, computationally optimized electrode design, and integration with inertial sensing. This design achieves higher sensitivity and enables a convenient wrist-based setup with only two electrodes, making it compatible with the current smartwatch form factor. Second, Z-Band achieves accurate and stateful touch segmentation not only on conductive surfaces but also on low-permittivity materials, such as wood, plastic, glass, and skin. To provide richer context to touch interactions, this system can sense touch pressure and utilize IMU data to capture motion during touch, enabling the creation of complex interactions, such as swipes, built upon the fundamental touch segmentation.

7.3 Theory of Operation

7.3.1 General Sensing Principle

Electrical impedance sensing offers a robust method for capturing subtle physiological changes within the human body, whether induced by movement or environmental interactions. This section elucidates the fundamental operational principles of electrical impedance sensing, specifically within the context of human-computer interaction (HCI).

Electrical impedance sensing operates by transmitting an alternating current (AC) signal through the body and quantifying its modulation by biological structures. The degree to which the body opposes this current flow is termed impedance (Z), which comprises two primary components: resistance (R) and reactance (X). Resistance (R) represents the real part of the impedance and quantifies the energy dissipated as heat as current traverses tissues. Reactance (X) constitutes the imaginary part and arises from the storage and subsequent release of energy due to the capacitive and inductive properties inherent within the tissue. In biological systems, capacitive reactance predominates, largely attributable to cell membranes acting as minute capacitors that momentarily store electrical charge before its propagation. These properties collectively dictate how electrical signals interact with the body, and their relationship is expressed as:

$$Z = R + jX \tag{7.1}$$

where j is the imaginary unit ($j = \sqrt{-1}$), utilized to distinguish between energy dissipation (resistance) and energy storage (reactance). Electrical signals interact distinctly with biological tissues at varying frequencies due to differences in reactance and electrode-skin impedance.

The capacitive reactance (X_C) of biological tissues, primarily influenced by cell membranes, is defined by:

$$X_C = \frac{1}{2\pi f C} \tag{7.2}$$

where f denotes the frequency of the applied signal, and C represents the capacitance of the biological structure. At low frequencies, X_C is high, meaning cell membranes act as significant barriers to signal propagation, compelling the current to follow the path of least resistance—typically deeper into the body where intracellular fluids offer a more conductive pathway.

Furthermore, the extent to which a signal remains on the surface versus penetrating deeper is governed by the impedance mismatch at the electrode (metal) and skin interface. The reflection coefficient (R), which quantifies the amount of signal reflected at the electrode-skin boundary, is given by:

$$R = \left| \frac{Z_2 - Z_1}{Z_2 + Z_1} \right|^2 \tag{7.3}$$

where Z_1 is the impedance of the electrode (a conductive metal) and Z_2 is the impedance of the skin. At high frequencies, Z_2 (skin impedance) decreases due to lower capacitive reactance, while Z_1 (electrode impedance) remains relatively constant. This increases the impedance mismatch, leading to greater signal reflection at the electrode-skin interface and confining the signals to the skin. Furthermore, at these high frequencies, the electromagnetic phenomenon known as the skin effect [240] becomes prominent. The rapidly changing magnetic fields associated with high-frequency currents induce eddy currents that oppose the main current flow in the interior of the conductive tissue, effectively forcing the current to flow predominantly along the surface. In contrast, at low frequencies, Z_2 is higher due to increased capacitive reactance. Additionally, the skin effect is negligible at low frequencies, allowing the current to distribute more uniformly throughout the tissue. This reduces the impedance mismatch and facilitates greater signal penetration into the body.

Consequently, high-frequency signals propagate along the skin, rendering them ideal for applications such as RF-based touch detection. Conversely, low-frequency signals penetrate deeper into tissues, making them more suitable for applications like deep tissue monitoring.

7.3.2 Impedance Measurement Setup

In this system, I galvanically inject a sweep of RF signals into the body (at the wrist), enabling it to function as an electrical waveguide [279, 83]. These signals then propagate

through the hand and interact with any contacted materials.

Figure 7.2a illustrates the equivalent circuit model for impedance measurement, depicting the signal source, electrode impedance, hand impedance, and surface impedance. The total impedance of the system, as perceived by the signal source, can be expressed as:

$$Z_{\text{total}} = 50\,\Omega + Z_{\text{electrode}} + Z_{\text{hand}} + Z_{\text{surface}} \tag{7.4}$$

At impedance transitions, such as at the hand-material interface, a portion of the signal is reflected, while the remainder is either dissipated within the hand or transmitted into the material. This behavior is influenced by the material's permittivity, which quantifies its ability to store and transmit electric fields. Materials with higher permittivity, such as water or conductive surfaces, facilitate greater signal transmission and absorption, whereas materials with lower permittivity, like plastic or wood, induce greater reflection and reduced signal penetration. The interaction between the injected signal and the contacted material modulates the overall impedance profile Z_{total}, allowing touch contact to be inferred from changes in the reflected and transmitted signals.

To capture these variations, I measure the reflected signal either at a secondary electrode (Figure 7.2b) or at the injection site (Figure 7.2c). By analyzing these signals, we can characterize the hand's function as a waveguide and quantify the impedance change introduced by different materials. The capability to detect alterations in wave propagation due to material contact enables robust touch sensing without requiring direct instrumentation of the surface.

However, wave behavior is influenced not only by material contact but also by several other factors, including signal frequency and electrode geometry [37]. These factors can introduce variability in impedance measurements, necessitating a comprehensive understanding of their effects. To address this, I conduct extensive simulations to analyze how these parameters impact signal changes in Section 7.4. By identifying distinct impedance variations associated with material interactions while mitigating confounding

effects, I aim to optimize sensing robustness and enhance the reliability of Z-Band's touch detection system.

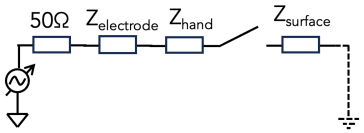

(a) The equivalent circuit model represents the total impedance pathway, including the signal source, electrode, hand, and contacted surface.

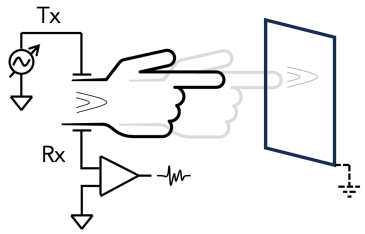

(b) S_{21}: The transmission measurement setup uses separate transmit (Tx) and receive (Rx) paths to capture signal propagation through the hand to the contacted surface.

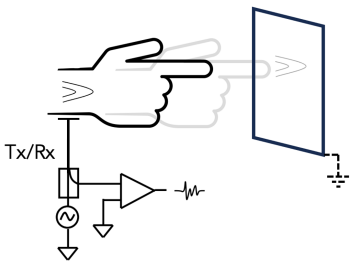

(c) S_{11}: The reflection measurement setup uses the same path for Tx and Rx to analyze impedance transitions at the injection site and the hand-material interface.

Figure 7.2: Illustrations of the equivalent circuit model, S_{21} transmission measurement, and S_{11} reflection measurement. S_{21} uses separate Tx/Rx paths, while S_{11} shares the same path for both.

7.3.3 Impedance Measurement Techniques

This paper explores impedance sensing with wideband frequency sweeps, a technique that offers rich insights into hand characteristics and enables diverse interactions, as demonstrated in [225]. Traditional bioimpedance measurement options include single- or multi-frequency impedance analysis, typically operating within the frequency range of 5 kHz to 1 MHz [204]. For applications requiring higher frequency measurements, several hardware options exist, each presenting its own set of challenges. High-end

bioimpedance analyzers, such as [215], provide extended bandwidth capabilities for measurements at higher frequencies but come at a significant cost. Custom-built systems offer affordability but necessitate specialized expertise. Software-defined radios (SDRs), while versatile, many commercially available or more accessible SDRs are limited by their narrow instantaneous bandwidth, requiring multiple sweeps for wideband measurements [70].

Vector network analyzers (VNAs) emerge as a compelling alternative, offering precise, wideband measurements across a broad spectrum in a single sweep, making them ideal for characterizing complex impedance variations [157]. Recent advancements, notably the advent of hobbyist-grade, low-cost VNAs like the NanoVNA [52], have further democratized access to this powerful tool, opening new avenues for impedance sensing research and applications [225, 118, 119].

Two standard methods can measure impedance with a vector network analyzer (VNA) for a device under test (DUT), which in this case is the hand: an S_{11} or an S_{21} measurement.

The S_{11} method (Figure 7.2c) measures the reflection coefficient, which quantifies how much of the injected signal is reflected back when a signal is applied to the DUT. In this configuration, a single electrode can be placed on the wrist, serving as both the transmitter (TX) and receiver (RX). The impedance (Z) can be determined from the measured reflection coefficient S_{11} using:

$$Z = Z_0 \frac{1 + S_{11}}{1 - S_{11}} \tag{7.5}$$

where Z_0 is the characteristic impedance of the system, typically $50\,\Omega$. A higher S_{11} value indicates stronger signal reflection, corresponding to higher impedance.

The S_{21} method (Figure 7.2b) measures the transmission coefficient, which quantifies how much of the signal passes through the DUT. In this setup, one electrode can be positioned at the top of the ulna (a common watch-wearing position), acting as TX/RX, while another is placed at the bottom of the hand, acting as RX/TX. The impedance can be estimated using the measured S_{21} parameter:

$$Z = Z_0 \frac{2(1 - S_{21})}{S_{21}} \tag{7.6}$$

A lower S_{21} value indicates greater attenuation through the DUT, corresponding to higher impedance. By analyzing both S_{11} and S_{21}, we can extract a comprehensive impedance profile of the hand, enabling precise touch and interaction sensing.

7.3.4 Impedance Sensing Challenges for Robust On-World Touch Detection

For Z-Band to successfully and robustly detect on-world touches from the wrist, three critical requirements must be satisfied.

First, there must be a non-line-of-sight (NLoS) signal transmission through the hand and fingers that is modulated by the contacted surfaces. Since the Z-Band operates from the wrist, the RF signals must effectively propagate through the hand and interact with external materials. This ensures that the resulting impedance changes can still be detected even when the fingers make contact with a surface not directly visible to the sensing system.

Second, the return signal change must be large and sufficiently unique to yield a distinguishable difference between various touch conditions. A small, ambiguous change in impedance would make it difficult to differentiate between distinct contact events and surface types.

Third, Z-Band must exhibit high sensitivity to detect touches even when the contacted material is ungrounded (i.e., not connected to a reference ground) or is strongly dielectric (i.e., possesses very low electrical conductivity). Detecting touch interactions in such cases is particularly challenging for impedance-based sensing systems. Typically, impedance sensing relies on measurable changes in electrical properties upon contact. However, ungrounded materials or highly dielectric surfaces do not readily alter the electrical impedance, making their detection more difficult.

To overcome these challenges, Z-Band leverages:

- High-frequency signal propagation: Ensuring that signals travel effectively through the hand and fingers to interact with external materials, even in non-line-of-sight conditions.

- Broadband impedance sensing: Capturing subtle variations in impedance across a range of frequencies to enhance detection robustness.

- Higher transmit signal strength: To ensure reliable sensing, I designed a custom RF front-end for the vector network analyzer (VNA), allowing for increased transmission power and improved signal-to-noise ratio (SNR). This enhancement compensates for signal attenuation through biological tissues and enables clearer detection of impedance changes across different materials.

By fulfilling these criteria, Z-Band ensures reliable on-world touch sensing under diverse real-world conditions, including on materials that are traditionally difficult for impedance-based detection systems.

7.4 Background Experiments

Following a theoretical analysis, I conducted simulations to evaluate the influence of key parameters on electrical impedance sensing. Specifically, the investigation focused on the impact of transmit frequency, electrode geometry, and contact with various materials.

7.4.1 Key Parameters Influencing Impedance Sensing

Frequency

Frequency plays a critical role in impedance-based sensing, directly affecting signal penetration depth and sensitivity to surface interactions. The intricate layered structure of the human hand, comprising tissues with distinct electrical properties (e.g., skin, fat, muscle, blood), creates a complex electrical environment. Biological tissues exhibit a

frequency-dependent impedance response due to the unique electrical characteristics of their cells, membranes, and fluids [37, 158]. Different frequency bands offer specific advantages and disadvantages for touch sensing. Table 7.1 summarizes the effects of various frequency bands on impedance sensing.

Table 7.1: Frequency bands and their impact on impedance-based touch sensing [37, 158]. Higher frequencies provide greater surface sensitivity, while lower frequencies are less sensitive to surface changes.

Frequency Band	Primary Target	Surface Sensitivity
kHz (typically $<$ 100 kHz)	Extracellular Fluid (Fluid outside cells)	Low
Hundreds of kHz - Several MHz	Cell Membranes (Cell boundaries)	Moderate to High
Tens of MHz and above	Intracellular Fluid (Fluid inside cells)	High

Frequency Band: Indicates the range of frequencies used for impedance sensing.

Primary Target: Describes the main biological component that the signal interacts with at that frequency band.

Surface Sensitivity: Indicates how responsive the impedance measurement is to surface changes, such as touch interactions. Higher values mean greater sensitivity to small variations at the skin surface.

This intricate interplay among frequency, tissue characteristics, and measurement objectives necessitates a meticulous selection of operating parameters to optimize both the depth and sensitivity of impedance measurements for the specific application.

Electrode Geometry

Electrode geometry is a critical factor in impedance-based touch sensing, influencing signal injection, detection, and overall measurement accuracy. The size of electrodes directly impacts the electric field distribution and, consequently, the sensitivity to impedance changes. Larger electrodes, by distributing the current over a broader surface area, in-

herently achieve lower contact impedance with the skin. This superior contact facilitates stronger signal transmission and minimizes signal loss at the interface. However, because the electric field generated by larger electrodes is more diffuse and averages the electrical properties over a greater volume of tissue, they tend to exhibit reduced sensitivity to subtle, localized impedance changes. Conversely, smaller electrodes, despite presenting a higher contact impedance due to their reduced surface area, concentrate the electric field within a much smaller volume. This localized electric field makes them significantly more sensitive to fine-grained or spatially restricted impedance variations, making them suitable for applications requiring higher spatial resolution.

The electrode shape affects the electric field distribution and current density at the electrode-skin interface; sharp corners can concentrate the field and potentially compromise accuracy, whereas smoother contours promote a more uniform current distribution. In the simulations, I opted for round electrodes due to their ability to generate a uniform electric field when injected at the center, ensuring consistent signal distribution across the measurement area [157].

The influence of electrode geometry is also frequency-dependent. At lower frequencies, the electric field is less focused, rendering electrode geometry less critical. However, at higher frequencies, the field becomes more concentrated, amplifying the impact of electrode geometry and potentially leading to edge effects and non-uniformities that can affect measurement accuracy. This necessitates careful consideration of electrode size in relation to the operating frequencies. While material also plays a role, the simulations and prototyping primarily focused on electrodes made up of gold, which is a common material for electrodes due to its excellent conductivity, stability, and bio-compatibility.

External Contact

External contact significantly alters the hand's overall impedance. When the hand touches a surface, the propagating signal through the hand encounters a new interface with distinct

conductivity and permittivity, thereby influencing the measured impedance. Contact with a conductive material provides a low-resistance pathway, leading to a decrease in impedance as the current is shunted through the conductive surface. Conversely, contact with an insulator impedes current flow, potentially increasing impedance as the current seeks alternative paths within the hand. Analyzing these impedance changes during external contact yields valuable information about the contact state and the electrical properties of the contacted material.

7.4.2 Simulation

I utilized finite integration technique (FIT) simulations with CST Studio Suite, which provides 3D electromagnetic (EM) analysis capabilities. I selected a frequency range from 1 MHz to 1 GHz, guided by research demonstrating substantial attenuation of wave propagation through the body beyond 1 GHz [158, 225]. I then constructed a detailed bio-model of a 38-year-old male (180 cm, 103 kg) using the CST Bio Models Library[1] and data from the US National Library of Medicine's Visible Human Project.[2] The model incorporated 31 distinct tissue types, including blood, bone, fat, muscle, and skin, with a resolution of $1 \times 1 \times 1$ mm. To optimize computational efficiency, the simulation focused solely on the right forearm and hand, isolating them from the rest of the body.

Signal Propagation Analysis

Understanding how RF signals propagate through the hand is crucial for determining the optimal frequency range for Z-Band. The human hand is a complex, lossy medium composed of multiple layers, including skin, fat, muscle, and bone, each exhibiting distinct electrical properties. These layers differ in conductivity, permittivity, and water content, all of which vary with frequency, influencing signal attenuation and propagation efficiency.

[1] https://space.mit.edu

[2] https://www.nlm.nih.gov

For Z-Band to function reliably, I needed to identify a frequency range that enables efficient signal transmission from the wrist to the fingers. Since signal strength diminishes as it propagates through the body, selecting an appropriate frequency ensures that sufficient signal reaches the interaction site, enabling robust sensing.

Experimental Setup To investigate frequency-dependent propagation, I conducted an experiment in which an RF signal was injected at the wrist and measured at the tip of the middle finger. The middle finger was chosen as the test point because it represents the longest path from the wrist, providing insight into signal attenuation over the maximum propagation distance. The experimental setup is illustrated in Figure 7.3. I performed a broadband frequency sweep from 1 kHz to 1000 MHz to evaluate signal transmission across a wide frequency range.

Results and Observations The simulated S-parameter results in Figure 7.3 reveal that lower frequency bands exhibit better propagation performance across the biological model of an open hand. Specifically, both S12 and S21 show relatively higher transmission (around -40 dB) in the frequency range 1-300 MHz, indicating lower signal attenuation and more efficient propagation through the hand tissue in this band. As the frequency increases, particularly past 600 MHz, both parameters experience a sharp decline in magnitude, dropping to around -70 dB, which reflects significantly higher attenuation and reduced transmission efficiency. These results suggest that the sub-600 MHz frequency band is more suitable for communication or sensing applications involving on-body or through-body signal propagation, as it enables better signal penetration and lower loss compared to higher frequency bands. These findings provide a guideline for selecting frequency bands for Z-Band, which can provide a superior balance between propagation efficiency and sensitivity to surface interactions.

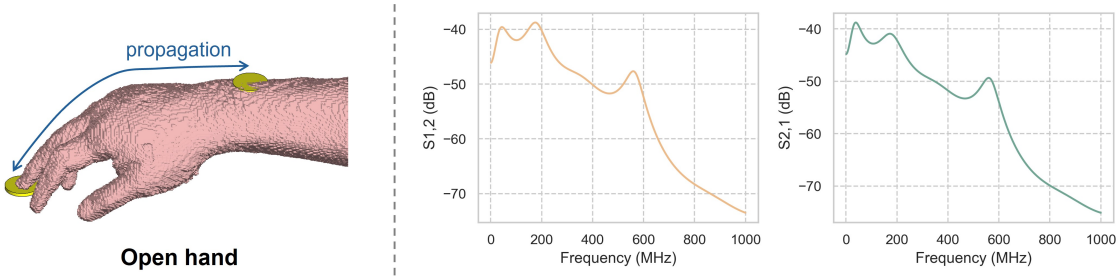

Figure 7.3: (Left) Propagation simulation setup of the biological model with open hand pose in CST Studio Suite. (Right) Simulated S12 and S21 results.

Electrode Size and Its Impact on Impedance Sensing To understand how electrode size influences impedance sensing, I tested round electrodes of varying radii (1.25 mm, 2.5 mm, 5 mm, 10 mm, and 15 mm) while sweeping through a broad frequency range from 1 kHz to 1000 MHz. In this experiment, a single electrode was placed on top of the wrist for S11 measurements, while an additional electrode was positioned at the bottom of the wrist to capture S21 signals.

The simulation results, shown in Figure 7.4, indicate that larger electrodes (15 mm radius) provide superior S11 and S21 signal quality. This improvement is attributed to their lower contact impedance, which enhances signal transmission efficiency [158, 126]. However, while smaller electrodes exhibit reduced performance, they still maintain reasonably good signal quality, particularly at higher frequencies. This suggests that while larger electrodes optimize signal strength, smaller electrodes can still provide acceptable signal quality, striking a balance between performance and practical design constraints.

Impact of Touching External Surfaces on Impedance Sensing To assess how different external surfaces influence impedance sensing, I examined interactions with commonly encountered materials: metal (copper), plastic (epoxy resin), and wood. In the CST simulations, these surfaces were modeled uniformly with dimensions of $100 \times 100 \times 3$ mm, varying only in material-specific properties such as conductivity and loss tangent. The

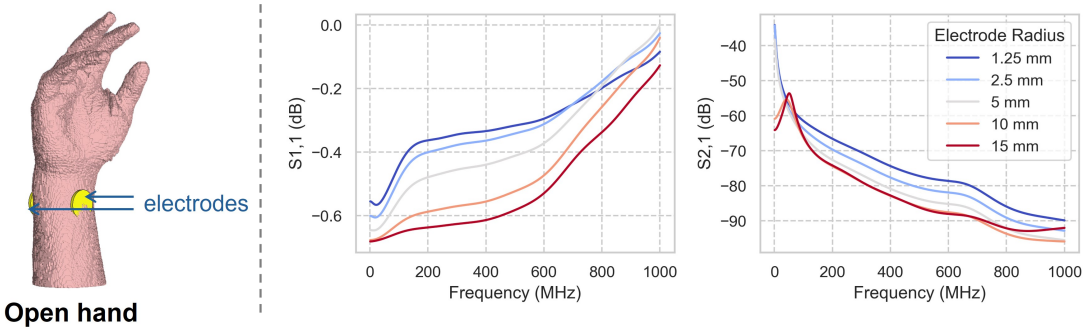

Figure 7.4: (Left) CST simulation setup with open hand pose and electrode positions. Simulated S11 and S21 results with different electrode radii, showing that the 15 mm radius provided the best S11 (center) and S21 (right) signal quality.

simulation setup, depicted in Figure 7.5, was designed to analyze how these materials affect S11 and S21 signal responses when touched, with the sensing electrodes positioned at the wrist.

Simulation results revealed distinct variations in S11 and S21 signals depending on the material of the contacted surface. While these variations may appear subtle, previous research [225, 273] has demonstrated that even small deviations—on the order of ~ 0.1 dB in S11—can be effectively utilized for surface classification. By employing a broad frequency sweep rather than single-point measurements, this approach captures a comprehensive impedance profile, enabling machine learning models to leverage variations across the frequency spectrum.

In summary, the simulations validated the feasibility of wrist-based impedance sensing for accurately detecting touch interactions.

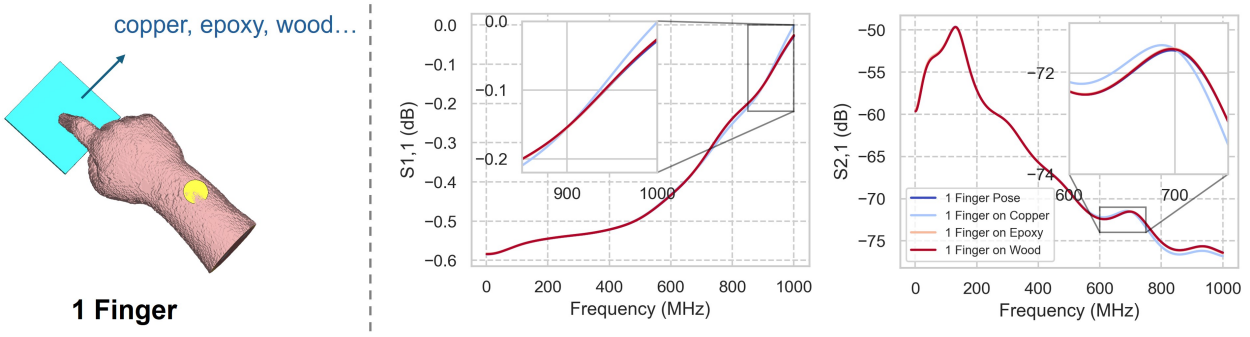

Figure 7.5: (Left top/bottom) CST Simulation setup of the models with open hand, one- and two-finger poses, as well as touching the external surface with different materials. Simulated S11 (middle top/bottom) and S21 (right top/bottom) results, showing that wrist-based impedance sensing can detect signal differences for varied configurations.

7.5 Impedance Sensing Front-End Architectures for VNA

7.5.1 Challenges and Solutions for Wrist-Based Impedance Sensing with VNAs

Vector Network Analyzers (VNAs) have been successfully employed for impedance-based interaction detection, including applications involving signal injection into the human body or air coupling [225, 118, 121]. However, a significant challenge emerges when attempting to inject the signal at the wrist to detect interactions occurring at the fingers.

Research Question: Can a portable VNA accurately measure impedance for hand interactions when signal injection occurs at the wrist, considering the constraints of signal attenuation and inherently low transmission power?

The human body acts as a lossy transmission medium, causing considerable attenuation of signals as they traverse through tissues. This attenuation, coupled with the intrinsically low transmission power of portable VNAs such as the NanoVNA, renders direct signal injection impractical without external amplification. Nevertheless, amplification introduces another challenge: simply adding an amplifier at the VNA's S11 (TX) port is

infeasible because amplifiers inherently isolate reverse signals, allowing the amplified forward signal to pass but blocking the reflected signal necessary for accurate S11 measurement. Conversely, the S21 measurement, which utilizes a dedicated RX port, permits amplification. However, even in S21 measurements, amplification can introduce signal distortion and thus requires careful design to ensure accurate impedance calculations.

Proposed Solution: External Analog Front Ends (AFEs) To address these challenges, I introduce external analog front ends (AFEs) specifically designed to interface with the VNA. I developed three distinct prototype designs to manage signal amplification for hand interaction detection. Two of these designs explore amplified S11 measurements, while the third focuses on amplified S21 measurements. Although these architectures theoretically measure the same impedance changes, their practical implementations introduce variations due to differences in component characteristics, signal attenuation, noise from extended signal paths, and variations in coupling with the body.

Experimental Evaluation of Designs To evaluate these designs, I implemented each architecture and conducted controlled experiments under comparable conditions. The impedance response was analyzed across different surfaces, mirroring the experimental setup described in Section 7.4. This comparative study provided valuable insights into the practical trade-offs of each design and guided the selection of the optimal architecture for Z-Band.

Implementation Details For all implementations, I utilized the LiteVNA [66], an enhanced version of the NanoVNA offering improved performance. While its default sweep rate is approximately 5 Hz, I leveraged an experimental firmware feature to increase the sampling rate to 30 Hz.[3] For signal amplification, I selected the Mini-Circuits LHA-13LN+ amplifier,

[3]The sweep time of LiteVNA can be decreased by writing the value 0x01 to registers at addresses 0xE0 and 0xE1.

which provides a 22 dB gain, a 1-1000 MHz bandwidth, and a low noise figure of 1.1 dB, ensuring minimal signal degradation. The electrodes employed in the setup were round, flexible, gold-coated copper electrodes with a 15 mm radius. The choice of gold coating ensures high conductivity, oxidation resistance, and biocompatibility, while the flexible design enhances comfort and adaptability to wrist contours. For S11 measurements, a single electrode was positioned on the top of the wrist, near the ulna area. For S21 measurements, two identical electrodes were placed—one on the top of the wrist (near the ulna, connected to the S11 port) and another on the bottom of the wrist (connected to the S21 port). All prototypes were battery-powered, with a Raspberry Pi handling VNA data collection and Wi-Fi streaming, enabling a fully wireless system.

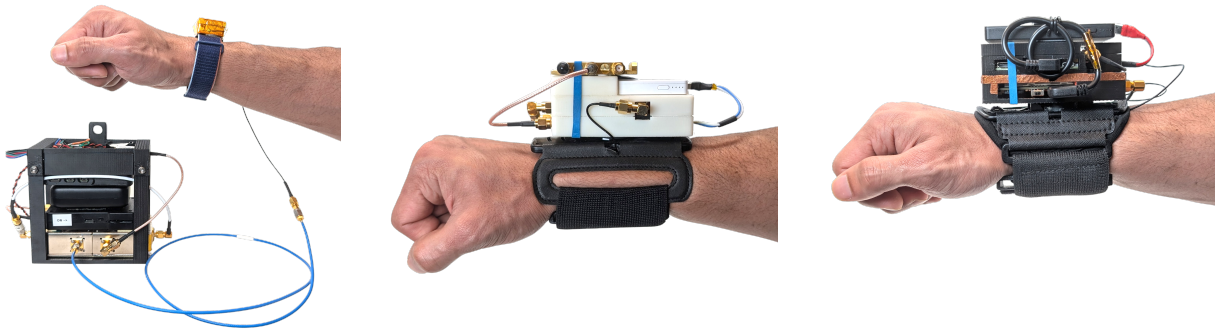

(a) Design 1: Circulator Prototype

(b) Design 2: Coupler Prototype

(c) Design 3: Through Transmission Prototype

Figure 7.6: Prototypes of different impedance sensing designs.

7.5.2 Design 1: Dual-Circulator Reflectometry

In the first design, I leverage circulators to perform S11 measurements. Figure 7.6a shows the physical prototype for this design. The RF architecture, depicted in Figure 7.7a, employs two circulators to achieve signal amplification, reflected signal measurement, and

isolation between stages. RF circulators are passive, non-reciprocal three-port devices that direct signal flow within a circuit: a signal entering port 1 exits port 2, a signal entering port 2 exits port 3, and a signal entering port 3 exits port 1.

The outgoing RF signal from the VNA enters port 1 of circulator 1, which routes it to port 2, connected to a power amplifier (PA). The amplified signal then passes through circulator 2 from port 1 to port 2 and is coupled to the body via body electrodes. The reflected RF signal from the body enters port 2 of circulator 2, which directs it to port 3. This signal then passes through an RF attenuator to reduce its power before entering port 3 of circulator 1, thereby safeguarding the VNA from damage. Circulator 1 then directs the attenuated reflected signal to port 1, which is connected to the VNA for measurement and analysis.

In this architecture, circulator 2 isolates the PA from the reflected signal by directing any energy entering port 2 to port 3, preventing potential damage. Similarly, circulator 1 isolates the VNA from the PA, protecting it from the high-power amplified signal. Both circulators collectively isolate the VNA from both the high-power PA and the reflected signal, preventing interference and potential damage. This architecture enables higher transmit power, bidirectional signal flow, measurement of the reflected signal, and isolation of each stage, leading to accurate and reliable measurements.

While wideband sweeps were desired, practical limitations of sub-GHz circulators, which typically exhibit bandwidths less than 100 MHz, necessitated a narrower sub-GHz bandwidth for my implementation. The frequency selection is guided by simulations, component constraints, and empirical testing. CST simulations revealed peak sensitivity to hand pose changes in the 1-500 MHz range, with other frequencies also showing signal variations. By balancing the need for high sensitivity and efficient propagation (favored at higher frequencies) with deeper biotissue penetration (characteristic of lower frequencies) [158], while also considering the practical limitations of available circulator bandwidths, I ultimately selected the 100-150 MHz range as the operational bandwidth. I therefore chose the TH6060ES circulator, manufactured by RFTYT Technology, for the implementation.

Figure 7.7b shows the S11 curves for different scenarios using this prototype.

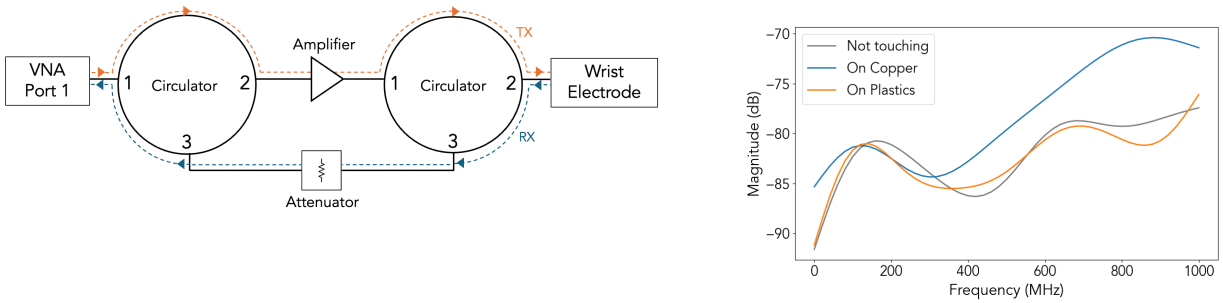

(a) (b)

Figure 7.7: The Dual-Circulator Reflectometry design (prototype 1) along with the results (S11) obtained from the prototype.

7.5.3 Design 2: Coupler Reflectometry

In contrast to design prototype 1, where circulators redirect the reflected signal back to the S11 port for measurement, design prototype 2 utilizes an RF coupler to route the reflected signal to the S21 port for measurement. A coupler is a passive RF device with four ports that samples a portion of the signal in the forward direction and any reflected signal in the reverse direction, enabling simultaneous monitoring without disrupting the main signal path. This approach requires only a single coupler instead of two circulators and benefits from the generally wider bandwidth available with couplers, even at lower frequencies. Specifically, I employ the MiniCircuits SCBD-16-63HP+ coupler with a bandwidth of 50 MHz to 1000 MHz for this prototype (see Figure 7.6b).

When a coupler is connected to the S11 port and the reflected signal is routed to the S21 port, the captured S21 signal becomes a composite of reflections from both the DUT (in this case, a hand) and the coupler itself, along with any signal leakage. This differs from a direct S11 measurement, where the captured signal solely represents the

DUT's reflection. However, assuming that the coupler's characteristics and signal leakage remain constant for a given frequency, changes in the acquired S21 signal primarily signify variations in the DUT's reflection, allowing us to indirectly infer changes in the DUT's impedance. Figure 7.8a illustrates the architecture for this prototype, and Figure 7.8b shows the S11 curves for different scenarios using this prototype.

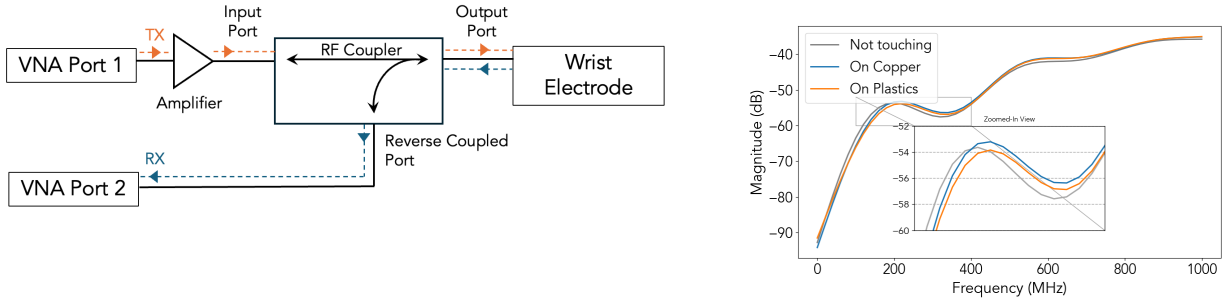

(a) (b)

Figure 7.8: The Coupler Reflectometry design (prototype 2) along with the results obtained from the prototype.

7.5.4 Design 3: Through Transmission Design

While the previous two approaches utilized S11 for sensing, this method employs S21 for measurement, requiring minimal external hardware since two ports are inherently available for this purpose. Figure 7.6c shows the prototype for this design. In this configuration, an amplifier is connected to the S11 port's output, which is then linked to an electrode placed on the top of the wrist. Another electrode, positioned at the bottom of the wrist, connects to the S21 port. Figure 7.9a illustrates this design, and Figure 7.9b shows the different S21 curves for various scenarios using this prototype.

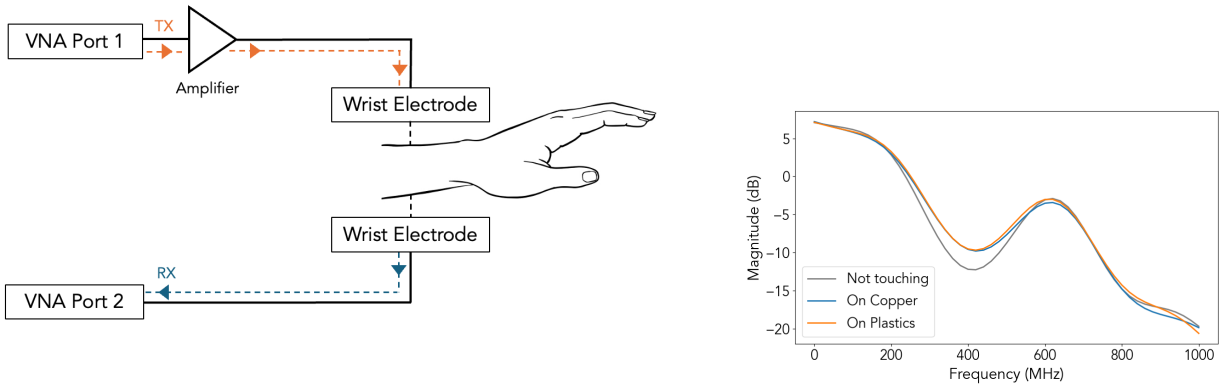

(a) (b)

Figure 7.9: The Through Transmission design (prototype 3) along with the results (S21) obtained from the prototype.

7.5.5 Comparison of Designs and Trade-offs

All three architectures demonstrated clear changes in response to different hand poses and contact with various surfaces, effectively reproducing the patterns observed in the simulations. However, each design presented distinct performance characteristics and trade-offs. Table 7.2 summarizes these trade-offs.

Design 1 (dual-circulator) exhibited the weakest received signals despite operating with the same initial transmit power and amplification as the other prototypes. This is likely attributable to the inherent insertion loss of the circulators, which attenuates both the transmitted and reflected signals at multiple points within the signal path. While Design 1 provides maximum isolation between stages (VNA, amplifier, and body), minimizing noise and interference, this benefit comes at the cost of limited bandwidth, potentially restricting the range of detectable impedance changes. Additionally, the increased component count adds complexity and potentially cost.

Design 2 (coupler) strikes a balance between performance and complexity. By utilizing

a coupler instead of two circulators, it reduces the component count while maintaining good isolation and achieving a wider bandwidth compared to Design 1. However, its sensitivity may be lower than Design 1 due to the coupler's coupling losses.

Design 3 (through-transmission) demonstrates the strongest received signal and employs the fewest components, thereby minimizing complexity and cost. However, the absence of isolation between stages can increase noise and interference, potentially reducing sensitivity. This is because, without isolation, a portion of the transmitted signal can directly leak to the receiver, and reflections from various points in the system can interfere with the desired signal. While this lower sensitivity might suffice for many touch-sensing applications, it could limit the ability to detect subtle impedance changes. Furthermore, Design 3 requires two electrodes, which could impose constraints on wearable form factors and user experience compared to the single-electrode designs.

Ultimately, the choice of design depends on the specific application's requirements and priorities. Design 1, with its high isolation and potential for high sensitivity, might be ideal for applications demanding precise impedance measurements, such as medical diagnostics or detecting subtle changes in grip force. Design 2 offers a versatile option for general-purpose applications, balancing complexity, cost, and performance. Design 3, with its simplicity and minimal components, is well-suited for compact and cost-sensitive devices where high sensitivity is not critical.

In this case, I prioritized a larger bandwidth for richer sensing capabilities and a smaller form factor to enable data collection in mobile scenarios. Consequently, I opted for Design 3 (through-transmission), which offers the simplest and most compact solution. While Design 3 presents opportunities for further optimization in terms of sensitivity, its inherent advantages make it a compelling choice for the target applications. Future work could explore techniques to improve signal strength or reduce noise in this design to enhance its performance.

Table 7.2: Comparison of different impedance measurement architectures in terms of signal strength, isolation, bandwidth, complexity, and sensitivity. Each design presents trade-offs between hardware complexity, measurement accuracy, and practicality for wearable touch sensing applications.

Feature	Design 1 (Dual-Circulator)	Design 2 (Coupler)	Design 3 (Through-Transmission)
Signal Strength	Weakest	Moderate	Strongest
Isolation	Maximum	Good	Low
Bandwidth	Limited (< 100 MHz)	Wider (50 MHz - 1 GHz)	Widest (inherent to VNA)
Complexity	Highest (more components)	Moderate	Lowest (fewest components)
Sensitivity	Highest (due to isolation)	Moderate	Lowest (due to noise and interference)
Electrodes	Single	Single	Dual
Cost	Highest	Moderate	Lowest
Advantages	High isolation, Strong noise reduction, Best for precision	Good balance of performance and complexity, Wider bandwidth than Design 1	Simplest, lowest cost, Smallest form factor
Disadvantages	Limited bandwidth, High complexity and cost	Lower sensitivity than Design 1	Lowest sensitivity, Dual electrodes

7.6 Implementation

Drawing upon the simulation and experimental results from Sections 7.5 and 7.4, I constructed the Z-Band prototype utilizing the through-transmission RF design (Design 3). While impedance sensing demonstrated strong performance in the controlled experiments, real-world scenarios introduce additional factors that can impact signal quality. Variations in body anatomy, external RF interference, and motion artifacts stemming from electrode movement can all contribute to noise. To mitigate these issues, I augmented the system with an IMU sensor, providing spatial awareness that aids in distinguishing intentional movements from noise and potentially enabling novel interaction modalities. Consequently, the final Z-Band system integrates both through-transmission impedance sensing and an IMU, leveraging their combined strengths for robust and versatile interaction capabilities.

The Z-Band implementation prototype (Figure 7.11a), employed for user evaluation and testing, mirrors the design outlined in Section 7.5.4, incorporating the same core components: LiteVNA, amplifier, and Raspberry Pi Zero 2W. Figure 7.10 provides an overview of the system, while Figure 7.11b presents an internal view of the prototype. These components were housed within a 3D-printed enclosure secured to the user's hand via a Velcro wristband. The frequency sweep was configured from 100 MHz to 800 MHz, aligning with the findings from Section 7.5, as this range exhibited the most pronounced signal differentiation across various scenarios. The IMU utilized was an ISM330DHCX, connected to an nRF52840 microcontroller, which relayed data to the Raspberry Pi via UART. The flexible electrodes (radius = 15 mm) were mounted on a 1 cm thick foam, ensuring conformability to the user's hand while maintaining uniform pressure. Figure 7.11c illustrates the electrodes used. Sensor data was grouped into batches to minimize latency and transmitted via TCP sockets over Wi-Fi to a laptop, where it underwent processing by a Python-based analysis program. The prototype weighed approximately 285 grams and consumed 0.7 Amperes of current at 5V.

The current prototype is larger and heavier than typical everyday wearables due to

the reliance on development boards, a full VNA, and a Raspberry Pi computer for rapid prototyping. These components necessitate a larger battery, further contributing to the overall size and weight. While not representative of a final product, this bulky prototype enabled us to quickly test and validate the sensing approach with users. Miniaturization is achievable through the use of custom hardware and by replacing general-purpose hardware with application-specific integrated circuits. To illustrate this potential, I built a more compact version of the Z-Band (Figure 7.22), discussed further in Section 7.9. Later in the paper, Section 7.10.3 outlines a progressive path towards miniaturizing the system to fit within a regular smartwatch form factor.

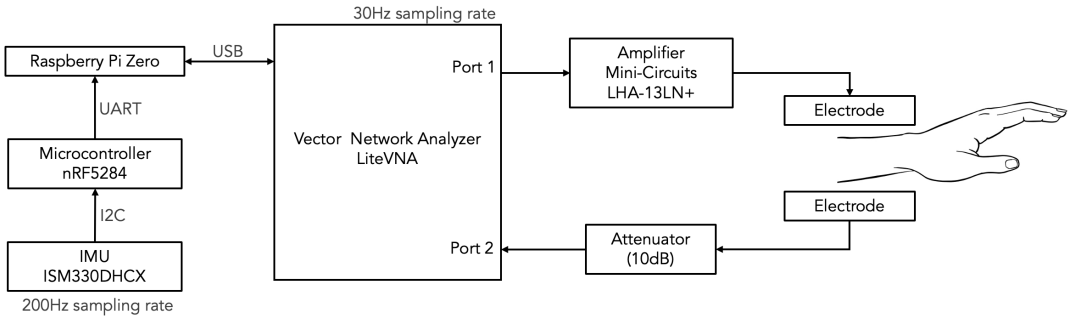

Figure 7.10: System overview of the Z-Band prototype.

7.7 Interactions

Z-Band facilitates a diverse set of interactions, including stateful touch, swipes, taps, and pressure-sensitive touch on external, un-instrumented surfaces. Figure 7.12 visually illustrates these interaction modalities.

Central to Z-Band's capabilities is its proficiency in detecting stateful touch. This involves accurately identifying and differentiating between distinct phases of touch interaction, such as touch down, touch hold, and touch release. Unlike simple tap detection, which only captures momentary contact, stateful touch enables continuous tracking of

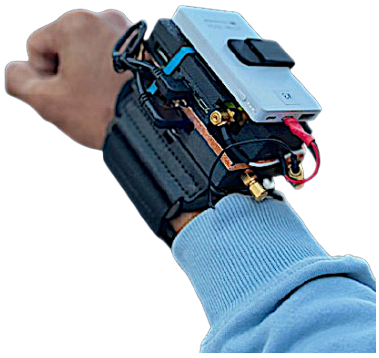

(a) The Z-Band prototype worn on the wrist.

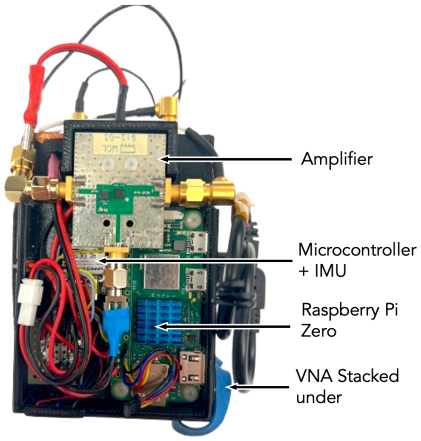

(b) Internal structure of the Z-Band implementation prototype. The design features a stacked configuration: VNA at the bottom, the middle layer (visible), and the battery on top (not shown).

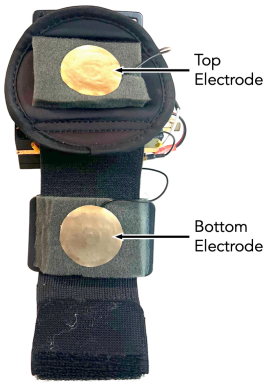

(c) Bottom view of the Z-Band prototype showing electrode placement and strap design for securing the device.

Figure 7.11: Z-Band prototype hardware overview.

touch, forming the bedrock for more intricate interactions. This capability is paramount for enabling higher-order interactions such as drag-and-drop, scrolling, and drawing, where sustained contact tracking is essential for advanced gesture recognition and interpretation.

Furthermore, Z-Band's inherent sensitivity to contact pressure introduces an additional dimension to its interaction capabilities. This sensitivity arises from how applied finger pressure alters the skin-surface contact area, thereby affecting the measured impedance. Greater pressure results in a larger contact area and a more pronounced impedance change, enabling nuanced, pressure-aware input.

Finally, I demonstrate higher-level interactions built upon the foundation of stateful touch—specifically, swipes and taps—to showcase gestural input. For swipe detection,

the system leverages IMU data to capture motion. However, this functionality could be extended through the incorporation of other motion-sensitive sensors, such as optical flow sensors, for more advanced gesture tracking. By seamlessly combining stateful touch, pressure detection, and motion sensing, Z-Band provides a versatile platform for sophisticated interaction design.

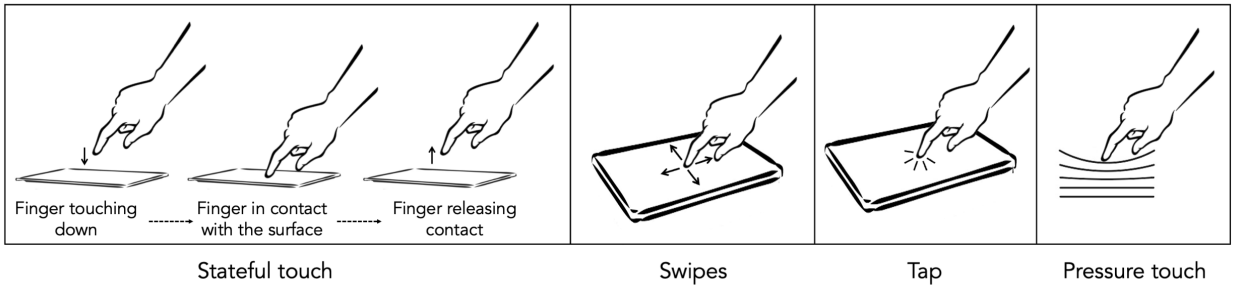

Figure 7.12: User interactions supported by Z-Band. Actions are performed on everyday un-instrumented surfaces.

7.7.1 Stateful Touch

Z-Band employs a hybrid approach, combining RF impedance sensing and IMU data for robust stateful touch detection. While RF impedance sensing provides continuous information regarding touch-induced signal variations, it is also susceptible to influences from hand movement. This poses a challenge for accurate touch detection, particularly on dielectric materials, which exhibit smaller impedance changes compared to conductive surfaces, making these subtle signals more prone to being obscured by noise. Figure 7.9b illustrates signal changes when touching different materials with the Z-Band prototype.

To overcome this challenge, I augment the system with IMU data. The IMU, while not directly sensitive to touch, provides invaluable information about hand movements and orientation. This motion data helps disambiguate genuine touch events from spurious signals caused by hand motion, especially on dielectric surfaces and in dynamic scenarios.

Figure 7.13 presents both RF and IMU data for a touch event in both stationary and walking scenarios. By integrating the continuous impedance information from RF with the precise motion data from the IMU, Z-Band accurately detects touch-down and touch-up events across a broader range of surfaces and interaction contexts.

Data Processing Pipeline

For real-time touch event recognition, both RF and IMU data streams are resampled to 100 Hz. A sliding window of 0.3 seconds duration scans the data stream to extract features for analysis. When no touch event is detected within the window, it advances with a 50% overlap to ensure continuous monitoring. However, upon detection of a touch event, the window progresses with zero overlap to capture the complete event without redundancy.

Feature Extraction from RF Data A 2D spectrogram, encompassing both the magnitude and phase of the RF signal, is generated and subsequently resized to 224×224 pixels. This resized spectrogram is then input into a ResNet51 model for feature extraction. Instead of utilizing the final classification layer, I extract a 2048-dimensional feature vector from the penultimate layer, which serves as the RF feature.

Feature Extraction from IMU Data Each IMU data window is resized to 200 samples. Frequency-domain features, including FFT, spectral centroid, bandwidth, flatness, and peak frequency, are computed. Statistical features, such as mean, median, standard deviation, maximum, minimum, variance, and zero-crossing rate, are calculated over 10 equally sized sub-windows. Additionally, cross-correlation and covariance matrices are computed between IMU axes to capture inter-axis relationships.

Feature Fusion and Classification The extracted RF and IMU feature vectors are flattened and concatenated into a single 1-D vector of length 4256. This combined vector is then fed into a random forest classifier comprising 300 trees for classification.

Data Augmentation for Robustness

To enhance generalization and robustness, temporal and frequency augmentation techniques are applied. To account for variability in gesture timing, the RF and IMU data window is shifted by up to 0.2 seconds both forward and backward in 50 ms increments. To mitigate frequency response variations across users, the RF data is rotated by up to 20 bins along the frequency axis in 5-bin increments in both directions.

Handling Non-Interaction Activities

To minimize false positives, a null class is incorporated, encompassing non-interaction activities such as hand waving, finger movements, arm movements, and stillness. The final classifier is trained to recognize three distinct classes: (1) Touch Down, (2) Touch Up, and (3) Null (No Interaction).

7.7.2 Pressure Touch

When interacting with a surface, users can apply varying levels of pressure to trigger distinct touch interactions. The intensity of the applied pressure directly affects the signal transmission between the finger and the surface, consequently altering the signal amplitude. I calculate pressure by summing the amplitude of the S21 signal across all frequencies.

The summed amplitude provides a continuous value that is then processed through a OneEuroFilter (alpha = 0.01, beta = 0.001) to ensure smooth and stable pressure detection. The filtered pressure values can be scaled to adjust sensitivity and mapped to continuous UI elements, such as sliders or knobs, enabling applications like adjusting speaker volume or screen brightness based on the applied pressure.

Figure 7.15 illustrates a user gradually increasing pressure (from 0.16N to 4.6N) while interacting with a plastic surface, along with the corresponding summed S21 values. The plot reveals a predominantly linear relationship between pressure and summed S21 values.

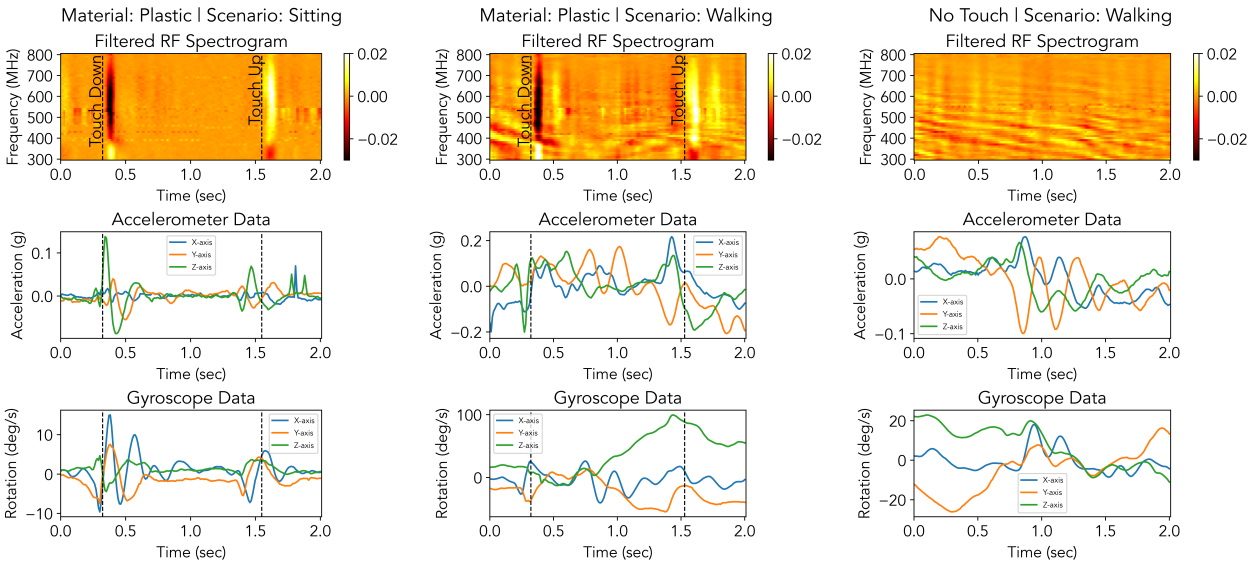

(a) Touching a plastic surface while sitting.

(b) Touching a plastic surface while walking.

(c) Walking without touching any surface.

Figure 7.13: The RF (deltas) and IMU raw data across three distinct scenarios: (a) stationary touch events on a plastic surface (demonstrating clear touch down and up events in both RF and IMU data), (b) mobile touch events while walking, where IMU data exhibits significant noise while RF data maintains distinguishable touch events in the frequency domain despite some artifacts, and (c) a no-touch scenario.

By integrating this input modality with real-time feedback and an adaptive UI, Z-Band can enable pressure-sensitive interactions similar to other continuous input techniques explored in prior work [205, 41].

7.7.3 Swipes and Taps

Z-Band extends its capabilities beyond stateful touch detection to enable swipe and tap interactions. It supports four cardinal direction swipes (up, down, left, right) for UI

navigation and tap gestures for selection. A state-model-based approach is employed to detect these interactions, as illustrated in Figure 7.16. Figure 7.14 presents the raw sensor data during the performance of swipe interactions.

Tap and Swipe Detection Logic

A tap is identified when a touch-up event occurs within 0.2 seconds of a preceding touch-down event. A swipe is considered when the duration between a touch-down and touch-up event falls within the range of 0.4 to 1 second. The data captured during this interval is subsequently analyzed to determine if a swipe occurred and to identify its direction. These time thresholds were empirically determined and can be adjusted to accommodate different user preferences.

To enhance robustness against incorrectly recognized touch events, an adaptive strategy is utilized. For swipe detection, if a touch-up event is not detected within 1 second of a touch-down, a 1-second data window following the touch-down event is analyzed to determine if a swipe occurred. Conversely, if a touch-up event occurs without a preceding touch-down, a 1-second window before the touch-up is evaluated for swipe detection. This approach helps compensate for instances where touch events are missed or misrecognized, ensuring more reliable detection of swipe interactions. As demonstrated in Section 7.8.4, this method effectively captures swipes while minimizing false positives.

Swipe Direction Recognition

For swipe direction classification, I employ a machine learning-based approach similar to tap detection but with a reduced feature set to improve surface-agnostic recognition. RF data is excluded to prevent surface characteristics from influencing the model, ensuring consistent swipe recognition across different surfaces. Additionally, frequency-based IMU features are omitted to reduce the potential impact of surface texture variations, focusing instead on statistical IMU features for classification. To further enhance robustness, time-

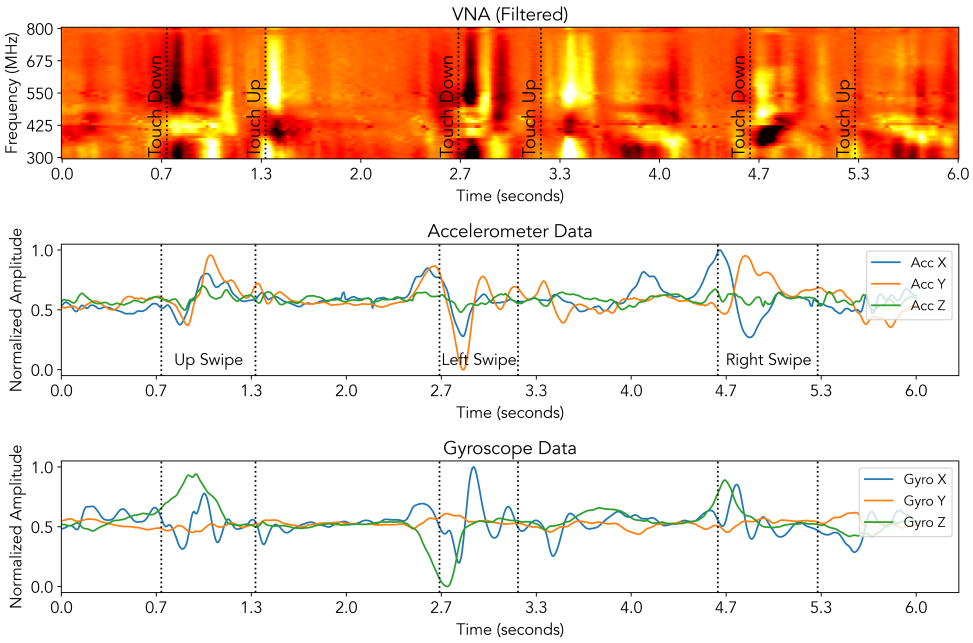

Figure 7.14: Data captured from both IMU and VNA sensors during the execution of three swipe gestures. The vertical dotted lines overlaid on the VNA heatmap indicate the start points of 'touch down' and 'touch up' events as classified by the touch detection model. The corresponding swipe directions (ground truth) are annotated on the accelerometer plot.

domain data augmentation techniques—similar to those used for touch-up and touch-down detection—are applied. The final classification is performed using a random forest model with 300 trees, leveraging only statistical IMU features for swipe direction recognition.

7.7.4 Putting it All Together

To create a complete user interface, all user interactions—stateful touch, swipes, taps, and pressure touch—must function seamlessly in tandem. Z-Band employs a state-model approach to integrate these interactions cohesively. When a touch-down event occurs, the system determines the appropriate interaction mode based on the detected motion

and timing.

If the touch-down is not followed by significant IMU motion within 0.2 seconds, the system activates pressure touch mode. Significant IMU motion is identified by analyzing motion magnitude from the IMU data, with thresholds empirically established through testing and data collection. In pressure touch mode, users can vary the pressure applied to the surface, yielding a continuous pressure value. The mode exits upon detection of a touch-up event or after five seconds have elapsed, ensuring interactions remain intuitive and time-bound.

Conversely, when significant IMU motion is detected within 0.2 seconds of a touch-down, the system transitions to swipe and tap detection mode, as detailed in Section 7.7.3. This ensures that dynamic gestures, such as swipes and taps, are accurately recognized without interfering with static pressure-based interactions.

This interaction logic is visually represented in Figure 7.16, illustrating the transitions between pressure touch, swipe, and tap states. By leveraging this structured approach, Z-Band ensures seamless and reliable recognition of user interactions across various contexts.

7.8 Evaluation and Results

I conducted a comprehensive evaluation of Z-Band to assess its performance across various interaction types, participants, and real-world scenarios. The primary objective was to understand the system's effectiveness under practical conditions, including natural interaction variability and the impact of repeated device wear and removal.

The evaluation comprised four distinct studies:

- Stateful Touch Study: To assess the system's ability to accurately detect and differentiate stateful touch interactions (touch-down, touch-up) across different users and surfaces.

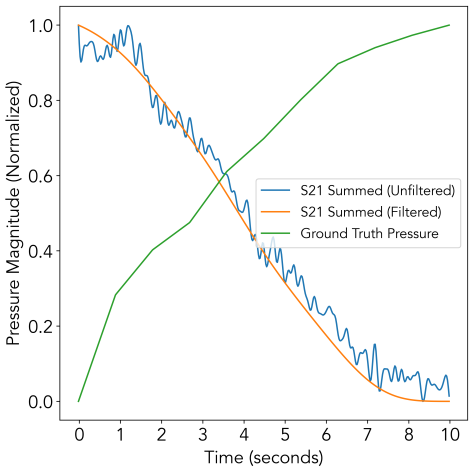

Figure 7.15: Summed S21 magnitude response to increasing pressure (from 0.16N to 4.6N), showing both unfiltered and filtered data alongside ground truth pressure measurements.

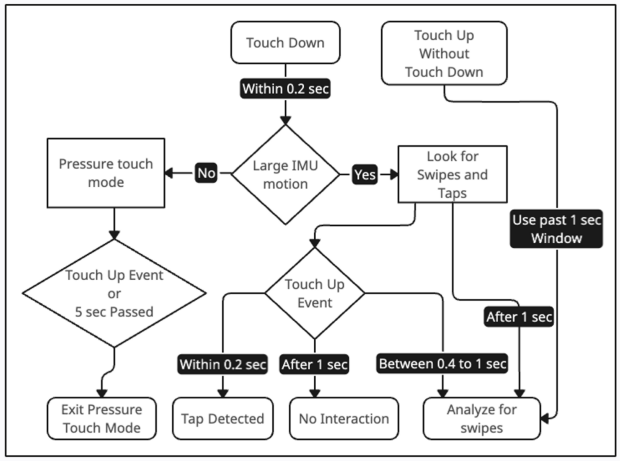

Figure 7.16: Interaction flow for Z-Band, illustrating detection logic for different touch interactions.

- Touch Sensitivity Study: To examine the system's performance in detecting interactions with varying pressure levels.
- Swipe Gesture Study: To evaluate the system's accuracy in recognizing swipe gestures.
- False Positive Study: To analyze the frequency of unintended detections in scenarios without deliberate interactions.

These studies were designed to evaluate the system's robustness in real-world contexts. Participants were encouraged to interact naturally, without restrictions on their finger, hand, or body posture, which introduced valuable variability into the collected data. For instance,

some users performed interactions with their index finger fully extended, while others kept their remaining fingers curled or partially folded. This diversity helped the inference model generalize better to a wider range of user behaviors and pose variations. Participants were also instructed to remove and re-wear the prototype device multiple times throughout the study (e.g., after each session) to simulate practical usage scenarios and evaluate the system's adaptability to device repositioning.

The user study, which received approval from the Institutional Review Board (IRB), involved 16 participants recruited from my university and the local community. Each participant received a $30 gift card as compensation for their time, and the study took approximately 60 minutes for each participant to complete.

7.8.1 Data Collection Tool

To facilitate accurate and consistent data collection, I developed a custom user interface (UI) inspired by the 'Guitar Hero' style. This UI provides dynamic visual cues, guiding users through specific interactions at designated times and for precise durations, as shown in Figure 7.17.

The interface features floating rectangles, each representing a distinct interaction. The length of a rectangle corresponds to the allocated time window for that action. These rectangles move across the screen, prompting users to perform the action when a rectangle intersects a vertical line, signifying its active state. Clear text labels beside each rectangle specify the action to be performed (e.g., "Tap," "Swipe," "Hold").

This dynamic design offers several advantages for data collection and analysis. The moving bar and rectangle intersections provide clear visual cues for the start and end times of each interaction, ensuring precise timing and synchronization. The speed of the moving bar is adjustable, allowing for customizable pacing of interactions to accommodate different user needs and data collection requirements. Additionally, the interface presents a preview of upcoming actions, enabling users to anticipate and prepare for interactions

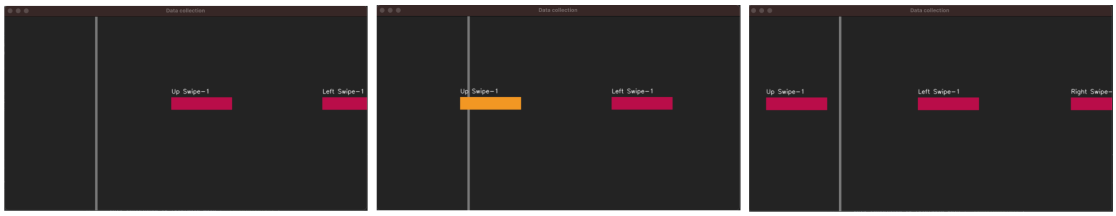

Figure 7.17: Three snapshots of the data collection UI at various points in time. (1) The next action for the user to perform is an “Up Swipe,” followed by a “Left Swipe.” (2) The “Up Swipe” action window is active (highlighted in yellow), prompting the user to perform the gesture. (3) The “Up Swipe” action window has concluded, and the upcoming actions are “Left Swipe” followed by “Right Swipe.”

in advance. Beyond guiding user input, the rectangle windows function as a ground truth annotation tool, automatically marking the exact start and end times of interactions. This ensures accurate segmentation of sensor data, facilitating reliable analysis and effective model training.

This tool streamlines data collection and ensures consistency by providing clear visual guidance and precise timing information, thereby enhancing the reliability and quality of the collected data, which is crucial for developing robust interaction models.

7.8.2 Study #1: Evaluating Stateful Touch Detection

This study evaluates Z-Band’s ability to accurately detect touch-down and touch-up events across various materials and movement conditions. The primary goal is to assess its robustness for real-world applications, ensuring reliable performance across diverse surfaces and usage scenarios.

Experimental Factors

Influence of Material Conductivity Material conductivity significantly impacts impedance sensing. Conductive materials, such as metals, generate strong signal variations, whereas dielectric materials, such as plastic and wood, produce weaker changes. To evaluate performance across a range of conductivities, I selected five test materials: plastic (low), wood (low), cotton cloth (medium), human palm (medium), and copper (high).

Impact of Motion and Movement Since the system incorporates an IMU and skin-worn electrodes, motion can affect its performance by introducing motion artifacts into IMU data and noise into the RF sensor readings due to electrode shifts on the skin. To assess this impact, I evaluated Z-Band's performance in both stationary (sitting) and dynamic (walking) scenarios. The system's wireless and battery-powered design enabled seamless data collection during walking scenarios.

Study Protocol

To evaluate the system's performance, participants were instructed to perform touch-down and touch-up actions on the five different materials (plastic, wood, cotton cloth, copper, and human palm) with a 2-second gap between actions, as displayed on a screen using the custom data collection tool. Each participant completed ten sessions, with each session involving five touch events on each material. To ensure diverse data and prevent overfitting to specific device orientations or electrode placements, the wristband prototype was removed and re-worn after each session. Data collection occurred under two conditions: stationary (seated) for the first four sessions and dynamic (walking) for the remaining six. This procedure allowed us to assess the impact of both material properties and motion on touch detection accuracy.

In addition to touch-up and touch-down events, I also recorded data for non-interactive motions (null), such as finger movement, arm movement, and stillness, in both sitting and

walking scenarios. This data is essential for training the system to differentiate between intentional user interactions and incidental motions, thereby filtering out false positives and preventing the system from misinterpreting incidental motions as deliberate touch interactions. The null data collected in this study is also utilized in subsequent studies presented in this paper.

Model Training

Touch-down and touch-up data from all surfaces were combined to form a comprehensive dataset for training machine learning models (see Section 7.7.1 for feature extraction details). To generate data for non-interaction or null classes, I segment the longer non-interaction data into smaller windows matching the duration of actual interactions. Given the surplus of null class data, I apply random upsampling to balance the class distribution during model training. I use this approach for both touch and swipe detection models to ensure a balanced distribution.

I trained models separately for sitting, walking, and combined sitting/walking scenarios. I employed leave-one-out cross-validation (LOOCV) for model evaluation. For user-independent models, I iteratively trained on data from all but one user, testing on the held-out user, and averaged results across all users. User-dependent models were trained on all but one session per user, tested on the remaining session, and results were averaged across all sessions for each user. All presented results reflect cross-session evaluations; no models were trained and tested on data from the same device wear session.

Results

In stationary (sitting) scenarios, both user-dependent and user-independent models achieved over 95% accuracy, with the user-dependent model reaching the highest accuracy of 97% across all scenarios. The sitting condition consistently outperformed the

walking condition, likely due to the motion-induced noise affecting both RF and IMU signals. The lowest accuracy was observed in the walking scenario with the user-independent model, at 89.6%, while all other scenarios maintained accuracy around 90%. Notably, touch-down and touch-up accuracy remained above 90% across all scenarios. However, during walking, null detection accuracy declined for the user-independent model scenario, indicating a higher likelihood of false positives. Expanding the dataset with additional non-interaction scenarios could help mitigate false positives and improve classification robustness. Figure 7.18 presents the confusion matrices for all scenarios.

Sensor Ablation Analysis

The previous section explored the combined impact of bio-impedance and IMU sensing on surface interactions across different materials and scenarios. Here, I present an ablation study to quantify the individual contributions of each sensor modality to the overall system performance. This analysis is crucial for understanding the relative importance of each sensor, identifying potential areas for optimization, and informing future design decisions regarding sensor selection and fusion strategies.

Figure 7.19 illustrates Z-Band's performance using IMU alone, RF alone, and the combined IMU+RF approach. Across all scenarios, the combined IMU+RF approach consistently outperforms either sensor individually, highlighting their complementary nature and mutually reinforcing benefits. Notably, RF consistently surpasses IMU in accuracy, with the single exception of the user-dependent model's sitting scenario. Furthermore, IMU performance degrades more significantly than RF during walking, demonstrating the superior robustness of RF sensing to motion artifacts.

7.8.3 Study #2: Evaluating Sensitivity to Touch Pressure

Combining bio-impedance sensing with IMU data enables the detection of subtle touch interactions, outperforming IMU-only approaches. This heightened sensitivity is attributed

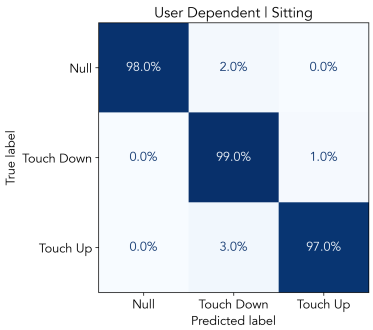

(a) User-dependent cross-session model performance for the sitting scenario.

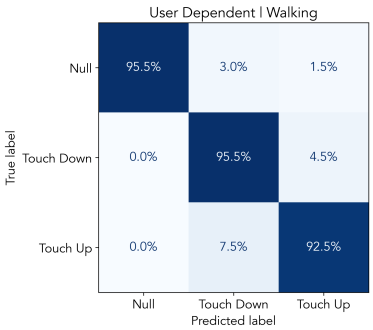

(b) User-dependent cross-session model performance for the walking scenario.

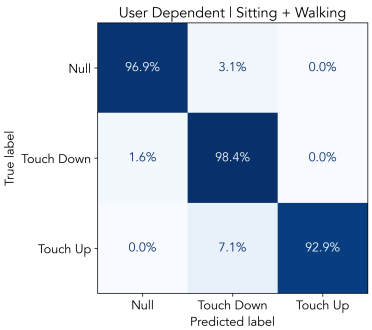

(c) User-dependent cross-session model performance for the combined (sitting & walking) scenario.

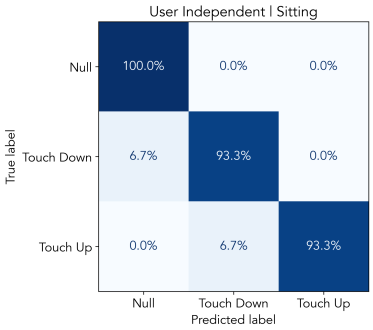

(d) User-independent model performance for the sitting scenario.

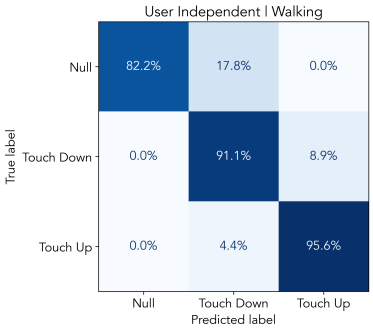

(e) User-independent model performance for the walking scenario.

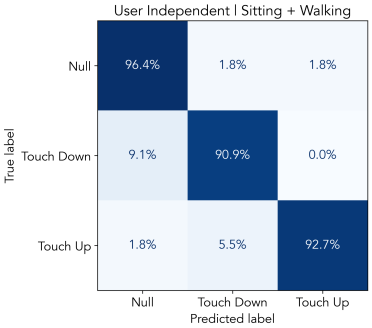

(f) User-independent model performance for the combined (sitting & walking) scenario.

Figure 7.18: Performance comparison of user-dependent and user-independent models for touch detection across sitting, walking, and combined scenarios.

to the active broadband nature of the impedance sensing, which can capture even minor variations in touch pressure.

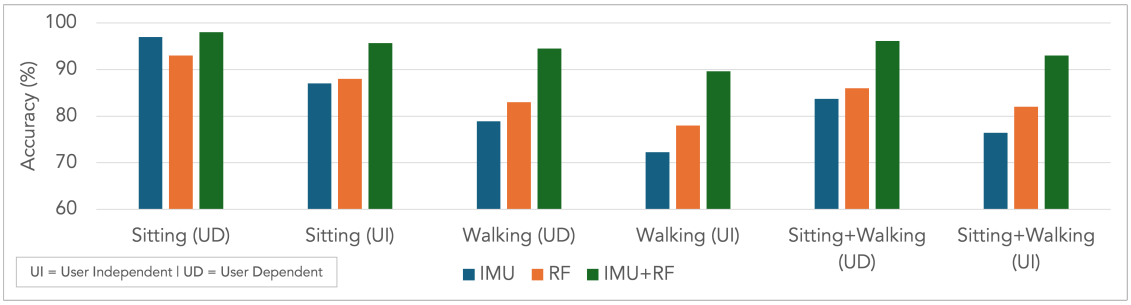

Figure 7.19: Sensor ablation analysis of touch detection accuracy across sitting, walking, and combined scenarios, using IMU, RF, and combined IMU+RF for user-independent (UI) and user-dependent (UD) models.

I evaluated Z-Band's touch sensitivity by conducting a user study with five participants, each performing three distinct tap interactions—soft, regular, and hard—on a plastic surface. Taps were chosen over touch-down and touch-up events because they provide a single, well-defined force application. In contrast, maintaining consistent force during sustained contact (as in touch-down and touch-up) proved challenging in a pilot study, leading to significant user variability. By utilizing taps, I minimized this variability and ensured that each interaction produced a distinct and controlled force measurement, thereby improving the reliability of the analysis.

Study Protocol

In this study, participants performed three types of taps on a plastic surface: soft, regular, and hard. The plastic surface was mounted on a sensitive weight scale to provide ground truth force measurements for each tap. Each participant performed 10 repetitions for each of the three tap types, resulting in a total of 30 taps per participant.

Model Training

During the study, RF and IMU data were collected synchronously. The data was processed using the feature extraction pipeline described in Section 7.7.1. Tap detection and classification were performed using a Random Forest classifier (number of trees = 300). For user-dependent analysis, I adopted a stratified approach, utilizing approximately 70% of each user's data for training and the remaining 30% for testing. For the user-independent model, I used leave-one-user-out cross-validation (LOOCV), iteratively training on all but one participant and testing on the held-out user.

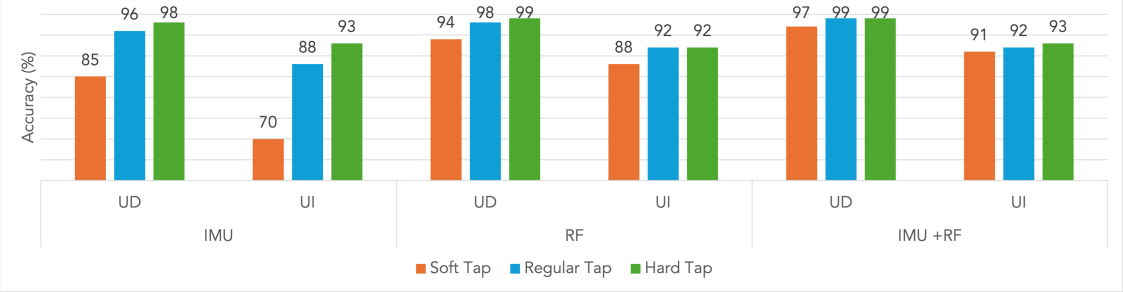

Figure 7.20: The comparative performance of IMU, RF, and their combination for classifying three tap types, i.e., soft, regular, and hard, in both user-dependent (UD) and user-independent (UI) scenarios.

Results

I developed models using IMU-only, RF-only, and combined IMU+RF inputs, with the results shown in Figure 7.20. The average forces applied for soft, regular, and hard taps were 0.18N, 0.48N, and 1.63N, respectively, as measured by the weighing scale across all participants.

The IMU-only model struggled with detecting soft taps, achieving 85% accuracy in the user-dependent (UD) scenario and dropping to 70% in the user-independent (UI) scenario.

This indicates its limitations in capturing subtle, low-pressure interactions. However, it performed better for regular and hard taps, with accuracies up to 98% in the UD and 93% in the UI cases, as these taps generate more pronounced motion signals.

In contrast, the RF-only model performed better at detecting soft taps, achieving 94% accuracy in the UD scenario and 88% in the UI scenario, demonstrating its sensitivity to subtle pressure changes. For regular and hard taps, the RF model delivered consistently high accuracy, comparable to or slightly exceeding the IMU's performance.

The combination of IMU and RF data yielded the best overall results, significantly improving soft tap detection to 97% in the UD and 91% in the UI scenarios, while achieving near-perfect accuracy (up to 99%) for regular and hard taps. These results underscore the critical role of RF sensing in enhancing sensitivity to subtle touches. They also highlight the robustness achieved through the fusion of IMU and RF data, making the system highly reliable across all touch types and user scenarios.

7.8.4 Study #3: Evaluating Swipe Gesture Recognition

This study evaluates swipe gestures performed on a plastic surface. Plastic, with its low conductivity, presents a challenging scenario for impedance-based touch sensing, allowing us to assess the robustness and sensitivity of the approach in a more demanding context.

Study Protocol

Sixteen participants were instructed to perform four directional swipes (left, right, up, down), each performed within a 1-second window. Each participant completed four sessions, performing five repetitions of each swipe direction per session. After each session, the Z-Band prototype was removed and re-worn to capture data from different device orientations and electrode placements. All sessions were conducted with participants in a seated position.

Model Training

I conducted a two-part evaluation of swipe gesture recognition:

1. Swipe Detection Accuracy: First, I assessed the accuracy of swipe recognition using segmented swipe data based on ground truth labels collected during the study. This allowed us to evaluate the performance of the gesture recognition model in isolation.

2. Swipe Segmentation in Continuous Data: Next, I evaluated the system's ability to segment swipe gestures within a continuous data stream. This involved using a stateful touch detection model (trained on data from all users in the sitting scenario from the previous study) to identify potential swipe gestures and then evaluating the accuracy of classifying those segmented gestures. This approach provides a more realistic assessment of the system's performance in a real-world scenario.

For both swipe detection and segmentation evaluations, I developed user-dependent and user-independent models using the IMU data and a Random Forest classifier (see Section 7.7.3 for feature extraction details). Leave-one-out cross-validation (LOOCV) was employed for model evaluation.

Results

Swipe Classification Accuracy Using ground truth swipe data windows, both user-dependent and user-independent models achieved high accuracy in classifying left, right, up, down, and null gestures. User-dependent models achieved an impressive average accuracy exceeding 96%, with a range of 96% to 100%. The user-independent model also performed well, with an average accuracy of 93%, ranging from 92.3% to 100%.

Swipe Segmentation Performance In evaluating swipe segmentation, 74% of swipes had both touch-up and touch-down correctly detected, while 11% had only one of these events identified. In 10% of cases, a single event was detected but misclassified (e.g., touch-up mistaken for touch-down), and 5% were not detected at all. To address cases where touch events were missed, I applied an adaptive correction strategy: for touch-up events without a preceding touch-down, a 1-second window before the touch-up was analyzed, and for touch-down events without a following touch-up within 1 second, a 1-second window after the touch-down was included for evaluation.

Additionally, I detected extra touch-up/down events that did not correspond to actual swipes. These spurious events constituted 4% of the total detected touch events. These extra events were included in the testing dataset to evaluate the robustness of the swipe detection model in handling spurious touch events and filtering out false positives.

Swipe Classification Accuracy in Continuous Data Stream For swipe classification, a model was trained using ground-truth-segmented data, while the test data was segmented using the touch detection model to simulate real-world performance. The classification model achieved 94.2% accuracy in user-dependent cases and 91.4% in user-independent cases. Importantly, non-swipe windows mistakenly segmented by the touch detection model were correctly classified as null, demonstrating the system's strong false-positive rejection and reliable real-world swipe recognition.

7.8.5 Study #4: Analyzing False Positives

In Human-Computer Interaction (HCI) research, minimizing false positives is crucial for creating seamless and reliable user experiences. A high rate of false positives—where the system mistakenly detects a gesture or interaction—can lead to frustration, reduce user trust, and ultimately degrade the interface's usability. To evaluate and minimize false positives, I utilized the data collected from previous studies to perform an evaluation.

Methodology

To evaluate false positive rates, I applied the touch-up/down and swipe recognition models trained in previous studies to a continuous stream of null test data, totaling 80 minutes, collected from earlier experiments. A sliding window approach was used to detect touch events, with a 0.2-second window and 50% overlap. When a touch-up or touch-down event was detected, the overlap was set to 0 to prevent redundant detections. Using this approach, all touch-up and touch-down events within the null dataset were identified, and their occurrences were analyzed to assess false positive rates.

Following this, gesture detection was applied to the detected touch events to further analyze false positive performance at the gesture level. Temporal constraints were imposed to ensure only valid gestures were recognized: taps were required to be shorter than 0.2 seconds, swipes had to fall within the 0.4 to 1-second range, and any window considered for a swipe was further processed through the swipe recognition model to confirm its validity.

Results and Analysis

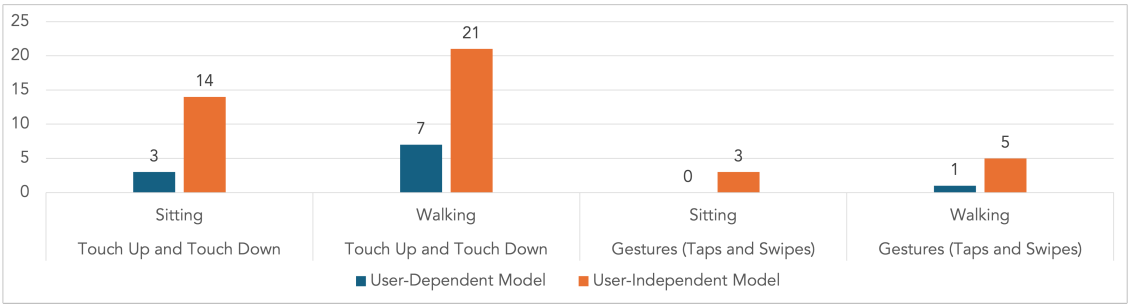

Figure 7.21: The chart depicts the false positive rates (per hour) for two interaction types—touch up/down events and gestures (taps and swipes)—under two conditions: sitting and walking.

Figure 7.21 presents the false positive rates for both user-dependent and user-independent models in different scenarios. As expected, the false positive rates were higher during walking compared to sitting, likely due to the increased motion artifacts affecting both IMU and RF data. The user-independent models also exhibited higher false positive rates than the user-dependent models, reflecting the challenge of generalizing across users.

Crucially, applying the temporal and gesture-specific constraints significantly reduced false positives. In the sitting scenario, the user-dependent model achieved a 0 false positive rate per hour for gesture recognition, while the user-independent model's rate was reduced to 3 per hour. This highlights the effectiveness of incorporating higher-level knowledge and constraints to improve the robustness of the system.

These results demonstrate that while Z-Band's basic touch detection exhibits some false positives, these can be effectively mitigated by incorporating constraints and more complex patterns. This multi-layered approach enhances the reliability of the system and paves the way for practical and user-friendly touch and gesture interfaces. Future work can explore additional strategies for minimizing false positives, such as adaptive thresholds and personalized calibration, to further improve the robustness of Z-Band in diverse real-world scenarios.

7.9 Prototype Refinement through Miniaturization

The Z-Band prototype employed for initial evaluation offered significant advantages, including expansive bandwidth and amplified transmission power, which enabled comprehensive testing of the system under challenging conditions. However, its complex hardware configuration, encompassing a full VNA and a Raspberry Pi computer, rendered the device bulky and less suitable for everyday wear.

In response to these limitations, I introduce Z-Band Lite, a compact, lightweight, and wearable alternative that retains effectiveness for core interaction tasks. This miniaturized prototype is depicted in Figure 7.1(B) and 7.22a.

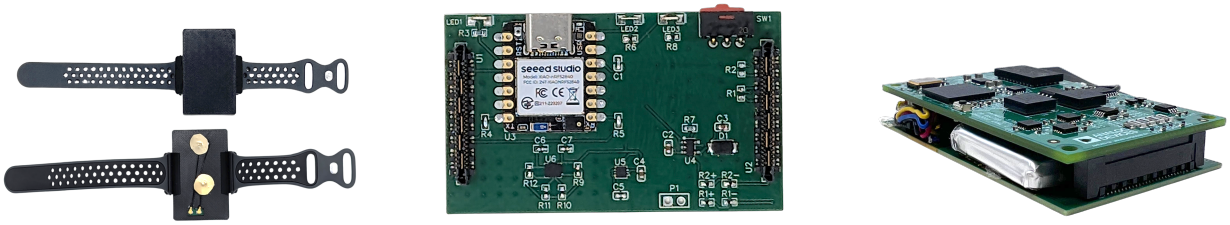

(a) Z-Band Lite Prototype: Top and Bottom Views.

(b) Custom expansion board for ADMX2001B.

(c) Stacked PCBs of Z-Band Lite.

Figure 7.22: Visual representations of the Z-Band Lite components.

7.9.1 Hardware Design and Components

At the core of Z-Band Lite is the ADMX2001B impedance analyzer measurement module from Analog Devices. This compact module, measuring only 63mm $\times$ 38mm, supports impedance measurements ranging from 0.2 Hz to 10 MHz. It operates at 3.3V and provides both UART and SPI interfaces, making it exceptionally well-suited for miniaturized designs.

Although the ADMX2001B module is available with an evaluation board (EVAL-ADMX2001EBZ) for testing and connectivity, its substantial size (150mm $\times$ 200mm) renders it impractical for my wearable application. To address this, I developed a custom expansion board that matches the compact dimensions of the ADMX2001B module. This custom board, shown in Figure 7.22b, stacks directly beneath the ADMX2001B module (Figure 7.22c) and integrates an ESP32 microcontroller, an ISM330DHCX IMU, and a battery charger for the onboard 400mAh battery. The prototype operates entirely wirelessly, with the microcontroller seamlessly transmitting impedance and IMU data over Wi-Fi.

The electronic components are housed within a 3D-printed enclosure, and a repurposed Apple wristband is used to secure the device to the user's wrist. Two gold-coated electrodes, each 20mm in diameter, are affixed to the bottom of the case to ensure stable skin contact for accurate impedance measurements. The prototype weighs approximately

100 grams and consumes about 300 mA of current at 3.3V.

7.9.2 Functional Capabilities and Limitations

The Z-Band Lite prototype operates within a 1–10 MHz frequency range. While its narrower bandwidth and lower transmission power, when compared to the original Z-Band prototype, result in a reduced overall sensing capability, it demonstrates excellent performance in detecting touch on medium to high-conductivity surfaces, such as human skin and various metals. This characteristic makes it particularly well-suited for on-body interactions, for example, using one hand to interact with the palm of the other, as illustrated in Figure 7.1(D).

The reduced capabilities of Z-Band Lite are not an inherent limitation of its compact form factor but rather a consequence of utilizing readily available, off-the-shelf hardware. With custom-designed hardware, a fully functional impedance-sensing system with expanded bandwidth and higher transmission power could realistically fit within a smartwatch-sized device. This potential for further miniaturization is discussed in greater detail in Section 7.10.3.

7.9.3 Open-Source Design

To foster further research and innovation, I have made the hardware and software designs for Z-Band Lite open source. Researchers and enthusiasts can access these designs to construct their own devices and experiment with interactions on this platform.

7.10 Discussion

Through comprehensive simulations, technical evaluations, and user studies, I have demonstrated how Z-Band effectively integrates impedance and inertial sensing to facilitate precise and versatile touch interactions on everyday surfaces. This capability directly addresses the limitations of traditional input methods, particularly within extended

reality (XR) environments. I now contextualize this work in relation to existing research, discuss the current limitations of my implementation, highlight promising directions for future research, and explore the broader applications of Z-Band in real-world scenarios.

7.10.1 Applications

Z-Band holds substantial potential across various domains, including XR, wearables, accessibility, and smart environments. Its unique capabilities enable several novel interaction paradigms.

Transforming Everyday Surfaces into Interactive Touch Interfaces Z-Band fundamentally redefines interaction by converting ordinary surfaces into touch-sensitive digital interfaces, thereby enabling seamless and intuitive control of smart environments. This capability allows users to interact with common objects—such as desks, tables, walls, or clothing—without the need for dedicated touchscreens or physical buttons. In smart home settings, users can tap or swipe on tables to adjust lighting, control media playback, or modify thermostat settings, eliminating the reliance on remote controls or voice commands. Walls and kitchen countertops can similarly function as interactive hubs for managing smart appliances. In wearable and on-body interaction contexts, Z-Band empowers users to control devices by tapping or swiping on garments, such as sleeves or pant legs, for discreet media playback or call management. Similarly, one hand can interact with the palm or forearm to control AR/VR headsets or smartwatches without disrupting immersion. By seamlessly integrating digital interactions into physical environments, Z-Band fosters more fluid and intuitive user experiences.

Enhance Accessibility Through Intentional Interaction Detection Z-Band offers particular utility for users facing motor control challenges due to its precise pressure-sensing capabilities. The system can effectively differentiate between intentional inputs and inadvertent contact by monitoring applied pressure, thereby filtering out unintended interactions

caused by tremors or involuntary movements [48]. This capability aligns well with existing research [106] indicating that users with motor control disabilities typically apply greater force during tapping interactions (averaging 6.2 N, compared to a standard 0.98 N activation threshold). Z-Band's S21 pressure sensitivity range readily accommodates these interaction patterns, enabling personalized pressure threshold calibration for individual users.

Context-Aware, Material-Based Interaction During my exploration, I identified a unique capability of Z-Band: its ability to distinguish between different surfaces, such as copper versus wood. Figure 7.9b displays the raw data captured by the Z-Band prototype for various materials. This capability supports two key applications. First, it enhances security by restricting interactions to specific surfaces—for example, allowing input only on wooden furniture to prevent accidental activations elsewhere. Second, it enables context-aware functionality, where interactions adapt based on the material—tapping on wood could adjust ambient lighting, while touching skin could trigger media playback controls. Future research will further explore and refine material differentiation to expand Z-Band's interactive potential.

7.10.2 Future Interactions

Multi-Finger and Hand-Specific Interactions While Z-Band currently focuses on single-finger touch interactions, expanding to multi-finger and hand-specific interactions could enable richer and more expressive inputs. Distinguishing between different fingers interacting with a surface would allow for gestures such as pinch-to-zoom, multi-finger scrolling, or chorded inputs similar to keyboard shortcuts. Future iterations could incorporate electrode arrays or machine learning models trained to recognize characteristic impedance changes caused by different fingers. Additionally, tracking impedance variations across the hand could enable differentiation between left and right hands, facilitating bimanual

interactions.

Beyond Touch Detection Z-Band's sensing capabilities could be leveraged for a broader range of interactions, including proximity-based gestures and grip recognition. Since RF impedance is affected by hand proximity, the system could detect hovering gestures, enabling touch-free interactions with virtual interfaces. Grip and hand pose recognition could further extend its use in augmented reality (AR) and virtual reality (VR) applications, where natural hand-based interactions are essential.

7.10.3 Hardware Miniaturization and Optimization

The current Z-Band prototype was intentionally designed with a modular form factor to prioritize rapid prototyping and streamlined debugging during user evaluation. By leveraging commercially available development boards, such as the LiteVNA and Raspberry Pi, I ensured reliability while minimizing debugging overhead. These off-the-shelf components, having undergone rigorous testing before market release, allowed us to focus on refining Z-Band's sensing capabilities rather than addressing hardware inconsistencies.

However, this prototype does not represent the fundamental limitations of this approach. The large and modular design primarily facilitates experimental flexibility rather than defining the ultimate form factor of Z-Band. I developed and demonstrated a compact prototype, detailed in Section 7.9, which utilizes an entirely different Analog Front-End (AFE) as an alternative to a VNA-based solution. Future iterations will replace the Raspberry Pi and off-the-shelf VNA with custom-designed circuits optimized specifically for bio-impedance sensing. Prior work by Zhang et al. [273] indicates that only 15% of the NanoVNA's (comparable to LiteVNA) physical area is dedicated to actual impedance measurement circuitry, with the remaining space occupied by displays and power management components. This suggests that a significant reduction in device size is feasible without compromising performance.

Recent advancements in impedance measurement hardware, such as the ADL5960 chip-based VNA[4], offer promising opportunities for miniaturization. This highly integrated solution eliminates the need for bulky external components by incorporating a built-in local oscillator. Similarly, active circulator designs [210] significantly reduce hardware size compared to their passive counterparts, further contributing to a compact implementation.

Additionally, the final S21 through-path measurement design (Figure 7.9) eliminates the need for inductive components, enabling a simpler circuit layout. Unlike the earlier Coupler Reflectometry design (Figure 7.8), which relied on additional RF components, the optimized S21-based architecture is well-suited for further miniaturization.

By integrating these improvements, Z-Band can evolve into a sleek, wrist-worn form factor without sacrificing functionality. These advancements pave the way for practical, real-world deployments, making Z-Band a viable sensing technology for next-generation wearable interfaces.

7.10.4 Battery Life and Future Improvements

Battery life is a critical consideration for wearable devices. The current Z-Band prototype, with its off-the-shelf components and continuous sensing, has limited battery life. However, we can significantly improve this in future iterations. One key strategy is duty cycling, where the system intelligently alternates between active sensing and sleep modes. We can drastically reduce power consumption by activating the sensors only when necessary, such as when the user is likely to interact with a surface. Duty cycling can be achieved through various techniques, including using the IMU to detect hand movements that suggest an impending interaction, employing proximity sensors to detect when the hand is near a surface, or even allowing the user to manually activate the sensing system when needed. Additionally, utilizing lower-power components, such as a more efficient microcontroller and a custom-designed impedance analyzer, can further reduce power

[4]https://www.analog.com/adl5960.html

consumption. Furthermore, replacing Wi-Fi with Bluetooth Low Energy (BLE) for wireless communication or logging data locally and transmitting it in bursts instead of continuously streaming can further conserve energy.

7.10.5 Real-World Deployment Challenges

While Z-Band demonstrates strong performance in controlled experiments, transitioning the system to real-world deployment introduces several challenges. One of the key issues is variability in electrode placement. Since RF impedance sensing is highly sensitive to the positioning of electrodes on the skin, shifts due to wrist movement or re-wearing the device can alter signal characteristics. This variability can introduce inconsistencies in touch detection, necessitating adaptive calibration methods or machine learning models that generalize well across different placements and users. Although the user study involved removing and re-wearing the band upright for each session, this controlled environment might not fully represent the diverse orientations encountered in everyday use.

Another challenge is environmental interference. RF signals can be affected by ambient electromagnetic noise from nearby electronics, humidity variations, or changes in skin condition (e.g., sweat or dryness), potentially impacting sensing reliability. Robust signal processing techniques, including adaptive filtering and real-time recalibration, could help mitigate these effects.

7.11 Conclusion

This research introduces Z-Band, a novel wearable device that enables intuitive interaction with everyday surfaces. By combining bio-impedance and inertial sensing, Z-Band offers robust and versatile touch detection, even on challenging dielectric materials. The investigation spans theoretical foundations, simulation-based analysis, and the development of analog front-end architectures specifically tailored for wrist-worn impedance sensing with VNAs. Through rigorous user evaluations, I demonstrate Z-Band's effectiveness in

accurately recognizing a diverse set of gestures, including taps and swipes, even amidst the complexities of real-world scenarios. The system's ability to achieve high accuracy for touch detection without requiring per-user calibration underscores its significant potential for seamless integration into daily life. By enabling natural and intuitive touch interactions on everyday surfaces, Z-Band paves the way for a future where digital and physical interactions are seamlessly intertwined.

Chapter 8
SUMMARY, INSIGHTS, AND OUTLOOK

8.1 Thesis Overview and Key Contributions

This dissertation has investigated novel techniques to expand the sensing capabilities of ubiquitous devices by strategically bridging the gap between the limited functional enhancements offered by software-only side-channel sensing and the high costs and lengthy redesign cycles associated with adding new hardware. I explored two primary techniques to achieve this balance: first, developing low-cost and low-power sensor add-ons that seamlessly integrate with existing devices without requiring internal modifications; and second, implementing targeted hardware modifications to enhance intrinsic device functionalities at reduced time and cost.

To demonstrate the effectiveness and real-world applicability of these approaches, this thesis presented several concrete examples across diverse domains. In Part II, focusing on sensor add-ons, I introduced GlucoScreen, a cost-effective, smartphone-based glucose testing add-on designed for at-home pre-diabetes screenings, aiming to make healthcare more accessible. I further accelerated this development paradigm with PhoneScreen, a hardware development toolkit engineered for rapid electrochemical test strip integration, streamlining the creation of future diagnostic add-ons. I also extended this concept to wearables with WatchLink, a modular add-on platform for smartwatches that enables low-cost, low-power integration of external sensors by leveraging the smartwatch's existing ECG hardware.

Part III shifted to targeted hardware modifications, demonstrating how enhancing the bandwidth of bio-impedance sensing in wearables can unlock new possibilities for contextual interaction and user input. I presented Z-Ring, a ring-based wideband bio-

impedance sensing system capable of gesture, object, touch, and user recognition from a single instrumentation point on the finger. Complementing this, Z-Band was introduced as a wristband-based wideband bio-impedance sensing system for stateful touch interaction on everyday uninstrumented surfaces, showcasing its ability to detect touch pressure and operate consistently even in dynamic mobile scenarios.

8.2 Key Learnings

Throughout this research, several high-level insights emerged, fundamentally reshaping the understanding of how to enhance the capabilities of ubiquitous devices through side-channel sensing.

8.2.1 Reconceptualizing Side-Channel Sensing

This thesis fundamentally reconceptualizes side-channel sensing by shifting its focus from exploiting unintended information leaks to actively engineering programmable data pathways. Traditional approaches passively observe system behaviors; however, this work demonstrates how to deliberately design communication and sensing channels that repurpose existing hardware for beneficial functionalities. I show that existing sensors can also function as communication channels for new sensors.

This thesis demonstrates that seemingly disparate modalities like capacitive touch, ECG, and bio-impedance can be effectively leveraged as programmable side-channels for novel sensing. By understanding and manipulating the inherent electrical characteristics of these interfaces, we can transcend their original design limitations and extract rich, contextual information from human-device and human-environment interactions. This moves beyond simple “information leaks ” to deliberate, engineered data pathways.

8.2.2 Design Philosophy Insights

Prioritizing Practicality for Adoption:

A foundational principle embedded throughout this work's design and development processes was the unwavering emphasis on practicality for adoption. This philosophy mandated a critical balance between introducing novel functionalities and the real-world constraints of cross-device compatibility, affordability, and minimal power consumption. The central trade-off explored in this thesis lies precisely in navigating the intricate relationship between extending the capabilities of existing devices and ensuring the broad accessibility and utility of these new functionalities.

Even the most innovative technological advancements hold limited value if they fail to bridge the gap to widespread accessibility. Solutions that demand custom firmware support from manufacturers for every device model or necessitate complex, device-specific calibration steps inherently restrict adoption. Such requirements introduce significant barriers, limiting an otherwise promising technology's potential reach and impact. The core criterion for viability dictated that solutions must operate "out of the box " to achieve significant adoption.

This critical criterion heavily influenced the design of the sensor add-ons. For instance, in the development of GlucoScreen, I devised a communication scheme leveraging existing touchscreen event APIs on smartphones. This approach deliberately eschewed any need for special low-level firmware access or elevated permissions. By encoding data transmission directly into binary touch events, I ensured straightforward interpretation by a simple application on the phone. My primary engineering focus, therefore, shifted not to the software interface but to guaranteeing the electrical touch interface's reliable operation across a diverse range of phone models and operating systems. To this end, I designed a touch simulation system using a cascode transistor configuration, providing sufficient electrical isolation to generate touch events across various devices consistently.

Similarly, in WatchLink, the data encoding strategy involved mimicking cardiac signals.

This deliberate choice ensured the modulated data signals would not be inadvertently filtered out by the existing heart signal processing hardware or software within smartwatches. For both GlucoScreen and WatchLink, alternative communication approaches were considered, such as modulating raw capacitance in GlucoScreen or modulating a simpler electrical property without generating an active modulated signal. While these alternatives might have potentially simplified the sensor hardware further, they would have invariably necessitated custom device firmware, manufacturer support, or elaborate calibration procedures for the add-ons to function. Such requirements would have rendered these approaches significantly less practical and, consequently, less viable for overall adoption.

Conversely, the approach in this thesis prioritized building devices with inherent and straightforward compatibility with existing hardware. By focusing on the simplest possible design that could achieve enhanced functionality at low-cost and with high power efficiency, I aimed to maximize the practical utility and ultimate adoption of the systems presented, demonstrating that advanced capabilities can be delivered without compromising accessibility.

Preserving User Familiarity in Hardware Modifications:

When undertaking internal hardware modifications, a core design objective was to introduce new functionalities without significantly altering the device's inherent form or existing functionality. This approach aimed to preserve user familiarity, allowing new features to integrate seamlessly into an existing device. Instead of introducing an entirely new device with a different interaction paradigm, which would necessitate a new learning curve and increase the barrier to adoption, I focused on enhancing the user's existing experience.

The Z-Ring and Z-Band exemplify this philosophy by leveraging interactions that are common in everyday life. Gestures like swiping or tapping, which users are already accustomed to, were incorporated to provide new functionalities. Furthermore, the ability

to hold an object and identify it in the background adds contextual information without requiring a change in user behavior or interaction. This enhances the user experience by providing valuable insights without demanding any behavioral adaptation.

From a manufacturing perspective, this strategic approach offers significant benefits. It not only reduces manufacturing costs and development time but also ensures a smoother transition and continued user comfort with familiar devices and their established interaction paradigms. This approach makes the development process more practical and efficient.

8.2.3 Implementation Insights

Modularity and Adaptability for Versatile Interfaces

The practical implementation of PhoneScreen, WatchLink, Z-Ring, and Z-Band highlighted the critical importance of modular hardware design. The use of flexible PCBs, adjustable probes, and various customizable form factors (strap sensors, case sensors, companion accessories for smartwatches) was fundamental for achieving cross-device compatibility and adaptability to different test strips and wearable contexts. This design strategy enabled the creation of versatile interfaces that can be easily reconfigured for diverse applications.

Machine Learning as an Enabler:

Advanced signal processing and machine learning emerged as essential components for translating raw sensor capabilities into reliable user experiences. Systems succeeded not merely through hardware improvements, but through sophisticated algorithms that could extract meaningful signals from noisy environments, generalize across users and contexts, and adapt to varying conditions without requiring extensive user calibration.

8.2.4 Prototyping Insights

Throughout the entirety of the projects undertaken during this doctoral research, an iterative prototyping methodology was consistently used. This approach proved instrumental in navigating the inherent uncertainties and challenges of novel research and development. The core philosophy underpinning this iterative process is centered on strategically prioritizing the most unknown or challenging aspects of a given problem.

A fundamental insight gained was the critical importance of tackling the highest-risk components first. By isolating and rapidly prototyping these elements, it was possible to empirically test their feasibility and efficacy. This initial validation or invalidation provided immediate feedback loops that guided subsequent development. The principle of “fail fast” was rigorously applied; rather than prematurely investing significant time and resources into a comprehensive, polished solution, the focus was on quickly identifying points of failure or unworkability. This approach accelerated learning and prevented resource misallocation.

The prototyping process was inherently iterative, with each successive prototype building upon the lessons learned from its predecessors. Major challenges identified in earlier iterations were directly addressed and resolved in subsequent versions. It became evident that the very first prototype, almost without exception, would not achieve its intended functionality or performance. This expectation allowed liberation from pursuing initial perfection, particularly regarding aesthetic considerations.

Instead, the early prototyping stages prioritized rapid construction and functional validation, even if the resulting artifacts were bulky or lacked visual refinement. The initial design of these prototypes, however, is always considered a potential path toward practical application or miniaturization, ensuring that fundamental architectural choices are aligned with long-term goals. As key unknowns were progressively resolved and the core solution became clearer, the focus naturally shifted. The latter stages of prototyping involved refining the solution, making the prototypes more compact, efficient, and aesthetically

pleasing, culminating in a robust and presentable outcome. This systematic progression from rapid exploration of unknowns to detailed refinement proved to be a highly effective strategy for complex problem-solving.

8.3 Concluding Remarks

This dissertation demonstrates that by thoughtfully repurposing existing device capabilities and implementing targeted hardware augmentations, we can unlock the full potential of side-channel sensing. The concrete examples of GlucoScreen, PhoneScreen, WatchLink, Z-Ring, and Z-Band highlight the transformative power of these approaches. By combining technical innovation with a deep understanding of user needs and practical constraints, this research paves the way for a future where ubiquitous devices are not merely smart but are seamlessly integrated, context-aware, and actively contribute to human well-being and interaction. This vision moves us closer to a world where interactions seamlessly integrate the digital and physical realms, fostering more accessible, personalized, and intuitive user experiences in daily life.

BIBLIOGRAPHY

[1] Los Angeles Times. https://www.latimes.com/archives/la-xpm-2007-nov-07-fi-lazarus7-story.html, 2007. [Online accessed 12-April-2022].

[2] Glucose oxidase — an overview. Biotechnology Advances, 27(4):489–501, 2009.

[3] Get ready for smartstraps - warm up your 3d printer!, Mar 2015.

[4] Screening for abnormal blood glucose and type 2 diabetes mellitus: U.s. preventive services task force recommendation statement. Annals of Internal Medicine, 163(11):861–868, 2015. PMID: 26501513.

[5] Apple watch charging wristband no longer works after apple closes loophole, Jan 2016.

[6] Clinical Diabetes/Therapeutics. https://doi.org/10.2337/db17-890-1488, 2017. [Online accessed 13-February-2022].

[7] Accu-Chek. https://www.accu-chek.com/test-strips/aviva-plus-test-strips, 2021. [Online accessed 13-February-2022].

[8] Diabetes now affects one in 10 adults worldwide. https://www.idf.org/news/240:diabetes-now-affects-one-in-10-adults-worldwide.html, 2021. [Online accessed 19-March-2022].

[9] Diabetes Tests. https://www.cdc.gov/diabetes/basics/getting-tested.html/, 2021. [Online accessed 13-February-2022].

[10] Prevalence of Prediabetes Among Adults. https://www.cdc.gov/diabetes/data/statistics-report/prevalence-of-prediabetes.html, 2021. [Online accessed 28-March-2022].

[11] Tracking Leap Motion Controller Ultraleap, 2021.

[12] True Metrix. https://www.trividiahealth.com/products/blood-glucose-meters-test-strips/true-metrix/, 2021. [Online accessed 13-February-2022].

[13] Glucose Meter Cost. https://health.costhelper.com/glucose-meter.html/, 2022. [Online accessed 13-February-2022].

[14] Meta Quest 2: Our Most Advanced New All-in-One VR Headset Meta Store, 2022.

[15] Octapart.com. https://octopart.com, 2022. [Online accessed 12-April-2022].

[16] Accu-Chek Guide Me meter. https://www.accu-chek.com/meters/guide-me-meter, 2023. [Online accessed 20-January-2023].

[17] Dario Blood Glucose Monitoring Starter Kit. https://shop.mydario.com/product/dario-blood-glucose-monitoring-starter-kit/, 2023. [Online accessed 20-January-2023].

[18] TRUE METRIX® AIR Self Monitoring Blood Glucose System. https://www.trividiahealth.com/products/blood-glucose-meters-test-strips/true-metrix-air/, 2023. [Online accessed 20-January-2023].

[19] Aura strap 2, Jan 2024.

[20] A. Ahlbom, U. Bergqvist, J. H. Bernhardt, J. P. Cesarini, L. A. Court, M. Grandolfo, M. Hietanen, A. F. McKinlay, M. H. Repacholi, D. H. Sliney, J. A.J. Stolwijk, M. L. Swicord, L. D. Szabo, M. Taki, T. S. Tenforde, H. P. Jammet, and R. Matthes. Guidelines for limiting exposure to time-varying electric, magnetic, and electromagnetic fields (up to 300 GHz). International Commission on Non-Ionizing Radiation Protection. Health physics, 74(4):494–521, 1998.

[21] Karan Ahuja. Practical and rich user digitization, 2024.

[22] Karan Ahuja, Sujeath Pareddy, Robert Xiao, Mayank Goel, and Chris Harrison. Lightanchors: Appropriating point lights for spatially-anchored augmented reality interfaces. In Proceedings of the 32nd Annual ACM Symposium on User Interface Software and Technology, pages 189–196, 2019.

[23] Amazon. Bactrack go keychain breathalyzer. https://www.amazon.com/gp/product/B00LVOU27U, 2024. Accessed: 2024-01-19.

[24] Amazon. Extech uv505 pocket uv-ab light meter. https://www.amazon.com/gp/product/B07DPFK35S, 2024. Accessed: 2024-01-19.

[25] Brian Amento, Will Hill, and Loren Terveen. The sound of one hand: A wrist-mounted bio-acoustic fingertip gesture interface. In CHI '02 Extended Abstracts on Human Factors in Computing Systems, CHI EA '02, page 724–725, New York, NY, USA, 2002. Association for Computing Machinery.

[26] Kecheng An, Qian Zhang, and Elaine Kwong. Viscocam: Smartphone-based drink viscosity control assistant for dysphagia patients. Proc. ACM Interact. Mob. Wearable Ubiquitous Technol., 5(1), mar 2021.

[27] V Andrea and I S Timan. Relationship between diabetes mellitus and blood viscosity as measured by the digital microcapillary® system. Journal of Physics: Conference Series, 1073(4):042046, aug 2018.

[28] Nivedita Arora, Ali Mirzazadeh, Charles Ramey, Yuhui Zhao, Daniela C Rodriguez, Gregory D Abowd, Thad E Starner, and Injoo Moon. MARS: Nano-Power Battery-free Wireless Interfaces for Touch, Swipe and Speech Input; MARS: Nano-Power Battery-free Wireless Interfaces for Touch, Swipe and Speech Input. The 34th Annual ACM Symposium on User Interface Software and Technology, page 21, 2021.

[29] Joan Aymerich, Augusto Márquez, Lluís Terés, Xavier Muñoz-Berbel, Cecilia Jiménez, Carlos Domínguez, Francesc Serra-Graells, and Michele Dei. Cost-effective smartphone-based reconfigurable electrochemical instrument for alcohol determination in whole blood samples. 117:736–742, 2018.

[30] Nur Ain Mohd Aziz, Norhana Arsad, P Susthitha Menon, Abdur Rehman Laili, Muhamad Hafiz Laili, and Amal Asyikin Abdul Halim. Analysis of difference light sources for non-invasive aqueous glucose detection. In 2014 IEEE 5th International Conference on Photonics (ICP), pages 150–152. IEEE, 2014.

[31] Joseph M. Azzarelli, Katherine A. Mirica, Jens B. Ravnsbæk, and Timothy M. Swager. Wireless gas detection with a smartphone via rf communication. 111(51):18162–18166, 2014. Publisher: National Academy of Sciences Section: Physical Sciences.

[32] Sandip B Bankar, Mahesh V Bule, Rekha S Singhal, and Laxmi Ananthanarayan. Glucose oxidase—an overview. Biotechnology advances, 27(4):489–501, 2009.

[33] Jessica Beagley, Leonor Guariguata, Clara Weil, and Ayesha A. Motala. Global estimates of undiagnosed diabetes in adults. Diabetes Research and Clinical Practice, 103(2):150–160, 2014.

[34] Tushar Kanti Bera. Bioelectrical Impedance Methods for Noninvasive Health Monitoring: A Review. Journal of Medical Engineering, 2014:1–28, 6 2014.

[35] Jorge Blasco, Thomas M. Chen, Juan Tapiador, and Pedro Peris-Lopez. A survey of wearable biometric recognition systems. 49(3), sep 2016.

[36] Alan Bränzel, Christian Holz, Daniel Hoffmann, Dominik Schmidt, Marius Knaust, Patrick Lühne, René Meusel, Stephan Richter, and Patrick Baudisch. Gravityspace: tracking users and their poses in a smart room using a pressure-sensing floor. In Proceedings of the SIGCHI Conference on Human Factors in Computing Systems, pages 725–734, 2013.

[37] B. H. Brown, R. H. Smallwood, D. C. Barber, P. V. Lawford, and D. R. Hose. Measurement science and technology. Meas. Sci. Technol., 12(10):1744, 2001.

[38] Thisum Buddhika, Haimo Zhang, Chamod Weerasinghe, Suranga Nanayakkara, and Roger Zimmermann. Osense: Object-activity identification based on gasping posture and motion. In Proceedings of the 10th Augmented Human International Conference 2019, AH2019, New York, NY, USA, 2019. Association for Computing Machinery.

[39] Attaullah Buriro, Bruno Crispo, Filippo Del Frari, and Konrad Wrona. Touchstroke: Smartphone user authentication based on touch-typing biometrics. In New Trends in Image Analysis and Processing–ICIAP 2015 Workshops: ICIAP 2015 International Workshops, BioFor, CTMR, RHEUMA, ISCA, MADiMa, SBMI, and QoEM, Genoa, Italy, September 7-8, 2015, Proceedings 18, pages 27–34. Springer, 2015.

[40] William A.S. Buxton. A three-state model of graphical input. In IFIP TC13 International Conference on Human-Computer Interaction, 1990.

[41] Jared Cechanowicz, Pourang Irani, and Sriram Subramanian. Augmenting the mouse with pressure sensitive input. In Proceedings of the SIGCHI Conference on Human Factors in Computing Systems, CHI '07, page 1385–1394, New York, NY, USA, 2007. Association for Computing Machinery.

[42] Justin Chan, Anandıtha Raghunath, Kelly E Michaelsen, and Shyamnath Gollakota. Testing a drop of liquid using smartphone lidar. Proceedings of the ACM on Interactive, Mobile, Wearable and Ubiquitous Technologies, 6(1):1–27, 2022.

[43] Justin Chan, Anandıtha Raghunath, Kelly E. Michaelsen, and Shyamnath Gollakota. Testing a drop of liquid using smartphone lidar. Proc. ACM Interact. Mob. Wearable Ubiquitous Technol., 6(1), mar 2022.

[44] Liwei Chan, Yi Ling Chen, Chi Hao Hsieh, Rong Hao Liang, and Bing Yu Chen. Cyclopsring: Enabling whole-hand and context-aware interactions through a fisheye ring. UIST 2015 - Proceedings of the 28th Annual ACM Symposium on User Interface Software and Technology, pages 549–556, 11 2015.

[45] Liwei Chan, Stefanie Müller, Anne Roudaut, and Patrick Baudisch. CapStones and ZebraWidgets: sensing stacks of building blocks, dials and sliders on capacitive touch screens. In Proceedings of the SIGCHI Conference on Human Factors in Computing Systems, CHI '12, pages 2189–2192, New York, NY, USA, May 2012. Association for Computing Machinery.

[46] Ishan Chatterjee. TouchPoint: A Wrist-Worn, On-Body Touch Interaction Device. 2016.

[47] Ke-Yu Chen, Gabe A Cohn, Sidhant Gupta, and Shwetak N Patel. utouch: sensing touch gestures on unmodified lcds. In Proceedings of the SIGCHI Conference on Human Factors in Computing Systems, pages 2581–2584, 2013.

[48] Tingyu Cheng, Zhihan Zhang, Bingrui Zong, Yuhui Zhao, Zekun Chang, Yejun Kim, Clement Zheng, Gregory D. Abowd, and HyunJoo Oh. SwellSense: Creating 2.5d interactions with micro-capsule paper. In Proceedings of the 2023 CHI Conference on Human Factors in Computing Systems, CHI '23, pages 1–13. Association for Computing Machinery.

[49] Gabe Cohn, Dan Morris, Shwetak N. Patel, and Desney S. Tan. Your noise is my command: Sensing gestures using the body as an antenna. pages 791–800, 2011.

[50] Gabe Cohn, Dan Morris, Shwetak N. Patel, and Desney S. Tan. Humantenna: Using the Body as an Antenna for Real-Time Whole-Body Interaction. Conference on Human Factors in Computing Systems - Proceedings, pages 1901–1910, 2012.

[51] Gabe Cohn, Erich Stuntebeck, Jagdish Pandey, Brian Otis, Gregory D Abowd, and Shwetak N Patel. Snupi: sensor nodes utilizing powerline infrastructure. In Proceedings of the 12th ACM international conference on Ubiquitous computing, pages 159–168, 2010.

[52] NanoVNA Developers Community. Nanovna: Vector network analyzer. Available online at the NanoVNA official website, 2024. Accessed: 2024-09-08.

[53] Cory Cornelius, Ronald Peterson, Joseph Skinner, Ryan Halter, and David Kotz. A wearable system that knows who wears it. MobiSys 2014 - Proceedings of the 12th Annual International Conference on Mobile Systems, Applications, and Services, pages 55–67, 2014.

[54] Ahmet F. Coskun, Justin Wong, Delaram Khodadadi, Richie Nagi, Andrew Tey, and Aydogan Ozcan. A personalized food allergen testing platform on a cellphone. 13(4):636–640, 2013. Publisher: The Royal Society of Chemistry.

[55] CTRL-labs at Reality Labs, David Sussillo, Patrick Kaifosh, and Thomas Reardon. A generic noninvasive neuromotor interface for human-computer interaction. Pages: 2024.02.23.581779 Section: New Results.

[56] Farzan Dehbashi, Ali Abedi, Tim Brecht, and Omid Abari. Are wifi backscatter systems ready for the real world? GetMobile: Mobile Comp. and Comm., 26(1):30–34, may 2022.

[57] Artem Dementyev, Steve Hodges, Stuart Taylor, and Josh Smith. Power consumption analysis of bluetooth low energy, zigbee, and ant sensor nodes in a cyclic sleep scenario. In Proceedings of IEEE International Wireless Symposium (IWS). IEEE, April 2013.

[58] Paul Dietz and Darren Leigh. DiamondTouch: a multi-user touch technology. In Proceedings of the 14th annual ACM symposium on User interface software and technology, UIST '01, pages 219–226. Association for Computing Machinery.

[59] Paul Dietz and Darren Leigh. Diamondtouch: A multi-user touch technology. In Proceedings of the 14th Annual ACM Symposium on User Interface Software and Technology, UIST '01, page 219–226, New York, NY, USA, 2001. Association for Computing Machinery.

[60] Yuran Ding, Craig Shultz, and Chris Harrison. Surface i/o: Creating devices with functional surface geometry for haptics and user input. In Proceedings of the 2023 CHI Conference on Human Factors in Computing Systems, CHI '23, New York, NY, USA, 2023. Association for Computing Machinery.

[61] Egan H. Doeven, Gregory J. Barbante, Anthony J. Harsant, Paul S. Donnelly, Timothy U. Connell, Conor F. Hogan, and Paul S. Francis. Mobile phone-based electrochemiluminescence sensing exploiting the 'USB on-the-go' protocol. 216:608–613, 2015.

[62] Paolo Donati, Tania Pomili, Luca Boselli, and Pier Pompa. Colorimetric nanoplasmonics to spot hyperglycemia from saliva. Frontiers in Bioengineering and Biotechnology, 8, 12 2020.

[63] I. Dove. Analysis of radio propagation inside the human body for in-body localization purposes, August 2014.

[64] Winncy Y. Du and Winston José. Design of an ecg sensor circuitry for cardiovascular disease diagnosis. Journal of Biosensors and Bioelectronics, 2, 2017.

[65] Amit Kumar Dutta, Sudipto Das, Suvendu Samanta, Partha Kumar Samanta, Bibhutosh Adhikary, and Papu Biswas. Cus nanoparticles as a mimic peroxidase for colorimetric estimation of human blood glucose level. Talanta, 107:361–367, 2013.

[66] Eleshop. LiteVNA User Guide, 2023. Accessed: September 9, 2024.

[67] Joshua F. Ensworth and Matthew S. Reynolds. Ble-backscatter: Ultralow-power iot nodes compatible with bluetooth 4.0 low energy (ble) smartphones and tablets. IEEE Transactions on Microwave Theory and Techniques, 65(9):3360–3368, 2017.

[68] J Eross, D Kreutzmann, M Jimenez, R Keen, S Rogers, C Cowell, R Vines, and M Silink. Colorimetric measurement of glycosylated protein in whole blood, red blood cells, plasma and dried blood. Annals of clinical biochemistry, 21(6):477–483, 1984.

[69] Espressif. Esp32 series. `https://www.espressif.com/en/products/socs/esp32`, 2024. Accessed: 2024-01-19.

[70] Nicholas D. Everett. Instantaneous bandwidth expansion using software defined radios, March 2019. Accessed: 2024-09-08.

[71] Junjun Fan, Xiangmin Fan, Feng Tian, Yang Li, Zitao Liu, Wei Sun, and Hongan Wang. What is that in your hand? recognizing grasped objects via forearm electromyography sensing. Proc. ACM Interact. Mob. Wearable Ubiquitous Technol., 2(4), dec 2018.

[72] Stefano Ferri, Katsuhiro Kojima, and Koji Sode. Review of glucose oxidases and glucose dehydrogenases: A bird's eye view of glucose sensing enzymes. Journal of diabetes science and technology, 5:1068–76, 09 2011.

[73] Masaaki Fukumoto and Yasuhito Suenaga. "FingeRing": A full-time wearable interface. Conference on Human Factors in Computing Systems - Proceedings, 1994-April:81–82, 4 1994.

[74] Robert Gabbay and Surendra Sivarajah. Optical coherence tomography-based continuous noninvasive glucose monitoring in patients with diabetes. Diabetes technology therapeutics, 10:188–93, 07 2008.

[75] S. Gabriel, R. W. Lau, and C. Gabriel. The dielectric properties of biological tissues: II. Measurements in the frequency range 10 Hz to 20 GHz. Physics in Medicine & Biology, 41(11):2251, 11 1996.

[76] Pascal Getreuer, Chet Gnegy, Richard F. Lyon, and Rif A. Saurous. Ultrasonic communication using consumer hardware. IEEE Transactions on Multimedia, 20(6):1277–1290, 2018.

[77] Gabriela F. Giordano, Marcia B. R. Vicentini, Rui C. Murer, Fabio Augusto, Marco F. Ferrão, Gilson A. Helfer, Adilson B. da Costa, Angelo L. Gobbi, Leandro W. Hantao, and Renato S. Lima. Point-of-use electroanalytical platform based on homemade potentiostat and smartphone for multivariate data processing. 219:170–177, 2016.

[78] Tansu Golcez, Volkan Kilic, and Mustafa Sen. A portable smartphone-based platform with an offline image processing tool for rapid paper-based colorimetric detection of glucose in artificial saliva. Analytical Sciences, page 20P262, 2020.

[79] Golf Pad. Faq about golf pad tags. `https://support.golfpadgps.com/support/solutions/articles/6000268290-frequently-asked-questions-about-golf-pad-tags`, 2023. Accessed: 2024-01-19.

[80] Jun Gong, Aakar Gupta, and Hrvoje Benko. Acustico: Surface tap detection and localization using wrist-based acoustic TDOA sensing. In Proceedings of the 33rd Annual ACM Symposium on User Interface Software and Technology, UIST '20, pages 406–419. Association for Computing Machinery.

[81] Jun Gong, Yang Zhang, Xia Zhou, and Xing-Dong Yang. Pyro: Thumb-Tip Gesture Recognition Using Pyroelectric Infrared Sensing. Proceedings of the 30th Annual ACM Symposium on User Interface Software and Technology, 2017.

[82] Tobias Grosse-Puppendahl, Christian Holz, Gabe Cohn, Raphael Wimmer, Oskar Bechtold, Steve Hodges, Matthew S. Reynolds, and Joshua R. Smith. Finding common ground: A survey of capacitive sensing in human-computer interaction. In Proceedings of the 2017 CHI Conference on Human Factors in Computing Systems, CHI '17, page 3293–3315, New York, NY, USA, 2017. Association for Computing Machinery.

[83] Tobias Grosse-Puppendahl, Christian Holz, Gabe Cohn, Raphael Wimmer, Oskar Bechtold, Steve Hodges, Matthew S. Reynolds, and Joshua R. Smith. Finding common ground: A survey of capacitive sensing in human-computer interaction. In Proceedings of the 2017 CHI Conference on Human Factors in Computing Systems,

CHI '17, page 3293–3315, New York, NY, USA, 2017. Association for Computing Machinery.

[84] Changzhan Gu and Jaime Lien. A Two-Tone Radar Sensor for Concurrent Detection of Absolute Distance and Relative Movement for Gesture Sensing. IEEE Sensors Letters, 1(3):1–4, 4 2017.

[85] Yizheng Gu, Chun Yu, Zhipeng Li, Weiqi Li, Shuchang Xu, Xiaoying Wei, and Yuanchun Shi. Accurate and low-latency sensing of touch contact on any surface with finger-worn imu sensor. In Proceedings of the 32nd Annual ACM Symposium on User Interface Software and Technology, UIST '19, page 1059–1070, New York, NY, USA, 2019. Association for Computing Machinery.

[86] Yizheng Gu, Chun Yu, Zhipeng Li, Weiqi Li, Shuchang Xu, Xiaoying Wei, and Yuanchun Shi. Accurate and low-latency sensing of touch contact on any surface with finger-worn imu sensor. In Proceedings of the 32nd Annual ACM Symposium on User Interface Software and Technology, UIST '19, page 1059–1070, New York, NY, USA, 2019. Association for Computing Machinery.

[87] Anhong Guo, Robert Xiao, and Chris Harrison. CapAuth: Identifying and Differentiating User Handprints on Commodity Capacitive Touchscreens. In Proceedings of the 2015 International Conference on Interactive Tabletops & Surfaces, ITS '15, pages 59–62, New York, NY, USA, November 2015. Association for Computing Machinery.

[88] Sidhant Gupta, Daniel Morris, Shwetak Patel, and Desney Tan. Soundwave: using the doppler effect to sense gestures. In Proceedings of the SIGCHI Conference on Human Factors in Computing Systems, pages 1911–1914, 2012.

[89] Sidhant Gupta, Matthew S Reynolds, and Shwetak N Patel. Electrisense: single-point sensing using emi for electrical event detection and classification in the home. In Proceedings of the 12th ACM international conference on Ubiquitous computing, pages 139–148, 2010.

[90] EB Hanlon, R Manoharan, T_W Koo, KE Shafer, JT Motz, M Fitzmaurice, JR Kramer, I Itzkan, RR Dasari, and MS Feld. Prospects for in vivo raman spectroscopy. Physics in Medicine & Biology, 45(2):R1, 2000.

[91] Chris Harrison and Scott E Hudson. Scratch input: creating large, inexpensive, unpowered and mobile finger input surfaces. In Proceedings of the 21st annual ACM symposium on User interface software and technology, pages 205–208, 2008.

[92] Chris Harrison and Scott E Hudson. Scratch input: creating large, inexpensive, unpowered and mobile finger input surfaces. In Proceedings of the 21st annual ACM symposium on User interface software and technology, pages 205–208, 2008.

[93] Chris Harrison, Munehiko Sato, and Ivan Poupyrev. Capacitive fingerprinting. page 537, 2012.

[94] Chris Harrison, Desney Tan, and Dan Morris. Skinput: appropriating the body as an input surface. In Proceedings of the SIGCHI Conference on Human Factors in Computing Systems, CHI '10, pages 453–462. Association for Computing Machinery.

[95] Souvik Hazra and Avik Santra. Robust Gesture Recognition Using Millimetric-Wave Radar System. IEEE Sensors Letters, 2(4):1–4, 11 2018.

[96] Jing He, Gang Xiao, Xiaodie Chen, Yan Qiao, Dan Xu, and Zhisong Lu. A thermoresponsive microfluidic system integrating a shape memory polymer-modified textile and a paper-based colorimetric sensor for the detection of glucose in human sweat. RSC advances, 9(41):23957–23963, 2019.

[97] Adam Heller and Ben Feldman. Electrochemical glucose sensors and their applications in diabetes management. Chemical reviews, 108(7):2482–2505, 2008.

[98] Christian Holz, Senaka Buthpitiya, and Marius Knaust. Bodyprint: Biometric User Identification on Mobile Devices Using the Capacitive Touchscreen to Scan Body Parts. In Proceedings of the 33rd Annual ACM Conference on Human Factors in Computing Systems, CHI '15, pages 3011–3014, New York, NY, USA, April 2015. Association for Computing Machinery.

[99] Christian Holz and Marius Knaust. Biometric touch sensing: Seamlessly augmenting each touch with continuous authentication. UIST 2015 - Proceedings of the 28th Annual ACM Symposium on User Interface Software and Technology, pages 303–312, 11 2015.

[100] Yann Hornych, Javier Cañada Toledo, Boyang Wang, Won-Jae Yi, and Jafar Saniie. Near-ultrasonic communications for iot applications using android smartphone. In 2020 IEEE International Conference on Electro Information Technology (EIT), pages 407–410, 2020.

[101] Yongzhi Huang, Kaixin Chen, Yandao Huang, Lu Wang, and Kaishun Wu. Vi-liquid: Unknown liquid identification with your smartphone vibration. In Proceedings of the 27th Annual International Conference on Mobile Computing and Networking,

MobiCom '21, page 174–187, New York, NY, USA, 2021. Association for Computing Machinery.

[102] Galen Chin-Lun Hung, Pei-Ching Yang, Chia-Chi Chang, Jung-Hsien Chiang, and Ying-Yeh Chen. Predicting negative emotions based on mobile phone usage patterns: an exploratory study. JMIR research protocols, 5(3):e5551, 2016.

[103] Jincy Immanuel and David Simmons. A Perspective on the Accuracy of Blood Glucose Meters During Pregnancy. Diabetes Care, 41(10):2053–2058, 09 2018.

[104] Yasha Iravantchi, Mayank Goel, and Chris Harrison. BeamBand: Hand gesture sensing with ultrasonic beamforming. Conference on Human Factors in Computing Systems - Proceedings, 5 2019.

[105] Yasha Iravantchi, Yi Zhao, Kenrick Kin, and Alanson P Sample. Sawsense: Using surface acoustic waves for surface-bound event recognition. In Proceedings of the 2023 CHI Conference on Human Factors in Computing Systems, pages 1–18, 2023.

[106] Curt B. Irwin and Mary E. Sesto. Performance and touch characteristics of disabled and non-disabled participants during a reciprocal tapping task using touch screen technology. 43(6):1038–1043.

[107] Alexander Refsum Jensenius. Proceedings of the International Conference on New Interfaces for Musical Expression - 30 May - 1 June 2011. page 2, 2011.

[108] Daizong Ji, Lei Liu, Shuang Li, Chen Chen, Yanli Lu, Jiajia Wu, and Qingjun Liu. Smartphone-based cyclic voltammetry system with graphene modified screen printed electrodes for glucose detection. 98:449–456, 2017.

[109] Peiqi Kang, Jinxuan Li, Bingfei Fan, Shuo Jiang, and Peter Shull. Wrist-worn hand gesture recognition while walking via transfer learning. IEEE Journal of Biomedical and Health Informatics, PP:1–1, 07 2021.

[110] Feneli Karachaliou, George Simatos, and Aristofania Simatou. The challenges in the development of diabetes prevention and care models in low-income settings. Frontiers in Endocrinology, 11, 2020.

[111] Petar Kassal, Jayoung Kim, Rajan Kumar, William R. de Araujo, Ivana Murkovi Steinberg, Matthew D. Steinberg, and Joseph Wang. Smart bandage with wireless connectivity for uric acid biosensing as an indicator of wound status. 56:6–10, 2015.

[112] Bryce Kellogg, Aaron Parks, Shyamnath Gollakota, Joshua R. Smith, and David Wetherall. Wi-fi backscatter: internet connectivity for rf-powered devices. In Proceedings of the 2014 ACM Conference on SIGCOMM, SIGCOMM '14, page 607–618, New York, NY, USA, 2014. Association for Computing Machinery.

[113] Bryce Kellogg, Aaron Parks, Shyamnath Gollakota, Joshua R. Smith, and David Wetherall. Wi-fi backscatter: internet connectivity for rf-powered devices. SIGCOMM Comput. Commun. Rev., 44(4):607–618, aug 2014.

[114] Rushil Khurana, Mayank Goel, and Kent Lyons. Detachable smartwatch: more than a wearable. Proceedings of the ACM on Interactive, Mobile, Wearable and Ubiquitous Technologies, 3(2):1–14, 2019.

[115] Wolf Kienzle and Ken Hinckley. Lightring: Always-available 2d input on any surface. In Proceedings of the 27th Annual ACM Symposium on User Interface Software and Technology, UIST '14, page 157–160, New York, NY, USA, 2014. Association for Computing Machinery.

[116] Wolf Kienzle, Eric Whitmire, Chris Rittaler, and Hrvoje Benko. ElectroRing: Subtle pinch and touch detection with a ring. In Proceedings of the 2021 CHI Conference on Human Factors in Computing Systems, CHI '21, pages 1–12. Association for Computing Machinery.

[117] Wolf Kienzle, Eric Whitmire, Chris Rittaler, and Hrvoje Benko. ElectroRing: Subtle Pinch and Touch Detection with a Ring. In Proceedings of the 2021 CHI Conference on Human Factors in Computing Systems, CHI '21, New York, NY, USA, 2021. Association for Computing Machinery.

[118] Daehwa Kim and Chris Harrison. EtherPose: Continuous hand pose tracking with wrist-worn antenna impedance characteristic sensing. In Proceedings of the 35th Annual ACM Symposium on User Interface Software and Technology, UIST '22, pages 1–12. Association for Computing Machinery.

[119] Daehwa Kim and Chris Harrison. Pantœnna: Mouth pose estimation for ar/vr headsets using low-profile antenna and impedance characteristic sensing. In Proceedings of the 36th Annual ACM Symposium on User Interface Software and Technology, UIST '23, pages 1–12. Association for Computing Machinery.

[120] Daehwa Kim and Chris Harrison. Etherpose: Continuous hand pose tracking with wrist-worn antenna impedance characteristic sensing. In Proceedings of the 35th Annual ACM Symposium on User Interface Software and Technology, UIST '22, New York, NY, USA, 2022. Association for Computing Machinery.

[121] Daehwa Kim and Chris Harrison. Pantoenna: Mouth pose estimation for ar/vr headsets using low-profile antenna and impedance characteristic sensing. In Proceedings of the 36th Annual ACM Symposium on User Interface Software and Technology, UIST '23, New York, NY, USA, 2023. Association for Computing Machinery.

[122] Daehwa Kim, Keunwoo Park, and Geehyuk Lee. AtaTouch: Robust Finger Pinch Detection for a VR Controller Using RF Return Loss. Conference on Human Factors in Computing Systems - Proceedings, 5 2021.

[123] Daehwa Kim, Eric Whitmire, Roger Boldu, Wolf Kienzle, and Hrvoje Benko. SoundScroll: Robust finger slide detection using friction sound and wrist-worn microphones. In Proceedings of the 2024 ACM International Symposium on Wearable Computers, ISWC '24. Association for Computing Machinery.

[124] David Kim, Otmar Hilliges, Shahram Izadi, Alex D. Butler, Jiawen Chen, Iason Oikonomidis, and Patrick Olivier. Digits. page 167, 2012.

[125] Jayoung Kim, Somayeh Imani, William R. de Araujo, Julian Warchall, Gabriela Valdés-Ramírez, Thiago R.L.C. Paixão, Patrick P. Mercier, and Joseph Wang. Wearable salivary uric acid mouthguard biosensor with integrated wireless electronics. Biosensors and Bioelectronics, 2015.

[126] Kwangsoo Kim, Mi-Hee Lee, Jungchae Kim, Seok Jung, Sun Jee, and Sun kyung Yoo. Performance evaluation of the electrode configuration in bioelectrical impedance analysis for visceral fat measurement. Conference proceedings : ... Annual International Conference of the IEEE Engineering in Medicine and Biology Society. IEEE Engineering in Medicine and Biology Society. Conference, 2009:892–5, 09 2009.

[127] David Klonoff. Overview of fluorescence glucose sensing: A technology with a bright future. Journal of diabetes science and technology, 6:1242–50, 11 2012.

[128] Jonas Kottmann, Julien M Rey, and Markus W Sigrist. Mid-infrared photoacoustic detection of glucose in human skin: towards non-invasive diagnostics. Sensors, 16(10):1663, 2016.

[129] Sven Kratz, Tilo Westermann, Michael Rohs, and Georg Essl. CapWidgets: tangile widgets versus multi-touch controls on mobile devices. In CHI '11 Extended Abstracts on Human Factors in Computing Systems, CHI EA '11, pages 1351–1356, New York, NY, USA, May 2011. Association for Computing Machinery.

[130] Wakaba Kuno, Yuta Sugiura, Nao Asano, Wataru Kawai, and Maki Sugimoto. 3d reconstruction of hand postures by measuring skin deformation on back hand. In Proceedings of the 27th International Conference on Artificial Reality and Telexistence and 22nd Eurographics Symposium on Virtual Environments, ICAT-EGVE '17, page 221–228, Goslar, DEU, 2017. Eurographics Association.

[131] Alexander Kyu, Hongyu Mao, Junyi Zhu, Mayank Goel, and Karan Ahuja. EITPose: Wearable and practical electrical impedance tomography for continuous hand pose estimation. In Proceedings of the CHI Conference on Human Factors in Computing Systems, CHI '24, pages 1–10. Association for Computing Machinery.

[132] Tassaneewan Laksanasopin, Tiffany W. Guo, Samiksha Nayak, Archana A. Sridhara, Shi Xie, Owolabi O. Olowookere, Paolo Cadinu, Fanxing Meng, Natalie H. Chee, Jiyoon Kim, Curtis D. Chin, Elisaphane Munyazesa, Placidie Mugwaneza, Alex J. Rai, Veronicah Mugisha, Arnold R. Castro, David Steinmiller, Vincent Linder, Jessica E. Justman, Sabin Nsanzimana, and Samuel K. Sia. A smartphone dongle for diagnosis of infectious diseases at the point of care. 7(273):273re1–273re1, 2015. Publisher: American Association for the Advancement of Science Section: Reports.

[133] Gierad Laput, Eric Brockmeyer, Scott E Hudson, and Chris Harrison. Acoustruments: Passive, acoustically-driven, interactive controls for handheld devices. In Proceedings of the 33rd Annual ACM Conference on Human Factors in Computing Systems, pages 2161–2170, 2015.

[134] Gierad Laput, Robert Xiao, and Chris Harrison. ViBand: High-fidelity bio-acoustic sensing using commodity smartwatch accelerometers. In Proceedings of the 29th Annual Symposium on User Interface Software and Technology, UIST '16, pages 321–333. Association for Computing Machinery.

[135] Gierad Laput, Robert Xiao, and Chris Harrison. Viband: High-fidelity bio-acoustic sensing using commodity smartwatch accelerometers. In Proceedings of the 29th Annual Symposium on User Interface Software and Technology, UIST '16, page 321–333, New York, NY, USA, 2016. Association for Computing Machinery.

[136] Gierad Laput, Chouchang Yang, Robert Xiao, Alanson Sample, and Chris Harrison. Em-sense: Touch recognition of uninstrumented, electrical and electromechanical objects. In Proceedings of the 28th Annual ACM Symposium on User Interface Software & Technology, pages 157–166, 2015.

[137] Gierad Laput, Chouchang Yang, Robert Xiao, Alanson Sample, and Chris Harrison. Em-sense: Touch recognition of uninstrumented, electrical and electromechanical

objects. In Proceedings of the 28th Annual ACM Symposium on User Interface Software & Technology, UIST '15, page 157–166, New York, NY, USA, 2015. Association for Computing Machinery.

[138] Eric Larson, Gabe Cohn, Sidhant Gupta, Xiaofeng Ren, Beverly Harrison, Dieter Fox, and Shwetak Patel. HeatWave: thermal imaging for surface user interaction. In Proceedings of the SIGCHI Conference on Human Factors in Computing Systems, CHI '11, pages 2565–2574. Association for Computing Machinery.

[139] Seoho Lee, Vlad Oncescu, Matt Mancuso, Saurabh Mehta, and David Erickson. A smartphone platform for the quantification of vitamin d levels. 14(8):1437–1442, 2014. Publisher: The Royal Society of Chemistry.

[140] Hanchuan Li, Eric Brockmeyer, Elizabeth J Carter, Josh Fromm, Scott E Hudson, Shwetak N Patel, and Alanson Sample. Paperid: A technique for drawing functional battery-free wireless interfaces on paper. In Proceedings of the 2016 CHI Conference on Human Factors in Computing Systems, pages 5885–5896, 2016.

[141] Hanchuan Li, Eric Brockmeyer, Elizabeth J Carter, Josh Fromm, Scott E Hudson, Shwetak N Patel, and Alanson Sample. Paperid: A technique for drawing functional battery-free wireless interfaces on paper. In Proceedings of the 2016 CHI Conference on Human Factors in Computing Systems, pages 5885–5896, 2016.

[142] Hanchuan Li, Can Ye, and Alanson P. Sample. IDSense: A human object interaction detection system based on passive UHF RFID. Conference on Human Factors in Computing Systems - Proceedings, 2015-April:2555–2564, 4 2015.

[143] Ziheng Li, Zhenyuan Lei, An Yan, Erin Solovey, and Kaveh Pahlavan. ThuMouse: A micro-gesture cursor input through mmWave radar-based interaction. Digest of Technical Papers - IEEE International Conference on Consumer Electronics, 2020-January, 1 2020.

[144] Chen Liang, Chun Yu, Yue Qin, Yuntao Wang, and Yuanchun Shi. DualRing. Proceedings of the ACM on Interactive, Mobile, Wearable and Ubiquitous Technologies, 5(3):27, 9 2021.

[145] Rong-Hao Liang, Shun-Yao Yang, and Bing-Yu Chen. Indexmo: Exploring finger-worn rfid motion tracking for activity recognition on tagged objects. In Proceedings of the 23rd International Symposium on Wearable Computers, ISWC '19, page 129–134, New York, NY, USA, 2019. Association for Computing Machinery.

[146] Jaime Lien, Nicholas Gillian, M. Emre Karagozler, Patrick Amihood, Carsten Schwesig, Erik Olson, Hakim Raja, and Ivan Poupyrev. Soli: Ubiquitous gesture sensing with millimeter wave radar. ACM Transactions on Graphics (TOG), 35(4), 7 2016.

[147] Ligo George. Fm generation using 555 timer. `https://electrosome.com/fm-generation-using-555-timer/`, 2013. Accessed: 2024-01-19.

[148] Peter B. Lillehoj, Ming-Chun Huang, Newton Truong, and Chih-Ming Ho. Rapid electrochemical detection on a mobile phone. 13(15):2950–2955, 2013. Publisher: The Royal Society of Chemistry.

[149] Jhe Wei Lin, Chiuan Wang, Yi Yao Huang, Kuan Ting Chou, Hsuan Yu Chen, Wei Luan Tseng, and Mike Y. Chen. BackHand: Sensing hand gestures via back of the hand. UIST 2015 - Proceedings of the 28th Annual ACM Symposium on User Interface Software and Technology, pages 557–564, 11 2015.

[150] Robert W. Lindeman, John L. Sibert, and James K. Hahn. Towards usable VR: an empirical study of user interfaces for immersive virtual environments. In Proceedings of the SIGCHI conference on Human Factors in Computing Systems, CHI '99, pages 64–71. Association for Computing Machinery.

[151] Vincent Liu, Aaron Parks, Vamsi Talla, Shyamnath Gollakota, David Wetherall, and Joshua R Smith. Ambient backscatter: Wireless communication out of thin air. ACM SIGCOMM computer communication review, 43(4):39–50, 2013.

[152] Yilin Liu, Shijia Zhang, and Mahanth Gowda. NeuroPose: 3d hand pose tracking using EMG wearables. In Proceedings of the Web Conference 2021, WWW '21, pages 1471–1482. Association for Computing Machinery.

[153] Christian Loclair, Sean Gustafson, and Patrick Baudisch. Pinchwatch: a wearable device for one-handed microinteractions. In Proc. MobileHCI, volume 10. Citeseer, 2010.

[154] Xiaoxuan Lou, Tianwei Zhang, Jun Jiang, and Yinqian Zhang. A survey of microarchitectural side-channel vulnerabilities, attacks, and defenses in cryptography. ACM Computing Surveys (CSUR), 54(6):1–37, 2021.

[155] Susann K. J. Ludwig, Christian Tokarski, Stefan N. Lang, Leendert A. van Ginkel, Hongying Zhu, Aydogan Ozcan, and Michel W. F. Nielen. Calling biomarkers in milk using a protein microarray on your smartphone. 10(8):e0134360, 2015. Publisher: Public Library of Science.

[156] Takuya Maekawa, Yasue Kishino, Yutaka Yanagisawa, and Yasushi Sakurai. Recognizing handheld electrical device usage with hand-worn coil of wire. In Proceedings of the 10th International Conference on Pervasive Computing, Pervasive'12, page 234–252, Berlin, Heidelberg, 2012. Springer-Verlag.

[157] S. Mansouri, Yousef Alharbi, Fatma Haddad, Souhir Chabcoub, Anwar Alshrouf, and Amr A. Abd-Elghany. Electrical impedance tomography – recent applications and developments. Journal of Electrical Bioimpedance, 2021.

[158] Ørjan G. Martinsen and Arto Heiskanen. Bioimpedance and Bioelectricity Basics, Fourth Edition. Elsevier, United Kingdom, 4th edition, 2023.

[159] Jess McIntosh, Asier Marzo Ultrasonics, and Mike Fraser. SensIR: Detecting Hand Gestures with a Wearable Bracelet using Infrared Transmission and Reflection. Proceedings of the 30th Annual ACM Symposium on User Interface Software and Technology, 2017.

[160] Roger J McNichols and Gerard L Cote. Optical glucose sensing in biological fluids: an overview. Journal of biomedical optics, 5(1):5–16, 2000.

[161] Manuel Meier, Paul Streli, Andreas Fender, and Christian Holz. Tapid: Rapid touch interaction in virtual reality using wearable sensing. In 2021 IEEE Virtual Reality and 3D User Interfaces (VR), pages 519–528, 2021.

[162] Manuel Meier, Paul Streli, Andreas Fender, and Christian Holz. TapID: Rapid touch interaction in virtual reality using wearable sensing. Proceedings - 2021 IEEE Conference on Virtual Reality and 3D User Interfaces, VR 2021, pages 519–528, 3 2021.

[163] Öykü Berfin Mercan, Volkan Kılıç, and Mustafa Sen. Machine learning-based colorimetric determination of glucose in artificial saliva with different reagents using a smartphone coupled μpad. Sensors and Actuators B: Chemical, 329:129037, 2021.

[164] Microsoft. Hand tracking - mrtk 2, 2022.

[165] Yoshihiro Minagawa, Hiroshi Ueno, Kazuhito V. Tabata, and Hiroyuki Noji. Mobile imaging platform for digital influenza virus counting. 19(16):2678–2687, 2019. Publisher: The Royal Society of Chemistry.

[166] Anoop Misra, Hema Gopalan, Ranil Jayawardena, Andrew P. Hills, Mario Soares, Alfredo A. Reza-Albarrán, and Kaushik L. Ramaiya. Diabetes in developing countries. Journal of Diabetes, 11(7):522–539, 2019.

[167] Martina Montagnana, Marco Caputo, Davide Giavarina, and Giuseppe Lippi. Overview on self-monitoring of blood glucose. Clinica Chimica Acta, 402(1):7–13, 2009.

[168] Adiyan Mujibiya, Xiang Cao, Desney S Tan, Dan Morris, Shwetak N Patel, and Jun Rekimoto. The Sound of Touch: On-body Touch and Gesture Sensing Based on Transdermal Ultrasound Propagation. Proceedings of the 2013 ACM international conference on Interactive tabletops and surfaces, 2013.

[169] Alex Nemiroski, Dionysios C. Christodouleas, Jonathan W. Hennek, Ashok A. Kumar, E. Jane Maxwell, Maria Teresa Fernández-Abedul, and George M. Whitesides. Universal mobile electrochemical detector designed for use in resource-limited applications. Proceedings of the National Academy of Sciences, 111(33):11984–11989, 2014.

[170] Alex Nemiroski, Dionysios C. Christodouleas, Jonathan W. Hennek, Ashok A. Kumar, E. Jane Maxwell, Maria Teresa Fernández-Abedul, and George M. Whitesides. Universal mobile electrochemical detector designed for use in resource-limited applications. 111(33):11984–11989, 2014. Publisher: National Academy of Sciences Section: Physical Sciences.

[171] Takehiro Niikura, Yoshihiro Watanabe, and Masatoshi Ishikawa. Anywhere surface touch: utilizing any surface as an input area. In Proceedings of the 5th Augmented Human International Conference, AH '14, pages 1–8. Association for Computing Machinery.

[172] Nordic Semiconductors. Bluetooth low energy and 2.4 ghz soc. `https://www.nordicsemi.com/products/nrf51822`, 2023. Accessed: 2024-01-19.

[173] Nymi. Zero-Trust Made Practical for the Modern Workforce. Technical report, Nymi, Inc., 08 2022.

[174] Seungjae Oh, Gyeore Yun, Chaeyong Park, Jinsoo Kim, and Seungmoon Choi. Vibeye: Vibration-mediated object recognition for tangible interactive applications. In Proceedings of the 2019 CHI Conference on Human Factors in Computing Systems, CHI '19, page 1–12, New York, NY, USA, 2019. Association for Computing Machinery.

[175] Vlad Oncescu, Matthew Mancuso, and David Erickson. Cholesterol testing on a smartphone. 14(4):759–763, 2014. Publisher: The Royal Society of Chemistry.

[176] Ivan Poupyrev, Chris Harrison, and Munehiko Sato. Touché: touch and gesture sensing for the real world. In Proceedings of the 2012 ACM Conference on Ubiquitous Computing, page 536, 2012.

[177] Swadhin Pradhan, Eugene Chai, Karthikeyan Sundaresan, Lili Qiu, Mohammad A. Khojastepour, and Sampath Rangarajan. RIO: A pervasive RFID-based touch gesture interface. Proceedings of the Annual International Conference on Mobile Computing and Networking, MOBICOM, Part F131210:261–274, 10 2017.

[178] AB Pravdin, VA Spivak, and DA Yakovlev. On the possibility of noninvasive polarimetric determination of glucose content in skin. Optics and Spectroscopy, 120(1):45–49, 2016.

[179] Christopher P Price. Point-of-care testing in diabetes mellitus. 2003.

[180] Georgeanne Purvinis, Brent D Cameron, and Douglas M Altrogge. Noninvasive polarimetric-based glucose monitoring: an in vivo study. Journal of diabetes science and technology, 5(2):380–387, 2011.

[181] Shiyu Qian, Yu Cui, Zheng Cai, and Lingling Li. Applications of smartphone-based colorimetric biosensors. Biosensors and Bioelectronics: X, 11:100173, 2022.

[182] Qorvo. Dw1000. `https://www.qorvo.com/products/p/DW1000`, 2023. Accessed: 2024-01-19.

[183] Vaishnavi Ranganathan, Sidhant Gupta, Jonathan Lester, Joshua R. Smith, and Desney Tan. Rf bandaid: A fully-analog and passive wireless interface for wearable sensors. Proc. ACM Interact. Mob. Wearable Ubiquitous Technol., 2(2), jul 2018.

[184] Mathieu Renauld, François-Xavier Standaert, Nicolas Veyrat-Charvillon, Dina Kamel, and Denis Flandre. A formal study of power variability issues and side-channel attacks for nanoscale devices. In Advances in Cryptology–EUROCRYPT 2011: 30th Annual International Conference on the Theory and Applications of Cryptographic Techniques, Tallinn, Estonia, May 15-19, 2011. Proceedings 30, pages 109–128. Springer, 2011.

[185] Simon Rogers, John Williamson, Craig Stewart, and Roderick Murray-Smith. AnglePose: robust, precise capacitive touch tracking via 3d orientation estimation. In Proceedings of the SIGCHI Conference on Human Factors in Computing Systems, CHI '11, pages 2575–2584, New York, NY, USA, May 2011. Association for Computing Machinery.

[186] Joseph Roth, Xiaoming Liu, and Dimitris Metaxas. On continuous user authentication via typing behavior. IEEE Transactions on Image Processing, 23(10):4611–4624, 2014.

[187] Julius Cosmo Romeo Rudolph, David Holman, Bruno De Araujo, Ricardo Jota, Daniel Wigdor, and Valkyrie Savage. Sensing hand interactions with everyday objects by profiling wrist topography. In Sixteenth International Conference on Tangible, Embedded, and Embodied Interaction, TEI '22, New York, NY, USA, 2022. Association for Computing Machinery.

[188] Sergio Rueda Linares, David Martin Garcia, Sen Yan, Vladimir Volski, and Guy AE Vandenbosch. The hantenna: experimental assessment of the human hand as an antenna. IET Microwaves, Antennas & Propagation, 12(5):773–778, 2018.

[189] T. Scott Saponas, Desney S. Tan, Dan Morris, Ravin Balakrishnan, Jim Turner, and James A. Landay. Enabling always-available input with muscle-computer interfaces. In Proceedings of the 22nd annual ACM symposium on User interface software and technology, UIST '09, pages 167–176. Association for Computing Machinery.

[190] Munehiko Sato, Ivan Poupyrev, and Chris Harrison. Touché: enhancing touch interaction on humans, screens, liquids, and everyday objects. In Proceedings of the SIGCHI Conference on Human Factors in Computing Systems, pages 483–492. ACM.

[191] Munehiko Sato, Rohan S. Puri, Alex Olwal, Yosuke Ushigome, Lukas Franciszkiewicz, Deepak Chandra, Ivan Poupyrev, and Ramesh Raskar. Zensei: Embedded, multi-electrode bioimpedance sensing for implicit, ubiquitous user recognition. Conference on Human Factors in Computing Systems - Proceedings, 2017-May:3972–3985, 5 2017.

[192] S. A. Schelkunoff. Theory of Antennas of Arbitrary Size and Shape. Proceedings of the IRE, 29(9):493–521, 1941.

[193] Martin Schmitz, Martin Herbers, Niloofar Dezfuli, Sebastian Günther, and Max Mühlhäuser. Off-Line Sensing: Memorizing Interactions in Passive 3D-Printed Objects. In Proceedings of the 2018 CHI Conference on Human Factors in Computing Systems, CHI '18, pages 1–8, New York, NY, USA, April 2018. Association for Computing Machinery.

[194] Martin Schmitz, Jürgen Steimle, Jochen Huber, Niloofar Dezfuli, and Max Mühlhäuser. Flexibles: Deformation-Aware 3D-Printed Tangibles for Capacitive Touchscreens. In Proceedings of the 2017 CHI Conference on Human Factors in

Computing Systems, CHI '17, pages 1001–1014, New York, NY, USA, May 2017. Association for Computing Machinery.

[195] Nordic Semiconductor. nrf52832 product specification v1.4. Technical report, Nordic Semiconductor, 2017.

[196] Jin Keun Seo and Eung Je Woo. Electrical tissue property imaging at low frequency using mreit. IEEE Transactions on Biomedical Engineering, 61(5):1390–1399, 2014.

[197] Jingwei Shao, Manman Lin, Yongqing Li, Xue Li, Junxian Liu, Jianpin Liang, and Huilu Yao. In vivo blood glucose quantification using raman spectroscopy. PloS one, 7(10):e48127, 2012.

[198] Huanhuan Shi, Yu Cao, Yining Zeng, Yanuo Zhou, Weihua Wen, Congxuan Zhang, Yali Zhao, and Zhen Chen. Wearable tesla valve-based sweat collection device for sweat colorimetric analysis. Talanta, 240:123208, 2022.

[199] Yilei Shi, Haimo Zhang, Kaixing Zhao, Jiashuo Cao, Mengmeng Sun, and Suranga Nanayakkara. Ready, steady, touch! sensing physical contact with a finger-mounted IMU. 4(2):59:1–59:25.

[200] Simulia. Biological Data, 2020.

[201] Chapa Sirithunge, Huijiang Wang, and Fumiya Iida. Soft touchless sensors and touchless sensing for soft robots. Frontiers in Robotics and AI, 11, 2024.

[202] Milton W Slein. D-glucose: Determination with hexokinase and glucose-6-phosphate dehydrogenase. In Methods of enzymatic analysis, pages 117–130. Elsevier, 1965.

[203] Andrew Spielberg, Alanson Sample, Scott E. Hudson, Jennifer Mankoff, and James McCann. RapID: A framework for fabricating low-latency interactive objects with RFID tags. Conference on Human Factors in Computing Systems - Proceedings, pages 5897–5908, 5 2016.

[204] Alexander Stahn, Elmarie Terblanche, and Hanns-Christian Gunga. Use of Bioelectrical Impedance: General Principles and Overview, pages 49–90. Springer New York, New York, NY, 2012.

[205] Craig Stewart, Michael Rohs, Sven Kratz, and Georg Essl. Characteristics of pressure-based input for mobile devices. In Proceedings of the SIGCHI Conference on Human Factors in Computing Systems, CHI '10, page 801–810, New York, NY, USA, 2010. Association for Computing Machinery.

[206] A. Sun, T. Wambach, A. G. Venkatesh, and D. A. Hall. A low-cost smartphone-based electrochemical biosensor for point-of-care diagnostics. In 2014 IEEE Biomedical Circuits and Systems Conference (BioCAS) Proceedings, pages 312–315, 2014. ISSN: 2163-4025.

[207] Alexander C. Sun, Chengyang Yao, Venkatesh A.g., and Drew A. Hall. An efficient power harvesting mobile phone-based electrochemical biosensor for point-of-care health monitoring. 235:126–135, 2016.

[208] Wen-Shing Sun, Chih-Hsuan Tsuei, and Yi-Han Huang. Simulating the illuminance and efficiency of the leds used in general household lighting. Physics Procedia, 19:244–248, 12 2011.

[209] Aditya Sundararajan, Arif I. Sarwat, and Alexander Pons. A survey on modality characteristics, performance evaluation metrics, and security for traditional and wearable biometric systems. ACM Comput. Surv., 52(2), may 2019.

[210] SV3ORA. A low frequency circulator/isolator for lab measurements and signal routing by SV3ora.

[211] Dassault Systemes. Cst studio suite, 2022.

[212] Adam G Tabák, Christian Herder, Wolfgang Rathmann, Eric J Brunner, and Mika Kivimäki. Prediabetes: a high-risk state for diabetes development. The Lancet, 379(9833):2279–2290, 2012.

[213] Ryosuke Takada, Buntarou Shizuki, and Junichiro Kadomoto. A sensing technique for data glove using conductive fiber. Conference on Human Factors in Computing Systems - Proceedings, 5 2019.

[214] Liu Tang, Shwu Jen Chang, Ching-Jung Chen, and Jen-Tsai Liu. Non-invasive blood glucose monitoring technology: a review. Sensors, 20(23):6925, 2020.

[215] Keysight Technologies. E4991b impedance analyzer, 1 mhz - 500 mhz, 1 ghz, 3 ghz, 2024. Accessed: 2024-09-08.

[216] Larisa Tereshchenko and Mark Josephson. Frequency content and characteristics of ventricular conduction. Journal of electrocardiology, 48, 09 2015.

[217] Texas Instruments. Relaxation oscillator circuit. `https://www.ti.com/lit/ab/snoa998/snoa998.pdf`, 2023. Accessed: 2024-01-19.

[218] Darshana Thomas, Edward Wilkie, and James Irvine. Comparison of power consumption of wifi inbuilt internet of things device with bluetooth low energy. International Journal of Computer and Information Engineering, 10(10):1856–1859, 2016.

[219] Valérian Turbé, Eleanor R. Gray, Victoria E. Lawson, Eleni Nastouli, Jennifer C. Brookes, Robin A. Weiss, Deenan Pillay, Vincent C. Emery, C. Theo Verrips, Hiromi Yatsuda, Dale Athey, and Rachel A. McKendry. Towards an ultra-rapid smartphone-connected test for infectious diseases. 7(1):11971, 2017. Number: 1 Publisher: Nature Publishing Group.

[220] S. Uma and M.K. Shobana. Metal oxide semiconductor gas sensors in clinical diagnosis and environmental monitoring. Sensors and Actuators A: Physical, 349:114044, 2023.

[221] Muhammad Usman, Shani Thapa, Adarsh K. Gupta, and Wei Xue. Ring Based Wearable Bioelectrical Impedance Analyzer for Body Fat Estimation. 2018 IEEE International Symposium on Signal Processing and Information Technology, ISSPIT 2018, pages 291–296, 2 2019.

[222] Aleksandar Višnjic, Vladica Velickovic, Dušan Sokolovic, Miodrag Stankovic, Kristijan Mijatovic, Miodrag Stojanovic, Zoran Miloševic, and Olivera Radulovic. Relationship between the manner of mobile phone use and depression, anxiety, and stress in university students. International journal of environmental research and public health, 15(4):697, 2018.

[223] Simon Voelker, Christian Cherek, Jan Thar, Thorsten Karrer, Christian Thoresen, Kjell Ivar Øvergård, and Jan Borchers. PERCs: Persistently Trackable Tangibles on Capacitive Multi-Touch Displays. In Proceedings of the 28th Annual ACM Symposium on User Interface Software & Technology, UIST '15, pages 351–356, New York, NY, USA, November 2015. Association for Computing Machinery.

[224] Tam Vu, Akash Baid, Simon Gao, Marco Gruteser, Richard Howard, Janne Lindqvist, Predrag Spasojevic, and Jeffrey Walling. Distinguishing users with capacitive touch communication. In Proceedings of the 18th Annual International Conference on Mobile Computing and Networking, Mobicom '12, page 197–208, New York, NY, USA, 2012. Association for Computing Machinery.

[225] Anandghan Waghmare, Youssef Ben Taleb, Ishan Chatterjee, Arjun Narendra, and Shwetak Patel. Z-ring: Single-point bio-impedance sensing for gesture, touch, object and user recognition. In Proceedings of the 2023 CHI Conference on Human

Factors in Computing Systems, CHI '23, New York, NY, USA, 2023. Association for Computing Machinery.

[226] Anandghan Waghmare, Ishan Chatterjee, and Shwetak Patel. Z-pose: Continuous 3d hand pose tracking using single-point bio-impedance sensing on a ring. In Proceedings of the 2nd Workshop on Smart Wearable Systems and Applications, pages 1–6, 2023.

[227] Anandghan Waghmare, Farshid Salemi Parizi, Jason Hoffman, Yuntao Wang, Matthew Thompson, and Shwetak Patel. Glucoscreen: A smartphone-based readerless glucose test strip for prediabetes screening. Proceedings of the ACM on Interactive, Mobile, Wearable and Ubiquitous Technologies, 7(1):1–20, 2023.

[228] Anandghan Waghmare, Qiuyue Xue, Dingtian Zhang, Yuhui Zhao, Shivan Mittal, Nivedita Arora, Ceara Byrne, Thad Starner, and Gregory D Abowd. Ubiquitouch: Self sustaining ubiquitous touch interfaces. Proceedings of the ACM on Interactive, Mobile, Wearable and Ubiquitous Technologies, 4(1):1–22, 2020.

[229] Anandghan Waghmare, Qiuyue Xue, Dingtian Zhang, Yuhui Zhao, Shivan Mittal, Nivedita Arora, Ceara Byrne, Thad Starner, and Gregory D Abowd. UbiquiTouch: Self sustaining ubiquitous touch interfaces. Proceedings of the ACM on Interactive, Mobile, Wearable and Ubiquitous Technologies, 4(1):1–22, 2020.

[230] N Wahba, S Hanna, and MM El-Sadr. A simple colorimetric method for determining blood glucose. Analyst, 81(964):430–432, 1956.

[231] Edward Jay Wang, Jake Garrison, Eric Whitmire, Mayank Goel, and Shwetak Patel. Carpacio: Repurposing capacitive sensors to distinguish driver and passenger touches on in-vehicle screens. UIST 2017 - Proceedings of the 30th Annual ACM Symposium on User Interface Software and Technology, pages 49–55, 10 2017.

[232] Nana Wang, Jianwei Niu, Xuefeng Liu, Dongqin Yu, Guogang Zhu, Xinghao Wu, Mingliang Xu, and Hao Su. BeyondVision: An EMG-driven micro hand gesture recognition based on dynamic segmentation. volume 7, pages 6044–6052. ISSN: 1045-0823.

[233] Rui Wang, Weichen Wang, Alex DaSilva, Jeremy F Huckins, William M Kelley, Todd F Heatherton, and Andrew T Campbell. Tracking depression dynamics in college students using mobile phone and wearable sensing. Proceedings of the ACM on Interactive, Mobile, Wearable and Ubiquitous Technologies, 2(1):1–26, 2018.

[234] Saiwen Wang, Jie Song, Jaime Lien, Ivan Poupyrev, and Otmar Hilliges. Interacting with soli: Exploring fine-grained dynamic gesture recognition in the radio-frequency spectrum. In Proceedings of the 29th Annual Symposium on User Interface Software and Technology, pages 851–860, 2016.

[235] Wei Wang, Alex X Liu, and Ke Sun. Device-free gesture tracking using acoustic signals. In Proceedings of the 22nd Annual International Conference on Mobile Computing and Networking, pages 82–94, 2016.

[236] Xinhao Wang, Manas Ranjan Gartia, Jing Jiang, Te-Wei Chang, Junle Qian, Yong Liu, Xiangrong Liu, and Gang Logan Liu. Audio jack based miniaturized mobile phone electrochemical sensing platform. 209:677–685, 2015.

[237] Yuntao Wang, Chun Yu, Lin Du, Jin Huang, and Yuanchun Shi. BodyRC: Exploring interaction modalities using human body as lossy signal transmission medium. In Proceedings of the 2014 IEEE 11th Intl Conf on Ubiquitous Intelligence and Computing and 2014 IEEE 11th Intl Conf on Autonomic and Trusted Computing and 2014 IEEE 14th Intl Conf on Scalable Computing and Communications and Its Associated Workshops (UIC-ATC-ScalCom), UIC-ATC-SCALCOM '14, pages 260–267. IEEE Computer Society.

[238] Yuntao Wang, Chun Yu, Lin Du, Jin Huang, and Yuanchun Shi. Bodyrc: Exploring interaction modalities using human body as lossy signal transmission medium. In 2014 IEEE 11th Intl Conf on Ubiquitous Intelligence and Computing and 2014 IEEE 11th Intl Conf on Autonomic and Trusted Computing and 2014 IEEE 14th Intl Conf on Scalable Computing and Communications and Its Associated Workshops, pages 260–267, Dec 2014.

[239] Yuntao Wang, Jianyu Zhou, Hanchuan Li, Tengxiang Zhang, Minxuan Gao, Zhuolin Cheng, Chun Yu, Shwetak Patel, and Yuanchun Shi. FlexTouch: Enabling Large-Scale Interaction Sensing Beyond Touchscreens Using Flexible and Conductive Materials. Proceedings of the ACM on Interactive, Mobile, Wearable and Ubiquitous Technologies, 3(3):109:1–109:20, September 2019.

[240] H.A. Wheeler. Formulas for the skin effect. Proceedings of the IRE, 30(9):412–424, 1942.

[241] Mathias Wilhelm, Daniel Krakowczyk, and Sahin Albayrak. Perisense: Ring-based multi-finger gesture interaction utilizing capacitive proximity sensing. Sensors, 20(14), 2020.

[242] Mathias Wilhelm, Daniel Krakowczyk, Frank Trollmann, and Sahin Albayrak. eRing: Multiple finger gesture recognition with one ring using an electric field. ACM International Conference Proceeding Series, 25-26-June-2015, 6 2015.

[243] World Health Organization. Radiation: Ultraviolet (uv). https://www.who.int/news-room/questions-and-answers/item/radiation-ultraviolet-(uv), 2023. Accessed: 2024-01-19.

[244] Robert Xiao, Scott Hudson, and Chris Harrison. DIRECT: Making touch tracking on ordinary surfaces practical with hybrid depth-infrared sensing. In Proceedings of the 2016 ACM International Conference on Interactive Surfaces and Spaces, ISS '16, pages 85–94. Association for Computing Machinery.

[245] XMINNOV. The nfc function of apple watch. https://www.rfidtagworld.com/news/nfc-tags-apple-watch.html, 2023. Accessed: 2024-01-19.

[246] Gang Xu, Chen Cheng, Wei Yuan, Zhaoyang Liu, Lihang Zhu, Xintong Li, Yanli Lu, Zetao Chen, Jinglong Liu, Zheng Cui, Jingjing Liu, Hong Men, and Qingjun Liu. Smartphone-based battery-free and flexible electrochemical patch for calcium and chloride ions detections in biofluids. 297:126743, 2019.

[247] Jackie Yang and James A Landay. Infoled: Augmenting led indicator lights for device positioning and communication. In Proceedings of the 32nd Annual ACM Symposium on User Interface Software and Technology, pages 175–187, 2019.

[248] Xing-Dong Yang, Tovi Grossman, Daniel Wigdor, and George Fitzmaurice. Magic Finger: Always-Available Input through Finger Instrumentation. Proceedings of the 25th annual ACM symposium on User interface software and technology, 2012.

[249] Xing-Dong Yang, Tovi Grossman, Daniel Wigdor, and George Fitzmaurice. Magic finger: always-available input through finger instrumentation. In Proceedings of the 25th annual ACM symposium on User interface software and technology, pages 147–156, 2012.

[250] Eun-Hyung Yoo and Soo-Youn Lee. Glucose biosensors: An overview of use in clinical practice. Sensors, 10(5):4558–4576, 2010.

[251] Shichao Yue and Dina Katabi. Liquid testing with your smartphone. In Proceedings of the 17th Annual International Conference on Mobile Systems, Applications, and Services, pages 275–286, 2019.

[252] Shichao Yue and Dina Katabi. Liquid testing with your smartphone. In Proceedings of the 17th Annual International Conference on Mobile Systems, Applications, and Services, MobiSys '19, page 275–286, New York, NY, USA, 2019. Association for Computing Machinery.

[253] ZeenKo. LiteVNA, 2022.

[254] Cheng Zhang, Qiuyue Xue, Anandghan Waghmare, Sumeet Jain, Yiming Pu, Sinan Hersek, Kent Lyons, Kenneth A. Cunefare, Omer T. Inan, and Gregory D. Abowd. SoundTrak. Proceedings of the ACM on Interactive, Mobile, Wearable and Ubiquitous Technologies, 1(2):1–25, 6 2017.

[255] Cheng Zhang, Qiuyue Xue, Anandghan Waghmare, Ruichen Meng, Sumeet Jain, Yizeng Han, Xinyu Li, Kenneth Cunefare, Thomas Ploetz, Thad Starner, Omer Inan, and Gregory D Abowd. FingerPing: Recognizing Fine-grained Hand Poses using Active Acoustic On-body Sensing. Proceedings of the 2018 CHI Conference on Human Factors in Computing Systems, 2018.

[256] Diming Zhang, Jing Jiang, Junye Chen, Qian Zhang, Yanli Lu, Yao Yao, Shuang Li, Gang Logan Liu, and Qingjun Liu. Smartphone-based portable biosensing system using impedance measurement with printed electrodes for 2,4,6-trinitrotoluene (TNT) detection. 70:81–88, 2015.

[257] Dingtian Zhang, Jung Wook Park, Yang Zhang, Yuhui Zhao, Yiyang Wang, Yunzhi Li, Tanvi Bhagwat, Wen Fang Chou, Xiaojia Jia, Bernard Kippelen, Canek Fuentes-Hernandez, Thad Starner, and Gregory D. Abowd. OptoSense. Proceedings of the ACM on Interactive, Mobile, Wearable and Ubiquitous Technologies, 4(3), 9 2020.

[258] Han Zhang, Zheyuan Chen, Jing Dai, Wei Zhang, Yuqian Jiang, and Anhong Zhou. A low-cost mobile platform for whole blood glucose monitoring using colorimetric method. Microchemical Journal, 162:105814, 2021.

[259] Maolin Zhang, Si Chen, Jia Zhao, and Wei Gong. Commodity-level ble backscatter. In Proceedings of the 19th Annual International Conference on Mobile Systems, Applications, and Services, MobiSys '21, page 402–414, New York, NY, USA, 2021. Association for Computing Machinery.

[260] Maolin Zhang, Jia Zhao, Si Chen, and Wei Gong. Reliable backscatter with commodity ble. In IEEE INFOCOM 2020 - IEEE Conference on Computer Communications, pages 1291–1299, 2020.

[261] Pengyu Zhang, Dinesh Bharadia, Kiran Joshi, and Sachin Katti. Hitchhike: Practical backscatter using commodity wifi. In Proceedings of the 14th ACM Conference on Embedded Network Sensor Systems CD-ROM, pages 259–271, 2016.

[262] Pengyu Zhang, Colleen Josephson, Dinesh Bharadia, and Sachin Katti. Freerider: Backscatter communication using commodity radios. In Proceedings of the 13th International Conference on emerging Networking EXperiments and Technologies, pages 389–401, 2017.

[263] Pengyu Zhang, Mohammad Rostami, Pan Hu, and Deepak Ganesan. Enabling practical backscatter communication for on-body sensors. In Proceedings of the 2016 ACM SIGCOMM Conference, pages 370–383, 2016.

[264] Tengxiang Zhang, Xin Zeng, Yinshuai Zhang, Ke Sun, Yuntao Wang, and Yiqiang Chen. ThermalRing: Gesture and Tag Inputs Enabled by a Thermal Imaging Smart Ring. Conference on Human Factors in Computing Systems - Proceedings, 4 2020.

[265] Yang Zhang and Chris Harrison. Tomo: Wearable, low-cost electrical impedance tomography for hand gesture recognition. In Proceedings of the 28th Annual ACM Symposium on User Interface Software & Technology, UIST '15, pages 167–173. Association for Computing Machinery.

[266] Yang Zhang and Chris Harrison. Tomo. pages 167–173, 11 2015.

[267] Yang Zhang, Wolf Kienzle, Yanjun Ma, Shiu S. Ng, Hrvoje Benko, and Chris Harrison. ActiTouch: Robust touch detection for on-skin AR/VR interfaces. In Proceedings of the 32nd Annual ACM Symposium on User Interface Software and Technology, UIST '19, pages 1151–1159. Association for Computing Machinery.

[268] Yang Zhang, Wolf Kienzle, Yanjun Ma, Shiu S Ng, Hrvoje Benko, and Chris Harrison. ActiTouch: Robust Touch Detection for On-Skin AR/VR Interfaces. 2019.

[269] Yang Zhang, Gierad Laput, and Chris Harrison. Electrick: Low-cost touch sensing using electric field tomography. In Proceedings of the 2017 CHI Conference on Human Factors in Computing Systems, CHI '17, pages 1–14. Association for Computing Machinery.

[270] Yang Zhang, Robert Xiao, and Chris Harrison. Advancing hand gesture recognition with high resolution electrical impedance tomography. In Proceedings of the 29th Annual Symposium on User Interface Software and Technology, UIST '16, pages 843–850. Association for Computing Machinery.

[271] Yang Zhang, Chouchang Yang, Scott E Hudson, Chris Harrison, and Alanson Sample. Wall++ room-scale interactive and context-aware sensing. In Proceedings of the 2018 chi conference on human factors in computing systems, pages 1–15, 2018.

[272] Yang Zhang, Junhan Zhou, Gierad Laput, and Chris Harrison. Skintrack: Using the body as an electrical waveguide for continuous finger tracking on the skin. In Proceedings of the 2016 CHI Conference on Human Factors in Computing Systems, CHI '16, page 1491–1503, New York, NY, USA, 2016. Association for Computing Machinery.

[273] Zhihan Zhang, Mallory Parker, Kuotian Liao, Jerry Cao, Anandghan Waghmare, Joseph Breda, Chris Matsumura, Serena Eley, Eleftheria Roumeli, Shwetak Patel, and Vikram Iyer. Biodegradable Interactive Materials, April 2024. arXiv:2404.03130 [cs].

[274] Chen Zhao, Ke-Yu Chen, Md Tanvir Islam Aumi, Shwetak Patel, and Matthew S Reynolds. Sideswipe: detecting in-air gestures around mobile devices using actual gsm signal. In Proceedings of the 27th annual ACM symposium on User interface software and technology, pages 527–534, 2014.

[275] Jian Feng Zhao, Xi Mei Chen, Bo Dong Liang, and Qiu Xia Chen. A review on human body communication: Signal propagation model, communication performance, and experimental issues. Wireless Communications and Mobile Computing, 2017(1):5842310, 2017.

[276] Junhan Zhou, Yang Zhang, Gierad Laput, and Chris Harrison. Aurasense: Enabling expressive around-smartwatch interactions with electric field sensing. In Proceedings of the 29th Annual Symposium on User Interface Software and Technology, UIST '16, page 81–86, New York, NY, USA, 2016. Association for Computing Machinery.

[277] Junyi Zhu, Jackson C Snowden, Joshua Verdejo, Emily Chen, Paul Zhang, Hamid Ghaednia, Joseph H Schwab, and Stefanie Mueller. EIT-kit: An electrical impedance tomography toolkit for health and motion sensing. In The 34th Annual ACM Symposium on User Interface Software and Technology, UIST '21, pages 400–413. Association for Computing Machinery.

[278] Lei Zhu, Huamin Shi, and W. Menzel. Coupling behaviors of quarter-wavelength impedance transformers for wideband cpw bandpass filters. IEEE Microwave and Wireless Components Letters, 15(1):13–15, 2005.

[279] T. G. Zimmerman. Personal area networks: Near-field intrabody communication. IBM Systems Journal, 35(3.4):609–617, 1996.

[280] Thomas G. Zimmerman, Joshua R. Smith, Joseph A. Paradiso, David Allport, and Neil Gershenfeld. Applying electric field sensing to human-computer interfaces. In Proceedings of the SIGCHI Conference on Human Factors in Computing Systems, CHI '95, page 280–287, New York, NY, USA, 1995. Association for Computing Machinery.